Analytic Properties of Potts and Ising Model Partition Functions and the Relationship between Analytic Properties and Phase Transitions in Equilibrium Statistical Mechanics

Siti Fatimah Binti Zakaria

Submitted in accordance with the requirements for the degree of Doctor of Philosophy

The University of Leeds

School of Mathematics

November 2016

The candidate confirms that the work submitted is his/her/their own and that appropriate credit has been given where reference has been made to the work of others.

This copy has been supplied on the understanding that it is copyright material and that no quotation from the thesis may be published without proper acknowledgement.

@2016 The University of Leeds and Siti Fatimah Binti Zakaria

For my parents and family –
my late father Zakaria Zainal Abidin,
my mother Ramah Mohamad,
and my siblings
Kadir, Hafiz, Arif, and Maznah.

Acknowledgements

In the name of Allah The Most Gracious and The Most Merciful.

First and foremost, I would like to express my biggest appreciation to my supervisor, Professor Paul Purdon Martin, for his thoughtful guidance and warm encouragement throughout my Ph.D journey. This research and thesis would not be possible without him. To me, his patience and encouragement are my greatest motivation to keep me strong and compose while being in this journey.

I wish to express my gratitude to Dr Mike Evans, my advisor, for his thoughtful comment especially when I just started my Ph.D. I thank Dr Sandro Azaele (Ph.D transfer assessor) and Dr Alison Parker (second year assessor) for their thought while monitoring my study progress and also to Professor Frank Nijhoff and Professor Uwe Grimm for letting my defence to be an enjoyable experience for me. I specially thank Dr Zoltan Kadar for the time he spent reviewing my thesis and also to Professor Michael E. Fisher for sending me a part of his lecture notes on the 'Fisher zero'.

I would like to also take this opportunity to thank my sponsors, the Ministry of Higher Education Malaysia and the International Islamic University Malaysia. Thank you for giving me the opportunity to further my study and also for supporting me financially.

Also not to forget, my appreciation to all my colleagues and friends in School of Mathematics for making my journey less lonely - especially Huda, Nada, Diana, Mufida, Amani, Eman, Chwas, Ahmed, Raphael, Alex, Konstant, Taysir, Khawlah, and Areena. I also want to thank Craig Hall for his help in setting up my dual-boot computer during my first year.

To my close friends especially Dr Rozaimah, Dr Ummu Atiqah, Fairuz Alwani, Afifah Hanum, Saidatun Nisa', Faieqah, Sarah, K. Fairuz, Syikin, Ernest, K. Juniza, and Fatin, I thank all of you for always be with me from the beginning of my study until the end.

Finally, my special and endless appreciation for my family especially my late father, my mother, and also my brothers and sister for their prayers and support. Words cannot describe how grateful I am for all the sacrifices they have made on my behalf.

Thank you so much for everything. May God bless us.

Abstract

The Ising and Q-state Potts models are statistical mechanical models of spins interaction on crystal lattices. We study the partition functions on a range of lattices, particularly two- and three-dimensional cases. The study aims to investigate cooperative phenomena − how higher level structure is affected by the detailed activity of a very large number of lower level structures. We investigate the analytic properties of the partition functions and their relationship to physical observables in equilibrium near phase transition. Our study is focussed on describing the partition function and the distribution of zeros of the partition function in the complex-temperature plane close to phase transitions. Here we first consider the solved case of the Ising model on square lattice as a benchmark for checking our method of computation and analysis. The partition function is computed using a transfer matrix approach and the zeros are found numerically by Newton-Raphson method. We extend the study of Q-state Potts models to a more general case called the Z_Q-symmetric model. We evidence the existence of multiple phase transitions for this model in case $Q = 5, 6$, and discuss the possible connection to different stages of disordered state. Given sufficient and efficient coding and computing resources, we extend many previously studied cases to larger lattice sizes. Our analysis of zeros distribution close to phase transition point is based on a certain power law relation which leads to critical exponent of physical observable. We evidence for example, that our method can be used to give numerical estimates of the specific heat critical exponent α.

Contents

List of Figures

List of Tables

Nomenclature

Symbols

$\mathbb{N}$	Natural numbers
$\mathbb{R}$	Real numbers
Q	number of spin directions
Z_Q	cyclic group of order Q
β	inverse temperature
T	absolute temperature
k_B	Boltzmann constant
J	interaction strength
$\mathcal{H}, \mathcal{H}_{Ising}, \mathcal{H}_{Potts}$	Hamiltonian functions
$\langle i, j \rangle$	nearest neighbour pair of lattice sites, i and j
$\sigma_I(i)$	spin configuration for Ising model at site i
$\sigma_P(i)$	spin configuration for Potts model at site i
σ_i	spin configuration at site i
Ω	set of all possible configuration states
σ	a configuration state, $\sigma \in \Omega$
$Z, Z', Z_{Ising}, Z_{Potts}$	partition functions
δ_{ij}	the Kronecker delta symbol
$\tilde{V}$	volume
$C_{\tilde{V}}$	specific heat
Λ, Γ, G	graph

d	dimension, $d \in \mathbb{N}$
$\mathcal{T}$	transfer matrix
$\mathcal{P}$	power set
α	specific heat exponent

Abbreviations

fcc	face-centered cubic
hcp	hexagonal close-packed
ferro	ferromagnetic
antiferro	antiferromagnetic
TOL	tolerance or computing error
GMP	GNU multiple precision
NR	Newton-Raphson method
RAM	random accessed memory

Chapter 1

Introduction

This thesis describes our research in statistical mechanics [30, 48, 65]. Statistical mechanics is an area where mathematical modelling is used to understand a physical system. In physics, it is a key problem to predict behaviour of a physical system [35, 46, 101]. This is useful for many applications [18, 43, 85].

Statistical mechanics models the microscopic properties of individual atom and molecule of a material that can be observed in nature, and relates them to the macroscopic or bulk properties [35, 96]. We study the statistical mechanical models of spin variables on a graph, representing the molecular dipoles on the crystal lattice of a physical system − such as a bar magnet.

One example of physical phenomena which can benefit from the statistical mechanical study is the event of phase transition [27, 101]. The study helps in predicting the critical properties of a phase transition by investigating the inner activity of molecular dipoles in a physical system.

The model in this thesis is a model of ferromagnetism [41, 44–46, 68] on solid state material that has a crystalline feature on its atomic scale. From experiment [28, 71, 91, 97], the crystalline structure shows the constituent particles being stack together in a regular and repeated pattern in $\mathbb{R}^3$. This is formed by the translations of some kind of basic cell, for example the translation of a cube to a cubic lattice [31].

In modelling the effective ferromagnetism, the dynamics of the lattice such as the vibrational and bulk motion are ignored. Instead, the dynamic is restricted to the molecular dipoles residing at the lattice sites. The molecular dipole centre of mass remain fixed in its location. We call the model variable represented by the molecular dipole as a spin variable of the crystal lattice. Here the degree of freedom is obtained from the spin orientation. The model is restricted to a system with identical atomic type. The dipole-dipole interactions are short range [4, 41]. Thus in the model we put a short range interaction between two neighbouring spin variables. Here the interaction with external magnetic field is excluded for simplicity. Also for simplicity, two spin variables interact with each other if they are close together. At larger distance, the interaction is assumed to be negligible.

Let $Q \in \mathbb{N}$ be the number of spin orientations. For $Q = 2$ we consider the Ising model [37, 62] which also called the 2-state Potts model [3, 79]. For $Q > 2$ we vary the model in this thesis by the Q-state Potts model and the Z_Q-symmetric model [58, 83].

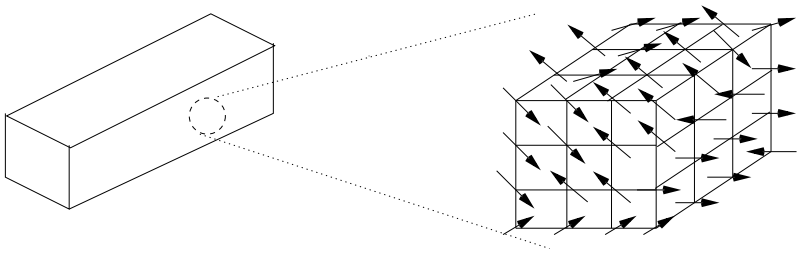

Figure 1.1: Bar magnet and its magnetic dipoles in cubic lattice.

1.1 The Potts models – definitions

The Q-state Potts model is a representation of ferromagnetism in which spins are allowed to be oriented from Q possible spin directions.

The physical spins are assumed to sit at a regular collection of points in $\mathbb{R}^3$, called a *lattice*. For these models, we represent the lattice by a graph [64]. The spin variable is associated to the vertex of the graph. The graph vertices can be thought

as the graph embedding to Euclidean space $\mathbb{R}^3$. The graph and the Potts model are defined as below.

Definition 1.1.1 ([19]). *A directed graph Λ is a triple $\Lambda = (V, E, f)$. The V is a set. The elements $v \in V$ are called vertices. The E is also a set. The elements $e \in E$ are called edges. The f is a function $f : E \to V \times V$. Given $e \in E$ and $v_1, v_2 \in V$, the images $f(e) = \langle v_1, v_2 \rangle$ gives the 'source' and 'target' vertex of edge e.*

Definition 1.1.2. *The distance $d_\Lambda(u, v)$ is the number of edges in the shortest path from u to v. Two vertices $u, v \in V$ are called nearest neighbours if $f(e) = \langle u, v \rangle$ for some $e \in E$ i.e. when $d_\Lambda(u, v) = 1$.*

A function $\sigma : V \to \underline{Q} = \{1, 2, ..., Q\}$ is called a spin configuration for Q-state Potts models. The value in set $\underline{Q}$ is the label representing the Q different spin orientations.

Let Ω be the set of all possible spin configuration states or *microstates* for a Q-state Potts model on a given lattice.

Definition 1.1.3 ([49]). *Let A, B be sets. Then $Hom(A, B)$ is the set of functions $f : A \to B$.*

We have immediately;

Theorem 1.1.1. *Let $\Lambda = (V, E, f)$ be a graph and $Q \in \mathbb{N}$. Then the configuration set on graph Λ is $\Omega = Hom(V, \underline{Q})$.* □

Thus, for a system of N vertices with Q possible spin directions, the total number of microstates $|\Omega| = Q^{|V|} = Q^N$.

In physics, an observable is any physical property of a system which can be experimentally measured. In a model with given Ω we have a corresponding operator:

Definition 1.1.4. *Consider a physical system in the form of a set Ω. A function $\mathcal{O} : \Omega \to \mathbb{R}$ is called an observable of the physical system.*

One possible observable on a system would be the total energy, also known as $\mathcal{H} : \Omega \to \mathbb{R}$, or Hamiltonian. It is the form of $\mathcal{H}$ which determines what kind of physical system we are modelling. Let $J \in \mathbb{R}$ be a constant representing the interaction strength of the nearest neighbour spins. The Hamiltonian of Potts model is defined as follows. Let $\sigma \in \Omega$.

Definition 1.1.5. *The Hamiltonian of Potts model on $\Lambda = (V, E, f)$ is defined as $\mathcal{H}_{Potts}(\sigma) = -J \sum_{\substack{\langle i,j\rangle = f(e), \\ e \in E}} \delta_{\sigma(i)\sigma(j)}$ where the Kronecker delta function,*

$$\delta_{\sigma(i)\sigma(j)} = \begin{cases} 1, & \text{if } \sigma(i) = \sigma(j) \\ 0, & \text{if } \sigma(i) \neq \sigma(j) \end{cases}.$$

The summation is over all the nearest neighbour interaction in Λ.

If $J > 0$ the system is in its lowest energy where all spin variables are oriented in the same direction. This state corresponds to a ferromagnetic state. Conversely, if $J < 0$ each spin variable is forced to be oriented anti-align to its nearest neighbours. This state corresponds to an antiferromagnetic state.

1.2 Partition Function Z

Now we are ready to introduce the main function of this thesis. A partition function denoted as Z is a special function that relates temperature with the states of a spin system. It provides important information on thermodynamic properties of the system [35, 58, 101].

Consider an ensemble of similar systems in a heat bath. The heat bath is a body which has a huge heat capacity that remains its temperature fixed at all times. The volume, pressure, number of particles and all other properties are assumed to be fixed except the energy which is allowed to be transferred to its neighbour. So, any system in contact with the heat bath will eventually reach a thermal equilibrium at

the temperature of the heat bath. This ensemble is called a *canonical ensemble* [10].

The partition function for a system which allows the transfer of energy to its environment while fixing other properties is called a *canonical partition function* or simply a partition function.

Definition 1.2.1. *For a given $\mathcal{H}_\Lambda$ (which requires given graph Λ), the partition function is defined as*

$$Z_\Lambda(\beta) = \sum_{\sigma \in \Omega_\Lambda} \exp(-\beta \mathcal{H}_\Lambda(\sigma)) \tag{1.1}$$

where the summation is over all possible microstates σ of a system and $\beta = 1/(k_B T)$ is the inverse temperature in which T is absolute temperature and k_B is the Boltzmann's constant.

The dimension for the physical quantities ($\beta, \mathcal{H}_\Lambda$ and J) in our model are not restricted to any specific dimension. But we know that the dimension of $\mathcal{H}_\Lambda$ that depends on J must be in inverse relation to β because of the exponent function for the partition function (1.1). The value of $\beta\mathcal{H}_\Lambda$ must be dimensionless.

Denote the Boltzmann weight $x = e^{\beta J}$ and $\widetilde{\mathcal{H}}(\sigma) = -\mathcal{H}_\Lambda(\sigma)/J$. For a given graph Λ, the partition function (1.1) can be written in polynomial form

$$Z_\Lambda(\beta) = \sum_{\sigma \in \Omega_\Lambda} x^{\widetilde{\mathcal{H}}(\sigma)}. \tag{1.2}$$

Suppose we have a system A in a particular configuration state $\sigma^i \in \Omega$ with energy $\mathcal{H}(\sigma^i)$. The probability of a system A to be in the state σ^i is then equal to the ratio of Boltzmann weight of the state σ^i over the sum of the weight of all possible configurations. Let p be the Boltzmann probability distribution $p : \Omega \to [0, 1]$, then

$$\begin{aligned} p(\sigma^i) &= \frac{\exp(-\beta \mathcal{H}_\Lambda(\sigma^i))}{\sum_{\sigma \in \Omega} \exp(-\beta \mathcal{H}_\Lambda(\sigma))} \\ &= \frac{\exp(-\beta \mathcal{H}_\Lambda(\sigma^i))}{Z_\Lambda} \end{aligned} \tag{1.3}$$

where

$$\sum_i p(\sigma^i) = 1.$$

The partition function Z_Λ as denominator is also called a normalizing constant. For simplicity we denote the partition function as Z.

1.3 Relation to physical observables

The role of the partition function Z does not stop at being a normalising constant as in (1.3) but it also leads to thermodynamic properties. In this section, we present some of the thermodynamic properties derived from Z.

The expectation value of an observable quantity $\mathcal{O}$ is given by

$$\langle \mathcal{O} \rangle := \sum_{\sigma \in \Omega} p(\sigma)\mathcal{O}(\sigma). \tag{1.4}$$

From the Boltzmann probability function (1.3), we can obtain the average energy of a system given by

$$\begin{aligned} \langle \mathcal{H} \rangle &= \sum_{\sigma \in \Omega} p(\sigma)\mathcal{H}(\sigma) \\ &= \sum_{\sigma \in \Omega} \frac{e^{-\beta \mathcal{H}(\sigma)}}{Z} \mathcal{H}(\sigma) \\ &= -\frac{\partial(\ln\, Z)}{\partial \beta}. \end{aligned} \tag{1.5}$$

The $\langle \mathcal{H} \rangle$ is also known as the internal energy [33, 35, 65] of a system. The *internal energy* is an energy that is associated with molecular motion. It is the sum of kinetic energy and potential energy at molecular level. This is a function of state.

By the second law of thermodynamics [10, 94], in real process, there exists a function of state called *entropy* [10, 15, 48]. It is a measure of the number of underlying microstates related to macroscopically measurable state [27]. In other words, it is the number of ways for a system to be in a specific macroscopic state [58].

In canonical ensemble (§ 1.2) of similar systems with constant volume and temperature, the entropy is expressed by the sum over the probability of every possible configuration state σ. The entropy S is defined as

$$S = -k_B \sum_{\sigma \in \Omega} p(\sigma) \ln(p(\sigma)). \tag{1.6}$$

Substituting (1.3) into (1.6), we get this relation:

$$S = \frac{\langle \mathcal{H} \rangle}{T} + k_B \ln(Z). \tag{1.7}$$

Similarly, the relation (1.7) can be rewritten as

$$-k_B T \ln(Z) = \langle \mathcal{H} \rangle - TS. \tag{1.8}$$

From the classical thermodynamic relation, the right hand side corresponds to the definition of *Helmholtz free energy* [14]

$$F = \langle \mathcal{H} \rangle - TS. \tag{1.9}$$

This equivalently gives

$$F = -k_B T \ln(Z). \tag{1.10}$$

For a system with constant volume, number of particles and temperature, the maximum entropy S also means that the Helmholtz free energy is a minimum at equilibrium.

From the free energy, the specific heat C_V is defined as the second derivative of logarithm of the partition function with respect to β, i.e.

$$\frac{C_V}{k_B} = -\beta^2 \frac{d^2 \ln Z}{d\beta^2}. \tag{1.11}$$

Further explanation here and elsewhere in physics on other thermodynamic properties can be found in [10, 35, 58, 101].

1.4 Physical motivation

1.4.1 Ising and Potts models

Q-state Potts models are statistical mechanical models of ferromagnetism [41, 44–46, 68] on crystal lattices [85, p. 60]. The case $Q = 2$ corresponds to Ising model via $1 \to +1$ and $2 \to -1$.

Ising [37] showed that one-dimensional Ising model case manifest no phase transition. Later, Peierls showed that at sufficiently low temperature, the Ising model does have ferromagnetism in two or three dimension [12, 70, 78].

One feature of this model is the study of the exact partition function [7, 55] of square lattice Ising model. Onsager [75] successfully described the exact solution of Ising model on square lattice. He considered the eigenvalue of a particular matrix proposed by Kramers and Wannier [44, 45] to find the solution for free energy. Other version of Onsager's solution also described by Kaufman in [40].

Kramers and Wannier [44] considered the exact result of transition temperature. They described the partition function in terms of the largest eigenvalue of certain matrix. A similar method was used by Montroll [66, 67] which calculated the problem separately. Kubo in [47] had also described the matrix formulation related to the degeneracy of largest eigenvalue. Some generalized model with more than two spins can be found in [3, 58, 79, 98] and in three dimension in [72, 73, 75, 89, 90].

1.4.2 Z_Q-symmetric model

The Z_Q-symmetric model [58, p. 295] is a general discrete planar model where the spin takes one of Q possible values distributed around clock-like circle. Detailed description on this model is described in Chapter 6.

One interesting problem for this model is to determine the cross over point, say Q_c where the spin-wave phase [36] would appear. Elitzur, Pearson and Shigemitsu in their paper [22] showed that by using the Villain form [93] of Clock model [21]

the spin-wave phase can be found above $Q = 4$. The study of the cross over point between the two-phase region and the three-phase region has suggested a relation to solvable manifolds of the Andrews-Baxter-Forrester model [2, 36].

The study of the Z_Q model further leads to the study of zeros analytic structure as introduced by Fisher [26]. Martin [57] studied the analytic structure of zeros of the partition function. The zeros distribution suggests that the complex plane may manifests the distribution which describes two- and three-phase regions. This approach explores the cross over point locally for specific value of Q. Martin presented the zeros distribution of the partition function on Z_5- and Z_6-symmetric models in [57, 58].

1.4.3 Onsager's solution

The Ising model was solved exactly on square lattice restricted to no external field by Onsager [75]. His work was later on simplified by his student Kaufman [40] using rotational matrix. The derivation of the Onsager's partition function is discussed in § 4.1 and Appendix § B.

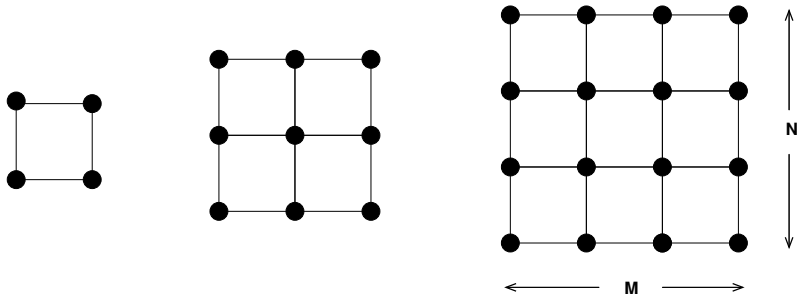

Figure 1.2: Square lattices with different system size N by M.

Let a square lattice have N row and M column (shown in Figure 1.2) with T be the temperature and $B = 0$ is the zero external magnetic field. We present his result for free energy (logarithmic of the partition function) [75] as the following,

$$\lim_{N\to\infty} \ln(Z_{N,N}(B=0,T)) = \ln(2\cosh(\beta J)) + \frac{1}{2\pi}\int_0^{\pi} \ln\left(\frac{1}{2}\left(1+\sqrt{1-\kappa^2\sin^2\phi}\right)\right)d\phi \tag{1.12}$$

where $\kappa = 2\sinh(2\beta J)/\cosh^2(2\beta J)$, β is the inverse temperature and J is the nearest neighbour interaction strength. $Z_{N,M}$ is the partition function for graph in Figure 1.2.

Other review on the work of Onsager and Kaufman exact solution can also be found in [6–8, 35, 58].

1.4.4 What can be computed and what it means

The study of model for ferromagnetism aims to investigate the thermodynamic properties of a physical system [7, 35]. For the Q-state Potts model and for the three-dimensional lattices, the exact results are still unknown.

Lee and Yang [50, 99] showed that the equation of states of phase transition is closely related to the root distribution of the partition function. They proved that under certain conditions the roots always lie on a circle − also known as Lee-Yang circle theorem. They proposed the concept of zeros in the complex plane to study the Ising model in magnetic field.

The thermodynamic properties and the phase transition however can only be explored through the complete distribution of the zeros of the partition function in the complex-temperature plane. Although only the real value has physical meaning, the analytic structure of the distribution surprisingly shows a specific behaviour in the thermodynamic limit [38, 39, 99]. Since the finite lattice partition function is a positive polynomial, the zeros will always stay off the real axis. The zeros may only touch the real axis at the thermodynamic limit. We will show the zeros distribution in details in later chapters.

The study of complex-temperature zeros of partition function for the Ising model on square lattice in zero magnetic field was first discussed by Fisher [26], and also by Abe [1], Katsura [38] and Ono and Suzuki [74]. The singularity of specific heat of the square lattice Ising model is discussed by observing the zeros distribution for finite lattice size and the endpoints of the arc in the zeros distribution.

The study of statistical mechanical model could be continued further by

investigating the model on different system i.e. different crystal lattice structure [31, 85] such as triangular, hexagonal and cubic lattices. See § 2.1.2 for detail.

Other study on triangular and hexagonal lattices Potts model can be found for example in [23, 25, 51, 60, 88, 98].

1.4.5 Phase transition − example of physical phenomena

A *phase transition* [46, p. 103] occurs when there is a thermodynamic change from one phase of matter to another phase. One of the study on phase transition is related to the prediction of critical point for a phase transition − for instance the Curie temperature [41, 43, 48].

The roots of the partition function are used to study the phase transition and critical properties in finite size system [29]. The phase transition occurs when the zeros are distributed in a nice pattern [26] consists of subsets of set of zeros. We called this a *locus of zeros*. This locus cut the real axis of the complex plane at the thermodynamic critical point [87].

The order of phase transition is defined by the behaviour of the derivatives of free energy [58]. It is called first order transition if there is a discontinuity in the first derivative of free energy. Similarly, for higher order transition, it is called n^{th} order if the first discontinuity is at the n^{th} derivative.

For example, consider a graph of specific heat in Figure 1.3. This graph shows the existence of the second order phase transition. Onsager in his square lattice Ising model showed that the phase transition was observed when there is a singularity in the graph of specific heat as shown in this figure.

1.5 Objectives and Aims

We study a model known as Potts model that was introduced by Potts [79]. It is a generalisation of the Ising model that was introduced by Wilhem Lenz to his student, Ernst Ising for his doctoral thesis [7, 12, 79]. The case of Ising model

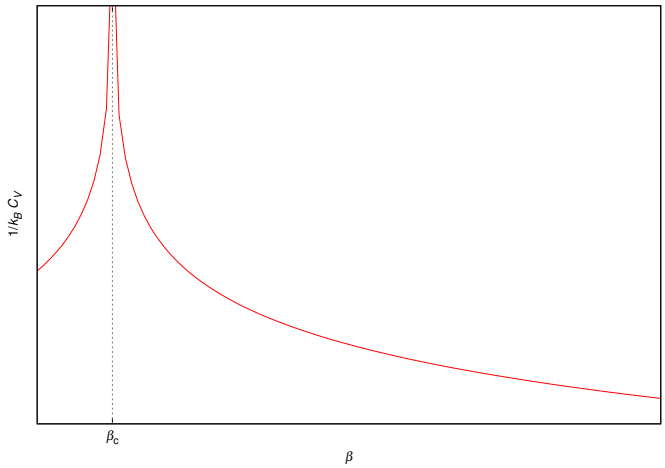

Figure 1.3: Specific heat of square lattice Ising model (Onsager's solution).

on square lattice considered in this thesis serves as a benchmark for checking our computation. Then we further extend this study to a more general case called the Z_Q-symmetric model.

Our interest is to investigate how macroscopic structure may result from a lower level activity of a very large number of microscopic structures. The approach in statistical mechanics can provides prediction when the phase transition of some material can take place.

The objective is to study the partition functions of these models and their distribution of zeros of the partition function in the complex plane close to the phase transition. We aim to investigate the analytic properties of the partition functions and the relationship between analytic properties and phase transition in equilibrium statistical mechanics.

In this thesis, we use the transfer matrix [7, 58] approach for computing the partition function. The partition function is described exactly on the finite lattice size. The zeros of the partition function are then computed and plotted in the complex-temperature Argand plane (see the new result of complex-e^{β} for example in Figure 1.4).

We study the limiting properties of a physical system by analysing the analytical behaviour of partition function as the lattice size changes. This is to relate the

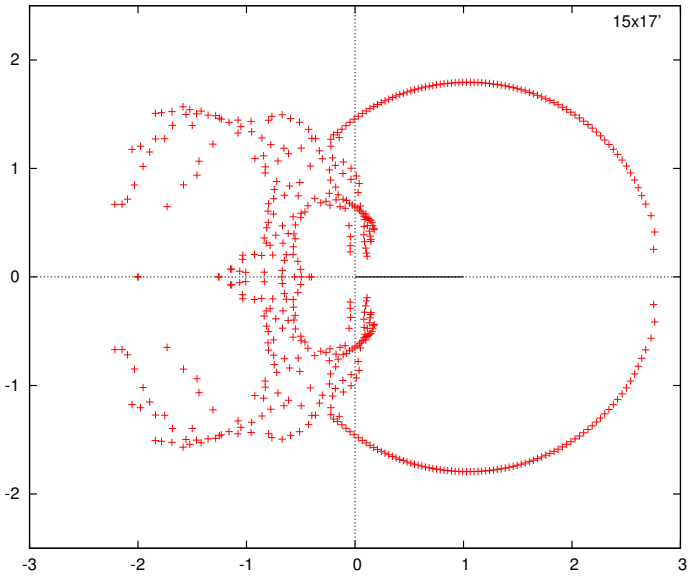

Figure 1.4: 3-state Potts model on 15 by 17 square lattice.

function to the experimental result (see e.g. [7, 35, 101]). With this model, we can aim to describe physical observable properties for a large system [35, 58].

Outline

The outline of this thesis is as follows. The definitions of Potts model and the partition function was initially presented in this chapter. This is continued with the lattice graphs under consideration in Chapter 2. In Chapter 3, the method of computation of transfer matrix is demonstrated. We show the computation by simple examples and state the method for finding roots of the partition function.

The results of zeros distribution for the Ising, Q-state Potts and Z_Q-symmetric models will follow in Chapters 4, 5 and 6, respectively. The description of results starts by considering the solved case of square lattice Ising model in Chapter 4. We implement the zeros finding approach to the Ising model partition function on square lattice in this chapter. Chapters 5 and 6 mainly present our investigation for Q-state Potts and Z_Q-symmetric model partition functions and their zeros distributions.

Later, the analysis of the zeros distribution for Ising and Potts models related

to critical exponent of phase transition is presented in Chapter 7. Finally Chapter 8 will discuss the energy-entropy relation and also discuss the possible existence of multiple phase transitions in Z_Q-symmetric models.

Chapter 2

Models on lattice

This chapter describes other details related to Q-state Potts models. The definitions of the Q-state Potts [3, 20] model was given in § 1.1.

The main object of the study of each model is the partition function. The models are studied on crystal lattices [64] which will be shown in section § 2.1. Then the duality relation on partition function will be introduced.

The modern technology like the X-ray crystallography facility [52, 85, 91, 100] allows us to see the lattice feature in solid state material. For example, the lattice arrangement in aluminium and magnesium is given by face-centered cubic and hexagonal close-packed respectively. This lattice arrangement is following the classification of lattice system described in the field of crystallography [11, 18, 82, 97].

2.1 Graph of regular lattice

This section will describe the lattice graphs under consideration in this thesis. The aim is to compute a partition function Z for a specific lattice graph Λ representing a laboratory size piece of crystal structure. Unfortunately, due to limitation of computing resources, we are not able to compute the Z on very large lattice size. So instead, we consider a sequence of finite lattices which in suitable sense (see § 4.3) extends to contain the laboratory sample.

2.1.1 Thermodynamic limit

The lattice graph is studied based on the motivation from physics. We consider a sequence of finite lattice graphs arranged in increasing lattice sizes. Although the result of physical observable is affected by the finite size effect (explain in § 4.3), at large enough size, some kinds of observation reach stability. The size dependence will vanish in a good model, since the bulk observables of a physical system do not depend strongly on lattice size in the laboratory [87, p. 69].

The study of statistical mechanics aims to predict the bulk behaviour for a physical system i.e. behaviour which is independent from the size of the system. In particular, a sequence of lattices all approaching a 'limit' lattice in a way that captures stable limiting behaviour is needed for the study. This sequence of lattices consists of many lattices of the same type but in different sizes (such as square lattices in Figure 2.2). Although the exact such sequence is not prescribed, from the Onsager's solution [40, 75], we know that the sequence of square lattices does have a stable limit (thermodynamic limit [35, 58]) for suitable observables.

Given these requirements, we define a sequence of lattices which includes computable cases and laboratory size cases. Our hope is that limiting behaviour is already observed in the computable cases. Here, we describe only the first step i.e. defining the sequence.

2.1.2 Lattice graph

Here the specific sequence of graphs for each Hamiltonian will be presented. In two-dimensional case, the regular patterns under consideration are the square, triangle and hexagon. In three-dimensional case, the patterns under consideration are the cubic, tetrahedron and octahedron. In literature what we refer to as the hexagonal pattern is often referred to as the honeycomb lattice.

In crystallography, the crystal structure is described in two ways [85, p. 60]. First they are based on seven basic geometry shapes of unit cell in three-dimensional

space. This type of shape is called the seven crystal systems. The second is related to the way in which atoms are arranged in a unit cell. The unit cell is the smallest structure in three-dimensional space which translated itself to form the whole crystal. This atomic arrangement is called the Bravais lattice [31, 48, 85]. The repetition of regular lattice shape is the nearest approximation towards many real structure of crystalline materials.

2.1.2.1 d-dimensional lattice

The lattice graph is constructed under a graph embedding to d-dimensional Euclidean space $\mathbb{R}^d$ [32] consist of a finite set of regularly spaced sites. The vertex of the graph is associated to the lattice site and the edge of the graph represents the nearest neighbour interaction between vertices.

Let a 1-dimensional Euclidean space $\mathbb{R}$ have collection of point labelled successively by u_i where $i = 1, 2, ... \in \mathbb{N}$. Each site u_i has exactly one successor. The nearest neighbour pair is connected by an edge denoted $\langle u_i, u_{i+1} \rangle$. For a graph with N vertices, this 1-dimensional lattice graph is a finite graph given by Figure 2.1.

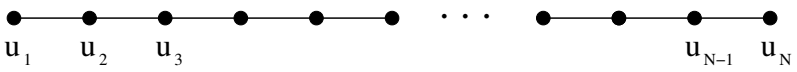

Figure 2.1: The one-dimensional lattice of N sites.

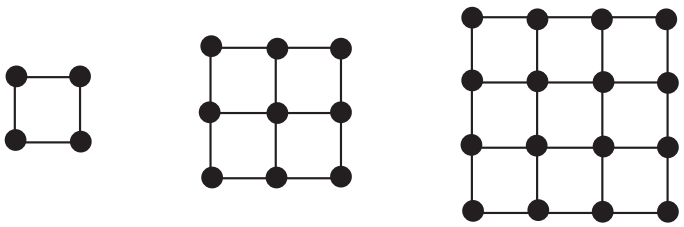

Figure 2.2: Square lattice N by N for $N = 2, 3, 4$.

Similar algorithm for construction applies for higher dimension, $d > 1$. In $\mathbb{R}^2$, the 2-dimensional lattice sites can be denoted by $v_{i,j}$ where the indices $i, j = 1, 2, \cdots \in \mathbb{N}$

correspond to the row vertices i and the column vertices j.

Let each lattice site $v_{i,j}$ have two successive nearest neighbours that are at $i+1$ given j and $j+1$ given i. The nearest neighbour pairs are denoted by $\langle v_{i,j}, v_{i+1,j}\rangle$ and $\langle v_{i,j}, v_{i,j+1}\rangle$. For N row and M column vertices, the graph forms N by M square lattice structure shown in Figure 2.2. We shall denote the d-dimensional lattice by $N_1 \times N_2 \times \cdots \times N_d$ for all number of vertices in respective directions, $N_i \in \mathbb{N}$.

A triangular lattice in contrary has three successive nearest neighbours at each lattice site. The nearest neighbours are given by pairs $\langle v_{i,j}, v_{i+1,j}\rangle$, $\langle v_{i,j}, v_{i,j+1}\rangle$ and $\langle v_{i,j}, v_{i+1,j+1}\rangle$.

The hexagonal lattice in addition is constructed as follows. For $i, j = 1, 2, \cdots \in \mathbb{N}$, if i is odd, the sites will have one successive neighbour, $\langle v_{i,j}, v_{i,j+1}\rangle$ when j is even and two successive neighbours, $\langle v_{i,j}, v_{i,j+1}\rangle$ and $\langle v_{i,j}, v_{i+1,j}\rangle$ when j is odd. Conversely if i is even, the sites will have two successive neighbours, $\langle v_{i,j}, v_{i,j+1}\rangle$ and $\langle v_{i,j}, v_{i+1,j}\rangle$ when j is even and one successive neighbour $\langle v_{i,j}, v_{i,j+1}\rangle$ when j is odd. See illustration in Figure 2.4. For computer program, we can drop the hexagon shape and compute the partition function by layering the lattice into a rectangular shape.

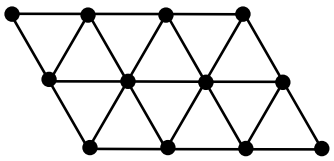

Figure 2.3: Triangular lattice.

2.1.2.2 Dense sphere packing

In this thesis we consider two types of dense sphere packing which are the face-centered cubic (fcc) and the hexagonal close packing (hcp).

The face-centered cubic packing is obtained from a simple cubic geometry. At each vertex point of a cubic lattice, there exist one spin variable and for each face of the cubic, there exist another spin variable. Each vertex point is assumed to be

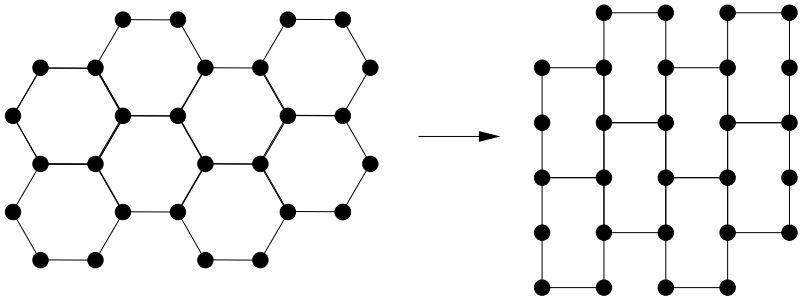

Figure 2.4: Hexagonal lattice (left) to rectangular graph layering (right) for computer program.

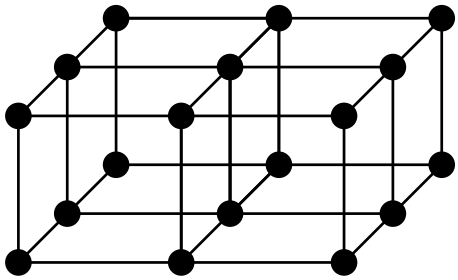

Figure 2.5: Cubic lattice.

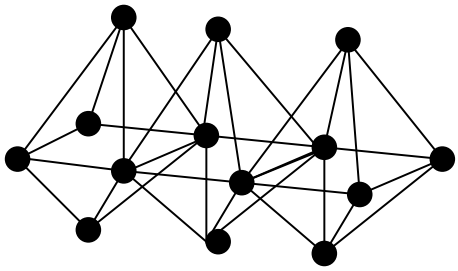

Figure 2.6: Octagonal lattice i.e. face-centered cubic lattice.

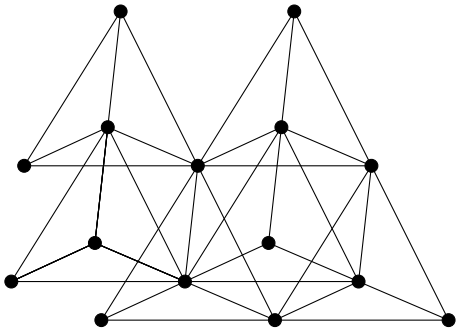

Figure 2.7: Tetragonal lattice i.e. hexagonal close-packed lattice.

a sphere of radius 1. See Figure 2.8. The cubic shape is the unit cell of the lattice. The dash lines correspond to edges in the lattice graph.

The length of each edge of the cube is $\sqrt{8}$ and the diagonal distance of each face is 4. In total, there are 4 spheres in the cubic unit cell of this face-centered cubic lattice.

A crystal lattice has dense sphere packing if it has highest number of atomic density in a unit cell. The number of atomic density is also called the atomic packing factor representing the fraction of volume occupied by atoms in a unit cell over the volume of the same unit cell [85] i.e.

$$\frac{4\pi(\frac{4}{3})}{(\sqrt{8})^3} = \frac{\pi}{\sqrt{18}}.$$

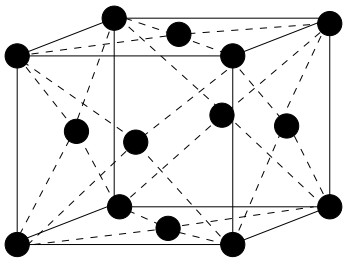

Figure 2.8: Structure showing the face-centered cubic lattice point arrangement in a unit cell.

Likewise, the case of hexagonal close packing has the same density packing i.e. $\frac{\pi}{\sqrt{18}}$. Their unit cells are occupied by the same number of atoms that is 12 atoms but are different by their packing sequence.

The packing construction is described based on the pattern of each layer of the lattice. See Figure 2.9 for illustration. For the face-centered cubic, the packing structure follows the successive layer with $\overline{ABC}$ sequence whereas the packing sequence for the hexagonal close-packed follows the $\overline{AB}$ pattern. The overline notation such as in the $\overline{AB}$ pattern means the repetition of atomic packing sequence in each lattice layer (first layer in position A, then second layer in position B, then repeat the position back to A and B and so on). More detailed explanation can be found in the book by Shackelford [85] and Hales [31].

We describe the dense sphere packing by the illustration of repeated polyhedra glued together forming a finite three-dimensional lattice. This choice assists the computation of the transfer matrix which will be explained in the next chapter. We call the face-centered cubic and the hexagonal close-packed as the octagonal and tetragonal lattices respectively.

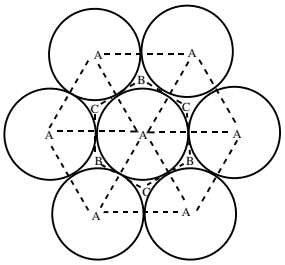

(a) $\overline{ABC}$ stacking sequence.

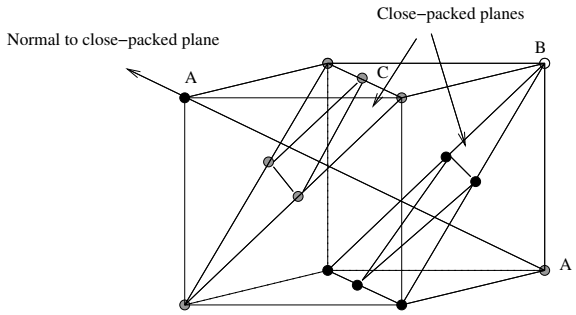

(b) Face-centered cubic.

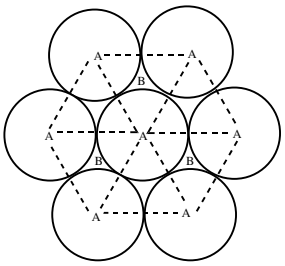

(c) $\overline{AB}$ stacking sequence.

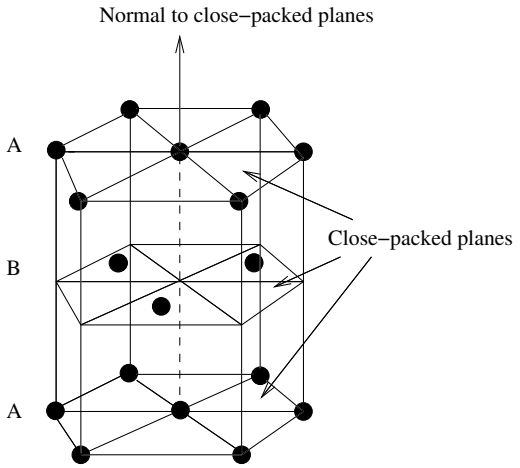

(d) Hexagonal close-packed.

Figure 2.9: Face-centered cubic, hexagonal close-packed and their stacking sequence respectively.

2.1.3 Boundary condition

Consider a finite cubic lattice $N_x \times N_y \times N_z$ embedded in $\mathbb{R}^3$. The rest of the $\mathbb{R}^3$ space is left empty (vacuum). The condition separating the vacuum space from the filled spaced is called the boundary condition. We call the outer sites of the lattice

as the boundary sites or exterior sites. The inner sites are called interior sites (see Figure 2.11). In general, each lattice site has $2d$ nearest neighbours except at the boundary [17].

The type of boundary condition is related to interaction among the boundary sites. Figures 2.2 and 2.7 are examples of lattices with open boundary condition whereas Figure 2.10 is an example of a lattice with periodic boundary condition in vertical direction.

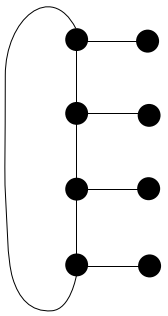

Figure 2.10: 4 by 2 square lattice with periodic boundary condition in vertical direction.

In addition to these two types, we can also study many other lattice graphs, for example, the graph with duality condition [7, 16]. See Figure 2.14 for this example. A concept of duality will be explain in the next section.

For the finite case, the boundary condition has significant role affecting the result of the partition function. For N by M lattices, the ratio of the number of vertices at the boundary over vertices in the whole lattice is given by

$$r = \frac{2N + 2M - 4}{2NM}. \tag{2.1}$$

The larger the lattice, the smaller this ratio will be. At thermodynamic limit, this ratio $r \to 0$ as $NM \to \infty$. We are interested in models where the effects of the boundary conditions vanish in the thermodynamic limit.

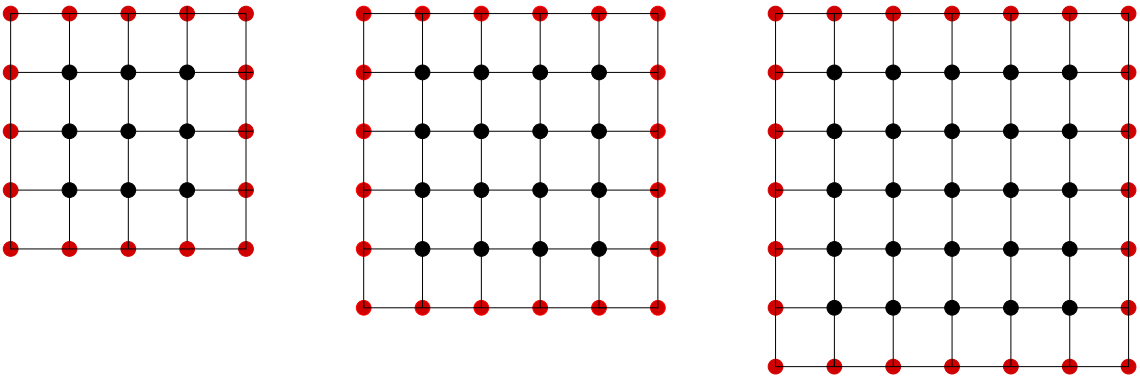

Figure 2.11: Increasing sizes of square lattices. The red sites highlight the spins at boundary and the black sites are the interior sites.

2.2 Duality

In this section, the concept of duality transformation [83] will be introduced.

Let $G = (V, E, f)$ be a graph defined as in § 1.1.

Definition 2.2.1 ([95]). *A curve is the image of a continuous map from* $[0, 1]$ *to* $\mathbb{R}^3$. *A polygonal curve is a curve composed of finitely many line segments. It is a polygonal* $u, v-$*curve when it starts at* u *and ends at* v. *It has no self crossing with individual polygonal curve.*

Definition 2.2.2 ([95]). *A drawing of a graph* G *is a function* $\tilde{f}$ *defined on* $V \cup E$ *that assigns each vertex* v *a point* $\tilde{f}(v)$ *in the plane and assigns each edge with endpoints* u, v *a polygonal* $\tilde{f}(u), \tilde{f}(v)-$*curve i.e.* $\tilde{f} : V \to \mathbb{R}^3$ *and* $\tilde{f} : E \to \tilde{f}(E)$. *The images of vertices are distinct. A point in* $\tilde{f}(e) \cap \tilde{f}(e')$ *that is not a common endpoints is a crossing. The curve cannot have a changing direction at the crossing point.*

Definition 2.2.3 ([95]). *Let* $G = (V, E, f)$ *be a graph. The graph* G *is planar if it has a drawing* $\tilde{f}$ *without crossings. Such drawing is a planar embedding of* G. *A plane graph is a particular planar embedding of a planar graph.*

For any planar graph G, we can form a related plane graph called its *dual*. Here we introduce a notion of face F. A face is a region bounded by edges including the

outer infinite region. Let F_G be the set of faces in G.

Suppose $G^* = (V^*, E^*, f^*)$ be another planar graph that is a dual to G. The graph G^* has the following construction. The set of vertices $v^* \in V^*$ corresponds to the face $F_i \in F_G$. For each $e \in E$ with face F_i on one side and F_j on another side, the endpoint of edge $e^* \in E^*$ are the vertices $v^*, w^* \in V^*$ that represent the faces F_i, F_j of G.

Now, we introduce a notion of a body that is region bounded by faces, separating its inner and outer regions.

Let $L = (V, E, f)$ be a graph defined as in § 1.1. A graph L embedded in Euclidean space $\mathbb{R}^3$ is a 1-to-1 function $\phi_1 : V \to \mathbb{R}^3$ and a continuous function $\phi_2 : \bigcup_{e\in E}^{[0,1]_e} \to \mathbb{R}^3$ that is also 1-to-1 on $\bigcup_{e\in E}^{[0,1]_e}$ such that $\{\phi_2(0), \phi_2(1)\} = \phi(f(e))$. The $[0,1]_e$ corresponds to the edge in the graph. The embedding of graph L has also a 1-to-1 function $\phi_3 : \bigcup_{p\in F_L}^{([0,1]\times[0,1])_p} \to \mathbb{R}^3$. The $([0,1] \times [0,1])_p$ corresponds to the face of the graph L.

Consider for example, the embedding for a cubic graph $L = (V, E, f)$. The body of a cubic is bounded by square faces $p \in F_L$. Let $L^* = (V^*, E^*, f^*)$ be the dual graph of L. The graph L^* has the following construction. The vertex of L corresponds to the body of L^*. The edge of L is then corresponds to the face of L^*. Also the face of L corresponds to the edge of L^* which is perpendicular to the surface of the face L. Finally the body of L corresponds to the point of L^* which located in the center of the cubic L. The dual graph for a cubic graph is again a cubic graph.

Figure 2.12 present the illustration of a square lattice and its dual, which is a self-dual up to boundary condition. Figure 2.13 in addition manifests the graph of hexagonal lattice and its dual graph i.e. the triangular lattice. The case shown in Figure 2.14 has been studied by Chen, Hu and Wu [16].

A dual of a model is a mapping of a model to another model. For example, a dual of a 2-dimensional Ising model using a certain transformation, could be exactly

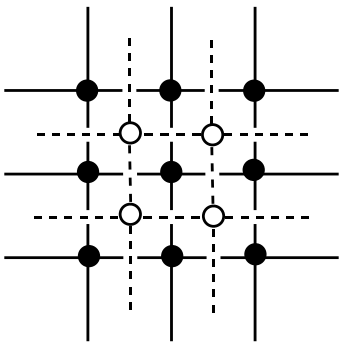

Figure 2.12: Square lattice and its dual.

rewritten as another 2-dimensional Ising model [42, 83]. The high-temperature regions of the original Ising model is mapped to the low-temperature regions of its dual, and vice versa. This is a self-dual model which had been showed by Kramers and Wannier [44].

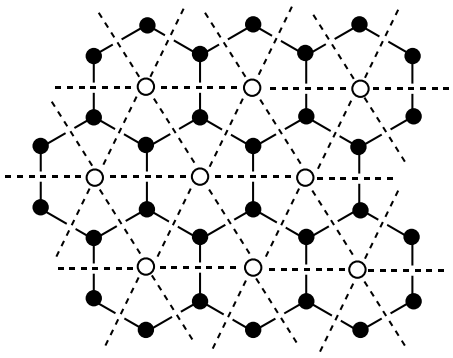

Figure 2.13: Hexagonal lattice and its dual, a triangular lattice.

The duality transformation on lattice model is a useful tool for passing information of one model to its dual. The duality relation for 2-dimensional Q-state Potts model will be given in § 2.2.2.

2.2.1 Z in dichromatic polynomial

Here we derive the partition function in a dichromatic polynomial form. We rewrite the partition function which will allow us to express the duality relation in the partition function. It relates the graph G and its dual graph G^*.

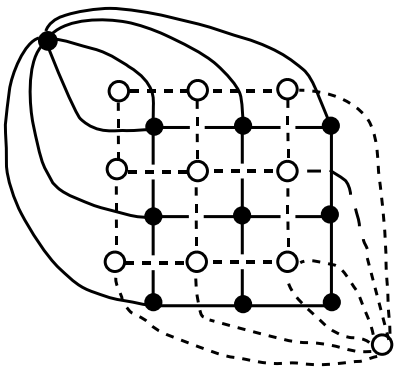

Figure 2.14: Self-dual square lattice.

With some modification, the partition function can be written in terms of graph G and its subgraph. Let $G' \subseteq G$, $V_{G'} = V$ and $E_{G'} \subseteq E$. Recall $x = e^{\beta J}$. For simplicity, let the interaction strength $J = 1$ and introduce a new variable $v = x - 1$. For writing purposes, we write $\sigma(j)$ as σ_j for any $j \in \mathbb{N}$.

The partition function (1.1) for Q-state Potts model can be written in terms of v,

$$\begin{aligned} Z_G &= \sum_{\sigma\in\Omega} \exp(-\beta\mathcal{H}(\sigma)) \\ &= \sum_{\sigma\in\Omega} \exp(\beta J \sum_{\substack{\langle i,j\rangle = f(e),\\ e\in E}} \delta_{\sigma_i\sigma_j}) \\ &= \sum_{\sigma\in\Omega} \prod_{\substack{\langle i,j\rangle = f(e),\\ e\in E}} \exp(\beta\delta_{\sigma_i\sigma_j}) \\ &= \sum_{\sigma\in\Omega} \prod_{\substack{\langle i,j\rangle = f(e),\\ e\in E}} (1 + v\delta_{\sigma_i\sigma_j}) \end{aligned} \tag{2.2}$$

where

$$(1 + v\delta_{\sigma_i\sigma_j}) = \begin{cases} 1, & \text{if } \sigma_i \neq \sigma_j \\ x, & \text{if } \sigma_i = \sigma_j \end{cases}.$$

The expansion of this relation will express Z in terms of a dichromatic polynomial [5, 56, 58]. One of the possible ways to describe the equation (2.2) is by considering a power set.

Definition 2.2.4. *Given a set A, the power set $\mathcal{P}$ of A is the set of all subsets of A.*

Alternatively, we call the edge in the graph a bond. Let $\mathcal{P}$ be the power set of the set of bonds in E to $Z_2 = \{0, 1\}$, i.e. $\mathcal{P} : E \to Z_2$. Then

$$\begin{aligned} Z_G &= \sum_{\sigma \in \Omega} \prod_{\substack{\langle i,j \rangle = f(e), \\ e \in E}} (1 + v\delta_{\sigma_i \sigma_j}) \\ &= \sum_{\sigma \in \Omega} \sum_{E_{G'} \in \mathcal{P}(E)} v^{|E_{G'}|} \prod_{\substack{\langle i,j \rangle = f(e), \\ e \in E_{G'}}} (\delta_{\sigma_i \sigma_j}). \end{aligned} \tag{2.3}$$

The first summation is over all possible configuration of Ω. The second summation is over the elements of the power set $\mathcal{P}$ of the set of edges. See illustration in Figure 2.15. The $E_{G'}$ can be illustrated by bond denoted with 0 and 1; respectively corresponds to missing bond and filled bond. We call this a bond covering 0 and 1 respectively.

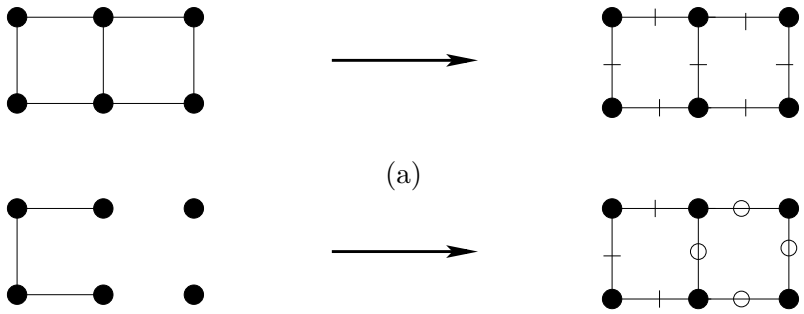

(a)

(b)

Figure 2.15: Set of bonds $E_{G'}$ can be illustrated by bond 0 and 1.

The expression $v^{|E_{G'}|} \prod_{\substack{\langle i,j \rangle = f(e), \\ e \in E_{G'}}} (\delta_{\sigma_i \sigma_j})$ is forced to zero for every configuration summation which all the spins connected by filled bonds that are not aligned.

Then the dichromatic polynomial is as the following:

$$Z_G = \sum_{G' \subseteq G} v^{|E_{G'}|} Q^{|C(G')|} \tag{2.4}$$

where $|C(G')| = c$ is the number of connected clusters in G', including isolated vertices. The connected cluster refer to the isolated sublattice with vertices connected by one or more edges and also the individual vertex (with no edge).

The value of Q^c is the total number of configurations in which the filled bonds form c connected clusters. Refer illustration below for examples.

a) b)

Figure 2.16: Example of connected cluster including its isolated vertices with a)$|C(G')| = 4$ and b)$|C(G')| = 3$.

For the 2-state Potts model, let $|E| = L$ be the total number of edges and $|V| = N$ be the number of vertices. Again by equation (2.2) we take

$$\begin{aligned} Z_G &= \sum_{\sigma\in\Omega} \prod_{\substack{\langle i,j\rangle=f(e),\\ e\in E}} (1 + v\delta_{\sigma_i\sigma_j}) \\ &= \sum_{\sigma\in\Omega} \prod_{\substack{\langle i,j\rangle=f(e),\\ e\in E}} (1 + (e^{\beta} - 1)\delta_{\sigma_i\sigma_j}) \\ &= \sum_{\sigma\in\Omega} \prod_{\substack{\langle i,j\rangle=f(e),\\ e\in E}} \left(\frac{e^{\beta}+1}{2} + \frac{e^{\beta}-1}{2}(2\delta_{\sigma_i\sigma_j} - 1)\right). \end{aligned} \tag{2.5}$$

Alternatively, the bond coverings mentioned earlier may be reinterpreted corresponding to the possible choices of the new summation in the expansion of the product in equation (2.5). A bond covering corresponds to the number of edges at each vertex. The lattice graph has even bond covering if each vertex of the subgraph G' has even number of edges.

Factor out the largest term of the product,

$$\begin{aligned} Z_G &= \sum_{\sigma\in\Omega}\sum_{E_{G'}\in\mathcal{P}(E)}\left(\frac{x+1}{2}\right)^{L-|E_{G'}|}\left(\frac{x-1}{2}\right)^{|E_{G'}|}\prod_{\substack{\langle i,j\rangle=f(e),\\ e\in E_{G'}}}(2\delta_{\sigma_i\sigma_j}-1) \\ &= \left(\frac{x+1}{2}\right)^{L}\sum_{\sigma\in\Omega}\sum_{E_{G'}\in\mathcal{P}(E)}\left(\frac{x-1}{x+1}\right)^{|E_{G'}|}\prod_{\substack{\langle i,j\rangle=f(e),\\ e\in E_{G'}}}(2\delta_{\sigma_i\sigma_j}-1). \end{aligned} \tag{2.6}$$

(a) (b)

Figure 2.17: Examples of non-even bond covering.

Example 2.2.1. Given a graph G with open boundary condition. For the expression $\sum_{\sigma\in\Omega}\prod_{\substack{\langle i,j\rangle=f(e),\\ e\in E_{G'}}}(2\delta_{\sigma_i\sigma_j}-1)$ the individual case shown in Figure 2.17a and 2.17b have value

$$\begin{aligned} \sum_{\sigma\in\Omega}(2\delta_{\sigma_1\sigma_2}-1) &= 0 \\ \sum_{\sigma\in\Omega}(2\delta_{\sigma_1\sigma_2}-1)(2\delta_{\sigma_2\sigma_3}-1) &= 0. \end{aligned}$$

respectively.

The expression $\sum_{\sigma\in\Omega}\prod_{\substack{\langle i,j\rangle=f(e),\\ e\in E_{G'}}}(2\delta_{\sigma_i\sigma_j}-1)$ always equal to 0 when the subgraph G'

describes the non-even covering of G; i.e.

$$\begin{aligned}
\sum_{\sigma\in\Omega}\prod_{\substack{\langle i,j\rangle=f(e),\\ e\in E_{G'}}}(2\delta_{\sigma_i\sigma_j}-1) &= \sum_{\sigma\in\Omega}(2\delta_{\sigma_i\sigma_j}-1)\\
&= \sum_{\sigma\in\Omega}2\delta_{\sigma_i\sigma_j}-\sum_{\sigma\in\Omega}1\\
&= 2\sum_{\sigma\in\Omega}\delta_{\sigma_i\sigma_j}-2^N\\
&= 2.2^{N-1}-2^N\\
&= 0. \qquad (2.7)
\end{aligned}$$

Thus we have,

$$\begin{aligned}
Z &= \left(\frac{x+1}{2}\right)^L 2^N \sum_{\substack{E_{G'}\in\mathcal{P}(E),\\ \text{even covering } G'}}\left(\frac{x-1}{x+1}\right)^{|E_{G'}|}\\
&= \left(\frac{x+1}{2}\right)^L 2^N \sum_{\text{even covering}}(\tanh(\beta/2))^{|E_{G'}|} \qquad (2.8)
\end{aligned}$$

The above formulation is another way of writing the function. The partition function is derived by the bond covering in the dual lattice. See also Martin [56].

2.2.2 Duality relation for partition function

Now, consider a lattice graph $D = (V_D, E_D, f_D)$ as the dual of graph G. For any subgraph $G' \subseteq G$, there exist subgraph $D' \subseteq D$ such that the E_D is the complement of set E. Then the number of edges in subgraph of dual lattice D' is $|E_{D'}| = L - |E_{G'}|$. Some islands are formed around cluster G'. The partition function of graph D is

$$Z_D = 2x^{|E_D|}\sum_{\text{island } I} x^{-|l(I)|} \qquad (2.9)$$

where $l(I)$ is the circumference of island I.

A 2-dimensional 2-state Potts (Ising) model partition function is invariant up to

the boundary condition under this transformation [58, §1.5]

$$x^{-1} \leftrightarrow \frac{x-1}{x+1}. \tag{2.10}$$

For arbitrary value of spin state Q, the duality has the following relation:

$$x \leftrightarrow \frac{x+(Q-1)}{x-1}. \tag{2.11}$$

A model on a square lattice is one simple example of this duality. It has the self-duality properties which holds up to the boundary.

Example 2.2.2. For the case of 2 by 2 square lattice with $Q = 2$, the partition function is

$$Z_{G_{2\times 2}}(x) = 2x^4 + 12x^2 + 2. \tag{2.12}$$

By equation (2.9), the partition function of the dual graph will be

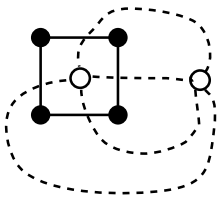

$$Z_{D_{2\times 2}}(x) = 2x^4 + 2. \tag{2.13}$$

Applying the duality relation on $Z_{D_{2\times 2}}$, then

$$\begin{aligned} Z_{D_{2\times 2}}\left(\frac{x+1}{x-1}\right) &= 2\left(\frac{x+1}{x-1}\right)^4 + 2 \\ &= \frac{2}{(x-1)^4} Z_{G_{2\times 2}}. \end{aligned} \tag{2.14}$$

Now, consider an example of a self-dual polygonal lattice that have 2 vertices and 2 edges.

Example 2.2.3. The drawing of the 2-gon is as below:

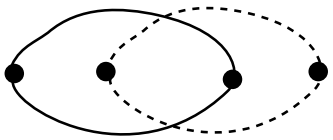

The partition functions are

$$\begin{aligned} Z_{G_{2\text{-gon}}}(x) &= Z_{D_{2-\text{gon}}}(x) = 2x^2 + 2, \\ Z_{D_{2\text{-gon}}}\left(\frac{x+1}{x-1}\right) &= 2\left(\frac{x+1}{x-1}\right)^2 + 2 \\ &= \frac{2}{(x-1)^2} Z_{G_{2\text{-gon}}}. \end{aligned}$$

Applying the transformation twice will reproduce the original equation. We can see for example in the duality transformation graph later in § 4.4 that the zeros of these two polynomial partition functions are invariant in some regions of the graph.

In general, we write these two polynomials of a graph and their duals as follows. Let P be some polynomial in Z_G, then

$$\begin{aligned} Z_G(x) &= 2^N \left(\frac{x+1}{2}\right)^{|E(G)|} P\left(\frac{x-1}{x+1}\right), \\ Z_D(x) &= 2x^{|E(D)|} P\left(\frac{1}{x}\right). \end{aligned}$$

The duality concept is a useful tool for validating any result found using our calculation. This validation is done by reproducing and comparing the zeros distribution of a specific lattice with the known result from previous study [35, 101].

We have described the lattice graph under study for this thesis. The duality relation has also been introduced here. Next chapter is devoted to present the computation technique for the partition function.

Chapter 3

Computation for partition function

In this chapter we present the computation of a transfer matrix [7, 58] for the partition function on finite lattice. We begin with an example of model configurations on lattice in the first section. Then it is followed by the description of the partition vector and transfer matrix. The final section will briefly stated the zeros finding for the partition function.

Initially a brute-force approach [81] is used for computation where the Hamiltonian is directly substituted into the partition function (1.1). This approach requires long period of time and requires many calculations as the lattice size increases. The number of configuration states increases exponentially with respect to number of vertices on graph.

For this reason, a better approach is needed to reduce the number of calculations for the partition function. For that we use a transfer matrix approach.

3.1 Models on lattice – example

In this chapter, we consider the Q-state Potts model on a square lattice. Let a square lattice have discrete variables called vertices with associated spin which can

take any value $\underline{Q} = \{1, 2, ..., Q\}$ representing the spin directions.

Recall Definition 1.1.1 of a graph. Let $\Gamma = (V, E, f)$ be a square lattice graph. Then $|V|$ is the number of vertices in the lattice. The total number of configuration states is given by $|\Omega| = Q^{|V|}$. The state $\sigma = \{\sigma_i | i$ is indexed for location of the spin$\} \in \Omega$. Each spin variable interacts with its nearest neighbours will gives value 1 if the pair spins in the same direction and 0 otherwise.

Figure 3.1 shows all possible microstates for 2 by 2 square lattice. The spin up denoted as '+' and down as '−' correspond to spin 1 and 2 respectively. For a 2-state Potts model on 2 by 2 square lattice, Ω is given by

$$\begin{aligned} \Omega &= \{(1,1,1,1),(1,1,1,2),(1,1,2,1),(1,1,2,2), \\ &\quad (1,2,1,1),(1,2,1,2),(1,2,2,1),(1,2,2,2), \\ &\quad (2,1,1,1),(2,1,1,2),(2,1,2,1),(2,1,2,2), \\ &\quad (2,2,1,1),(2,2,1,2),(2,2,2,1),(2,2,2,2)\} \qquad (3.1) \\ |\Omega| &= 2^4 = 16\,. \end{aligned}$$

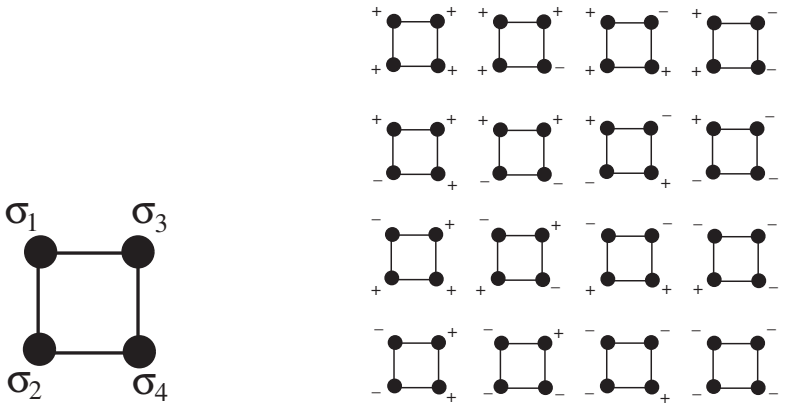

(a) (b)

Figure 3.1: 2 by 2 square lattices.

Recall Definition 1.1.5 of the Q-state Potts model Hamiltonian. For any $\sigma^{(i)} =$

$(\sigma_1, \sigma_2, \sigma_3, \sigma_4) \in \Omega$, if $\sigma^{(1)} = (1,1,1,1)$ and $\sigma^{(2)} = (1,2,1,2)$, we have Hamiltonian

$$\begin{aligned} \mathcal{H}(\sigma^{(1)}) &= -J(\delta_{\sigma_1\sigma_2} + \delta_{\sigma_2\sigma_4} + \delta_{\sigma_1\sigma_3} + \delta_{\sigma_3\sigma_4}) \\ &= -J(1+1+1+1) = -4J \end{aligned}$$

and

$$\begin{aligned} \mathcal{H}(\sigma^{(2)}) &= -J(\delta_{\sigma_1\sigma_2} + \delta_{\sigma_2\sigma_4} + \delta_{\sigma_1\sigma_3} + \delta_{\sigma_3\sigma_4}) \\ &= -J(0+1+1+0) = -2J. \end{aligned}$$

Computing the Hamiltonian for all its microstates and $x = e^{\beta J}$ gives partition function

$$\begin{aligned} Z &= 2e^{4\beta J} + 12e^{2\beta J} + 2 \\ &= 2x^4 + 12x^2 + 2. \end{aligned}$$

This is the result we see in equation (2.12).

3.2 Partition Vector and Transfer Matrix

This section will describe the approach used to expedite the computation of the partition function. For this purpose, we use the partition vector and transfer matrix approach.

The Hamiltonian information on the lattice model is arranged into a vector in the space of all configurations of the boundary spin variables. We call this a partition vector. We describe in details as follows.

For any lattice graph, we denote $\{c\}$ as the set of all exterior sites. The set of microstate of graph G is denoted Ω_G. Let V_G be all vertices in a graph G. The $V' \subseteq V_G$ is the set of exterior on the graph with set of state $\Omega_{V'}$. Denote $\sigma_B \in \Omega_{V'}$ as the spin configurations at boundary. A set of microstates given fixed spin configurations at boundary is denoted as $\Omega_{V_G}|_{\sigma_B} \subset \Omega_G$.

Example 3.2.1. Let $\Gamma = (V_\Gamma, E_\Gamma, f)$ be a graph of 2 by 2 square lattice for 2-states Potts model shown in Figure 3.1. Denote $V_\Gamma = \{\sigma_1, \sigma_2, \sigma_3, \sigma_4\}$ and $V' = \{\sigma_3, \sigma_4\} \subset V_\Gamma$. The set of all configuration states Ω_Γ is given by (3.1). Let spin configurations at boundary given by $\Omega_{V'}$, i.e.

$$\Omega_{V'} = \{(1,1),(1,2),(2,1),(2,2)\}.$$

So if $\sigma_{B_1} = (1,1)$ and $\sigma_{B_2} = (2,1)$, we have

$$\begin{aligned} \Omega_\Gamma|_{(1,1)} &= \{(1,1,1,1),(1,2,1,1),(2,1,1,1),(2,2,1,1)\} \\ \Omega_\Gamma|_{(2,1)} &= \{(1,1,2,1),(1,2,2,1),(2,1,2,1),(2,2,2,1)\}. \end{aligned}$$

The partition function with the fixed spin configurations at σ_B is given by

$$Z_\Gamma^{V'}|_{\sigma_B} := \sum_{\sigma \in \Omega_\Gamma|\sigma_B} \exp(-\beta \mathcal{H}(\sigma)).$$

Definition 3.2.1. *The partition vector $Z_G^{V'}$ is the vector arrangement in space of all fixed boundary or exterior sites of a lattice system. For $\sigma_B \in \Omega_{V'}$, we have*

$$Z_G^{V'} = \{Z_G^{V'}|_{\sigma_1}, Z_G^{V'}|_{\sigma_2}, ...\}.$$

The full partition function is then defined as

$$Z_G = \sum_{\sigma_B \in \Omega_{V'}} Z_G^{V'}|_{\sigma_B}. \tag{3.2}$$

This vector arrangement can produce a partition function for two combined lattice graphs. A bigger lattice can be formed by combining two lattices through a vector multiplication.

Definition 3.2.2. *Let G, G' be two lattice graphs. For the union of two graphs $G \cup G'$ we have*

$$\begin{aligned} V_{G \cup G'} &= V_G \cup V_{G'} \\ E_{G \cup G'} &= E_G \cup E_{G'}. \end{aligned}$$

The E is the set of edges and $E_G \cap E_{G'} = \emptyset$.

The partition function of the new graph GG' is given by a summation of the product of partition vectors for graph G and G' (as in Definition 3.2.1). This is given by

$$Z_{GG'} = \sum_{\sigma \in \Omega_{V'}} (Z_G^{V'}|_\sigma)(Z_{G'}^{V'}|_\sigma). \tag{3.3}$$

This equation is given by the Chapman-Kolmogorov theorem [76]. See Figure 3.3 for example of a combined graph.

Theorem 3.2.1 (Chapman-Kolmogorov [76])**.** *Let G and G' be graphs such that $E_G \cap E_{G'} = \emptyset$. Let GG' denote $G \cup G'$ and $V' = V_G \cap V_{G'}$. Then*

$$Z_{GG'} = \sum_{\sigma \in \Omega_{V'}} (Z_G^{V'}|_\sigma)(Z_{G'}^{V'}|_\sigma) = Z_G^{V'} Z_{G'}^{V'}. \tag{3.4}$$

Proof. Recall partition function (1.1). For graph $GG' = G \cup G'$, we have

$$Z_{GG'} = \sum_{\sigma \in \Omega_{V_{GG'}}} \exp(\beta \mathcal{H}_{GG'}(\sigma)). \tag{3.5}$$

For $E_G \cap E_{G'} = \emptyset$ and $\sigma \in \Omega_{V_{GG'}}$,

$$\mathcal{H}_{GG'}(\sigma) = \mathcal{H}_G(\sigma) + \mathcal{H}_{G'}(\sigma).$$

For $V' = V_G \cap V_{G'}$, we have

$$\begin{aligned} Z_{GG'} &= \sum_{\sigma \in \Omega_{V_{GG'}}} (\exp(\beta \mathcal{H}_G(\sigma)))\,(\exp(\beta \mathcal{H}_{G'}(\sigma))) \\ &= \sum_{\tilde{\sigma} \in \Omega_V} \left(\sum_{\sigma \in \Omega_{V_G}|_{\tilde{\sigma}}} \exp(\beta \mathcal{H}_G(\sigma)) \right) \left(\sum_{\sigma \in \Omega_{V_{G'}}|_{\tilde{\sigma}}} \exp(\beta \mathcal{H}_{G'}(\sigma)) \right) \\ &= \sum_{\tilde{\sigma} \in \Omega_V} \left(Z_G^{V'}|_{\tilde{\sigma}} \right) \left(Z_{G'}^{V'}|_{\tilde{\sigma}} \right). \end{aligned} \tag{3.6}$$

□

3.2.1 Transfer matrix

We describe the transfer matrix formulation in this section. Note that the partition function has a property that allows it to be presented as a product of matrices. It can be arranged into product of terms each depending only on nearest neighbour pairs [7].

Recall the partition vector $Z_G^{V'}$. The vector is now reorganised into a matrix denoted as $\mathcal{T}$. Two column configurations are fixed as incoming and outgoing sites denoted as V_I and V_O respectively such that $V = V_I \cup V_O$. The entries in matrix $\mathcal{T}$ are indexed and the row and column matrix are associated with the set of all possible configuration states Ω_{V_I} and Ω_{V_O} respectively. Each entry at i-th row and j-th column is given by

$$\mathcal{T}_{ij} = Z_G^V|_{\sigma_i \in \Omega_{V_I}, \sigma_j \in \Omega_{V_0}}. \tag{3.7}$$

The $\mathcal{T}$ is called a transfer matrix.

Refer Figure 3.1. Each configuration can be written as the entry in a matrix $\mathcal{T}$ where the row matrix corresponds to two left vertices and the column matrix corresponds to two right vertices.

Example 3.2.2. For a square lattice as in Figure 3.2, we have

$$(\sigma_1, \sigma_2) \quad = \quad (\sigma_3, \sigma_4) = \{(1,1), (1,2), (2,1), (2,2)\}$$

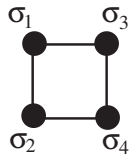

Figure 3.2: 2 by 2 square lattice.

and the transfer matrix

$$\mathcal{T} = \begin{array}{c} \\ (1,1) \\ (1,2) \\ (2,1) \\ (2,2) \end{array} \begin{array}{c} \begin{array}{cccc} (1,1) & (1,2) & (2,1) & (2,2) \end{array} \\ \begin{pmatrix} e^{4\beta J} & e^{2\beta J} & e^{2\beta J} & e^{2\beta J} \\ e^{2\beta J} & e^{2\beta J} & 1 & e^{2\beta J} \\ e^{2\beta J} & 1 & e^{2\beta J} & e^{2\beta J} \\ e^{2\beta J} & e^{2\beta J} & e^{2\beta J} & e^{4\beta J} \end{pmatrix} \end{array} = \begin{pmatrix} x^4 & x^2 & x^2 & x^2 \\ x^2 & x^2 & 1 & x^2 \\ x^2 & 1 & x^2 & x^2 \\ x^2 & x^2 & x^2 & x^4 \end{pmatrix}.$$

Consider a lemma which related to Theorem 3.2.1 as follows. Denote $V \setminus V'$ as the set of all elements in V that are not in V'.

Lemma 3.2.2. *Let G_1 and G_2 be two graphs such that $E_{G_1} \cap E_{G_2} = \emptyset$. Let $G_1 G_2 = G_1 \cup G_2$ and $V = V_{G_1} \cap V_{G_2}$ and $V' \subseteq V_{G_1 G_2}$. Then*

$$Z^{V'}_{G_1 G_2}|_{c'} = \sum_{c \in \Omega_{V \setminus V'}} \left(Z^{V}_{G_1}|_{c',c} \right) \left(Z^{V}_{G_2}|_{c',c} \right). \tag{3.8}$$

Here c', c is the configuration associated to V' and then to V . □

The proof of Lemma 3.2.2 is similar to the proof of Theorem 3.2.1 (cf. Chapman-Kolmogorov equation [76]).

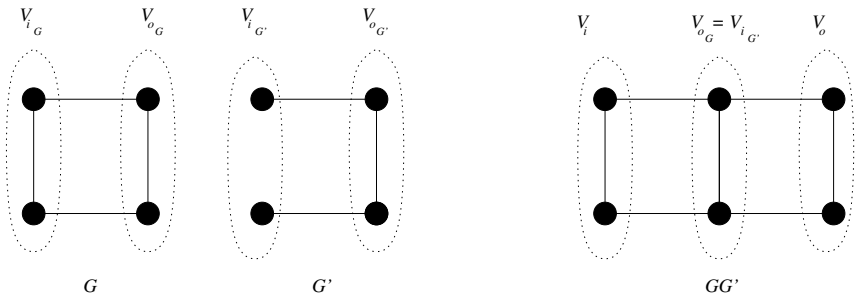

Figure 3.3: Lattice graphs G, G' and GG' where G and G' connected to form GG'. The dot circles represent the incoming and outgoing spins, for example, V_{i_G} and V_{O_G} respectively.

If $\mathcal{T}_G$ and $\mathcal{T}_{G'}$ are the transfer matrices associated to graph G and G' and $E_G \cap E_{G'} = \emptyset$, now we could use these transfer matrices to combine to graph. The

incoming and outgoing spins are denoted as V_{i_G} and V_{O_G} respectively for graph G and $V_{i_{G'}}$ and $V_{O_{G'}}$ respectively for graph G'.

Similar to partition vector multiplication, we can now combine two graphs by a matrix multiplication. By equation (3.7) and Lemma 3.2.2, the transfer matrix of two combined graph is given by matrix product

$$\mathcal{T}_{GG'} = \mathcal{T}_G \mathcal{T}_{G'}$$

where $V_{i_{GG'}} = V_{i_G}$ and $V_{O_{GG'}} = V_{O_{G'}}$.

The partition function of the new graph is given by

$$Z_{GG'} = \sum_{i=1}^{d} \sum_{j=1}^{d} (\mathcal{T}_{GG'})_{i,j} \tag{3.9}$$

where i, j is the index of matrix $\mathcal{T}_{GG'}$ and d is the dimension of the matrix.

This combining process is restricted to the incoming and outgoing spins. Once combined the outgoing spins of G and incoming spins of G' become the interior spin variables of graph GG', or $V_{O_G} = V_{i_{G'}}$.

Example 3.2.3. Let graph $G \cup G'$ given by Figure 3.3. The transfer matrices of individual graph are given by $\mathcal{T}_G$ and $\mathcal{T}_{G'}$, i.e.

$$\mathcal{T}_G = \begin{pmatrix} x^4 & x^2 & x^2 & x^2 \\ x^2 & x^2 & 1 & x^2 \\ x^2 & 1 & x^2 & x^2 \\ x^2 & x^2 & x^2 & x^4 \end{pmatrix} \text{ and } \mathcal{T}_{G'} = \begin{pmatrix} x^3 & x & x & x \\ x^2 & x^2 & 1 & x^2 \\ x^2 & 1 & x^2 & x^2 \\ x & x & x & x^3 \end{pmatrix}.$$

A combination of graph G and $G^{'}$ gives

$$\mathcal{T}_{GG'} = \mathcal{T}_G \mathcal{T}_{G'}$$

$$= \begin{pmatrix} x^7 + 2x^4 + x^3 & x^5 + x^4 + x^3 + x^2 & x^5 + x^4 + x^3 + x^2 & 2x^5 + 2x^4 \\ x^5 + x^4 + x^3 + x^2 & x^4 + 2x^3 + 1 & 2x^3 + 2x^2 & x^5 + x^4 + x^3 + x^2 \\ x^5 + x^4 + x^3 + x^2 & 2x^3 + 2x^2 & x^4 + 2x^3 + 1 & x^5 + x^4 + x^3 + x^2 \\ 2x^5 + 2x^4 & x^5 + x^4 + x^3 + x^2 & x^5 + x^4 + x^3 + x^2 & x^7 + 2x^4 + x^3 \end{pmatrix}.$$

And finally the partition function for GG' is given by

$$Z_{GG'} = 2x^7 + 12x^5 + 18x^4 + 18x^3 + 12x^2 + 2.$$

3.2.2 Boundary Condition

Here we present two types of boundary condition that we consider in this thesis. The boundary conditions are called open and periodic boundary conditions (we refer to § 2.1.3 and also [58]).

We say a lattice has an open boundary condition when there is no connecting edge between two exterior vertices. Otherwise, it is a periodic boundary condition.

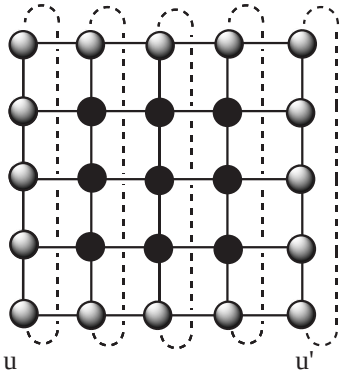

Figure 3.4: 5 by 5 square lattice with periodic boundary in vertical direction.

Figure 3.4 shows a 5 by 5 square lattice with both types of boundary condition. The grey coloured particles correspond to the exterior sites of the lattice. The disconnected dashed lines correspond to edges connecting the first and the lowest rows whereas there is no edge connecting the first and the last column. The latter shows an open boundary condition in horizontal direction and the former refers to the periodicity in vertical direction. We had assumed an open boundary condition for all previous examples.

For $N, M \in \mathbb{N}$, let N by M be the size of any square lattice graph Γ with N row and M column vertices. Let $\mathcal{T}$ be the transfer matrix. The partition function for

lattices with open horizontal boundary conditions is defined as [58].

$$Z_{open} = \sum_{ij} (\mathcal{T}^M)_{ij} \tag{3.10}$$

The partition function for a lattice with periodic boundary condition in all directions eventually becomes a trace of the matrix.

$$Z_{periodic} = \sum_{ii} (\mathcal{T}^M)_{ii} = \mathrm{tr}(\mathcal{T}^M). \tag{3.11}$$

3.2.3 Symmetry on graph

Here we present some available symmetries in some lattices which will further speed up the calculation for partition function [58].

The implementation of the symmetries in the computation is as follows. We classify all the configurations $\sigma \in \Omega$ into some subsets of Ω. We call them a symmetry class where its elements are the result of the translation, spin, reflection and rotation symmetries.

All the microstates that are related to each other by these symmetries are categorised into the same subset. Here only one configuration is chosen as the class representative. The transfer matrix is then represented by this representative configuration from each symmetry class. This matrix is a 'reduced' transfer matrix and is used for numerical computation.

For $Q = 2$, the spin symmetry is obvious with only 1 choice of permutation between spin 1 and 2. For $Q > 2$, we describe the spins permutation by symmetric group.

Definition 3.2.3 (Symmetric group [63])**.** *Let $n \in \mathbb{N}$ be a positive integer. The group of all permutations of a set A with n elements is called the symmetric group on n symbols and will be denoted as S_n.*

One way to describe the role of representative configuration is by the construction of a representative vector from the reduced transfer matrix. Let $\Omega_i \subset \Omega_{NM}$ be a set

of configuration for a symmetry class i and Ω_{NM} is the set of all configurations for N by M lattice. The reduced transfer matrix $\mathcal{T}_S$ has entries denoted as $(\mathcal{T}_S)_{ij}$ with row index i and column index j.

We denote a representative vector of symmetry class as $\mathcal{R}$ with each its entry $\mathcal{R}_i$ is associated with the symmetry class i. Let $\mathcal{R} = \{\mathcal{R}_1, \mathcal{R}_2, ...\}$, we take

$$\mathcal{R}_i = \sum_j (\mathcal{T}_S)_{ij} \, .$$

Each entry in $\mathcal{T}_S$ corresponded to a specific representative element in $\mathcal{R}$ (based on which Ω_i the column configuration belongs to. See example 3.2.4). The number of elements in each class i is given by $|\Omega_i| = M_i$ where $\sum_i |\Omega_i| = |\Omega_{NM}|$.

Here we are working with matrix-vector multiplication to build M lattice layers. Each multiplication gives new representative vector $\mathcal{R}$. Here we add another notation as in $\mathcal{R}_i^{(m)}$ to indicate the recurrence relation (eg. $m = 2$ means second multiplication which build the third layer) where $m = 1, 2, ..., M-2$ and $M > 2$. Let $\mathcal{R}_i^{(1)} = \mathcal{R}_i$, each matrix-vector multiplication gives new entries for $\mathcal{R}$, i.e.

$$\mathcal{R}_i^{(m+1)} = \sum_j (\mathcal{T}_S)_{ij} \mathcal{R}_k^{(m)} \tag{3.12}$$

where $\mathcal{R}_k^{(m)}$ when $k = 1, 2, ...$ is the representative class associated with element $\mathcal{T}_{ij}$.

Then the partition function for N by M lattice is given by

$$Z = \sum_i M_i \mathcal{R}_i^{(M-1)} \tag{3.13}$$

where M_i is the number of elements in each class i. For an example of symmetry class, consider example 3.2.4.

Example 3.2.4. Consider a 4 by 2 square lattice of 2-states Potts model with open and periodic boundary condition in horizontal and vertical direction respectively as shown in Figure 3.5.

Let $\Omega_i \subset \Omega$ be the configurations in the first column with $\Omega_i =$

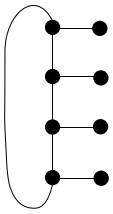

Figure 3.5: 4 by 2 square lattice with periodic boundary condition in vertical direction.

$\{(a_1, a_2, a_3, a_4)|a_i = 1 \text{ or } 2\}$. We have a list of symmetry class for the first column of the lattice as follows.

$$\begin{aligned}
\Omega_1 &= \{(1,1,1,1),(2,2,2,2)\} \\
\Omega_2 &= \{(1,1,1,2),(2,1,1,1),(1,2,1,1),(1,1,2,1), \\
&\quad (2,2,2,1),(1,2,2,2),(2,1,2,2),(2,2,1,2)\} \\
\Omega_3 &= \{(1,1,2,2),(2,1,1,2),(2,2,1,1),(1,2,2,1), \\
\Omega_4 &= \{(1,2,1,2),(2,1,2,1)\} \\
|\Omega| &= 2^4 = |\Omega_1| + |\Omega_2| + |\Omega_3| + |\Omega_4| = 16.
\end{aligned}$$

Then the reduced transfer matrix is

$$\mathcal{T}_S = \begin{pmatrix}
x^8 & x^7 & x^7 & x^6 & x^7 & x^6 & x^6 & x^5 & x^7 & x^6 & x^6 & x^5 & x^6 & x^5 & x^5 & x^4 \\
x^5 & x^6 & x^4 & x^5 & x^4 & x^5 & x^3 & x^4 & x^4 & x^5 & x^3 & x^4 & x^3 & x^4 & x^2 & x^3 \\
x^4 & x^5 & x^5 & x^6 & x^3 & x^4 & x^4 & x^5 & x^3 & x^4 & x^4 & x^5 & x^2 & x^3 & x^3 & x^4 \\
x^2 & x^3 & x^1 & x^2 & x^3 & x^4 & x^2 & x^3 & x^1 & x^2 & x^0 & x^1 & x^2 & x^3 & x^1 & x^2
\end{pmatrix} \tag{3.14}$$

and the partition function for this 4 by 2 lattice case is

$$\begin{aligned}
Z &= \sum_i \sum_j |\Omega_i| (\mathcal{T}_S)_{ij} \\
&= 2x^8 + 8x^7 + 24x^6 + 56x^5 + 76x^4 + 56x^3 + 24x^2 + 8x + 2.
\end{aligned}$$

The space and spin symmetries are very useful in reducing the number of computations for the transfer matrix multiplication.

3.3 Zeros of partition function

We study the analytical properties of partition function by setting $Z = 0$ [53, 80]. Here we state the numerical method used for zeros finding approximation. Consider the fundamental theorem of algebra below.

Theorem 3.3.1 (Fundamental Theorem of Algebra)**.** *Given any positive* $n \geq 1$ *and any choice of complex numbers* $a_0, a_1, ..., a_n$*, such that* $a_n \neq 0$*, the polynomial equation* $a_n z^n + ... + a_1 z + a_0 = 0$ *has at least one solution* $z \in \mathbb{C}$*.* □

See [53, p. 151] for the proof.

The fundamental theorem of algebra states that every non-constant single-variable polynomial with complex coefficients has at least one complex root. This includes polynomials with real coefficients.

In this study, we use a Newton-Raphson (NR) method [81] to find the complex root of the partition function. All programs use a C++ programming language. This method is described in Appendix § A.

We have shown the computational approaches used for the study on partition function in this chapter. The zeros of partition function for specific models are discussed in the next three chapters. We begin by presenting the case of Ising model, followed by Q-state Potts models and then continue with Z_Q-symmetric models.

Chapter 4

Square lattice Ising model partition function zeros

This chapter is focused on the study of Ising model partition function on finite size square lattice. We derive the partition function of the Onsager's Ising model [40, 75] in the first section. Then the partition function for finite size square lattice and its zeros are computed in the next section. The zeros are plotted into the complex-$e^{2\beta}$ Argand plane.

A function $\sigma_I : V \to \{1, -1\}$ is called a spin configuration for Ising model. We call the σ_I spin up for value $+1$ and spin down for -1. For a given graph Λ and Ω, we define the Hamiltonian function for Ising model as follows.

Definition 4.0.1. *The Hamiltonian of Ising model on graph $\Lambda = (V, E, f)$ is defined as* $\mathcal{H}_{Ising}(\sigma_I) = -J \sum_{\substack{\langle i,j\rangle = f(e),\\ e\in E}} \sigma_I(i)\sigma_I(j)$.

For writing purposes, we write $\sigma_I(j)$ as σ_j for any $j \in \mathbb{N}$. The Ising and Potts models are related to each other by this relation:

$$\frac{\sigma_i\sigma_j + 1}{2} = \delta_{\sigma_i\sigma_j} \tag{4.1}$$

i.e. when $\sigma_i, \sigma_j = \{1, -1\}$.

4.1 Exact solution – the Onsager's solution

Here we present the partition function of Onsager's exact solution on square lattice Ising model.

Let $N, M \in \mathbb{N}$ be the number of vertices in vertical and horizontal directions respectively. Let the partition function Z be produced by multiplication of transfer matrices (as explained in § 3.2). Recall (3.11) that for spins on N by M square lattice with periodic boundary condition in all directions, the partition function is given by

$$Z = \mathrm{tr}(\mathcal{T}^M)$$

where $\mathcal{T}$ is the transfer matrix.

Alternatively, a lattice graph can be built locally by adding a single local bond or edge at a time. We could work on the local transfer matrix for each bond to construct the transfer matrix. We introduce them here.

Let t_i be a matrix representing a horizontal edge interaction in i-th row and $t_{i(i+1)}$ be a matrix representing a vertical edge interaction in i-th and $(i+1)$-th rows. Let $\mathbb{1}_2$ denote a 2×2 identity matrix and for $k \in \mathbb{N}$,

$$\mathbb{1}_2^{\otimes k} := \underbrace{\mathbb{1}_2 \otimes \mathbb{1}_2 \otimes \cdots \otimes \mathbb{1}_2}_{k}$$

is a $2k \times 2k$ identity matrix. We add layer of lattice graph locally by these local transfer matrices.

Recall $x = e^{\beta J}$. For $N \times M$ lattice, t_i and $t_{i(i+1)}$ can be written as

$$t_i = \mathbb{1}_2^{\otimes i-1} \otimes \begin{pmatrix} x & x^{-1} \\ x^{-1} & x \end{pmatrix} \otimes \mathbb{1}_2^{\otimes N-i}$$

and

$$t_{i(i+1)} = \mathbb{1}_2^{\otimes i-1} \otimes \begin{pmatrix} x & 0 & 0 & 0 \\ 0 & x^{-1} & 0 & 0 \\ 0 & 0 & x^{-1} & 0 \\ 0 & 0 & 0 & x \end{pmatrix} \otimes \mathbb{1}_2^{\otimes N-(i+1)}.$$

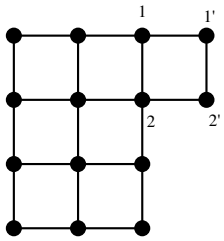

Figure 4.1: Square lattice with local bond construction.

Consider a square lattice as in Figure 4.1. For the local transfer matrix below (t_1, t_2, and $t_{1(2)}$), each edge is added depending only on the vertices 1 and 2. These vertices are the outgoing vertices for this example. Other vertices are not involve with this addition. The matrix for the interaction between vertices 1 and $1'$ is then given by

$$t_1 = \begin{pmatrix} x & 0 & x^{-1} & 0 \\ 0 & x & 0 & x^{-1} \\ x^{-1} & 0 & x & 0 \\ 0 & x^{-1} & 0 & x \end{pmatrix}$$

and the matrix for the interaction between 2 and $2'$ is given by

$$t_2 = \begin{pmatrix} x & x^{-1} & 0 & 0 \\ x^{-1} & x & 0 & 0 \\ 0 & 0 & x & x^{-1} \\ 0 & 0 & x^{-1} & x \end{pmatrix}.$$

The matrix interaction between $1'$ and $2'$ is then given by

$$t_{1(2)} = \begin{pmatrix} x & 0 & 0 & 0 \\ 0 & x^{-1} & 0 & 0 \\ 0 & 0 & x^{-1} & 0 \\ 0 & 0 & 0 & x \end{pmatrix}.$$

The above matrices are called local transfer matrices.

We can express a transfer matrix in this form,

$$\begin{aligned} \mathcal{T} &= V_1 V_2 \\ &= \left(\prod_{i=1}^{N} t_i\right)\left(\prod_{i=1}^{N} t_{i(i+1)}\right) \end{aligned} \tag{4.2}$$

where $t_{N(N+1)} = t_{N(1)}$ for a periodic boundary condition in vertical direction.

Example 4.1.1. Let $N = 5$, then the transfer matrix is given by

$\mathcal{T} = t_1 t_2 t_3 t_4 t_5 t_{1(2)} t_{2(3)} t_{3(4)} t_{4(5)} t_{5(1)}$.

Theorem 4.1.1 (Perron-Frobenius theorem)**.** *Let A be a d-dimensional positive matrix. Then there exist a unique largest magnitude eigenvalue λ which is itself positive. The associated eigenvector can be chosen to be positive.* □

See [69] for the proof.

Suppose that a transfer matrix $\mathcal{T}$ has dimension d with real value β. The matrix $\mathcal{T}$ is symmetric and positive since it is associated with real and positive Hamiltonian function. This allow us to diagonalise matrix $\mathcal{T}$ by similarity transformation [13, p. 549]. For any matrix $\mathcal{T}$, there exist a matrix S such that a diagonal matrix $\tilde{\mathcal{T}} = S\mathcal{T}S^{-1}$. This transform

$$\mathcal{T} \longrightarrow S\mathcal{T}S^{-1}.$$

By this similarity transformation, for any $M \in \mathbb{N}$,

$$\mathcal{T}^M = S^{-1}S\mathcal{T}S^{-1}S\mathcal{T}S^{-1}S\cdots$$

with

$$\tilde{\mathcal{T}} = S\mathcal{T}S^{-1} = \begin{pmatrix} \lambda_1 & 0 & \cdots & 0 \\ 0 & \lambda_2 & \cdots & 0 \\ \vdots & \vdots & \ddots & \vdots \\ 0 & 0 & \cdots & \lambda_d \end{pmatrix} \tag{4.3}$$

where $\{\lambda_i\}$ are the eigenvalues of the matrix $\mathcal{T}$. This gives

$$\mathcal{T}^M = S^{-1} \begin{pmatrix} \lambda_1^M & 0 & \cdots & 0 \\ 0 & \lambda_2^M & \cdots & 0 \\ \vdots & \vdots & \ddots & \vdots \\ 0 & 0 & \cdots & \lambda_d^M \end{pmatrix} S\,. \tag{4.4}$$

Recall the eigenvalue and eigenvector relation $\mathcal{T}\,v = \lambda\,v$. The ket-vector $|i>$ has relation $\mathcal{T}\,|i> = \lambda_i\,|i>$ and the bra-vector $<j|$ has relation $<j|\,\mathcal{T} = <j|\,\lambda_j$, such that

$$<i|j> = \delta_{ij} \quad \text{and} \quad |i><j| = \mathbb{1}_d$$

for any $i, j = 1, 2, \ldots, d$ and $\mathbb{1}_d$ is the d-dimensional identity matrix.

Example 4.1.2. Let $\mathcal{T}$ be the transfer matrix and $a_i, b_i \in \mathbb{R}$ are associated to any basis vectors $|i>$ and $<j|$. For some a_i and b_i we could have a basis vector given by equation below.

$$\begin{pmatrix} 1 & 1 & \cdots 1 \end{pmatrix}^{\intercal} = \sum_{i=0}^{d-1} a_i\,|i>$$

and

$$\begin{pmatrix} 1 & 1 & \cdots 1 \end{pmatrix} = \sum_{j=0}^{d-1} b_j\ <j|\,.$$

By induction,

$$\begin{aligned} \mathcal{T}\,|i> &= \lambda_i\,|i>, \\ \mathcal{T}^2\,|i> &= \lambda_i\,\mathcal{T}\,|i> \\ &= \lambda_i^2\,|i>\,. \end{aligned}$$

Then,

$$\begin{aligned}\mathcal{T}^{M-1}\,|i> &= \lambda_i^{M-2}\mathcal{T}\,|i> \\ &= \lambda_i^{M-2}\lambda_i\,\mathcal{T}\,|i> \\ &= \lambda_i^{M-1}\,|i>\,.\end{aligned}$$

Hence

$$\mathcal{T}^M\,|i> = \lambda_i^M\,|i>\,.$$

Then we may have a partition function given by

$$\begin{aligned}Z &= \begin{pmatrix}1 & 1 & \cdots 1\end{pmatrix}\mathcal{T}^M\begin{pmatrix}1 & 1 & \cdots 1\end{pmatrix}^{\intercal} \\ &= \sum_{j=0}^{d-1} b_j\ <j|\,\mathcal{T}^M\sum_{i=0}^{d-1} a_i\,|i> \\ &= \sum_{j=0}^{d-1} b_j\ <j|\,\sum_{i=0}^{d-1} a_i\lambda_i^M\,|i> \\ &= \sum_{i,j=0}^{d-1} a_i b_j\lambda_i^M\ <j|i> \\ &= \sum_{i,j=0}^{d-1} a_i b_j\lambda_i^M\delta_{ij} \\ &= \sum_{i=0}^{d-1} a_i b_i\lambda_i^M.\end{aligned}$$

By Perron-Frobenius theorem 4.1.1 there exist a unique largest eigenvalue for any positive matrix. Denote λ_0 as the largest eigenvalue, we have

$$Z = a_0 b_0\lambda_0^M + \sum_{i=1}^{d-1} a_i b_i\lambda_i^M \tag{4.5}$$

$$= \lambda_0^M\left(a_0 b_0 + \sum_{i=1}^{d-1} a_i b_i\left(\frac{\lambda_i}{\lambda_0}\right)^M\right). \tag{4.6}$$

Let $\{\lambda_i\}$ be the eigenvalues of $\mathcal{T}$, equivalently, for N by M lattice, the partition

function

$$\begin{aligned} Z &= \mathrm{tr}(\mathcal{T}^M) && (4.7)\\ &= \sum_{i=0}^{d-1} \lambda_i^M && (4.8)\\ &= \lambda_0^M \left(1 + \sum_{i=1}^{d-1} \left(\frac{\lambda_i}{\lambda_0}\right)^M\right). && (4.9) \end{aligned}$$

For $M \to \infty$, the other eigenvalues give only small contribution which leads to

$$Z \sim \lambda_0^M.$$

One approach for this exact solution was studied by Kaufman [40]. Kaufman describes the relation between a transfer matrix problem with a rotational matrix. Both matrices are linked by matrix algebra. From this relation, the eigenvalue of a suitable rotational matrix is equal to the eigenvalue of a transfer matrix. See formulation of this relationship in detail in [92, p. 70 – 86].

We briefly present parts of the derivation of the eigenvalue λ in Appendix § B. This derivation gives

$$\lambda^M = \prod_{k=1}^{N} \prod_{r=1}^{M} \big(K - 2(\cos(2\pi k/N) + \cos(2\pi r/M))\big) \qquad (4.10)$$

where

$$K = \frac{(1 + e^{-4\beta})^2}{e^{-2\beta}(1 - e^{-4\beta})}\,. \qquad (4.11)$$

Then we have,

$$\begin{aligned} Z_{NM} &\sim \lambda^M\\ &= \prod_{k=1}^{N} \prod_{r=1}^{M} \big(K - 2(\cos(2\pi k/N) + \cos(2\pi r/M))\big)\,. && (4.12) \end{aligned}$$

For $y = e^{2\beta}$ and $C = \cos(2\pi k/N) + \cos(2\pi r/M)$, each factor in (4.12) can be written

in a polynomial form when $Z = 0$. We can find the zeros for each factor where

$$\begin{aligned} K - 2(\cos(2\pi k/N) + \cos(2\pi r/M) &= 0 \\ e^{-8\beta} + 2Ce^{-6\beta} + 2e^{-4\beta} - 2Ce^{-2\beta} + 1 &= 0 \\ y^{-4} + 2Cy^{-3} + 2y^{-2} - 2Cy^{-1} + 1 &= 0 \\ y^4 - 2Cy^3 + 2y^2 + 2Cy + 1 &= 0 \end{aligned} \tag{4.13}$$

for any N by M square lattice with $k = 1, 2, ..., N$ and $r = 1, 2, ..., M$.

4.2 Ising model on finite lattice case

In this section the zeros of the partition function are plotted in the complex-$e^{2\beta}$ Argand plane for Ising model on square lattice. The zeros are computed by the Newton-Raphson method [81]. The Onsager's square lattice Ising model has a periodic boundary condition in the vertical and horizontal directions.

The partition function is derived from equation (4.13) (we refer to Appendix § B). Since the size is finite, the partition function has positive coefficients. Its zeros will always lie off the real axis. The closest zeros to the real axis (we call endpoints) move closer to the real axis as the size increases.

Figures 4.2 to 4.5 show the zeros distributions for Ising model on square lattices with $N = M = 14, 90, 99, 100$. Figure 4.3b for example is the enlargement for $N = 90$ zeros distribution near the ferromagnetic region (explained later in § 4.5). We can see that the zeros are very close to the real axis. These zeros distributions form a pattern of two circles as we increase the lattice sizes. Each distribution has subsets of points with zeros located exactly on two circles. These two circles are the loci of the zeros for the square lattice Ising model [50, 99].

At thermodynamic limit, the zeros distribution is manifested by the two circles shown in Figure 4.6. One of the circles cut the real axis at the critical point $1 + \sqrt{2}$.

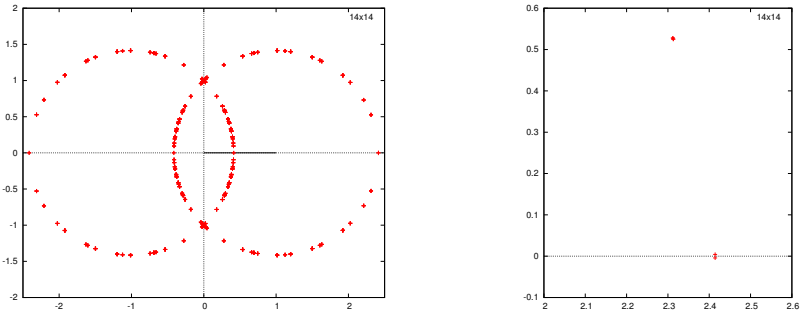

(a) (b)

Figure 4.2: Zeros plane for 14 by 14 square lattice, a) complete distribution and b) a blow up picture near real axis.

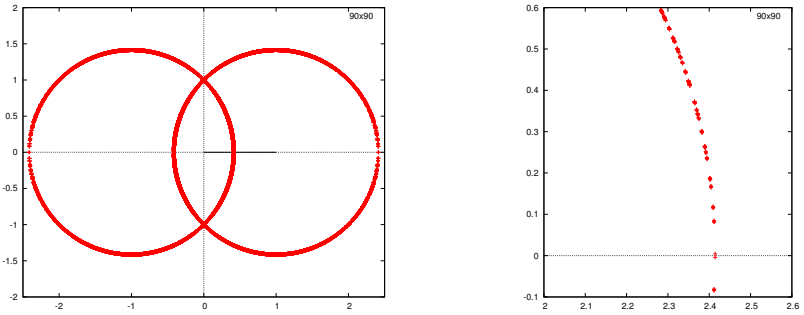

(a) (b)

Figure 4.3: Zeros plane for 90 by 90 square lattice, a) complete distribution and b) a blow up picture near real axis.

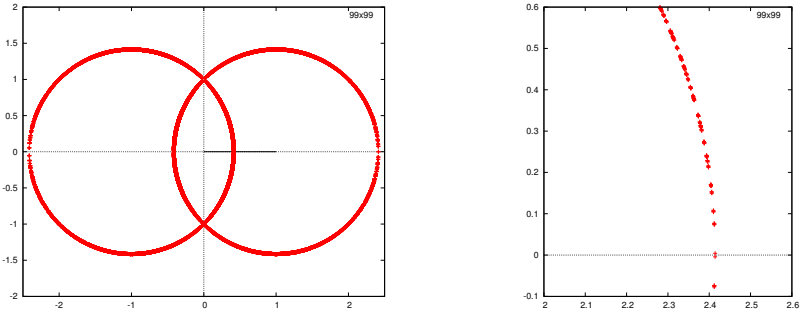

(a) (b)

Figure 4.4: Zeros plane for 99 by 99 square lattice, a) complete distribution and b) a blow up picture near real axis.

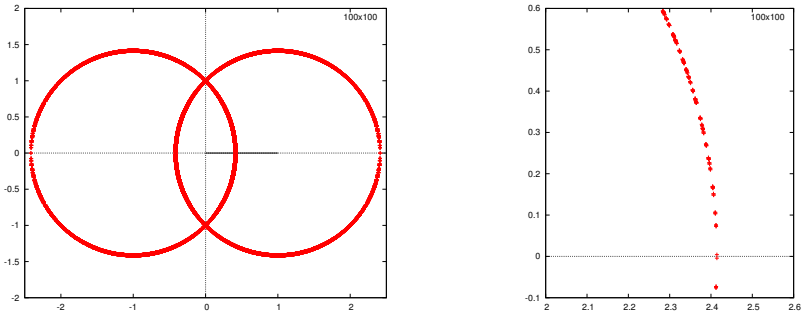

(a) (b)

Figure 4.5: Zeros plane for 100 by 100 square lattice, a) complete distribution and b) a blow up picture near real axis.

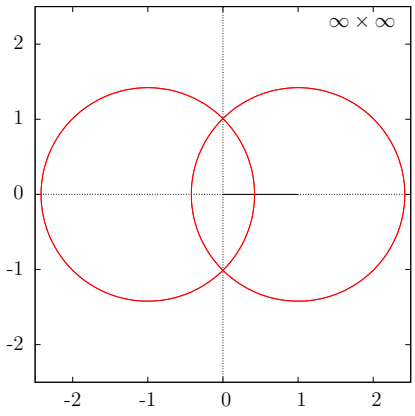

Figure 4.6: $\infty \times \infty$ square lattice Ising model.

4.3 Finite size effect

The list of zeros distribution of Ising model in previous section (§ 4.2) gives the evidence that the lattice size has significant effect on the zeros distribution especially in determining the analytic structure of the zeros distribution. We will see variety of analytic structure of the finite case with respect to the specific boundary condition explained later in § 5.1.

Here we consider a simple function for visualising the finite size effect on the locus of zeros in the complex plane. For example, consider a toy model [58] where $N \in \mathbb{N}$ and

$$Z = x^N + 1. \tag{4.14}$$

The partition function can be written in its zeros form [86] i.e.

$$Z = \prod_{r=0}^{N-1} \left(x - e^{\frac{i\pi}{N}(1+2r)} \right).$$

Example 4.3.1. Suppose $N = 4$, then

$$\begin{aligned} Z &= x^N + 1 \\ &= x^4 + 1. \end{aligned}$$

The zeros of Z is given by

$$\begin{aligned} x^4 + 1 &= 0 \\ x &= \sqrt[4]{-1} \\ &\sim \{e^{\frac{i\pi}{4}(1+2r)}\};\ r = \{0, 1, 2, 3\}. \end{aligned}$$

Similarly, suppose $N = 10$, then

$$\begin{aligned} x^{10} + 1 &= 0 \\ x &= \sqrt[10]{-1} \\ &\sim \{e^{\frac{i\pi}{10}(1+2r)}\};\ r = \{0, 1, 2, ..., 9\}. \end{aligned}$$

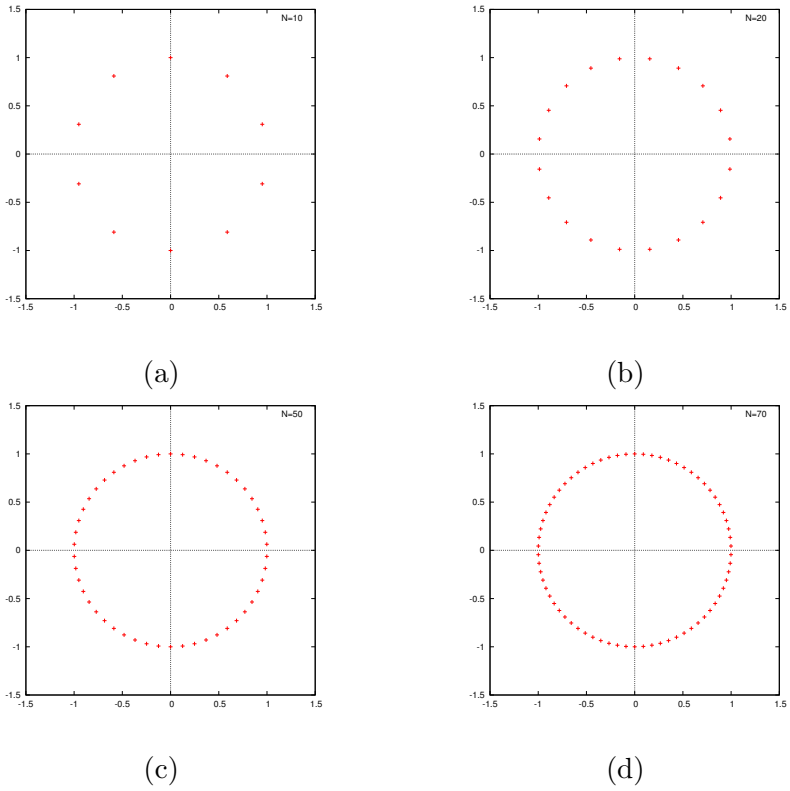

(a) (b)

(c) (d)

Figure 4.7: Zeros plane for $N = 10, 20, 50$ and 70.

Figure 4.7 shows the zeros distributions for different value of N from equation (4.14). The zeros are equally distributed in this plane and the gap between two zeros is decreases as N increases. This distribution has locus of a unit circle where the zeros cut the real axis at $Re(x) = \pm 1$.

The zeros distribution for the Ising model shows similar behaviour as suggested by the example in Figure 4.7. The zeros for different value of N are distributed in a specific pattern and become denser as N increases. The endpoints of the zeros move closer to the real axis.

We show in Figures 4.8 and 4.9 the distributions for the Ising model on square and cubic lattices in some value of N. Both figures are called the overlay distributions where we plot the result from two different cases in one complex plane. Note well here, though, that these results follow a very careful and special choice of boundary conditions without which the locus of zeros will also experience finite size effect.

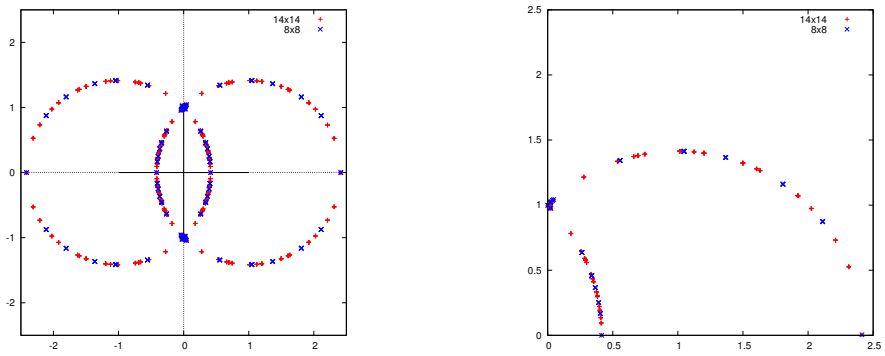

(a) (b)

Figure 4.8: Overlay distributions on square lattices with different system size N.

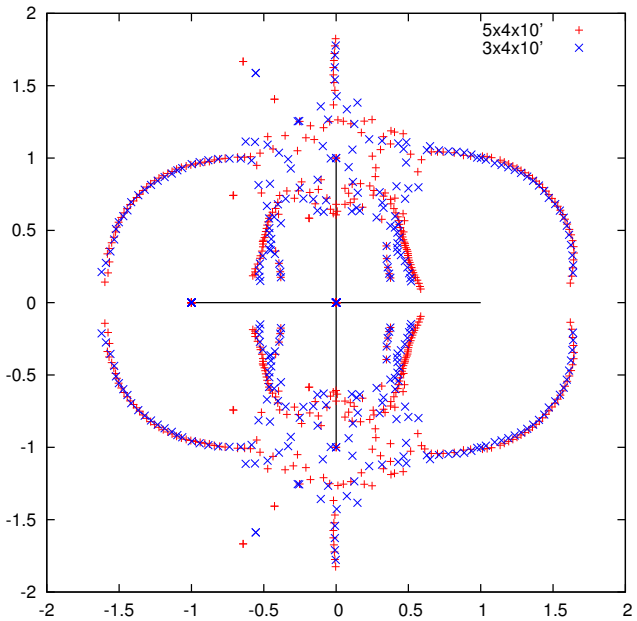

Figure 4.9: Overlay distributions on cubic lattices with different system size N.

4.4 Duality relation

We discuss a duality relation for the Ising model in this section. Recall $y = e^{2\beta}$ and the duality transformation [58] of the Ising model described in § 2.2 is given by relation

$$\frac{1}{y} \to \frac{y-1}{y+1}.$$

We can study this relation and see the change in the locus of the zeros. For $a, b \in \mathbb{R}, y = a + bi$, let

$$\frac{1}{y} = \frac{\bar{y}-1}{\bar{y}+1} \tag{4.15}$$

where y is a complex number and $\bar{y}$ is its complex conjugate. Then

$$\begin{aligned} \frac{1}{a+bi} &= \frac{a-bi-1}{a-bi+1} \\ a-bi+1 &= (a-bi-1)(a+bi) \\ a^2-2a+b^2-1 &= 0 \\ b &= \pm\sqrt{2a-a^2+1}. \end{aligned} \tag{4.16}$$

Recall that the exact solution has locus of two circles where one of the interception points is at $1+\sqrt{2}$. Plotting relation (4.16) will give a structure which is the same with one of the circles in the exact solution. At real axis when $b = 0$, we have $a = 1+\sqrt{2}$ that is equal to the point in the exact solution.

From the above observation, the circle in the exact solution that has interception point at $1+\sqrt{2}$ is invariant under a duality transformation. The zeros which are fixed under the duality transformation (4.15) are just a complex conjugates of one another. The duality circle has radius $\sqrt{2}$ centered at (1,0) in the complex plane.

An overlay plot of (4.16) with the zeros from specific case of square lattice will highlight the invariance property. The majority of zeros lie in part of the plane, exactly on an arc of a circle but not all of the zeros are confined to the circle. Figure 4.10 plot the dual case of a 14 by 14 Ising square lattice together with the complex conjugation circle (4.16). The zeros are computed directly from relation (4.15).

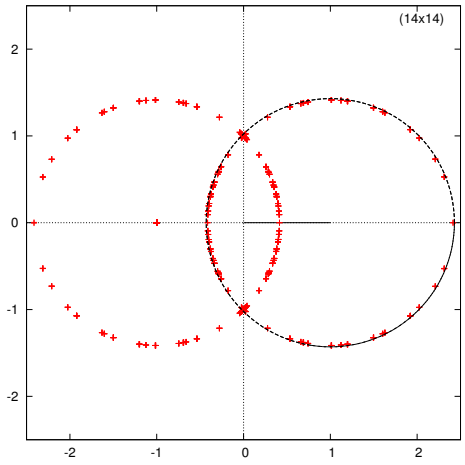

Figure 4.10: Distribution of dual zeros for 14 by 14 Ising square lattice and the circle (4.16).

4.5 Ferromagnetic and antiferromagnetic regions

Here we explain the relation between the complex plane of the zeros distribution and the ferromagnetic and antiferromagnetic states [41, 46, 68] in a physical system.

The ferromagnetic (ferro) state corresponds to the state where all the molecular dipoles point in the same direction. Conversely an antiferromagnetic (antiferro) state corresponds to the state where each molecular dipole tends to point in the different direction from its neighbours.

Note that the interaction energy J is assumed to be the same for every dipole-dipole nearest neighbour interaction and $x = e^{\beta J}$. If $J > 0$, the Hamiltonian function will be in its lowest energy where all spin variables spin in the same direction. The system is said to be in the ferromagnetic state. Otherwise, if $J < 0$, the negative coupling constant J will force the variables to be anti-align to its neighbour. This is the antiferromagnetic state.

Since temperature $T > 0$ gives $\beta > 0$, when $J > 0$, the $(0, 1)$-region is not physical i.e. $e^{\beta J\mathcal{H}} = 1$ for $\beta = 0$. Hence the $(1, \infty)$-region corresponds to the physical state of ferromagnetism. But if $J < 0$, the $e^{-J\beta\mathcal{H}} > 0$. Hence the $(0, 1)$-region can be interpreted as the antiferro region.

From this chapter, we see that the study of zeros of the partition function allow us to study the limiting behaviour of the zeros in the complex plane. The zeros distribution may suggest the limiting behaviour of a bulk system at large enough lattice size.

For comparison, we describe the result for the 2-state Potts model in different boundary conditions. We present their zeros distributions and observe any zeros structure in the next chapter.

Chapter 5

The Q-state Potts model partition function zeros

This chapter presents the zeros for the Q-state Potts model partition function for several lattice types and $Q = 2, 3, 4, 5, 6$. Recall that the partition function for a given lattice $\Lambda = (V, E, f)$ and Q is defined as

$$Z_{Potts} = \sum_{\sigma \in Hom(V, \underline{Q})} \exp(-\beta \mathcal{H}_{Potts}(\sigma))$$

where $\mathcal{H}_{Potts}$ is as in Definition 1.1.5. We consider two- and three-dimensional lattice graphs as described in Chapter 2.

The zeros are plotted in a complex-e^{β} Argand plane for observation. The zeros distributions for a given lattice type are arranged in increasing sizes.

As discussed in § 2.1.1 and § 4.2, we may search for the convergence sequence of analytic structure from the zeros distribution. We search for the structure or pattern formed by the collection of zeros in the complex plane.

The partition function calculation for lattices bigger than the previously studied case [9, 23, 58, 60, 77] will be one new finding in this thesis. In § 2.1.1 we explained why results for larger finite lattice sizes of a given type are valuable.

Recall in Chapter 4, we showed the emergence of pattern of zeros structure

as we change the lattice size. Then we relate them to the critical point in the thermodynamic limit in the example of square lattice Ising model [40].

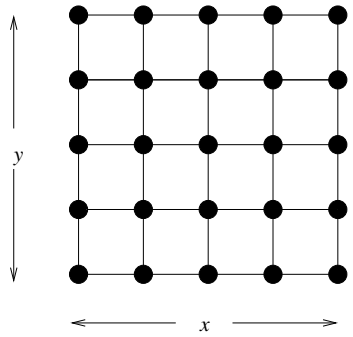

Figure 5.1: Number of row vertices denoted y (also we denote this $y = N$) and column vertices denoted x (also we denote this $x = M$).

Main results

Table 5.1: Largest sizes for all considered lattice types including the new results (highlighted in grey).

Q	2	3	4	5	6
Square	20x20'	13x13' 14x14' 15x17'	10x10' 11x13' 12x13'	8x9' 9x9' 10x13'	8x9' 9x9'
Triangular	13x13' 14x14' 15x15'	13x13' 14x17'	7x7' 8x8' 9x9' 10x10' 11x13'	7x7' 8x8'	
Hexagonal	18x18'	12x12'	10x13'		
Cubic	5x5x5'	3x4x10'	3x3x10'	3x3x5'	3x3x6'
Tetragonal (hcp)	3x3x7' 3x4x7' 4x4x7'	3x3x7' 3x4x7'			
Octagonal (fcc)	3x3x7' 3x4x7' 4x4x7'	3x3x7' 3x4x7'			

First we give the notation for specifying a graph Λ in the case of square or cubic lattice type. Let N_x, N_y, N_z correspond to the number of vertices in the three

directions x, y and z. We write $N_x \times N_y \times N_z$ for periodic boundary conditions in each direction. A notation with prime such as N_z' for z direction represents the open boundary condition. Note that $N_y \times N_x$ and $N_x \times N_y \times N_z$ represent the two- and three-dimensional case respectively. We write $(N_y \times N_x)$ for the dual lattice and $(N_y \times N_x)'$ corresponds to the self-dual lattice as defined in § 2.2.

Table 5.1 summarises the lattices considered in this thesis for Q-state Potts models. Each result of zeros distribution for different lattice graph is discussed in separate section.

Three new results extending the existing literature such as in [59, 92] for the 3-state Potts model on square lattice are produced for $N = 13, 14, 15$. We have also produced new results for the triangular lattice for 2-, 3-, 4- and 5-state Potts model. The octagonal and tetragonal lattices are another new cases we have considered for this thesis.

We have considered all computable cases up to specific lattice sizes (based on our current computing resources). For cubic lattice however, we could not produce a new result due to computing limitation. The number of configurations in one layer of the $5 \times 6 \times 5'$ for example, contains 30 vertices (5 column in z-axis and 6 row in y-axis). This equivalent to 2^{30} configuration states. This huge number of states however, exceed the maximum value of the standard integer in the computer. For comparison, each 1 step expansion in the square lattice involves only an increment of Q^{2N}. This number of configurations is much smaller than the lattice layer configuration state for cubic lattice i.e. for Q^{2N^2}.

Each case except for the 2-state Potts model has periodic vertical and open horizontal boundary conditions. We consider this type of boundary condition since we could produce a zeros distribution that is not fuzzy especially in the ferromagnetic region. This boundary condition also has translation symmetry in the vertical direction which is essential to reduce the number of computations. The computer program for computing the partition function in this thesis is designed to use a matrix-vector multiplication. This strategy is implemented to reduced the memory

usage in the computing resources.

Previous results

The Onsager's partition function for square lattice Ising model allows us to find the zeros distribution for any square lattice size (but in general for boundary conditions different from ours − as given in Chapter 4). The paper by Chen, Hu and Wu [16] is another example for the study on square lattice with self-dual boundary conditions.

The previous largest result for the 3-state Potts model on square lattice was due to Martin [59] where he produced $12 \times 13'$ square lattice. Similar to this, Valani also considered the 3-state Potts model on a $(12 \times 16)'$ self-dual square lattice. In addition to this, Matveev and Shrock [61] in the earlier paper showed the result for 10 by 8 lattice for several boundary conditions. Valani in his thesis [92] produced the zeros distributions for state $Q = 2, 3, 4, 5, 6$ for different boundary conditions.

Furthermore, the Ising model on hexagonal lattice had been previously studied by Feldman, Shrock and Tsai [25] on 24 by 18 and also 20 by 20 lattice sizes. They also considered for the $Q = 3, 4$ on hexagonal lattice particularly for $12 \times 16'$ lattice. By duality transformation, Feldman, Guttmann, Jensen, Shrock and Tsai [24] plotted the zeros distribution for triangular lattice up to boundary condition similar to $12 \times 9'$ and $10 \times 10'$ for $Q = 2$ and $6 \times 8'$ for $Q = 3, 4$. They consider several types of boundary condition including all periodic and also mixed periodic and open boundary conditions. Martin and Maillard [60] on the other hand extended the triangular lattice for 3-state Potts model for 108 sites i.e. 12 by 9 lattice.

In addition, Pearson [77] described the Ising model on $4 \times 4 \times 4$ cubic lattice and then Bhanot and Sastry [9] presented two steps larger with $4 \times 5 \times 5'$ cubic lattice. The latest and largest lattice for the cubic case however still due to Valani [92]. In his thesis, he discussed a sequence of cubic lattices up to $5 \times 5 \times 10'$.

5.1 2-state Potts (Ising) model on square lattice – revisited

As a check for the programs we start with running them on the exactly solved case of square lattice 2-state (Ising) Potts model. The comparison between the result of zeros distribution at limit and at finite sizes is also presented here. We consider the finite case restricted to some boundary conditions.

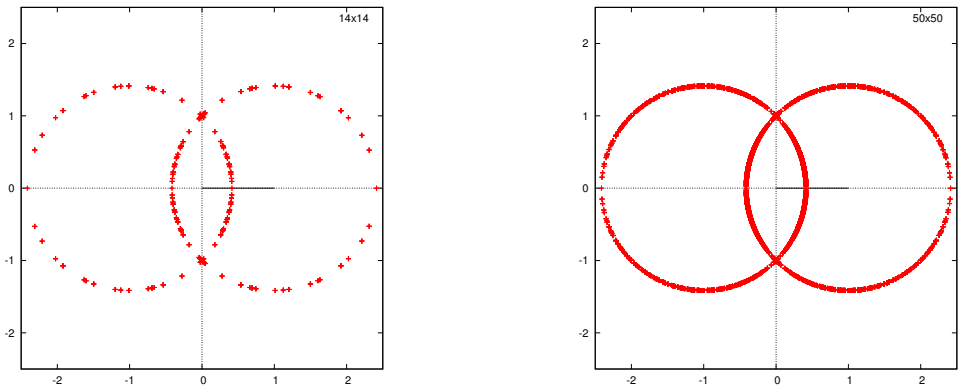

(a) (b)

Figure 5.2: Square lattice Ising model with Onsager's partition function a) 14×14 and b) 50×50.

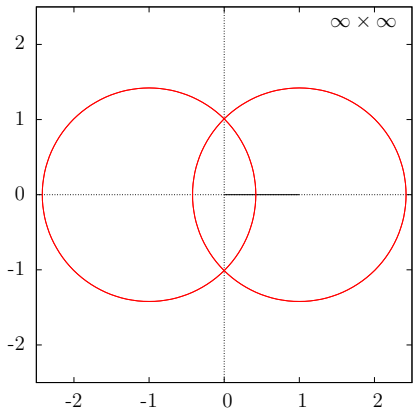

Figure 5.3: $\infty \times \infty$ square lattice Ising model.

The square lattice Ising model zeros distribution is discussed in § 4.2 where the

lattice size is varied. See Figures 5.2 and 5.3. All the zeros lie on the subsets of points with zeros forming two circles. It is evidence from here that the zeros are distributed in a pattern of two circles. This is their limiting *locus of points*. At thermodynamic limit, the two circles is shown in Figure 5.3. We refer to Chapter 4 for other zeros distribution for this model. The zeros distributions for all the finite cases are produced using our own computation.

Figures 5.4 and 5.5 show the zeros distributions for square lattice with open boundary and periodic boundary in horizontal and vertical directions respectively. See Figure 5.4f. The limiting two circles are drawn in this figure. As the lattice size increases, the zeros are approximately approaching the two circles. Notice that some of the zeros are distributed exactly on these circles. The endpoints near the real axis getting closer to the real axis.

Consider for example the 8 by 8 and 14 by 14 square lattices. The overlay zeros distributions with the zeros generated from Onsager's partition function (4.13) are shown in Figure 5.6. The distributions are different relative to their boundary conditions. The locus at thermodynamic limit is drawn as two incomplete circles.

5.1.1 The effect of boundary conditions

To highlight further the boundary effect on the zeros distribution, we present the square lattice of same lattice size with all the considered boundary conditions.

Consider the zeros distribution in Figure 5.7 for periodic-periodic boundary conditions. The distributions show the existence of symmetries under inversion of a unit circle $x \to \frac{1}{x}$, complex conjugation, duality relation and the sign reversal symmetry $x \to -x$. This is a complete 8 symmetries.

When N is an even number, this gives an exact symmetry which satisfies all the 8 symmetries. When N is odd number, the distribution has only an approximated inversion of a unit circle. For even N, the spin configuration state can forms a checkerboard pattern where every vertex is allowed to point in different direction from its nearest neighbour.

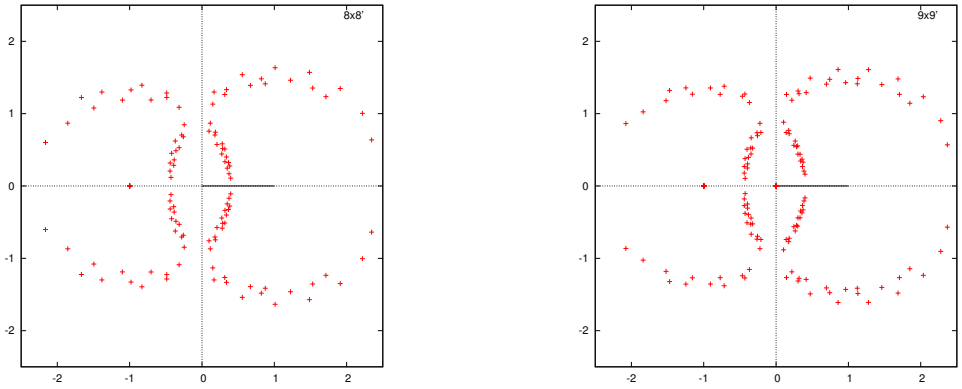

(a)

(b)

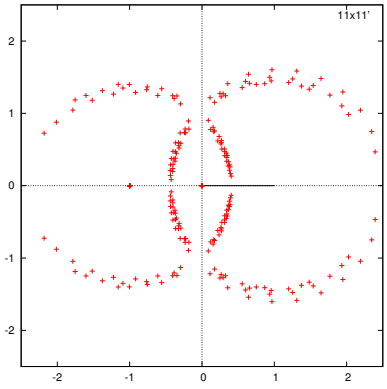

(c)

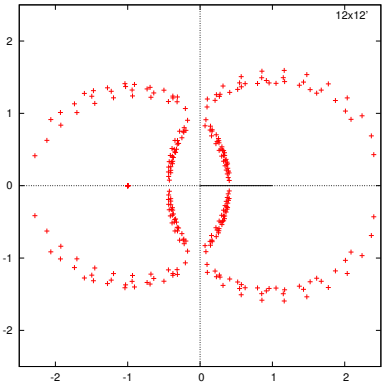

(d)

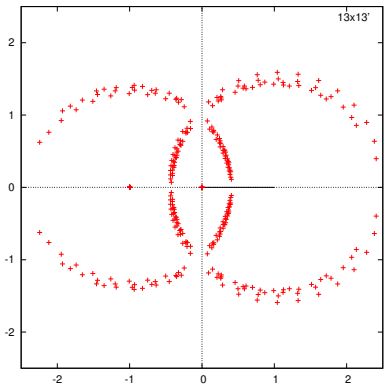

(e)

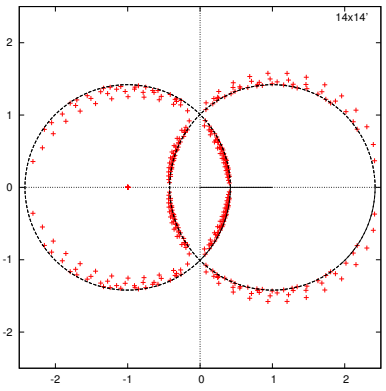

(f)

Figure 5.4: 2-state, square lattice with periodic-open boundary conditions.

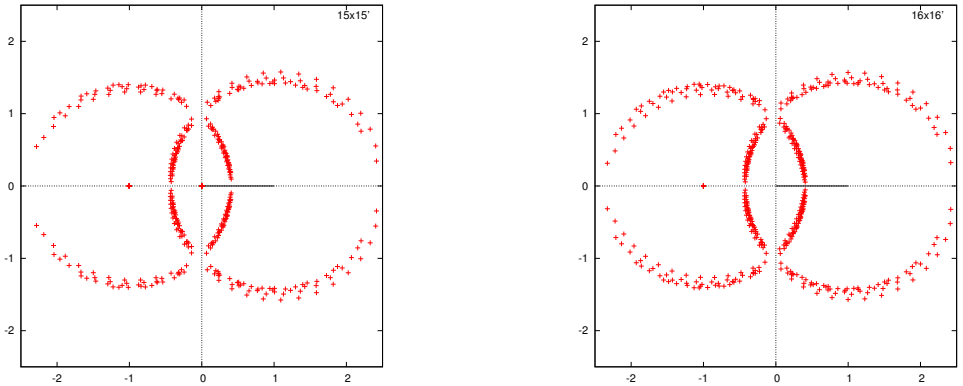

(a)

(b)

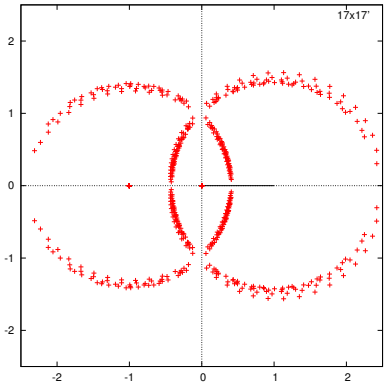

(c)

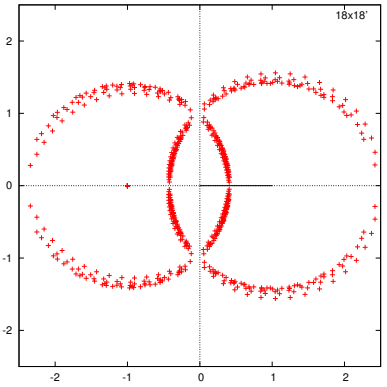

(d)

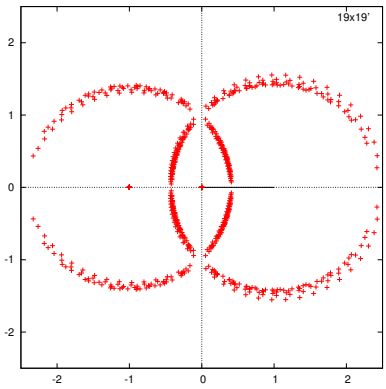

(e)

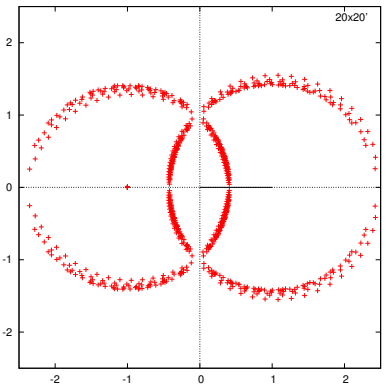

(f)

Figure 5.5: 2-state, square lattice with periodic-open boundary conditions (cont.).

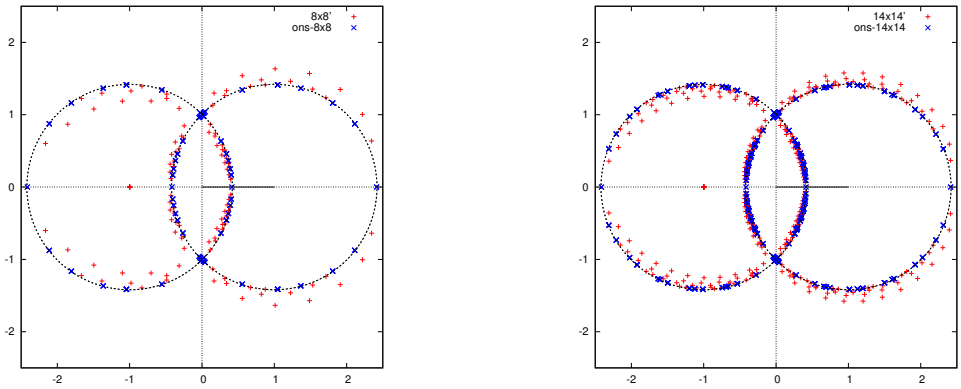

Figure 5.6: Zeros distributions for $N = 8, 14$ square lattices: ons-8×8 and ons-14×14 are generated from the Onsager's partition function (4.13).

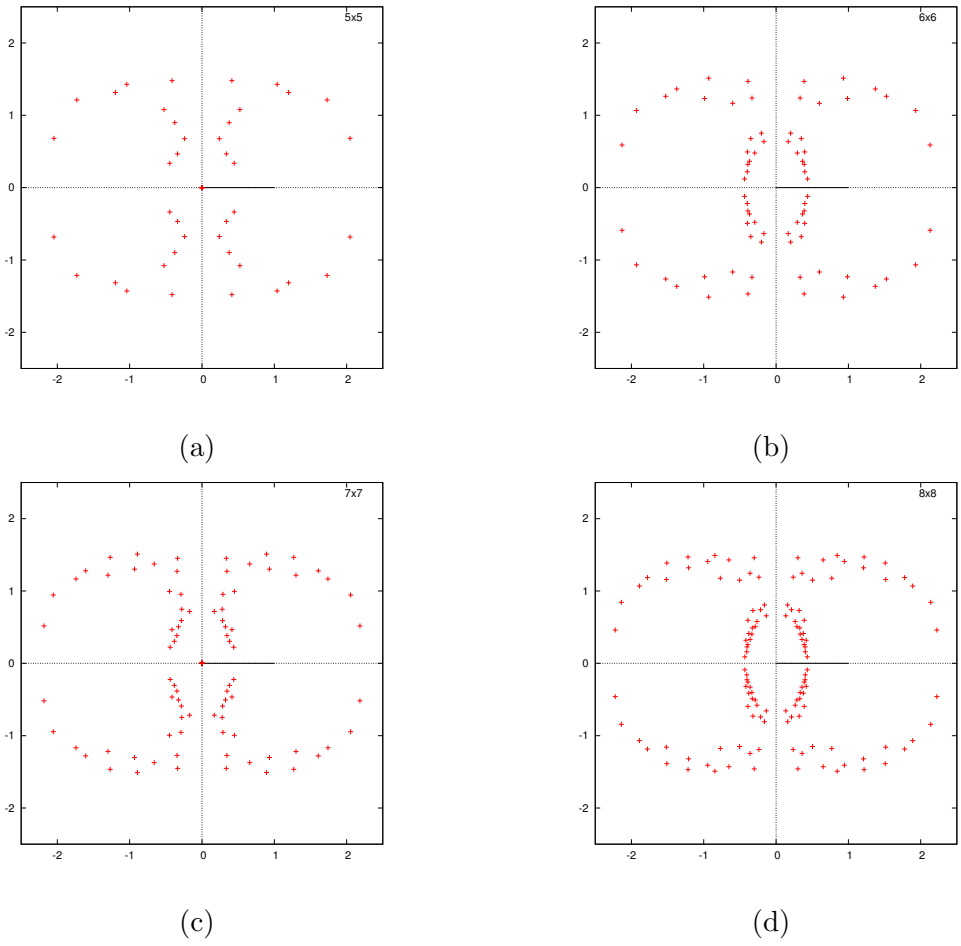

(a) (b)

(c) (d)

Figure 5.7: 2-state, square lattice with periodic-periodic boundary conditions.

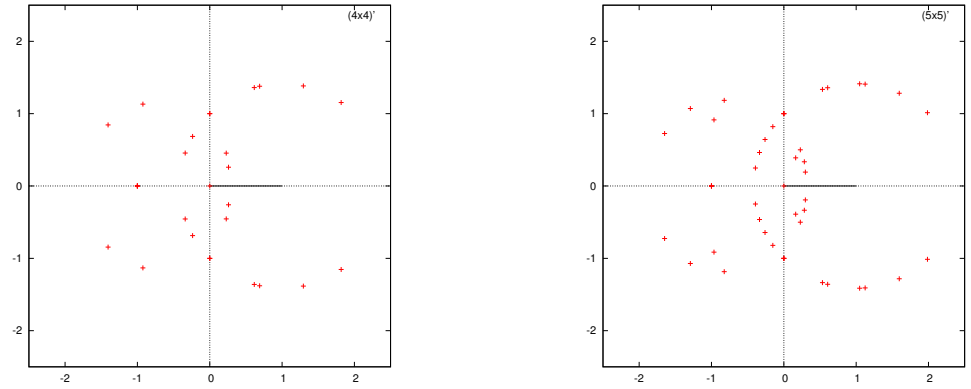

(a)

(b)

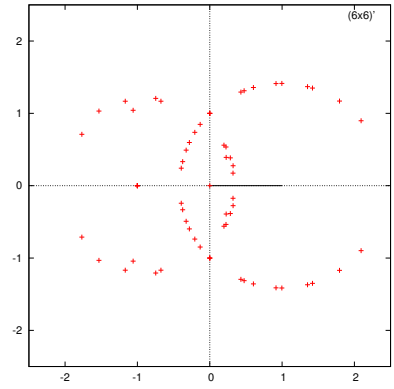

(c)

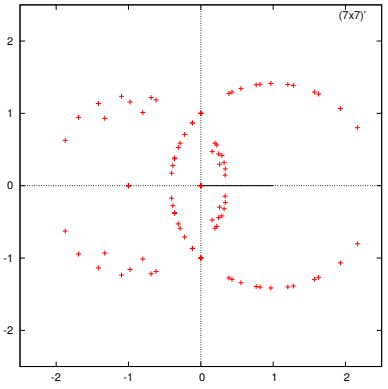

(d)

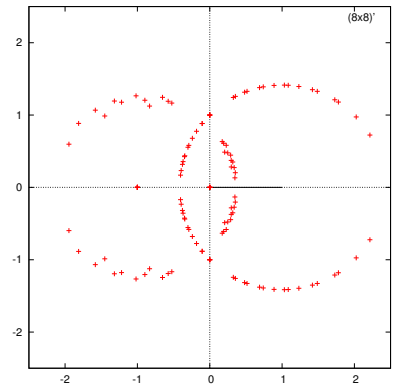

(e)

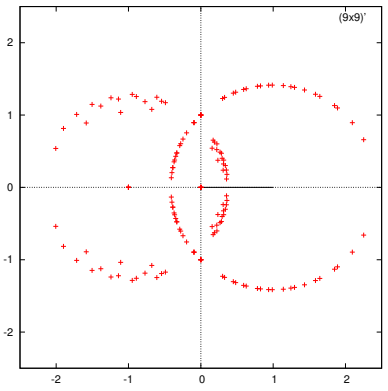

(f)

Figure 5.8: 2-state, square lattice with self-dual boundary conditions.

Figure 5.8 shows the distribution for the 2-state Potts model on square lattice with self-duality condition. A smooth zeros distribution is forming a pattern of a circle in the physical region.

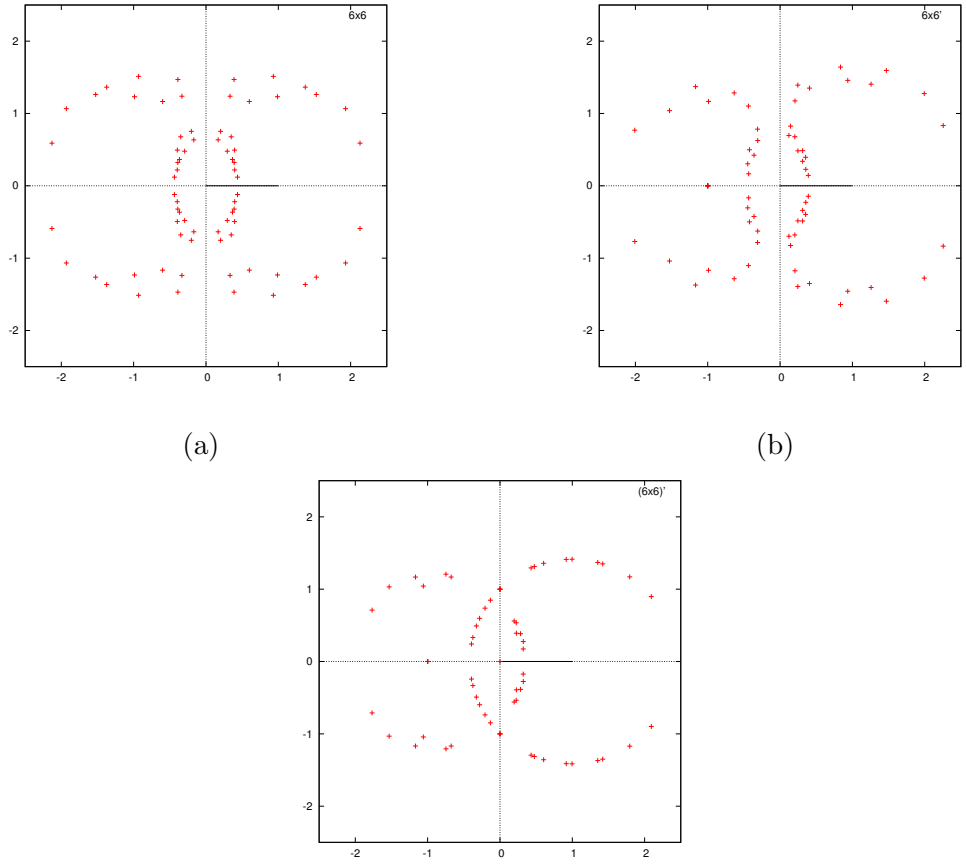

(a) (b)

(c)

Figure 5.9: 2-state, square lattice with different boundary conditions.

Figure 5.9 shows the zeros distributions for the 6 by 6 square lattice with different boundary conditions. The zeros for model with mixed periodic and open boundary conditions (Figure 5.9b) are distributed around two circles but mostly are not exactly lie on the limiting two circles. In contrast, the zeros for self-dual lattice case (Figure 5.9c) shows a clear line distribution especially in the positive real axis part (first and forth quadrant). The two circles are apparent even at small lattice size.

5.2 3-state Potts model on square lattice

Here we present the zeros distribution for the 3-state Potts model on a square lattice with periodic vertical and open horizontal boundary conditions. The study for higher state $Q > 2$ is interesting because until now there is no exact solution found for these cases.

In Figure 5.10, a structure which we call a branch can be seen in the non-physical axis $(-\infty, 0]$. This branch is related to the $(0, 1)$ antiferro region by the duality transformation (2.11). The increment in size shows multiple branch structures start to get closer to the real axis. Close to real axis, we observe an arm of dense zeros in the antiferro region. In the first and forth quadrants, an arc of a smooth circle is also observed. Note that the different structure between odd and even N is due to the finite size effect.

See particularly the new results for $N = 13, 14$ and 15 in Figures 5.12 to 5.14. Figure 5.15a shows the overlay distribution of zeros for $N = 12, 13$ and Figure 5.15b for $N = 14, 15$. The different in the non-physical region is particularly obvious between these figures (also see Figure 5.16).

Nevertheless, the zeros curves are the same for all cases at the $(1, \infty)$ ferro region except that their ending points have different value. The endpoint here is represented by the closest point near the real axis. The biggest size $N = 15$ has the closest point to this axis as compared to other sizes $N < 15$.

Figures 5.17 and 5.18 in addition emphasize the enlargement of the zeros distribution for $N = 12, 13, 14$ and 15 especially for the physical regions. Correspondingly, the zeros structure in the antiferro region moves closer to the real axis.

Although we expect that the closest point to the real axis comes from the largest case, Figure 5.16 shows otherwise. The closest point in this region is represented by the zeros from $N = 14$. As discussed earlier, we know that the partition function is always affected by the finite size effect.

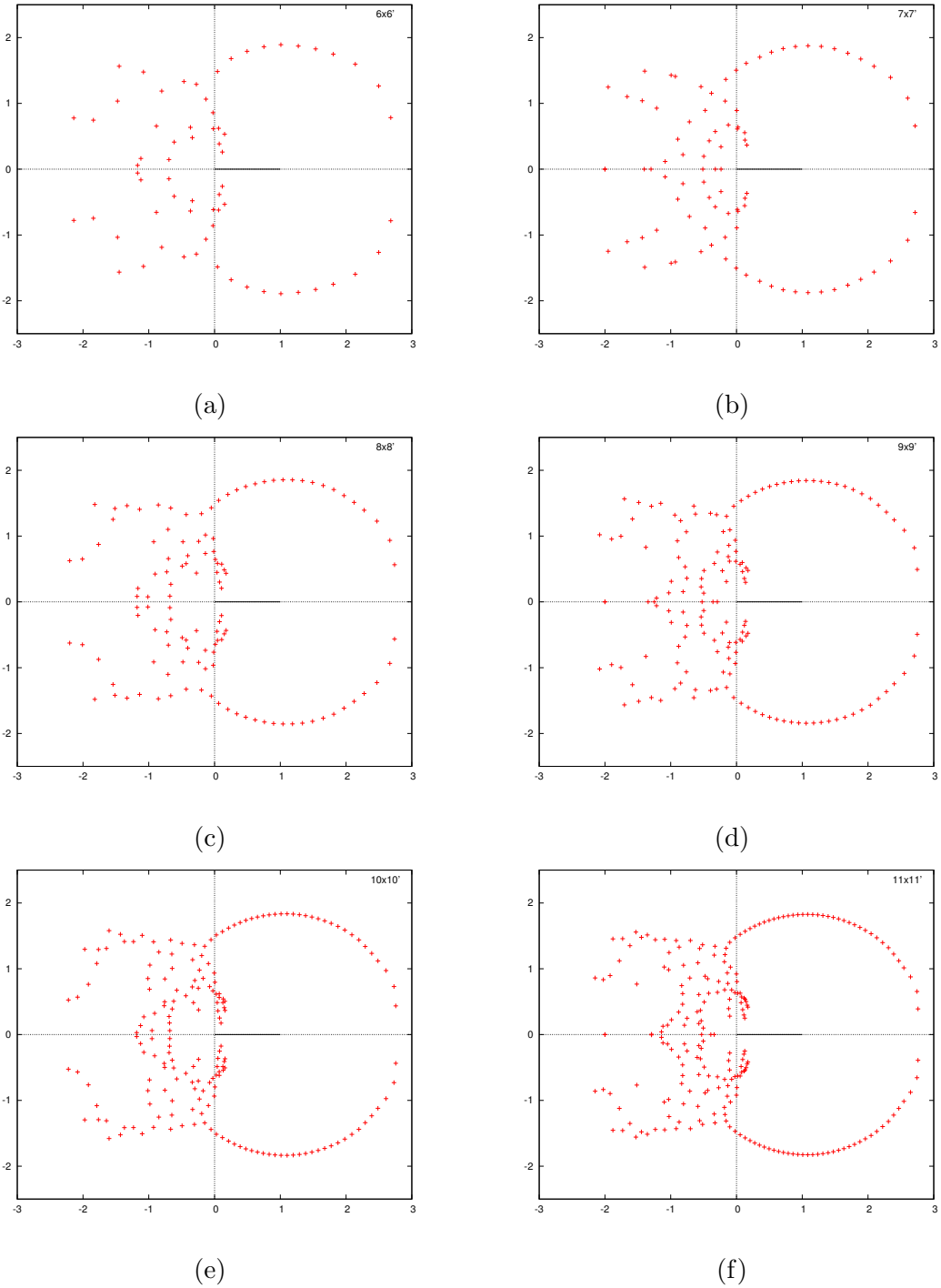

(a) (b) (c) (d) (e) (f)

Figure 5.10: 3-state, square lattice with periodic-open boundary conditions.

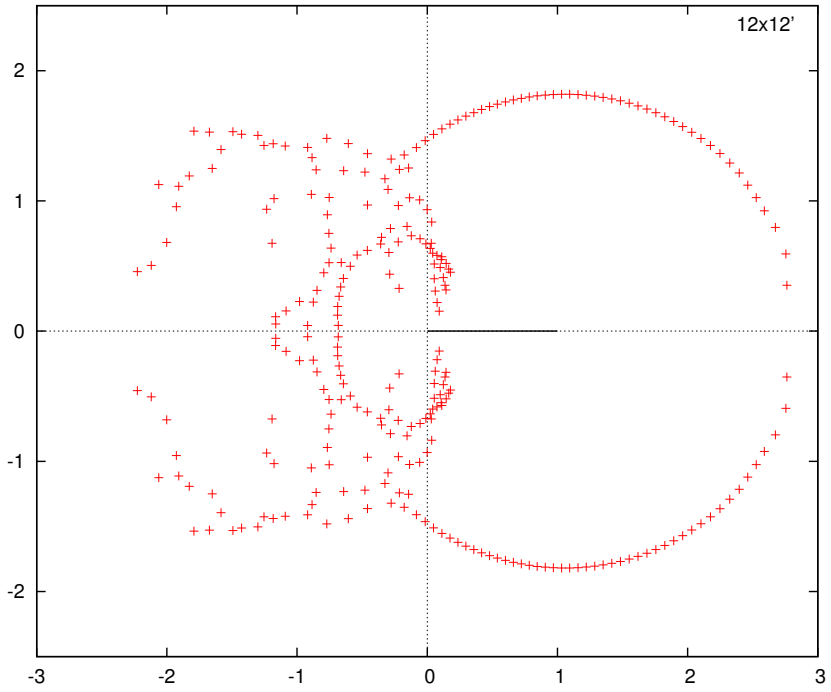

Figure 5.11: 3-state Potts model on 12 by 12 square lattice.

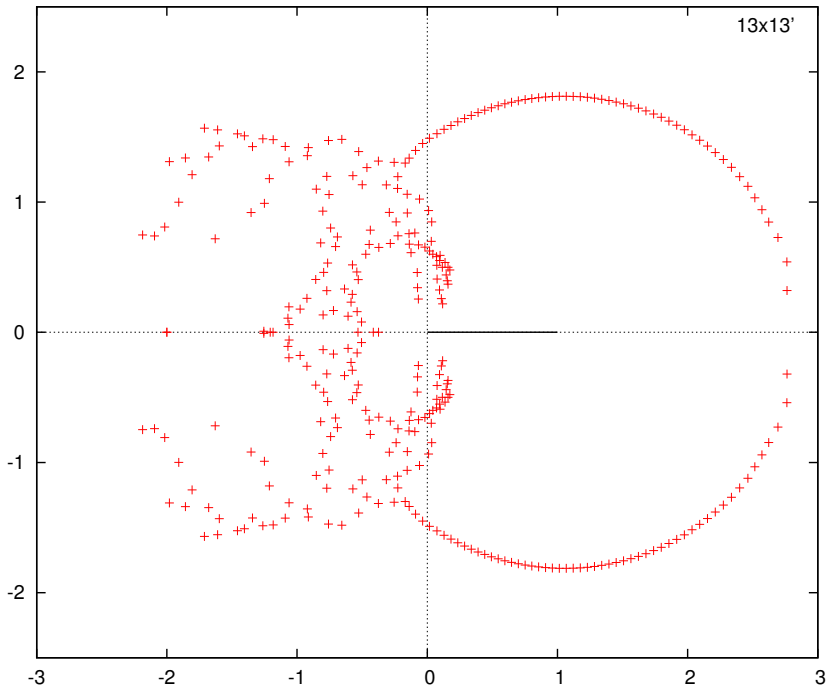

Figure 5.12: 3-state Potts model on 13 by 13 square lattice.

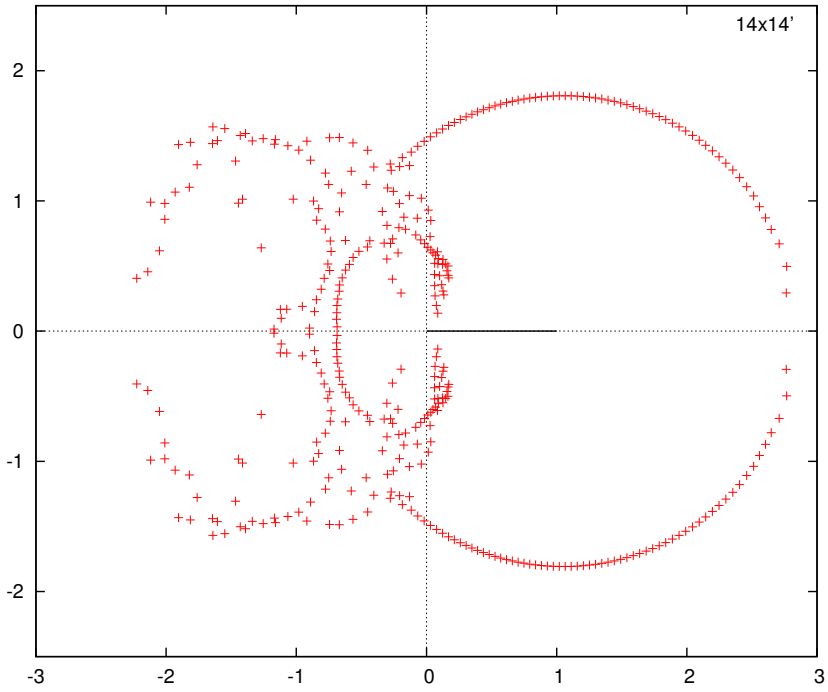

Figure 5.13: 3-state Potts model on 14 by 14 square lattice.

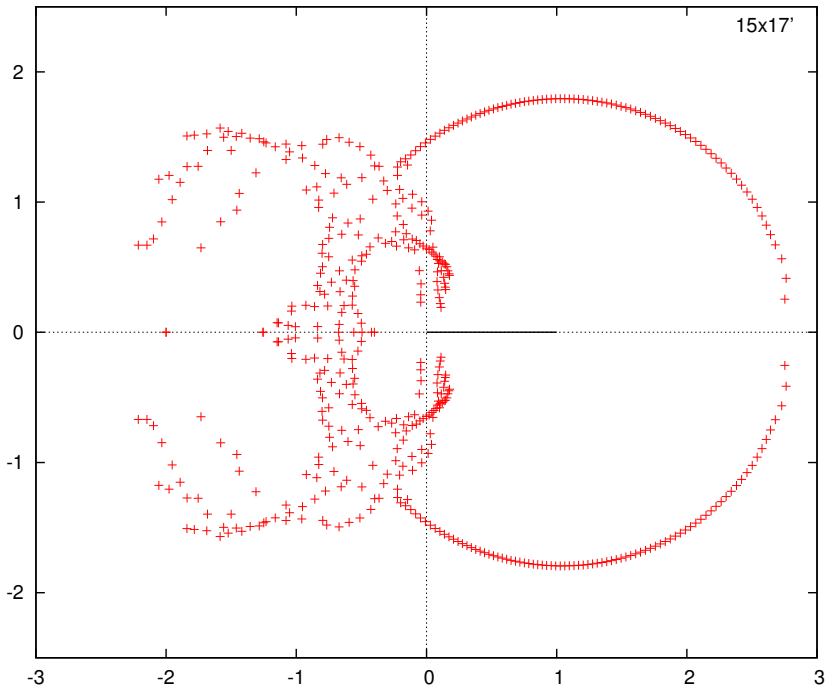

Figure 5.14: 3-state Potts model on 15 by 17 square lattice.

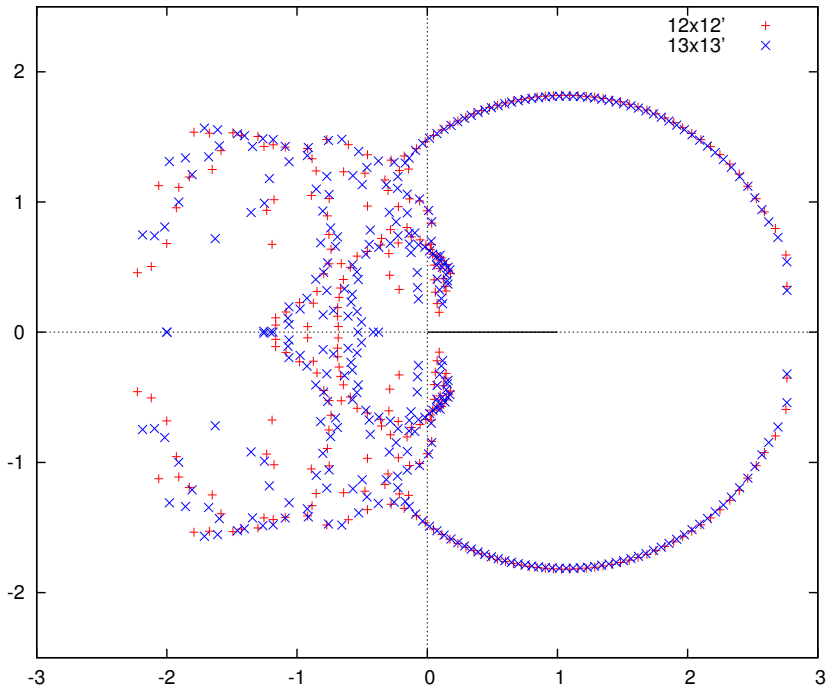

(a)

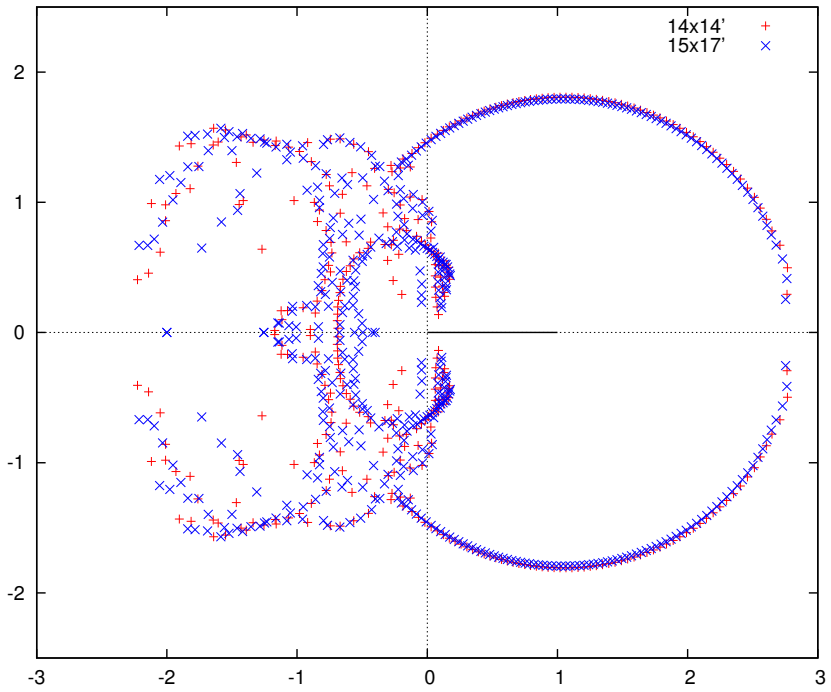

(b)

Figure 5.15: 3-state Potts model on a) $12 \times 12'$ and $13 \times 13'$ and b) $14 \times 14'$ and $15 \times 17'$ square lattices.

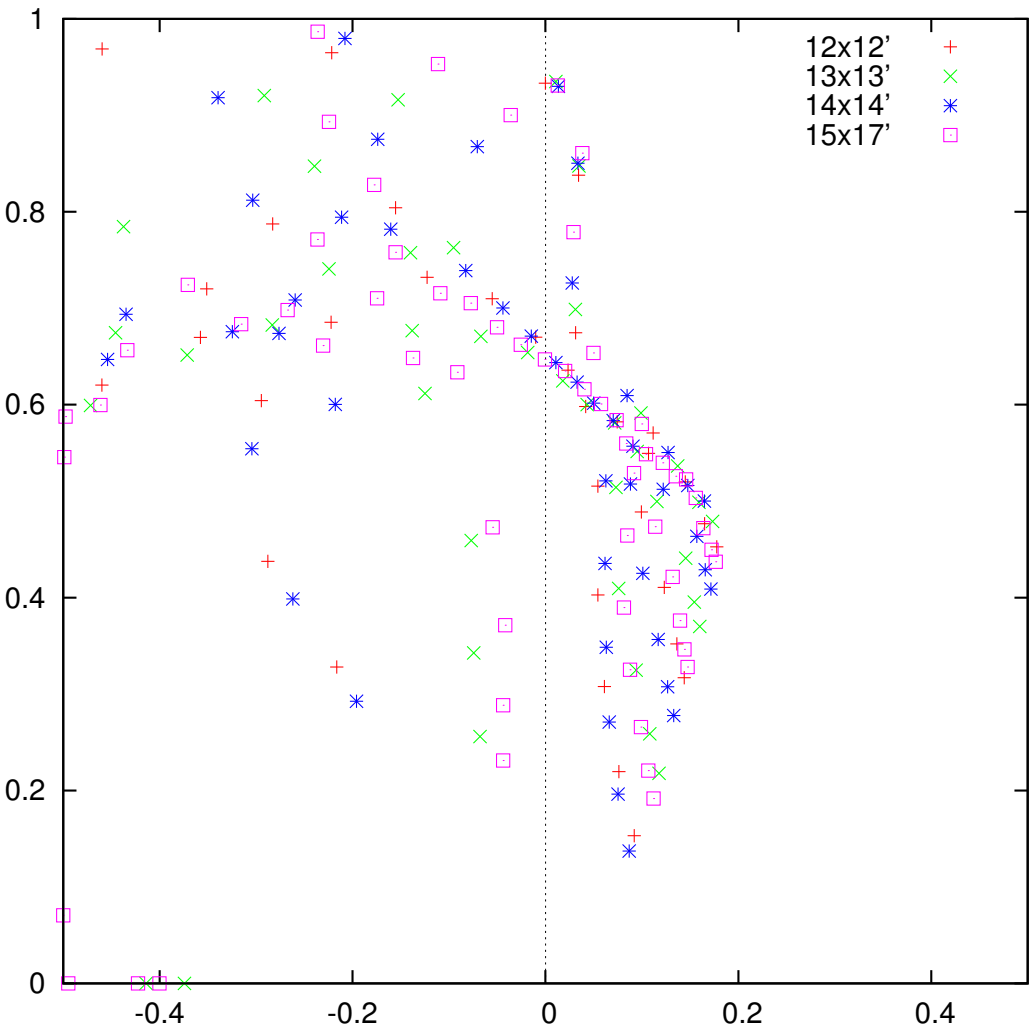

Figure 5.16: Antiferro [0,1]-region: 3-state Potts model on $N = 12, 13, 14, 15$ square lattices.

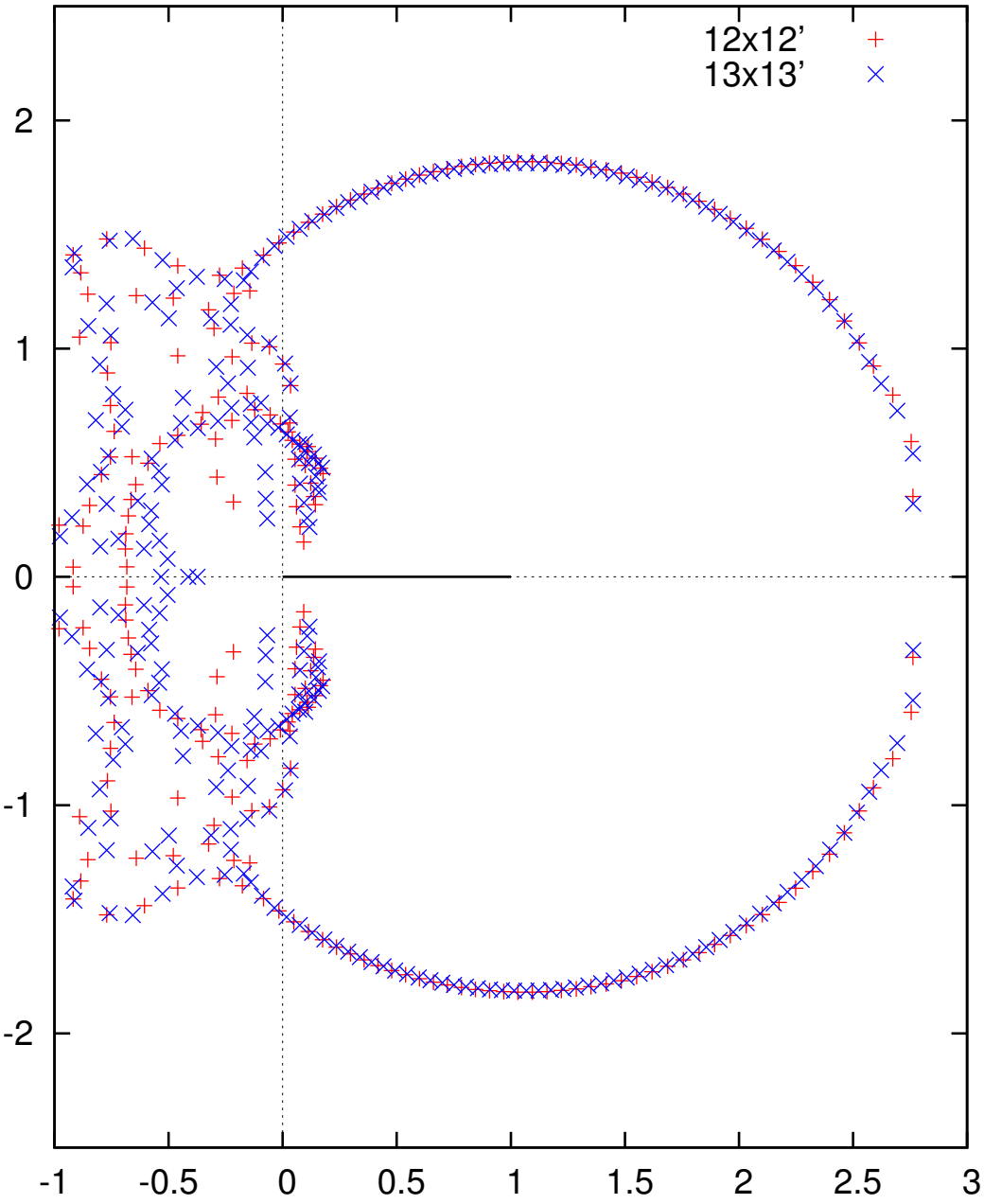

Figure 5.17: Zoom in: 3-state Potts model on $12 \times 12'$ and $13 \times 13'$ square lattices.

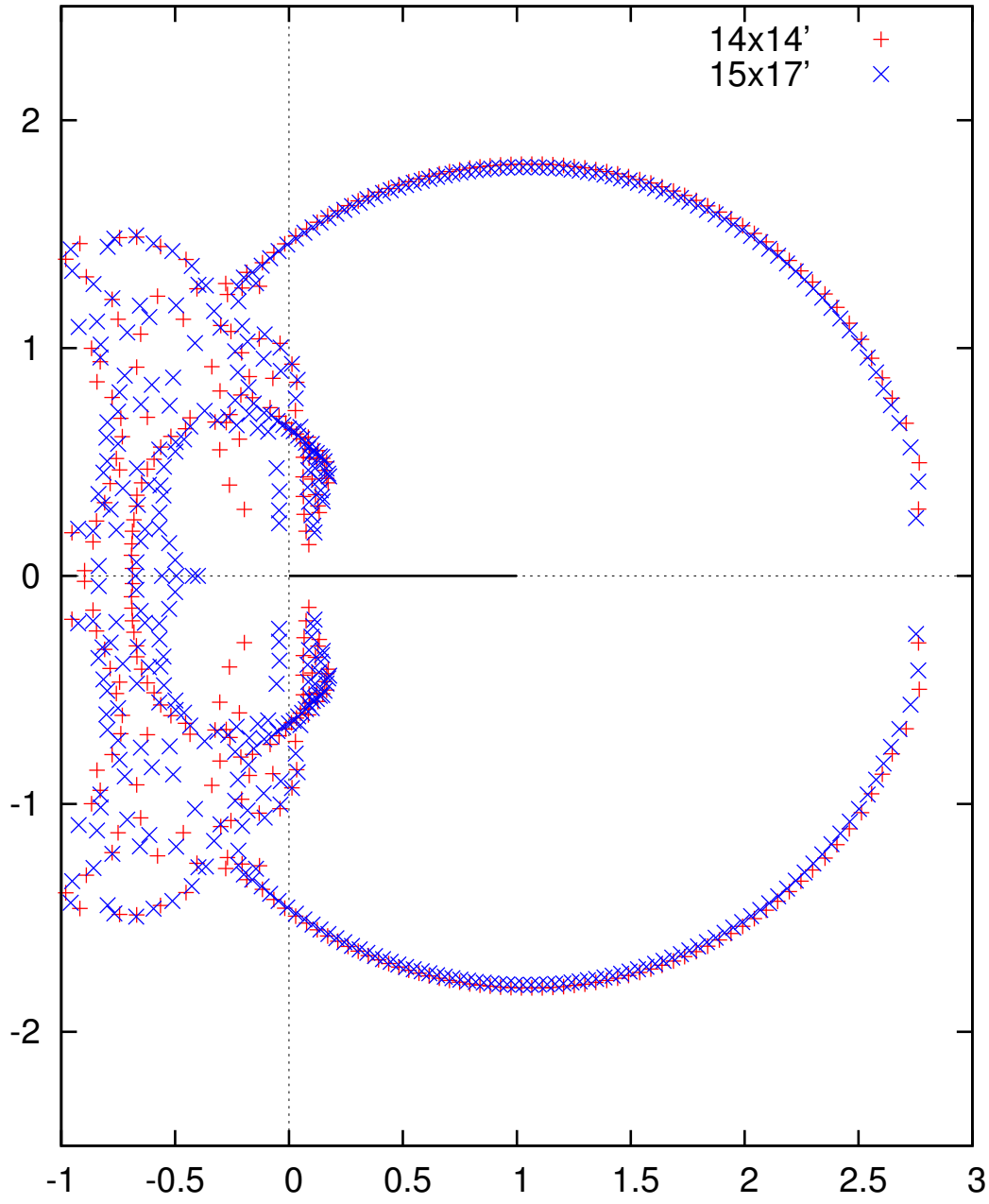

Figure 5.18: Zoom in: 3-state Potts model on $14 \times 14'$ and $15 \times 17'$ square lattices.

5.2.1 Self-duality partition function

We investigate the duality transformation for the 3-state Potts model on square lattice in this section.

On an infinite lattice, the square lattice is self-dual where the partition function is invariant under the duality transformation (2.11) given by

$$x \leftrightarrow \frac{x + (Q-1)}{x-1}. \tag{5.1}$$

Similarly, this duality transformation gives the same mapping for the zeros of the partition function. But for a finite lattice the effect of the transformation depends on the boundary conditions. However the boundary effect will be reduced at large lattice size when the partition function is approximately self-dual.

The zeros of the Ising model partition function lie on the locus of two circles where the dual for each zero must be its complex conjugate. Recall from § 4.4 that in this model the duality circle has radius $\sqrt{2}$ centered at (1,0) in the complex plane. Similarly, for the 3-state Potts model we may deduce its locus of zeros by this duality transformation. In this case the circle has radius $\sqrt{3}$ centered at (1,0) (see Figures 5.19 and 5.20).

Generally, a self-dual polynomial partition function may be constructed from a linear combination of partition functions from various boundary conditions [26, 54, 55]. Recall also the dual graph relation in § 2.2. Let Z_d be the dual of Z given by

$$Z\left(\frac{x + (Q-1)}{x-1}\right) = Z_d(x).$$

Here we will construct the linear combination of partition functions, denoted Z^* which preserve the self-duality condition. Let $M \in \mathbb{N}$ be the degree of Z, then

$$Z^*(x) = \frac{1}{(x-1)^{M/2}} Z(x) + Z_d(x) \tag{5.2}$$

where

$$Z^*\left(\frac{x+(Q-1)}{x-1}\right) = Z_d(x) + \frac{1}{(x-1)^{M/2}}Z(x)$$
$$= Z^*(x).$$

The polynomial Z^* has zeros distribution which lie on an arc of a circle that is invariance under duality transformation. This transformation corresponds to a zeros complex conjugation but not all the zeros are confined in that circle [34, 58]. This circle is given by

$$e^{\beta} = \frac{1-Q}{1+\sqrt{Q}e^{i\theta}} \quad \text{for } 0 \leq \theta \leq 2\pi \ . \tag{5.3}$$

The zeros distribution for Z^* on 12 by 12 and 13 by 13 square lattice with open horizontal and periodic vertical boundary conditions for $Q = 3$ are presented in Figure 5.19.

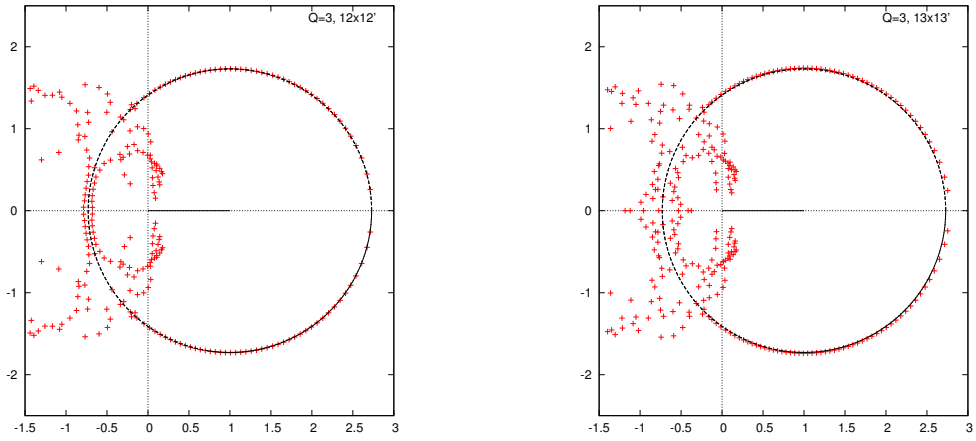

(a) (b)

Figure 5.19: Zeros distribution for polynomial Z^*: a) $N = 12$ and b) $N = 13$.

Figure 5.20 in addition plots the overlay zeros distribution for the Z, Z_d and Z^* (denoted as Z' in the plane). The incomplete circle in Figures 5.19 and 5.20 correspond to the circle (5.3).

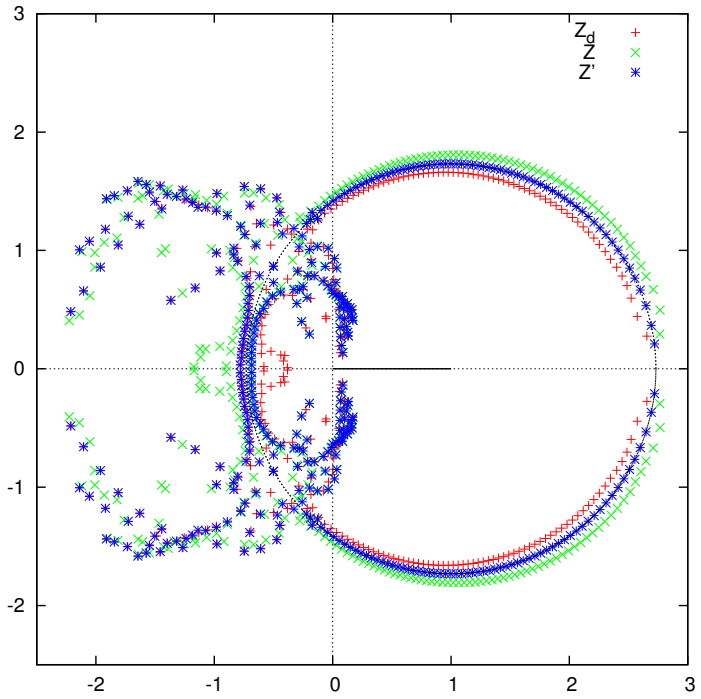

(a)

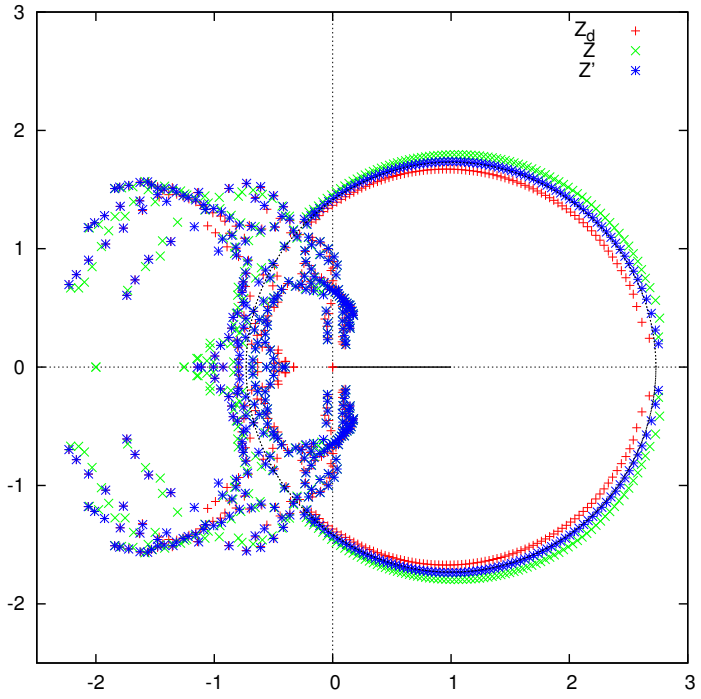

(b)

Figure 5.20: Zeros distribution for polynomial Z, Z_d and $Z^* = Z'$: a) $N = 14$ and b) $N = 15$.

5.3 $Q \geq 4$, square lattice Potts model

Here we consider the square lattice Potts model with state $Q = 4, 5$ and 6.

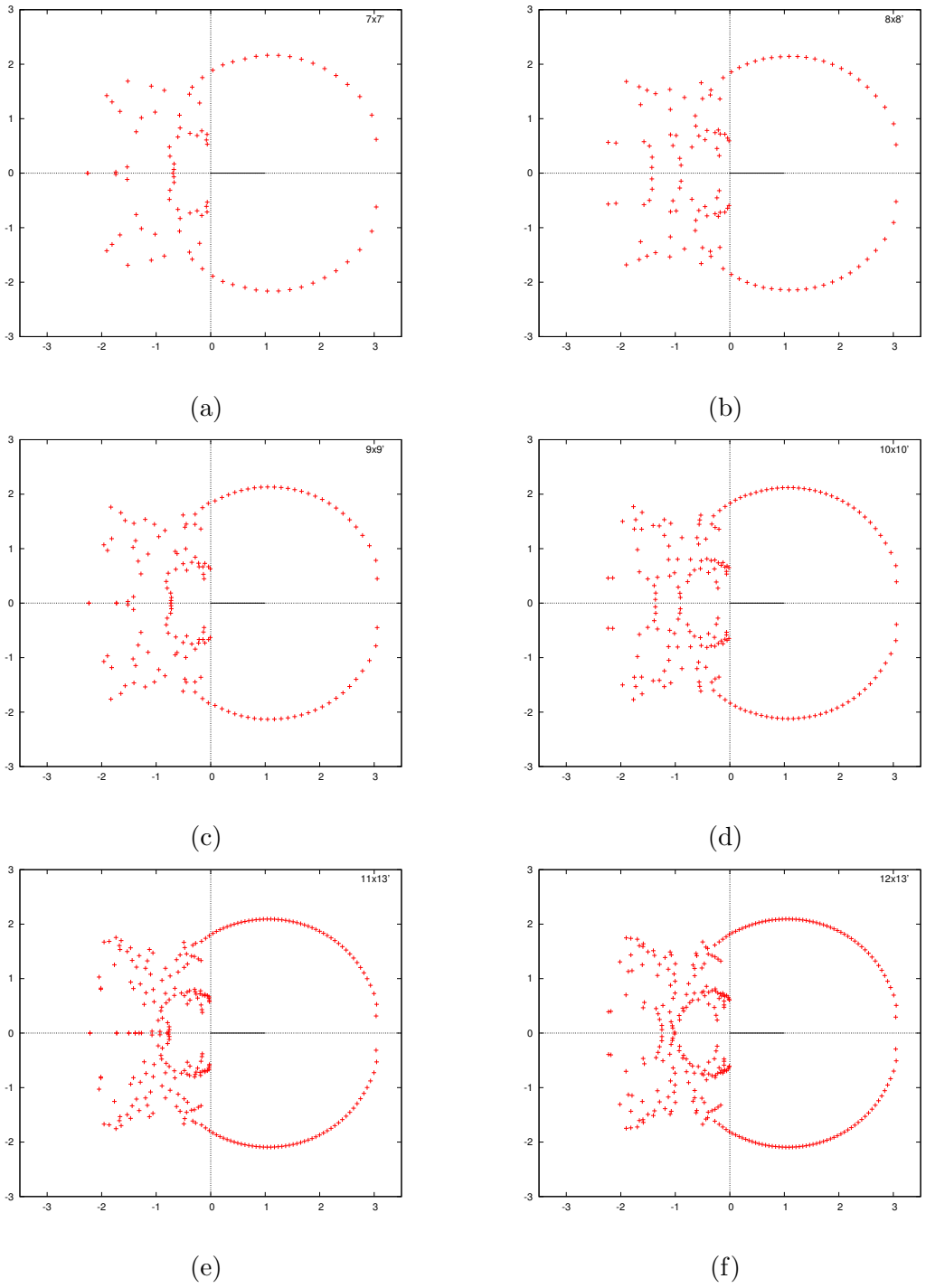

(a) (b) (c) (d) (e) (f)

Figure 5.21: 4-state, square lattice with periodic-open boundary conditions.

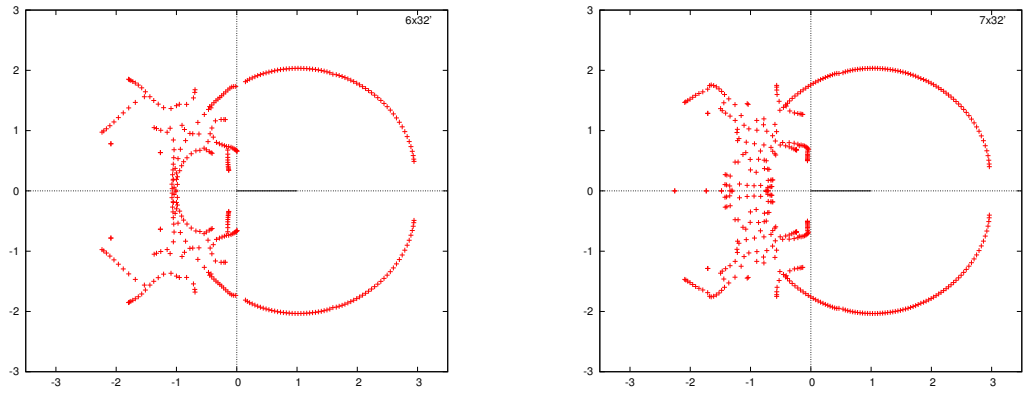

(a) (b)

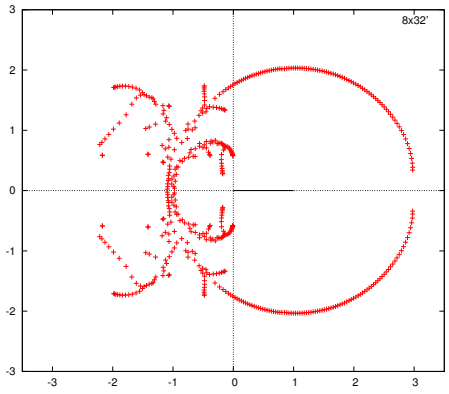

(c)

Figure 5.22: 4-state, square lattice with periodic-open boundary conditions (cont.).

The results of the 4-state case are shown in Figures 5.21 and 5.22. The zeros distribution in ferro region form a circle-like structure and the endpoints getting closer to the real axis as the size increases. We call the thick zeros collection that is very dense in some parts in the complex plane an arm band. In this figure, there is no obvious arm band in the antiferro region. For the non-physical region however, there are visible branches of zeros getting denser as the size increases. See this also in Figure 5.22.

Similarly, Figures 5.23 and 5.24 show the distribution for $Q = 5$ and 6, respectively. For both cases, we can see a steady curve in the ferro region as we change the lattice size. Our result is not large enough to suggest the limiting

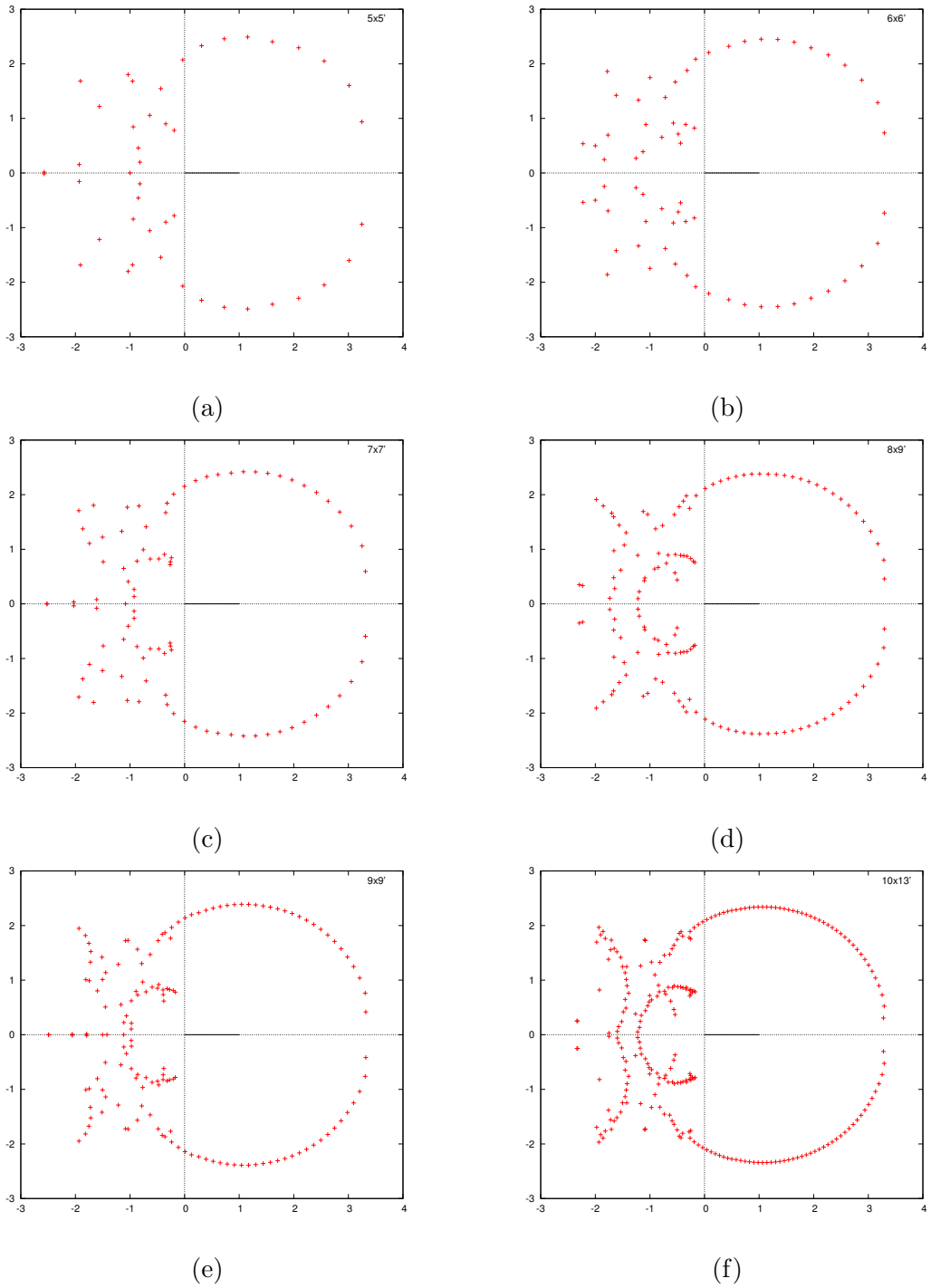

(a) (b) (c) (d) (e) (f)

Figure 5.23: 5-state, square lattice with periodic-open boundary conditions.

behaviour especially in the antiferro region, although a circle-like structure is obvious in the ferro region.

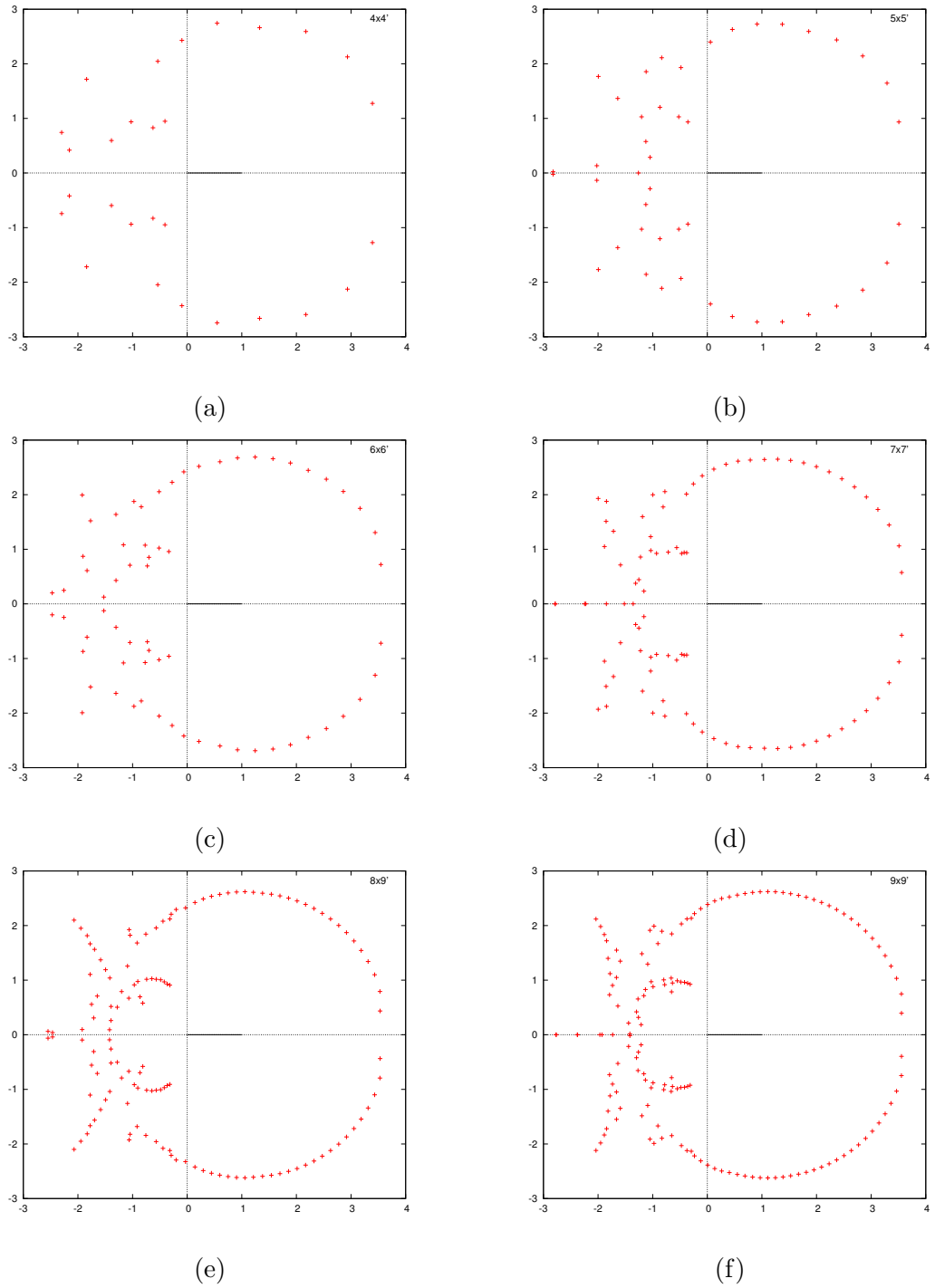

(a) (b) (c) (d) (e) (f)

Figure 5.24: 6-state, square lattice with periodic-open boundary conditions.

5.4 On triangular and hexagonal lattice

We know from Chapter 2 that the triangular and hexagonal lattice, up to boundary condition are dual to each other. This means we can get the hexagonal lattice distribution from the triangular case and vice versa.

Here we consider Q-state Potts models on triangular and hexagonal lattices with periodic and open boundary conditions in vertical and horizontal directions respectively.

For the 2-state Potts model on triangular lattice, the zeros distributions shown in Figures 5.25 and 5.26 have values near a pattern of a double 'horseshoe'. The scattered points are due to the boundary condition and the finite size effect. At the thermodynamic limit, the zeros distribution is expected to be smooth in this locus.

Figure 5.27 shows the zeros distribution for the 3-state Potts model on triangular lattice. The positive real axis shows the existence of arcs of zeros approaching the ferro and antiferro regions.

In addition, the zeros distributions of the 4- and 5-state Potts models on triangular lattice are presented respectively in Figures 5.28 and 5.29. We can see the line of zeros approaching the real axis in the ferro region as the size increases.

In the 4-state case, we can see some zeros move closer to the antiferro region as the size increases. This region either has a transition at the origin or interestingly at small positive value close to origin. A bigger lattice is needed for studying this region.

The case for 5-state however has a line of zeros approaching the real axis in ferro region but not in the antiferro region. Here some branches in the non-physical region move closer to the origin as the size increases.

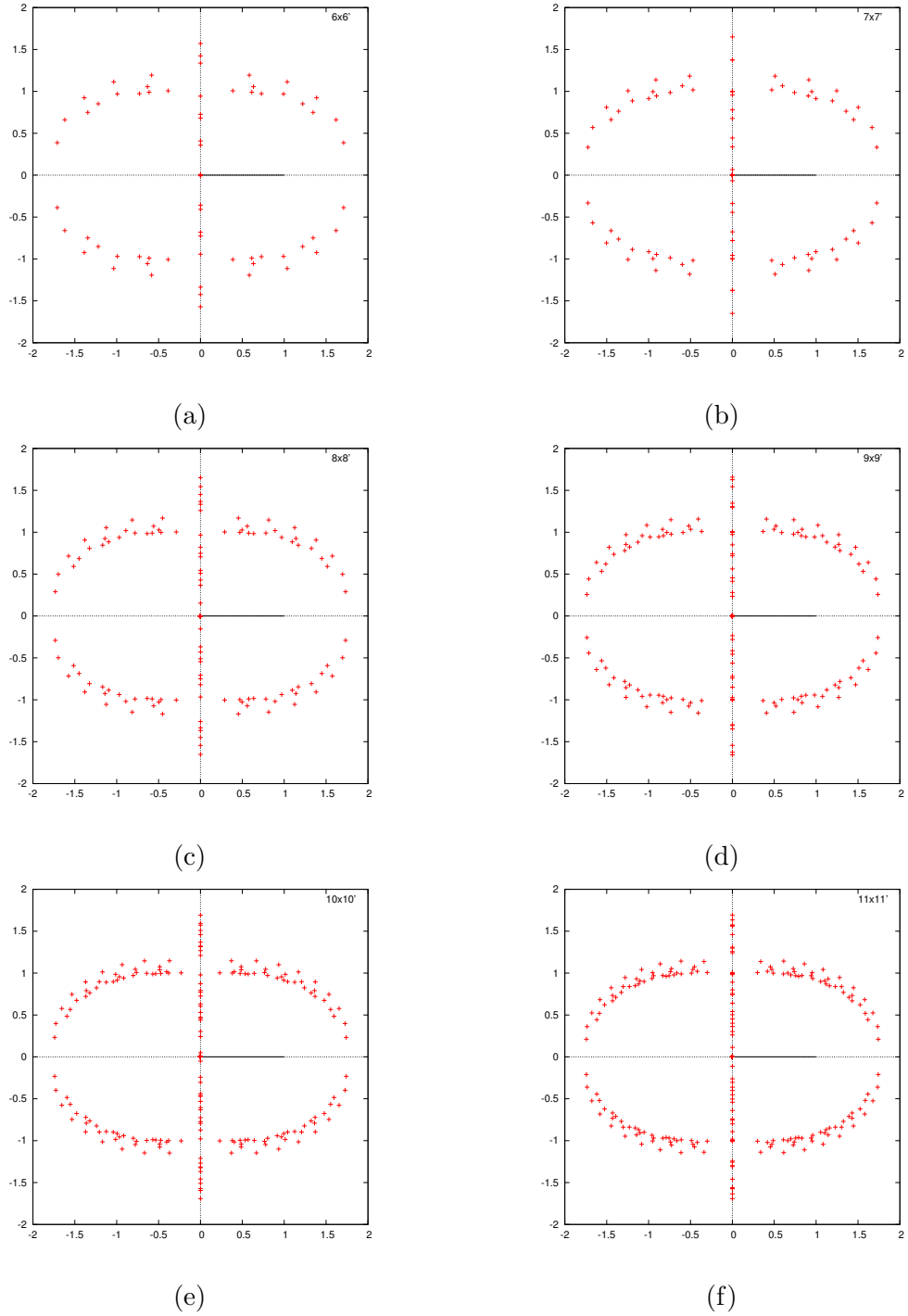

(a) (b) (c) (d) (e) (f)

Figure 5.25: 2-state, triangular lattice with periodic-open boundary conditions.

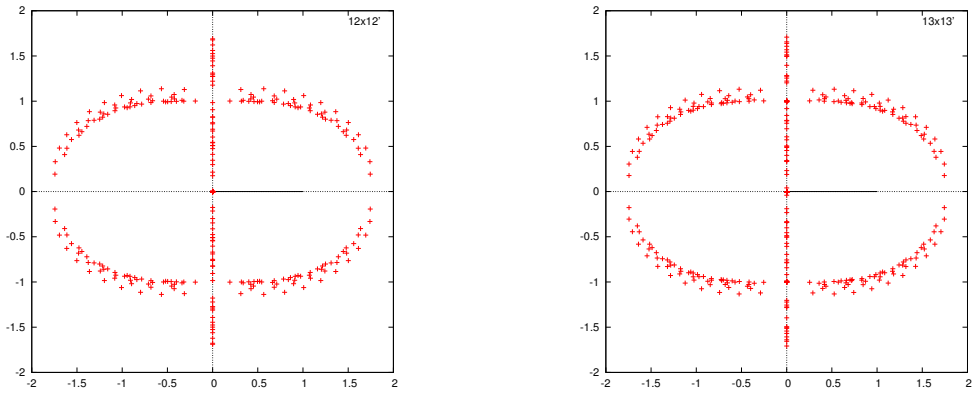

(a)

(b)

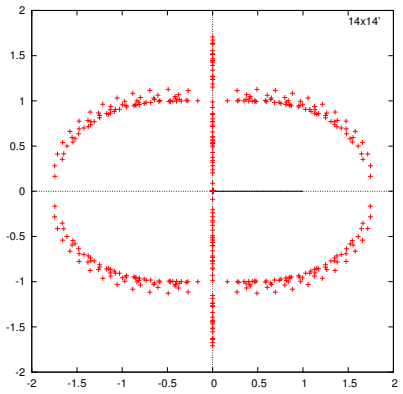

(c)

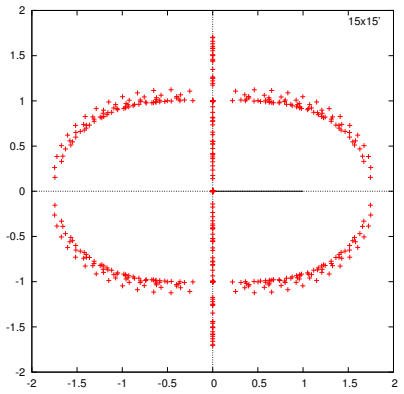

(d)

Figure 5.26: 2-state, triangular lattice with periodic-open boundary conditions (cont.).

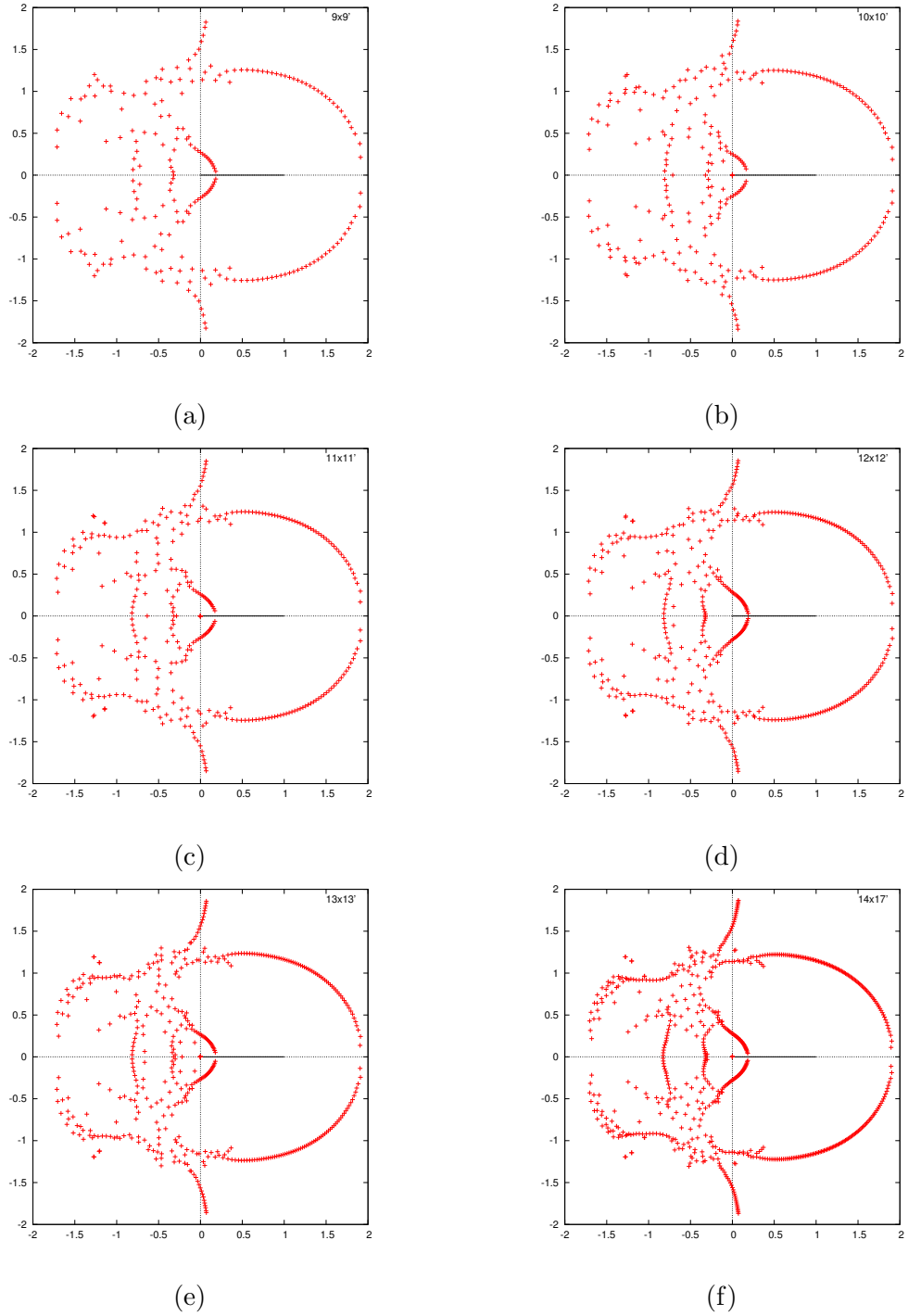

(a) (b) (c) (d) (e) (f)

Figure 5.27: 3-state, triangular lattice with periodic-open boundary conditions.

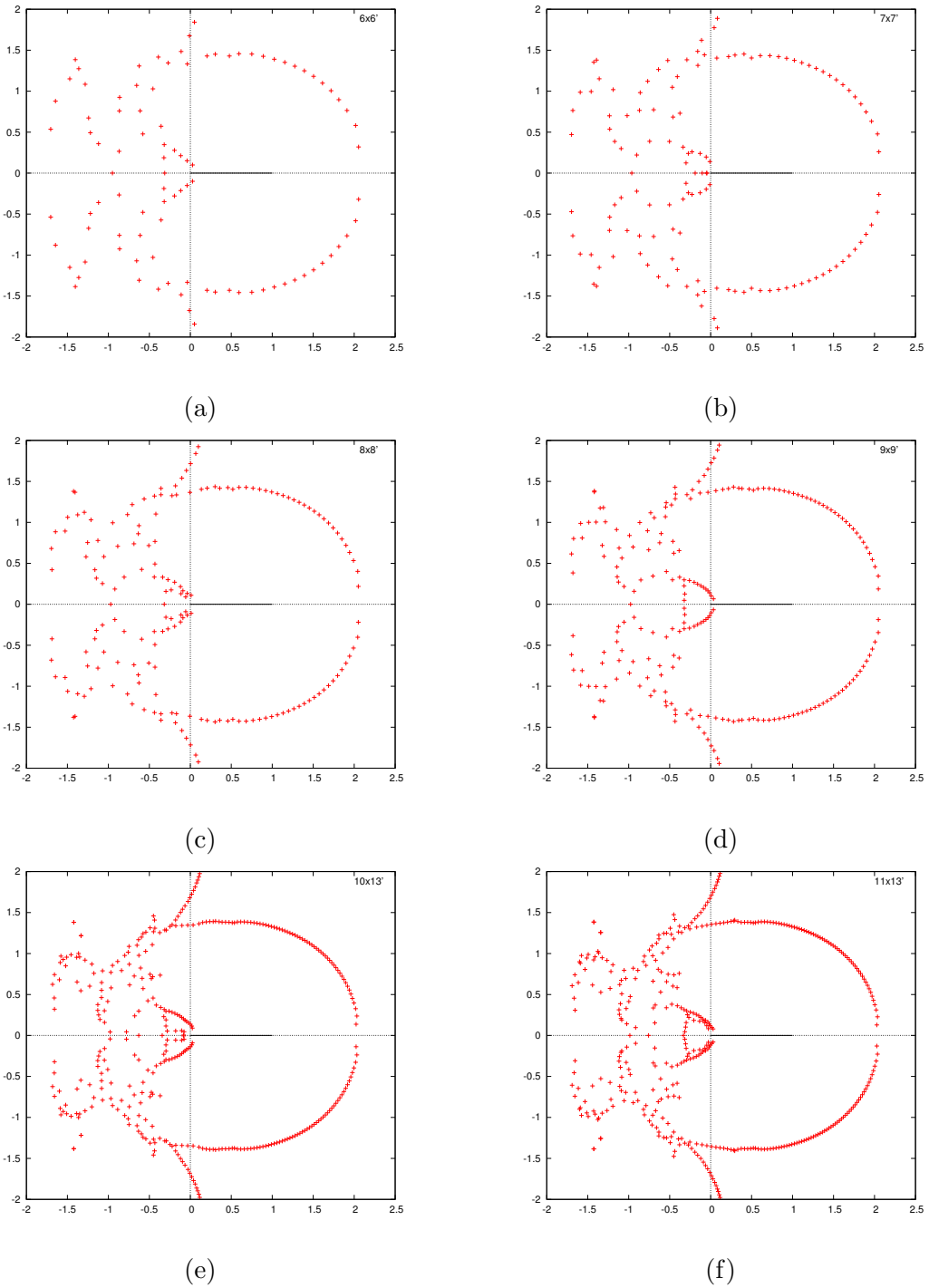

(a) (b) (c) (d) (e) (f)

Figure 5.28: 4-state, triangular lattice with periodic-open boundary conditions.

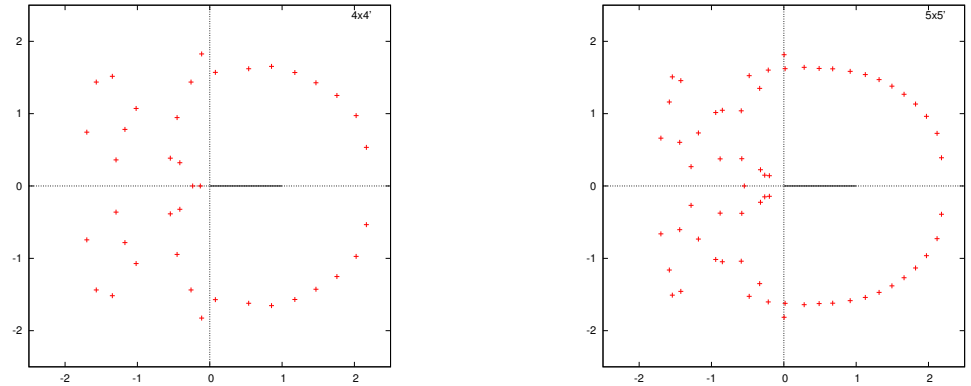

(a)

(b)

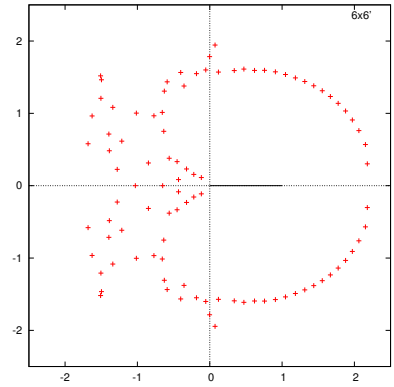

(c)

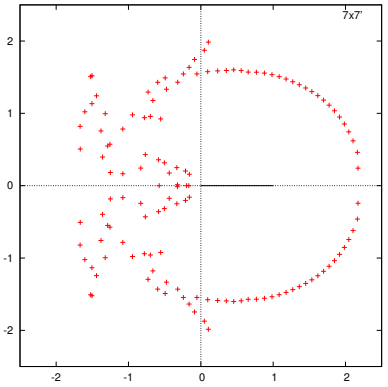

(d)

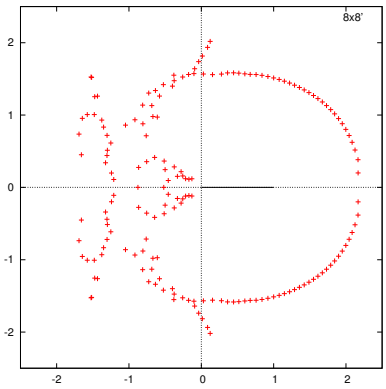

(e)

Figure 5.29: 5-state, triangular lattice with periodic-open boundary conditions.

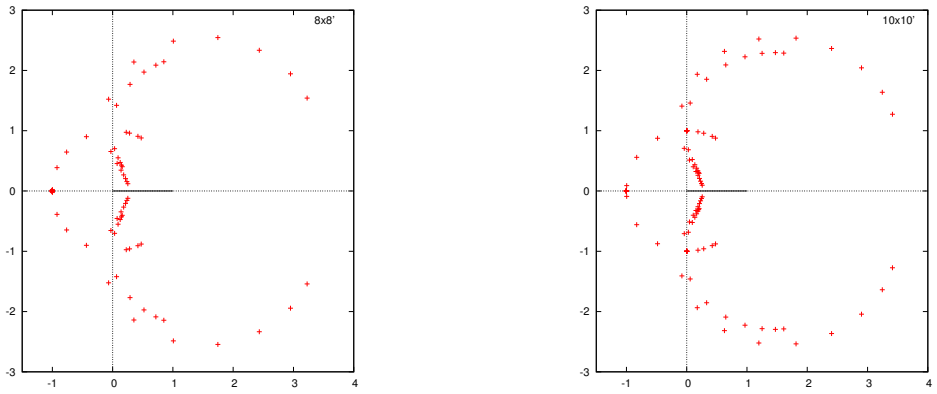

(a)

(b)

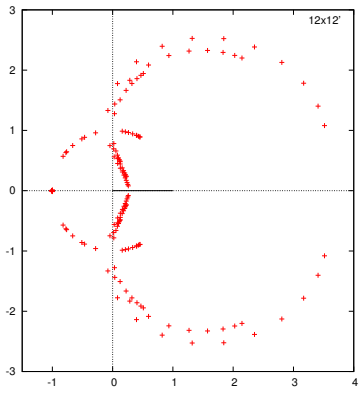

(c)

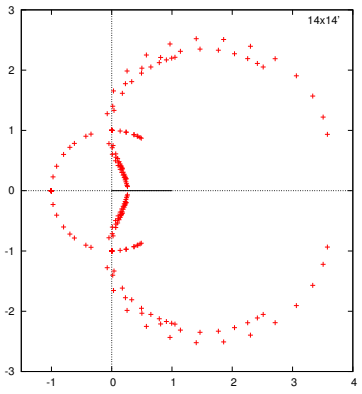

(d)

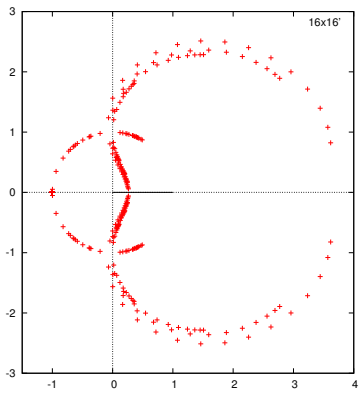

(e)

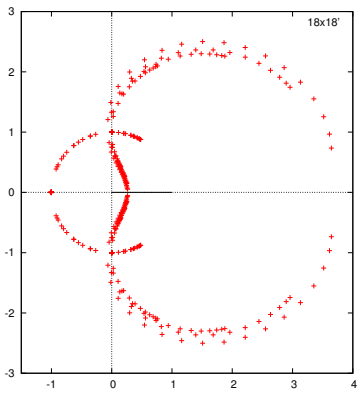

(f)

Figure 5.30: 2-state, hexagonal lattice with periodic-open boundary conditions.

For the 2-state hexagonal lattice in Figure 5.30, the zeros in the physical region form a pattern looking like a bean, especially in the first and forth quadrants. A visible locus of small circle near the origin and a 'bean'-like structure starts to appear in the physical region as we increase the size. At large enough lattice, it is expected that the distribution will have smooth structures.

For the 3-state case in Figure 5.31, the zeros are still far from the real axis in the ferro and antiferro regions. However a short arm at the antiferro region seems to move into the real axis direction. In the 4-state case, the antiferro region in Figure 5.32 also shows a short branch starts to emerge as we increase the lattice size.

We shall see a duality relation between the zeros distributions of triangular lattice and hexagonal lattice in the next section § 5.4.1. Note that the hexagonal lattice has polynomial order that is twice the order of polynomial for triangular lattice.

5.4.1 Duality transformation

Here we present the result from the duality transformation (2.11) on the triangular lattice. The lattice graph duality relation was described in § 2.2. For example, consider the zeros distributions as shown in Figure 5.33 to Figure 5.36. We can produce similar zeros distribution for hexagonal lattice using this transformation.

These examples show the implementation of duality transformation on the available zeros which gives result for its dual case. The result for a bigger hexagonal lattice can be produced from the triangular lattice; for example the $24\times24'$ hexagonal lattice from $12 \times 12'$ triangular lattice.

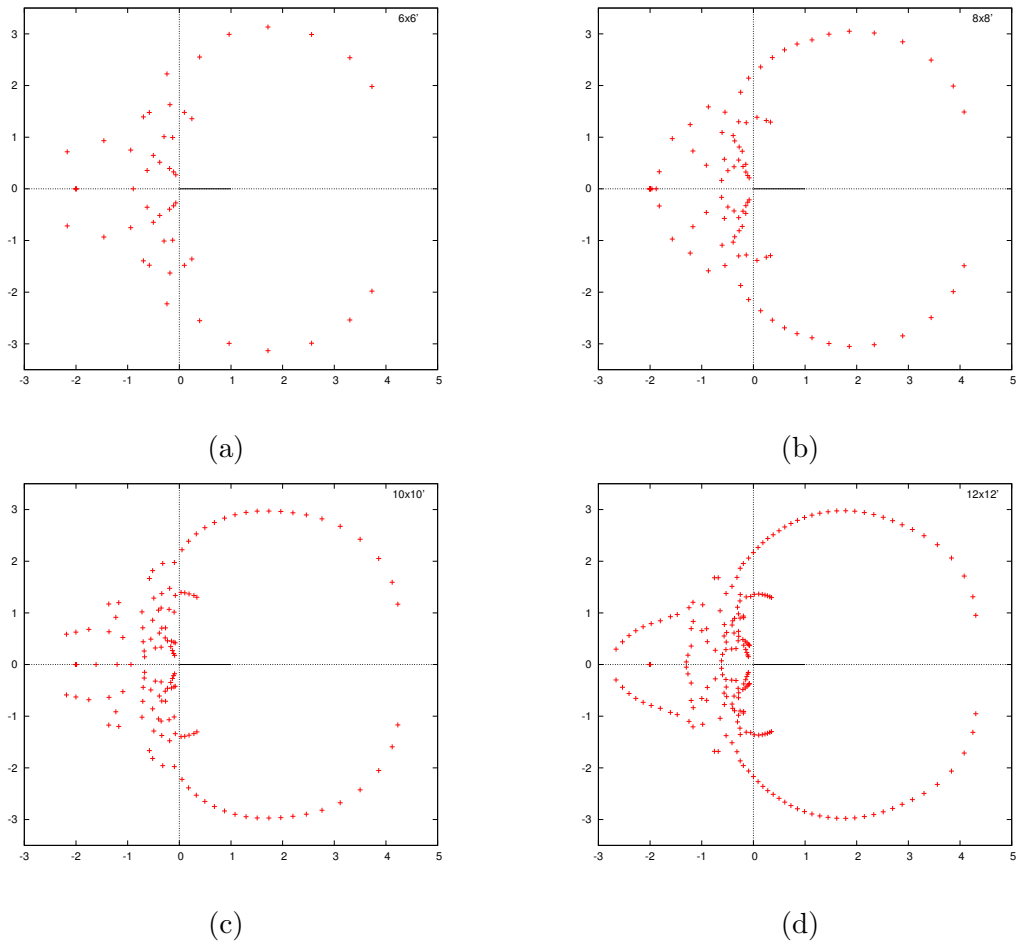

(a) (b)

(c) (d)

Figure 5.31: 3-state, hexagonal lattice with periodic-open boundary conditions.

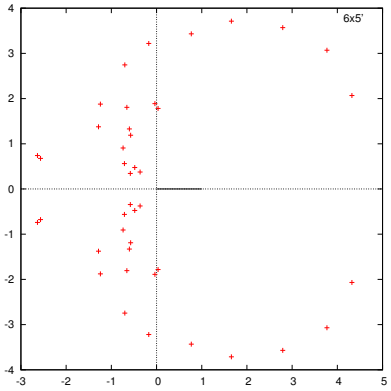

(a)

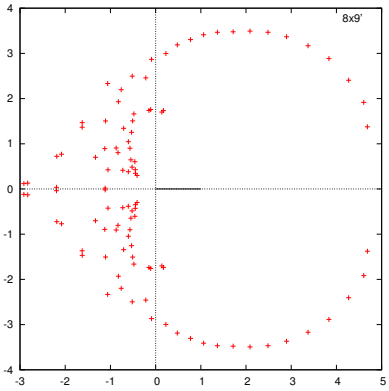

(b)

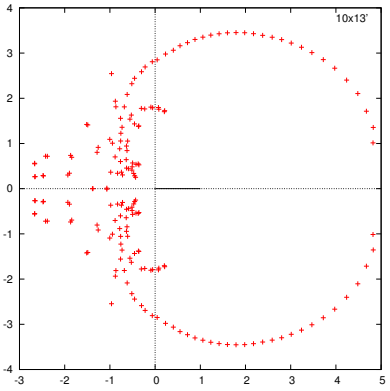

(c)

Figure 5.32: 4-state, hexagonal lattice with periodic-open boundary conditions.

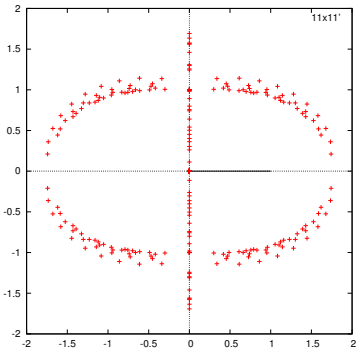

(a)

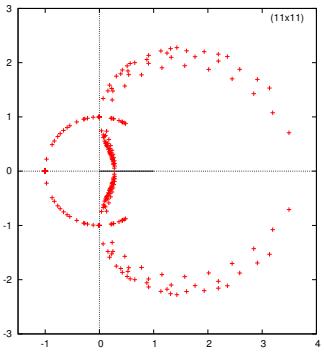

(b)

Figure 5.33: 2-state, duality transformation of 11 by 11 triangular lattice with periodic-open boundary conditions.

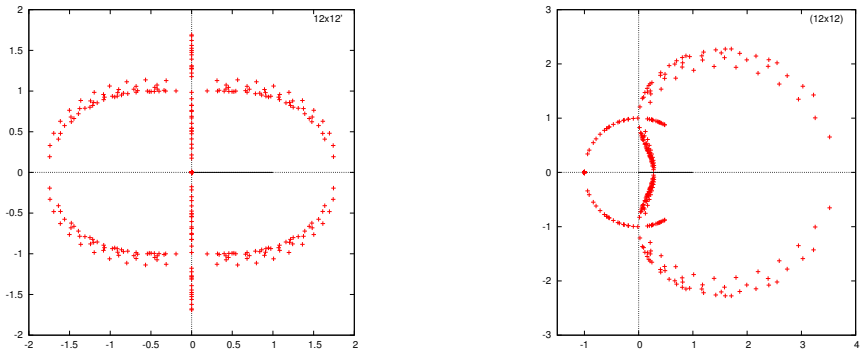

(a) (b)

Figure 5.34: 2-state, duality transformation of 12 by 12 triangular lattice with periodic-open boundary conditions.

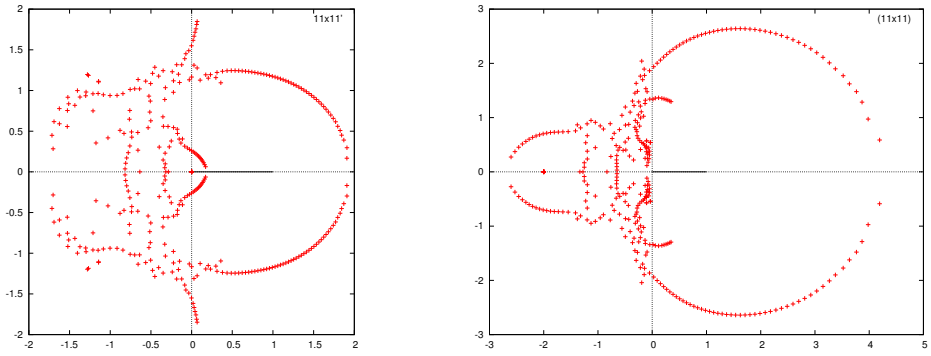

(a) (b)

Figure 5.35: 3-state, duality transformation of 11 by 11 triangular lattice with periodic-open boundary conditions.

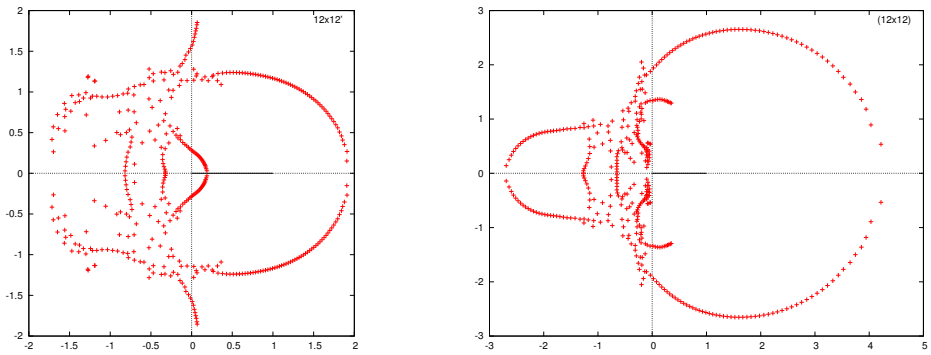

(a) (b)

Figure 5.36: 3-state, duality transformation of 12 by 12 triangular lattice with periodic-open boundary conditions.

5.5 On cubic lattice

Here we show the zeros distribution for cubic lattice Q-state Potts models with $Q \geq 2$. Figures 5.37 through 5.42 present the zeros distributions for number of states $Q = 2, 3, 4, 5, 6$ on cubic lattice with periodic boundary conditions in x and y direction and open boundary condition in z direction.

The largest 2-state Potts model on a cubic lattice in this thesis is the size $5 \times 5 \times 5'$ (see Figure 5.38c). We checked the result for big cases for example the zeros distribution for $5 \times 5 \times 5'$ and $6 \times 4 \times 5'$ (see Figure 5.38b) are correct as discuss in Valani's thesis [92].

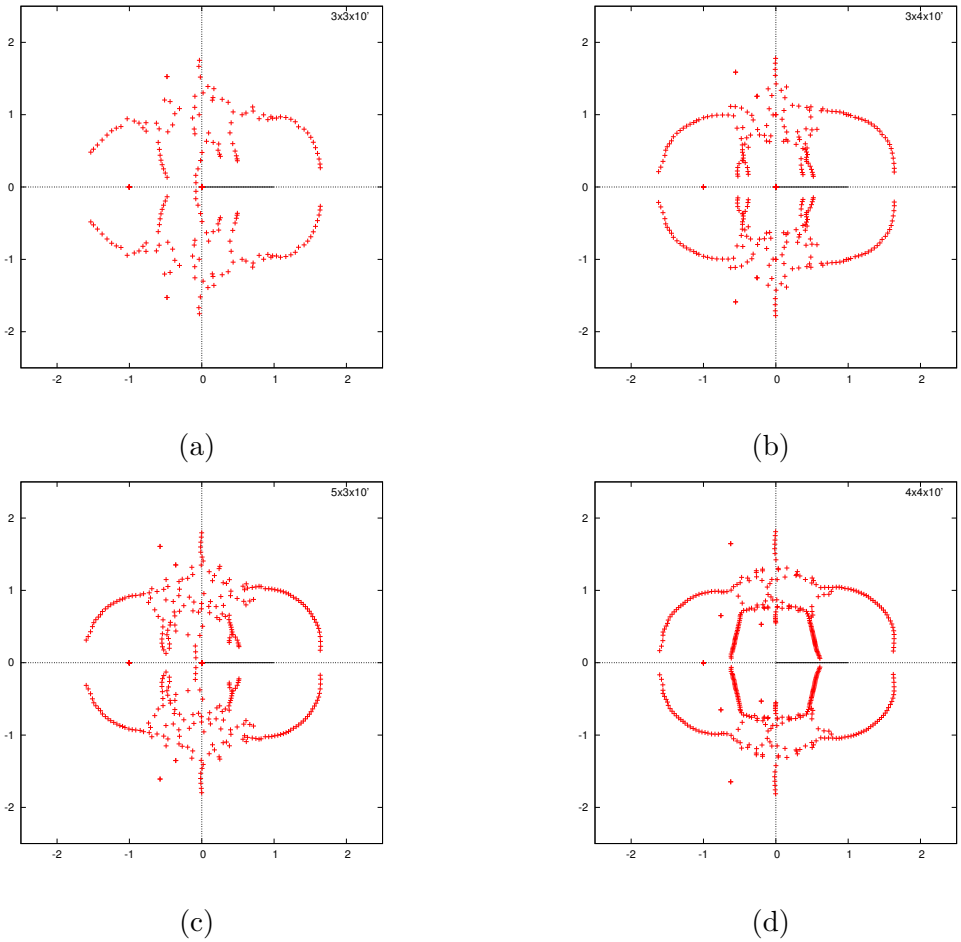

(a) (b)

(c) (d)

Figure 5.37: 2-state, cubic lattice with periodic-periodic-open boundary conditions.

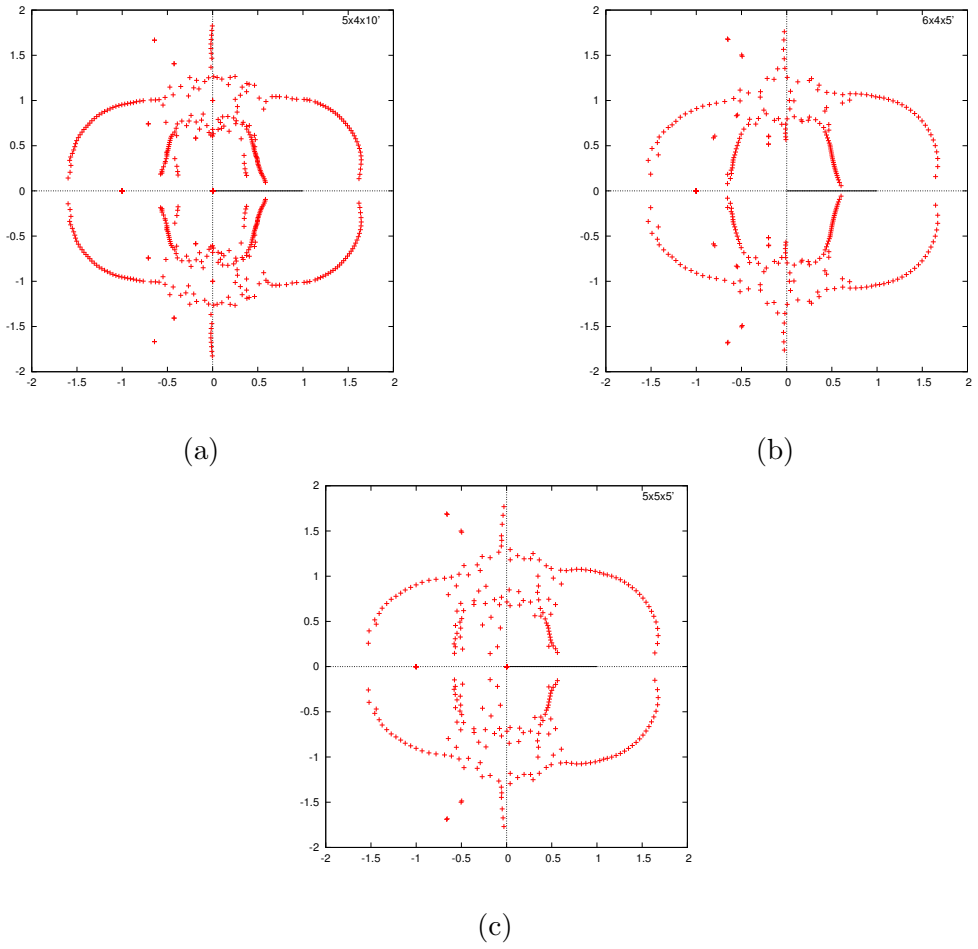

(a) (b)

(c)

Figure 5.38: 2-state, cubic lattice with periodic-periodic-open boundary conditions (cont.).

For small lattice sizes, no specific pattern can be extracted from the zeros distribution. But as the size increases, the pattern of zeros becomes more apparent. This can be seen for example for $4 \times 4 \times 10$ case in Figure 5.37d. The multiple branches near antiferro region only exist for odd N_x or N_y. This effect is due to the checkerboard pattern in the configuration. The odd case has no perfect checkerboard because of the periodic boundary condition. The distribution gives almost complete inverse symmetry $x \to \dfrac{1}{x}$.

The zeros distribution for the 3-state cubic lattice is presented in Figure 5.39. As the size increases the zeros move toward real axis but not in the same locus as the 2-state cubic case. Again, multiple branches are seen at the antiferro region.

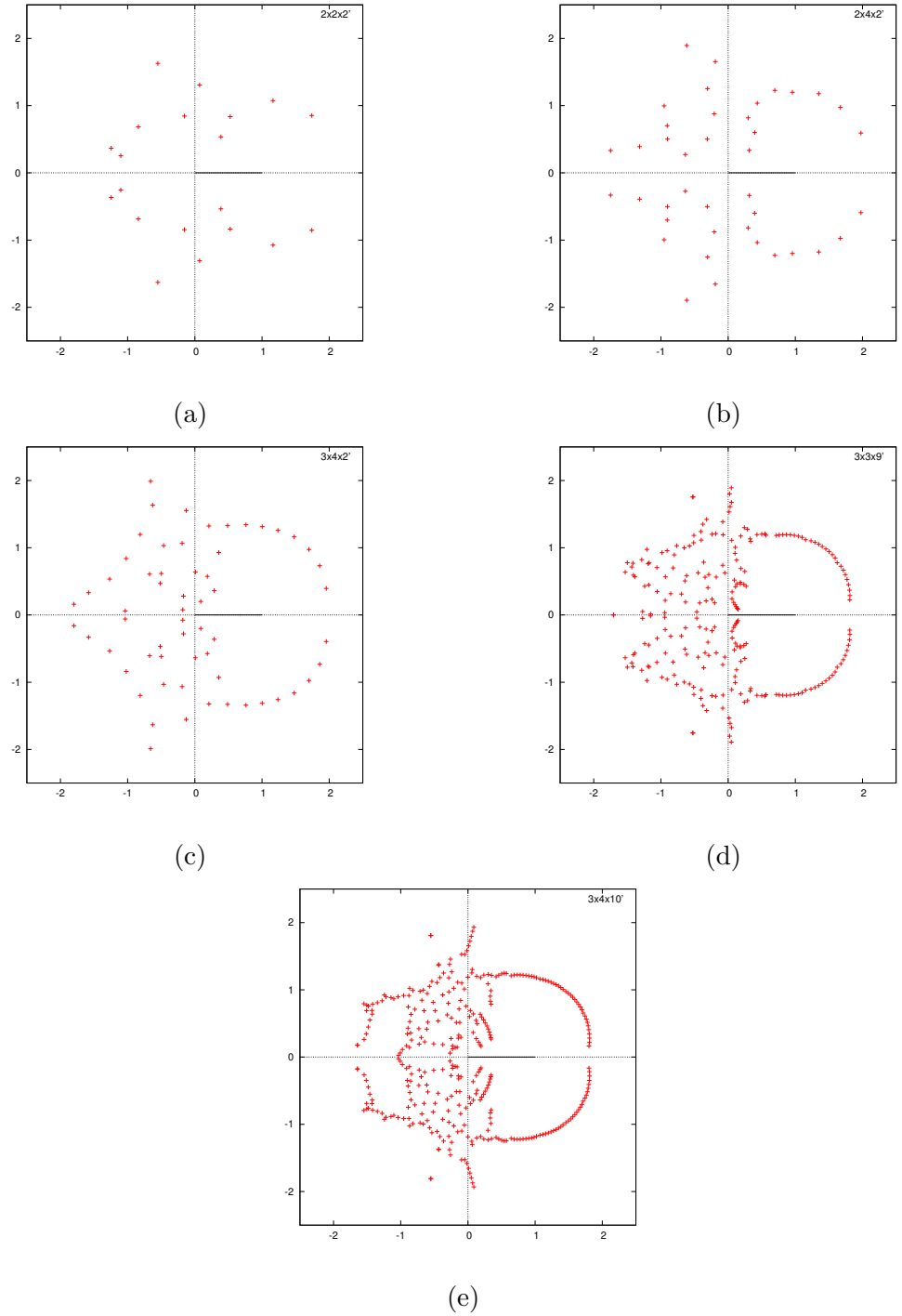

(a) (b) (c) (d) (e)

Figure 5.39: 3-state, cubic lattice with periodic-periodic-open boundary conditions.

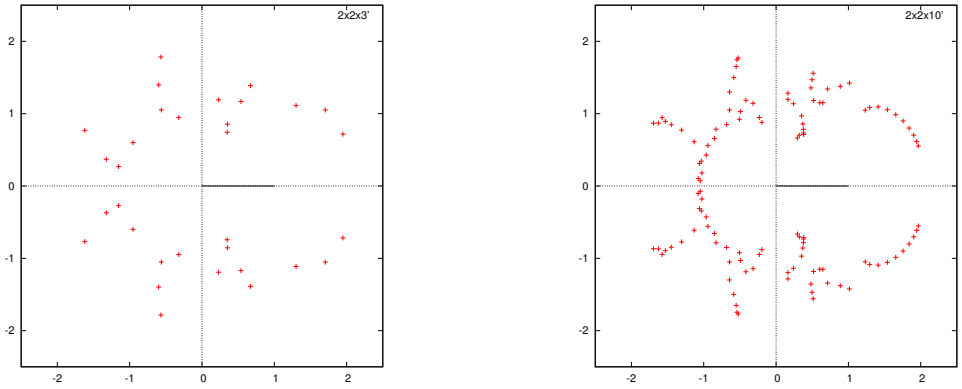

(a)

(b)

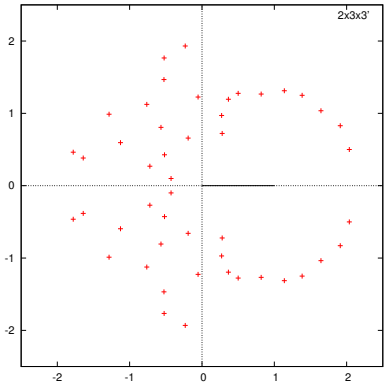

(c)

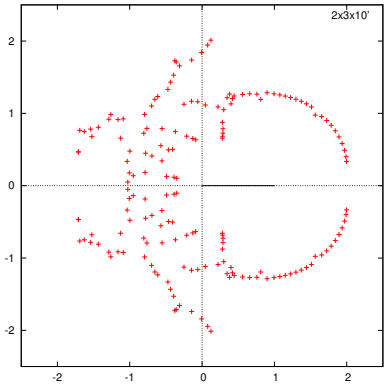

(d)

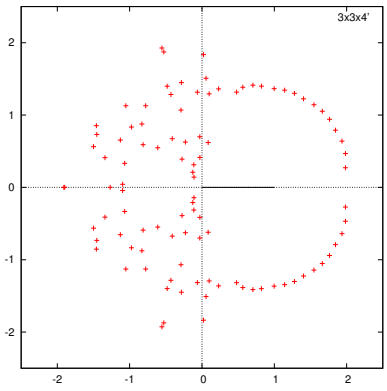

(e)

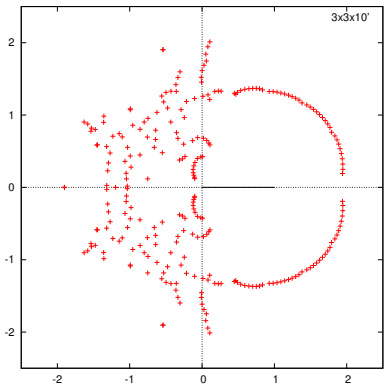

(f)

Figure 5.40: 4-state, cubic lattice with periodic-periodic-open boundary conditions.

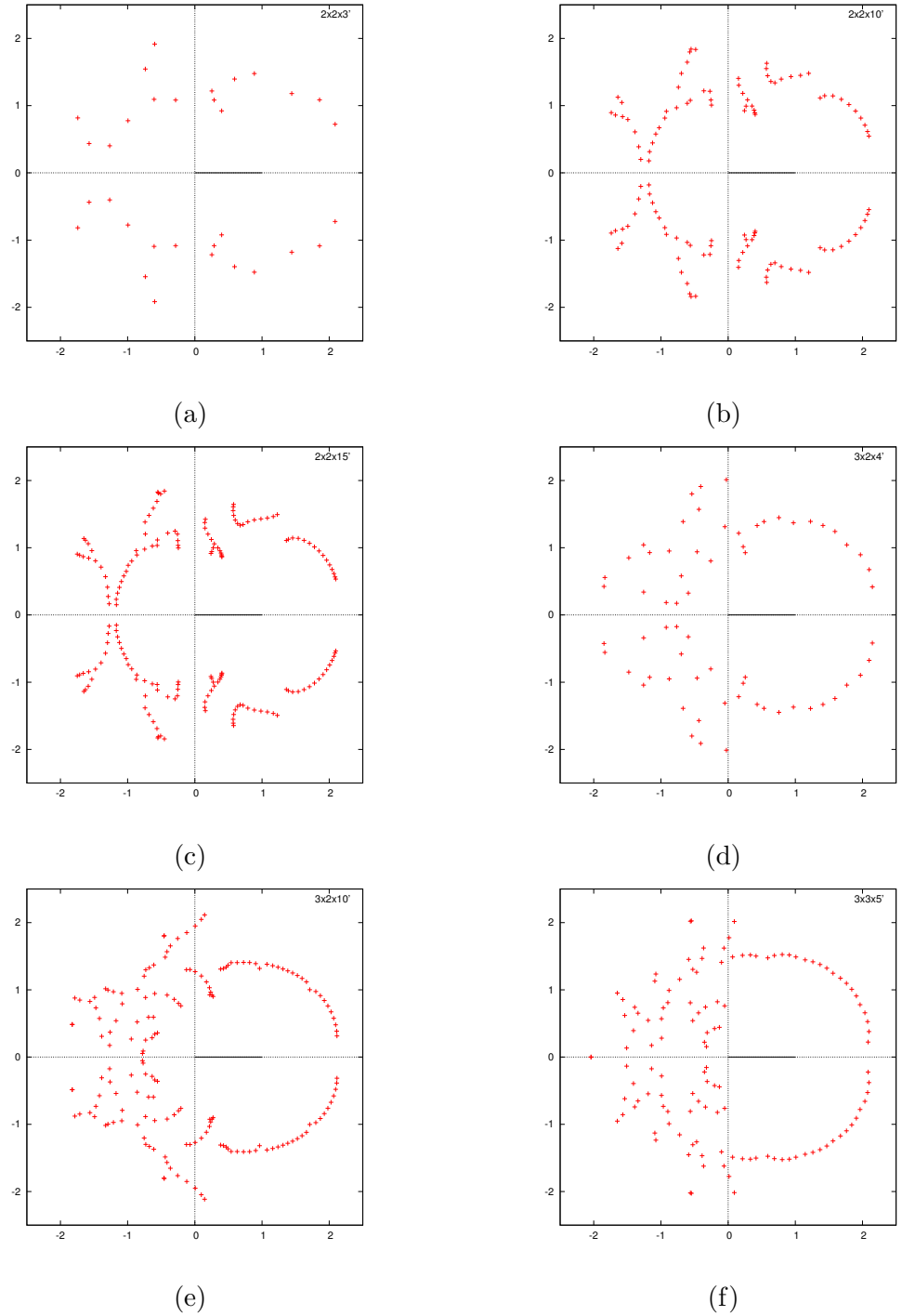

Figure 5.41: 5-state, cubic lattice with periodic-periodic-open boundary conditions.

The zeros distributions for 4-, 5- and 6-state Potts models on cubic lattices are presented in Figures 5.40, 5.41, and 5.42. The distributions are dominated by the finite size effect since the pattern is largely changing as the size increases. Although we can see the zeros move closer to real axis in the ferro region, that is difficult to conclude exactly for the antiferro part.

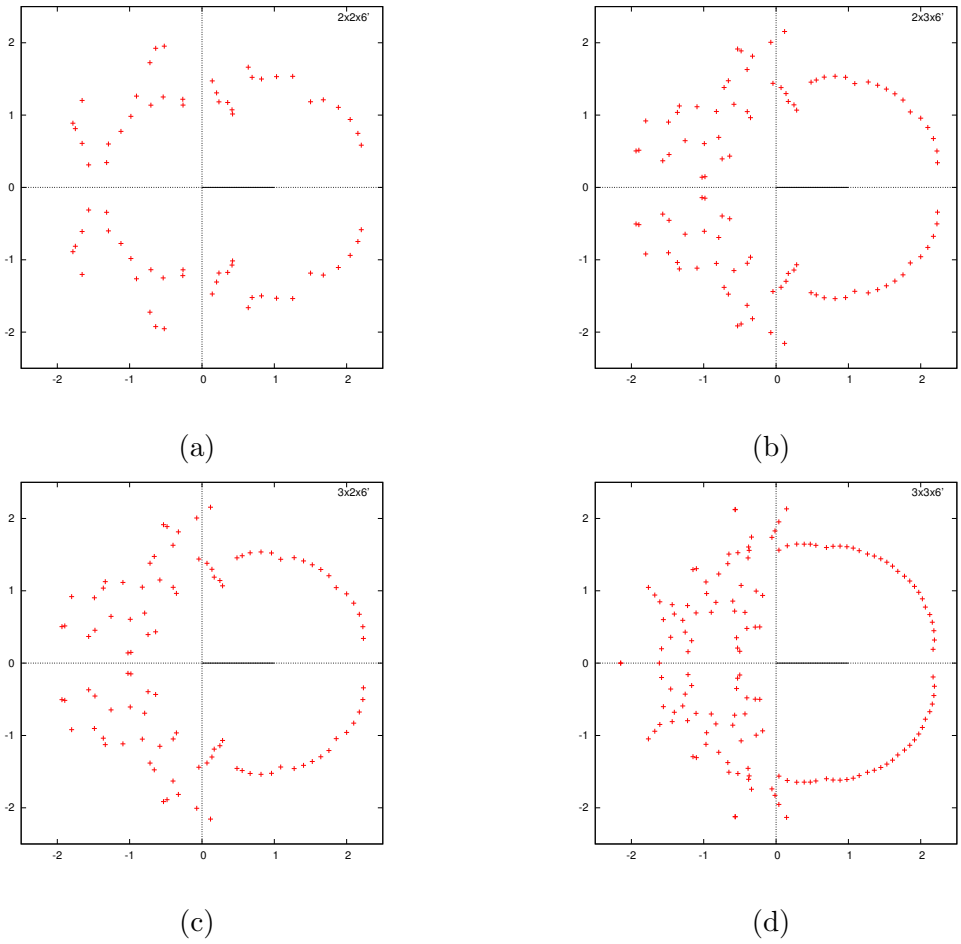

(a) (b)

(c) (d)

Figure 5.42: 6-state, cubic lattice with periodic-periodic-open boundary conditions.

5.6 On tetragonal and octagonal lattice

The final case that has been considered for the Q-state Potts model is the three-dimensional cubic lattices with closed packing. Here we consider two types of lattice

with closed packing known as the face-centered cubic lattice and the hexagonal close-packed lattice. Respectively, we call this two cases by their regular shapes portrayed in their lattice layer which are the octagonal and tetragonal lattices.

The zeros of the partition function for the 2-state Potts models on tetragonal lattice is shown in Figure 5.43. For small N_x and N_y, we can see the pattern of zeros distribution is changing. As the size increases, the pattern develops into more clear curve towards stability. We can see more symmetries such as $x \to -x$. A smooth line of zeros approaching the physical axis is also observed. This suggests the existence of a positive antiferro transition point.

For the tetragonal lattice 3-state case in Figure 5.44, the distribution is particularly scattered at some part of the non-physical region including the antiferro region. In ferro region, the zeros getting closer to real axis with dense line. The $3 \times 3 \times 7'$ case in Figure 5.44c shows a line emerges in the antiferro region. The finite size effect is obvious in these distributions portrayed by the zeros that is scattered in some parts of the plane.

The zeros distribution for the 2-state octagonal lattice is shown in Figure 5.45. As the size changes, an arm of zeros starts to form and moves closer to the antiferro region. The behaviour of this zeros is very similar to the tetragonal 2-state case.

Furthermore, the zeros distributions for the 3-state octagonal cases are shown in Figure 5.46. Again, the similarity with the tetragonal case is observed. The locus of zeros in the physical region is more stable as compared to the scattered zeros in the non-physical region.

For the hexagonal close-packed lattice, the vertices are placed in repeated tetrahedron shape. This arrangement forms another shape of octahedron at some middle layer of the lattice. This is similar to the face-centered cubic case. For this reason, although we portrayed them with different regular shape, the zeros distribution has a similar pattern of distribution. In all these four cases in this section, the zeros endpoints in ferro region are very close to the real axis.

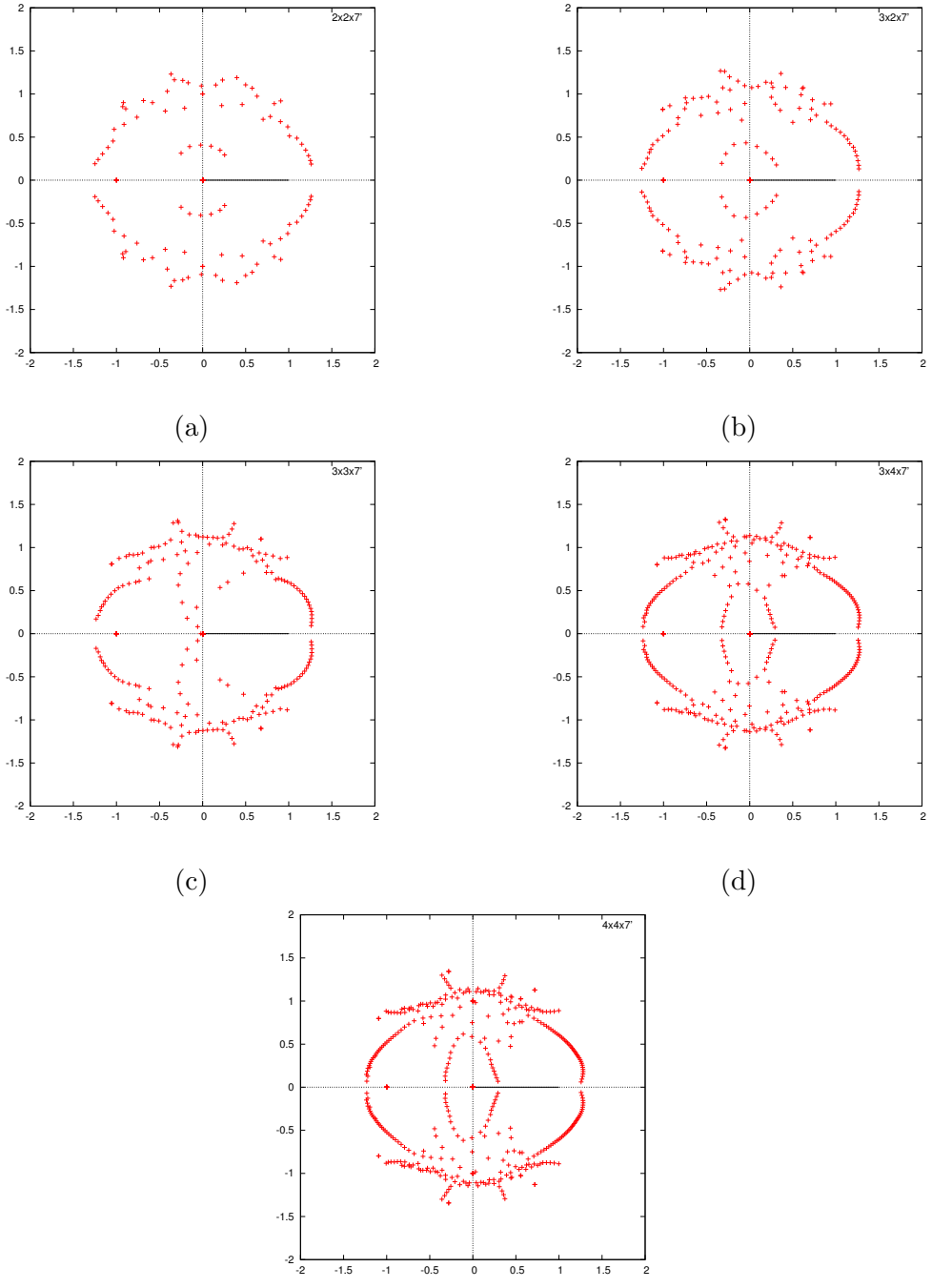

(a) (b) (c) (d) (e)

Figure 5.43: 2-state, tetragonal lattice with periodic-open boundary conditions.

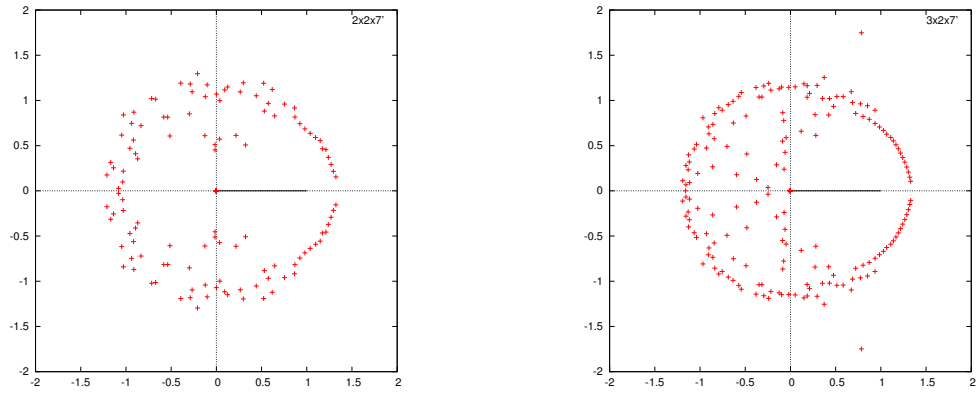

(a) (b)

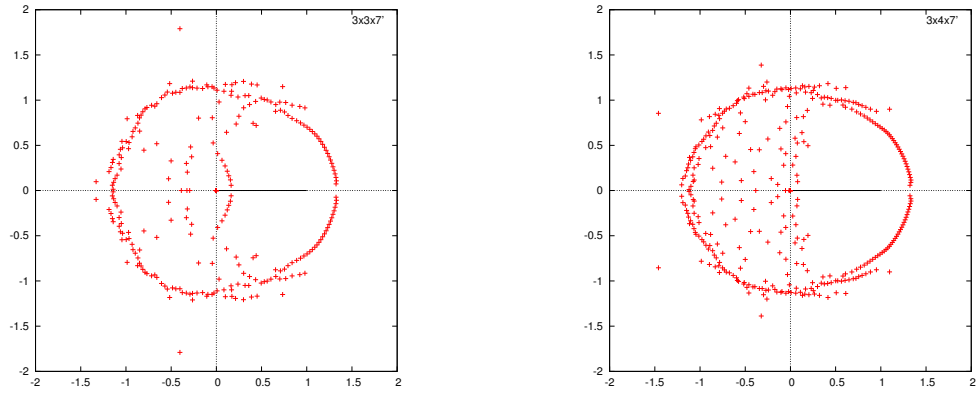

(c) (d)

Figure 5.44: 3-state, tetragonal lattice with periodic-open boundary conditions.

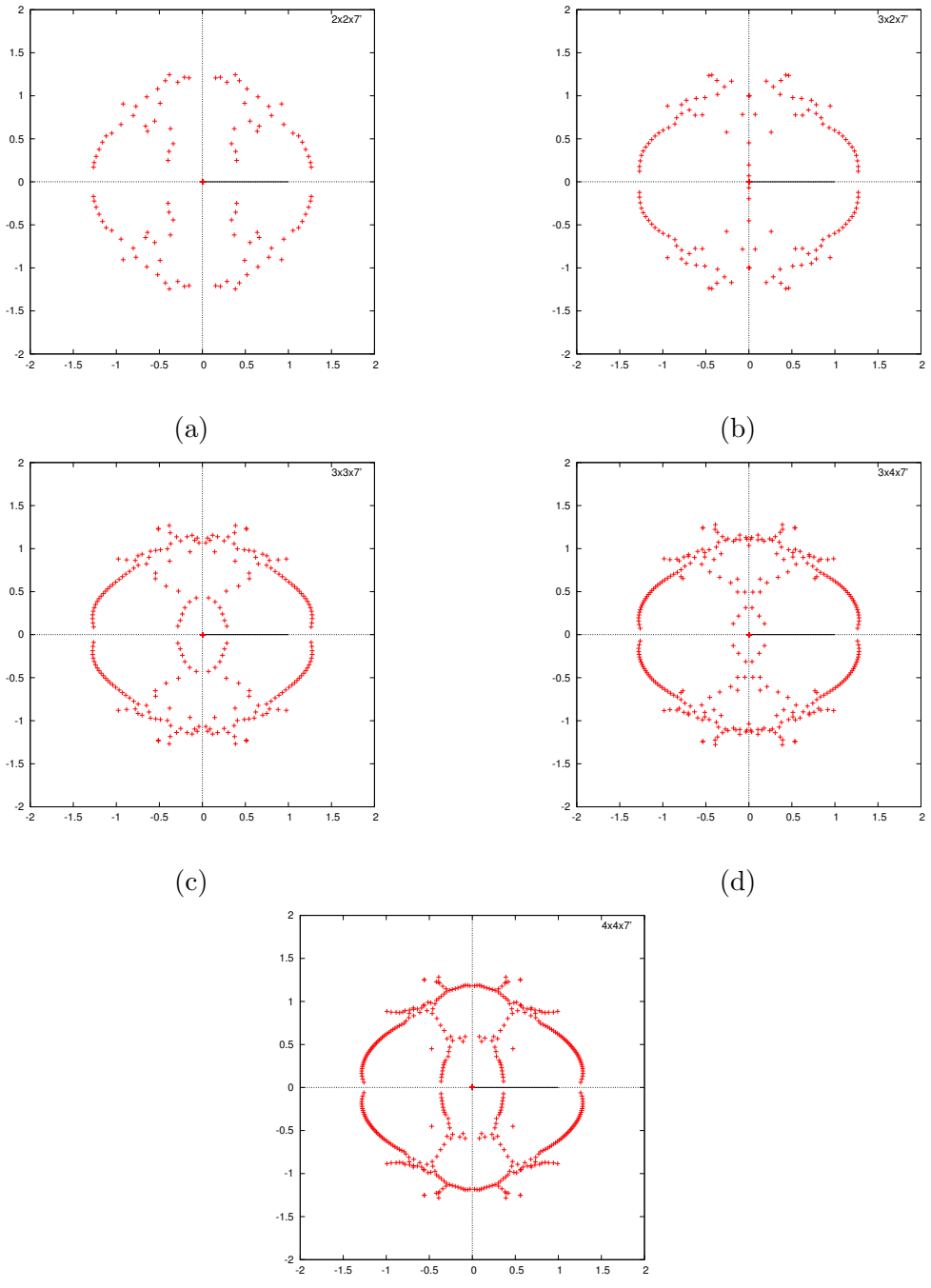

(a) (b) (c) (d) (e)

Figure 5.45: 2-state, octagonal lattice with periodic-open boundary conditions.

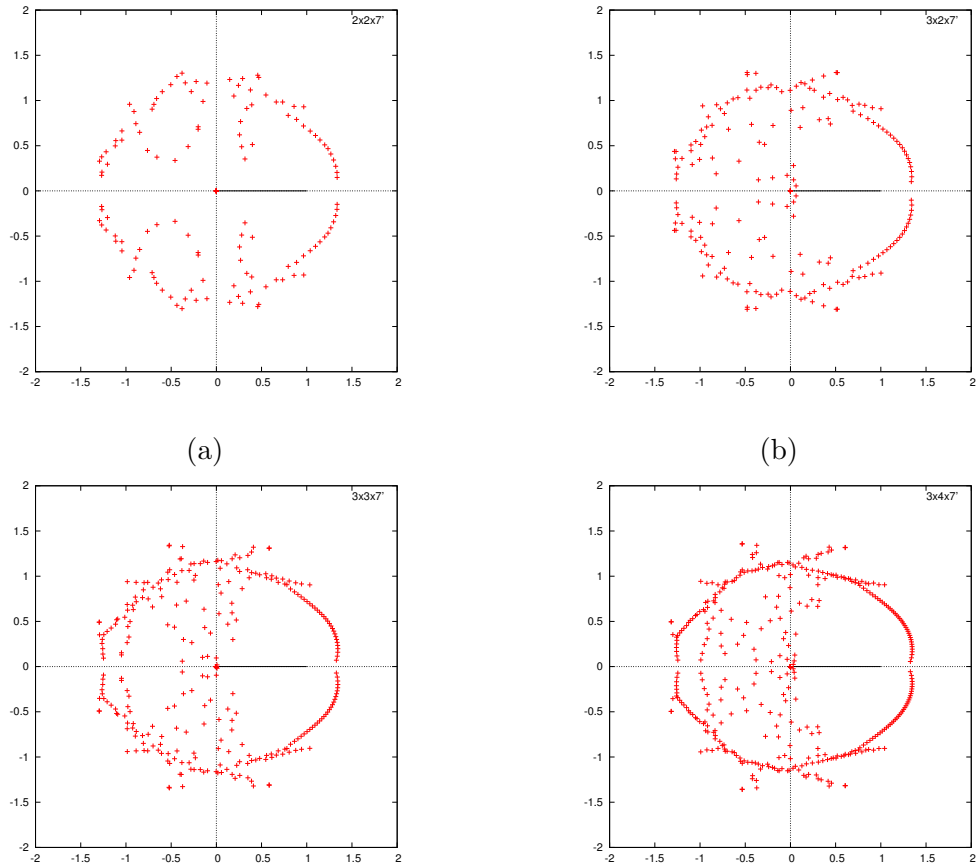

(a) (b)

(c) (d)

Figure 5.46: 3-state, octagonal lattice with periodic-open boundary conditions.

5.7 Discussion

We have considered many computable cases of Q-state Potts models on sequence of crystal lattices from two-dimensional to three-dimensional cases. For each case, we vary the lattice size and continue to investigate the model for given Q spin directions. We are interested to investigate the zeros distribution analytic structure particularly in the physical region.

The locus of points for the 2-state Potts model on square lattice for example satisfies the result in Chapter 4 i.e. two circles. The exact solution of Ising model on square lattice by Onsager is the benchmark for checking our computation.

For $Q > 3$, Q-state Potts models on square lattices show the line of zeros distribution that is smooth in ferromagnetic region. As the size increases, we can see the zeros form a nice arc approaching the real axis. However, no visible structure is manifested in the antiferromagnetic $(0, 1)$-region. Similar behaviour is observed for zeros distribution on triangular and hexagonal lattices for $Q = 4$.

Although the 2-state Potts model on triangular lattice suggests no interesting structure in the antiferro region, its dual case of hexagonal lattice shows otherwise. The hexagonal lattice shows the presence of the transition point at ferro and antiferro regions. Conversely, the 3-state Potts model on triangular lattice has similar behaviour.

The behaviour of zeros near the positive real axis is understood to be a corresponding to the behaviour of a physical property near a phase transition [56, 60]. The locus of points formed by the approximation of the zeros distribution near the limiting size can suggest a particular point on the real axis. The locus cut the real positive axis at a singular interception point. It corresponds to the critical point where the system change phases.

For finite lattice, the zeros distribution is always affected by the finite size effect. For small cases, this effect is dominating the partition function. As the size increases for a good model, the fuzziness in the distribution (as shown in Figure 5.4) will eventually stabilise into a limiting pattern of the zeros distribution. From there a good approximation for the locus of points can be inferred. A stable limiting zeros distribution is essential to estimate the critical exponents [101] (as explained in Chapter 7) of phase transition.

The cases that have been considered corresponds to the types of crystal lattice in solid state [31, 85]. In the next chapter we will consider another model which is related to Q-state Potts model. The model is called the Z_Q-symmetric model.

Chapter 6

The Z_Q-symmetric model partition function zeros

We continue with one more model that is related to the Q-state Potts model called the Z_Q-symmetric model [57, 58]. In this chapter we describe several particular cases of spin states $Q = 5, 6$ on square lattice. As before, the Hamiltonian function for this model is defined and the partition function will then be computed. The energy relation is studied and the zeros distribution of the partition function is presented in the complex-e^{β} plane.

The Z_Q-symmetric model is suitable to study a system with many spin directions especially for $Q > 4$ and to study a system with possibly multiple phase transitions. Let $\Lambda = (V, E, f)$ be a graph. By Definition 1.1.5, the Hamiltonian function of the Q-state Potts model is defined by $\mathcal{H} : \Omega \to \mathbb{R}$. For any $\sigma \in \Omega$ the Hamiltonian function $\mathcal{H}$ can be written in general function $g : \underline{Q} \times \underline{Q} \to \mathbb{R}$ where $(\sigma_i, \sigma_j) \mapsto g(\sigma_i, \sigma_j)$, that is

$$\mathcal{H}(\sigma) = -J \sum_{\substack{\langle i,j \rangle = f(e), \\ e \in E}} g(\sigma_i, \sigma_j).$$

Without loss of generality, the function g can be rescaled to be $g'(\sigma_i, \sigma_j) = \gamma_1 g(\sigma_i, \sigma_j) + \gamma_2$ where $\gamma_1, \gamma_2 \in \mathbb{R}$ are rescaling factors. The rescaling factor is also present in the relation (4.1) between Ising and Potts models.

6.1 Z_Q-symmetric model – definitions

We write the definitions for the Z_Q-symmetric model in this section. The idea of this model is that the spin directions are drawn in a clock-like circle. Each spin direction is associated with an interaction energy of one spin relative to another spin, written outside of the circle. As we move any pair of spin direction with fixed angle around the clock, the energy difference will always remains the same. This property represents the symmetry for this model.

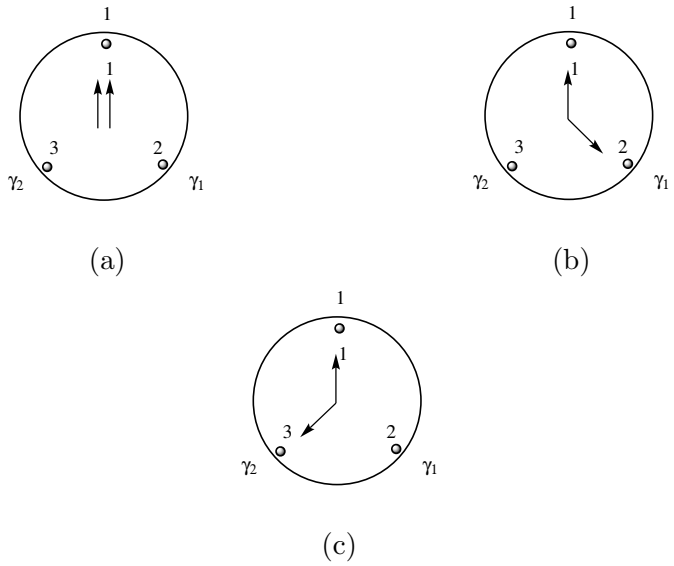

Figure 6.1: The interaction of a spin relative to spin 1 represented by a pair of arrow.

We restrict our study into the case with positive energy value. Given graph $\Lambda = (V, E, f)$, let the space of spin configuration for the Z_Q-symmetric model be similar to the Q-state Potts model. A function $\sigma : V \to \underline{Q} = \{1, 2, ..., Q\}$ is a spin configuration for a Z_Q-symmetric model.

For any microstate $\sigma \in \Omega$ we define the Hamiltonian function of the Z_Q-symmetric model below.

Definition 6.1.1. *The Hamiltonian of Z_Q-symmetric model is defined as*

$$\begin{aligned}\mathcal{H}_\chi(\sigma) &= -J \sum_{\substack{\langle j,k\rangle = f(e),\\ e\in E}} \chi[\sigma(j)-\sigma(k)] \\ &= -J \sum_{\substack{\langle j,k\rangle = f(e),\\ e\in E}} \sum_{r=1}^{[\frac{Q}{2}]} \gamma_r \cos\left(\frac{2\pi r(\sigma(j)-\sigma(k))}{Q}\right) + \gamma_r' \end{aligned} \tag{6.1}$$

where $[Q/2]$ is the discrete value of the division and $\gamma_r, \gamma_r' \in \mathbb{R}$ are model parameters fixed for a given model.

The calculation of the Hamiltonian (6.1) depends on the distance between two spin directions or simply by the angle separating them. Two spin directions that are close together will lose less energy as compared to the spin directions with large angle. This energy loss is called the *energy penalty*. The pair of spin variables $(\sigma(j), \sigma(k))$ that point in the same direction is equivalent to the Potts model. For fixed $\gamma_1 = 1$ and $\gamma_{r\neq 1} = 0$, the Hamiltonian function is reduced to the Clock model [93].

Example 6.1.1 shows the calculation of the Hamiltonian for each interacting pair of spins. The existence of spins symmetry is also observed through this example.

Example 6.1.1. Let $Q = 3$ and the energy value for each pair of spin variables is represented by Table 6.1. Let $g_r(\sigma(j), \sigma(k)) = \cos(2\pi r(\sigma(j) - \sigma(k))/Q)$ and $[Q/2] = 1$.

Table 6.1: $g_r(\sigma(j), \sigma(k))$ for Z_3-symmetric model.

σ	1	2	3
1	1	$-1/2$	$-1/2$
2	$-1/2$	1	$-1/2$
3	$-1/2$	$-1/2$	1

This table of g_r can be rescaled to $g_r'(\sigma(j), \sigma(k)) = \gamma_r\, g_r(\sigma(j), \sigma(k)) + \gamma_r' = \frac{2}{3}\, g_r(\sigma(j), \sigma(k)) + \frac{1}{3}$. This example is now reduced to the 3-state Potts model as shown in Table 6.2.

Table 6.2: $g'_r(\sigma(j), \sigma(k))$ for Z_3-symmetric model.

σ	1	2	3
1	1	0	0
2	0	1	0
3	0	0	1

For the Potts model, a pair of nearest neighbour vertices pointing in the same direction gives an energy value 1 and 0 otherwise. This choice of value corresponds to a large energy penalty. For the Z_Q-symmetric model, the energy value is between 0 and 1. The cases with $Q = 2, 3$, and 4 are covered by the Potts and Ising models. The interesting case for this model is thus given by $Q > 4$.

Figures 6.1 and 6.2 give illustrations of the following statement. The energy values of the model can be written as a list of possible choices of energy $\tilde{\chi} = (\tilde{\chi}[0], \tilde{\chi}[1], \tilde{\chi}[2], ...) \in [0, 1]$. The $\tilde{\chi}$ is a list of energy between Q different spin directions. The arrows in the clock correspond to the spin directions of one spin relative to spin 1. The list is arranged in the order of increasing angles relative to one spin direction.

We consider the value of energy on the clock that has reflection symmetry (see Figure 6.2). We write the energy list up to half of the total spin direction i.e. $\tilde{\chi} = (\tilde{\chi}[0], \tilde{\chi}[1], ..., \tilde{\chi}[n])$ where $n = \dfrac{Q}{2}$ if Q is even and $n = \dfrac{Q-1}{2}$ if Q is odd. Let θ be the angle between 2 spin directions. The energy value 1 corresponds to $\cos\theta = 1$ (i.e. $\theta = 0$) and energy value 0 corresponds to $\cos\theta = 0$ (i.e. $\theta = \pi/2$).

In all cases, we let the first element $\tilde{\chi}[0] = 1$ and the last element $\tilde{\chi}[n] = 0$. Figure 6.2 illustrates the arrangement of this energy list for $Q = 4, 5$ and 6 where $\tilde{\chi} = (1, \tilde{\chi}[1] = \gamma_1, \tilde{\chi}[2] = \gamma_2, ...)$. The $\tilde{\chi} = (1, \gamma_1, 0)$ corresponds to the case with spin state $Q = 4, 5$ and the $\tilde{\chi} = (1, \gamma_1, \gamma_2, 0)$ corresponded to $Q = 6$.

Similar to the Potts model, the number of calculations can be reduced by using symmetry. For this model we are able to translate all the spin directions around the clock.

The energy list $\tilde{\chi}$ can be rescaled into discrete number by multiplying with an

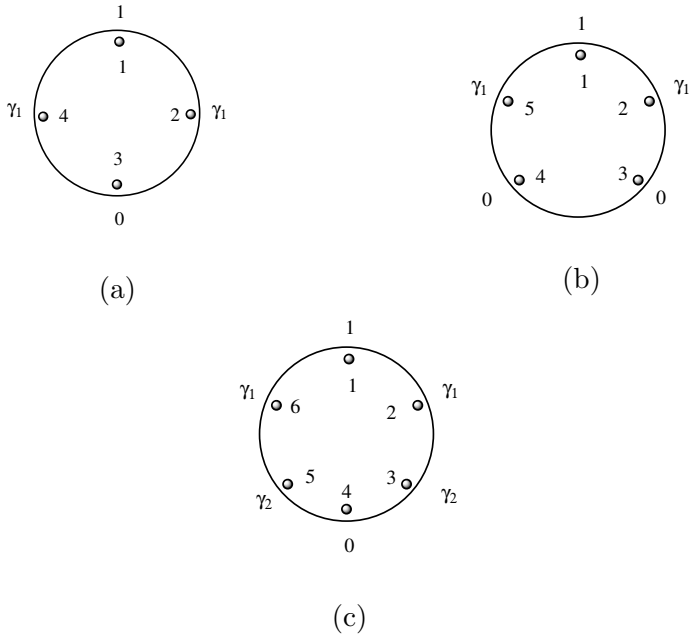

Figure 6.2: The illustration of energy list with: (a) $\tilde{\chi}_a = (1, \gamma_1, 0)$, (b) $\tilde{\chi}_b = (1, \gamma_1, 0)$, and (c) $\tilde{\chi}_c = (1, \gamma_1, \gamma_2, 0)$.

appropriate integer, i.e. $\chi = C\tilde{\chi}$ where $C \in \mathbb{N}$. The energy value can be chosen in this range $0 \leq \chi[i] \leq C$. See Example 6.1.2.

Example 6.1.2. See Figure 6.3. Suppose the spin state has $Q = 4$. The energy list $\tilde{\chi} = (1, 2/3, 0)$ corresponds to

$$\begin{aligned} g(\sigma_1, \sigma_1) &= 1, \\ g(\sigma_1, \sigma_2) &= 2/3, \\ g(\sigma_1, \sigma_3) &= 0, \\ g(\sigma_1, \sigma_4) &= 2/3. \end{aligned}$$

Without loss of generality, the new energy list is $\chi = 3\tilde{\chi} = (3, 2, 0)$ which

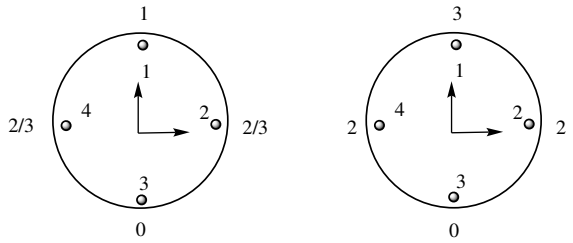

Figure 6.3: The illustration of Z_4-symmetric model with energy value $\tilde{\chi} = (1, 2/3, 0)$ (left) and $\chi = 3\tilde{\chi} = (3, 2, 0)$ (right).

corresponds to

$$\begin{aligned} g'(\sigma_1, \sigma_1) &= 3, \\ g'(\sigma_1, \sigma_2) &= 2, \\ cg'(\sigma_1, \sigma_3) &= 0, \\ g'(\sigma_1, \sigma_4) &= 2. \end{aligned}$$

To show how the energy list χ is related to Hamiltonian $\mathcal{H}_\chi$, we give example for $Q = 4$ and $Q = 6$.

Example 6.1.3. Let $Q = 4$. For $\chi = (\chi[0], \chi[1], \chi[2]) = (2, 1, 0)$ the Hamiltonian is given by

$$\begin{aligned} \mathcal{H}_{(2,1,0)}(\sigma) &= -J \sum_{\substack{\langle j,k\rangle = f(e), \\ e \in E}} \chi[\sigma(j) - \sigma(k)] \\ &= -J \sum_{\substack{\langle j,k\rangle = f(e), \\ e \in E}} 1 + \cos\left(\frac{\pi(\sigma(j) - \sigma(k))}{2}\right) \end{aligned} \tag{6.2}$$

where $\gamma_1 = \gamma_1' = 1$ and $\gamma_2 = \gamma_2' = 0$.

Example 6.1.4. Let $Q = 6$. For $\chi = (\chi[0], \chi[1], \chi[2], \chi[3]) = (2, 1, 0, 0)$ the

Hamiltonian is given by

$$\begin{aligned}\mathcal{H}_{(2,1,0,0)}(\sigma) &= -J \sum_{\substack{\langle j,k\rangle = f(e),\\ e\in E}} \chi[\sigma(j)-\sigma(k)] \\ &= -J \sum_{\substack{\langle j,k\rangle = f(e),\\ e\in E}} \frac{2}{3} + \cos\left(\frac{\pi(\sigma(j)-\sigma(k))}{3}\right) \\ &\quad + \frac{1}{3}\cos\left(\frac{2\pi(\sigma(j)-\sigma(k))}{3}\right) \end{aligned} \tag{6.3}$$

where $\gamma_1 = 1, \gamma_1' = 2/3, \gamma_2 = 1/3$, and $\gamma_2' = \gamma_3 = \gamma_3' = 0$.

The partition function for the Z_Q-symmetric model on Λ is given by (1.1), i.e.

$$Z = \sum_{\sigma\in\Omega} \exp(-\beta \mathcal{H}_\chi(\sigma))$$

where $\mathcal{H}_\chi$ is as in Definition 6.1.1.

Let $N, M \in \mathbb{N}$. We consider a Z_Q-symmetric model on a square lattice of N by M size. We restrict our study of partition function for the case of mixed boundary condition i.e. periodic in vertical direction and open in horizontal direction. We denote the energy penalty between two spins in the energy list χ by an energy step notation given by value $(\chi[1]-\chi[0], \chi[2]-\chi[1], ...)$-step. We will use this notation later for comparing the χ values.

6.2 The zeros distribution on square lattice

Here we present the result of the zeros distribution of the partition function for Z_5- and Z_6-symmetric models.

The figures of zeros distribution are arranged in increasing lattice sizes for respective χ value. Table 6.3 shows all the cases under study for Z_5- and Z_6-symmetric models in this chapter.

Our hypothesis is that the emergence of circular arcs in the physical region can be used to determine the number of phase transitions for a physical system

[58]. Multiple arcs of zeros approaching the real axis correspond to the existence of multiple phase transitions.

Table 6.3: The Z_5- and Z_6-symmetric models with arbitrary χ. New results are highlighted grey.

	χ	5x5'	6x6'	6x7'	7x7'	8x8'	9x9'
Q=5	(2,1,0)	✓	✓	✓	✓	✓	✓
	(3,1,0)	✓	✓	✓	✓	✓	✓
	(3,2,0)	✓	✓	✓	✓	✓	✓
	(4,1,0)	✓	✓	✓	✓	✓	✓
	(4,3,0)	✓	✓	✓	✓	✓	✓
	(5,3,0)	✓	✓	✓	✓	✓	
	(5,4,0)	✓	✓	✓	✓	✓	
	(6,1,0)	✓	✓	✓	✓	✓	
	(6,5,0)	✓	✓	✓	✓	✓	
Q=6	(2,1,0,0)	✓	✓	✓	✓	✓	
	(2,1,1,0)	✓	✓	✓	✓	✓	
	(3,1,0,0)	✓	✓	✓	✓	✓	
	(3,2,0,0)	✓	✓	✓	✓	✓	
	(3,2,1,0)	✓	✓	✓	✓	✓	

6.2.1 5-state: Z_5-symmetric

Consider the Z_5-symmetric model on finite size square lattice with some energy value χ. The study on 6 by 7 square lattice which was described by Martin [58] is our reference for checking and comparison.

Figure 6.4 shows the zeros distribution of Z_5-symmetric model with $\chi = (2, 1, 0)$. The χ value has a (1,1)-step energy penalty. In the antiferro region, two behaviours are observed. For even N, few lines indicated in Figure 6.4 are merged forming single curve move closer to the real axis. As the lattice size increases, a clear curve is observed. For odd N, we see multiple lines are approaching the antiferro region.

In the ferro region, as the number of vertices N increases, the zeros show the emergence of multiple lines near the real axis. It is not clear either the lines will remain or merge to form a thin arm suggesting single phase transition. The case of $\chi = (2, 1, 0)$ for 6 by 7 square lattice has been described by Martin [58] in the

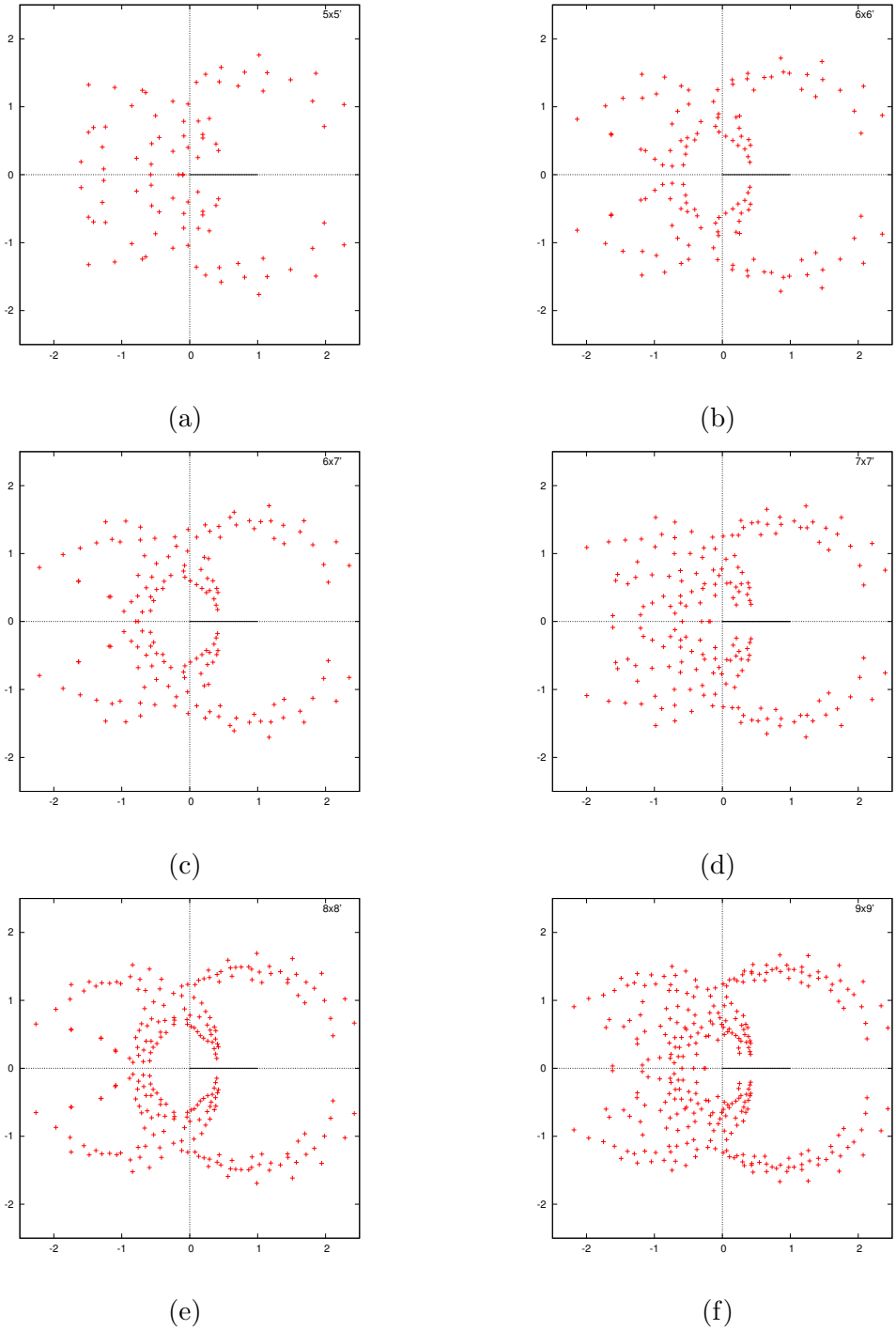

(a) (b) (c) (d) (e) (f)

Figure 6.4: Zeros distribution for $\chi = (2, 1, 0)$ 5-state model.

complex-$e^{-\beta}$ plane. He shows that this case has only 1 transition in the ferro region. That case is just the inverse version of the one presented in Figure 6.4c.

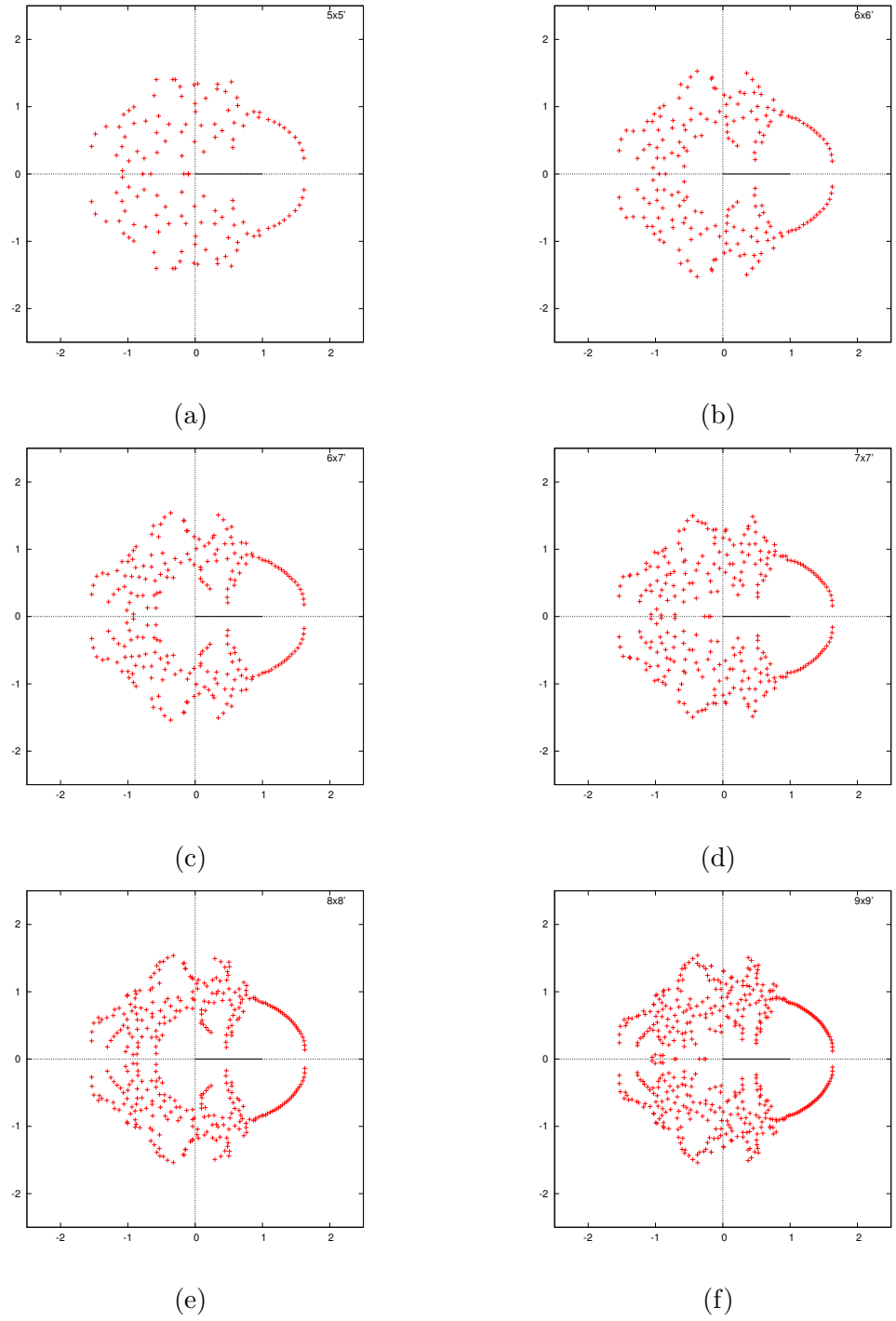

(a) (b) (c) (d) (e) (f)

Figure 6.5: Zeros distribution for $\chi = (3, 1, 0)$ 5-state model.

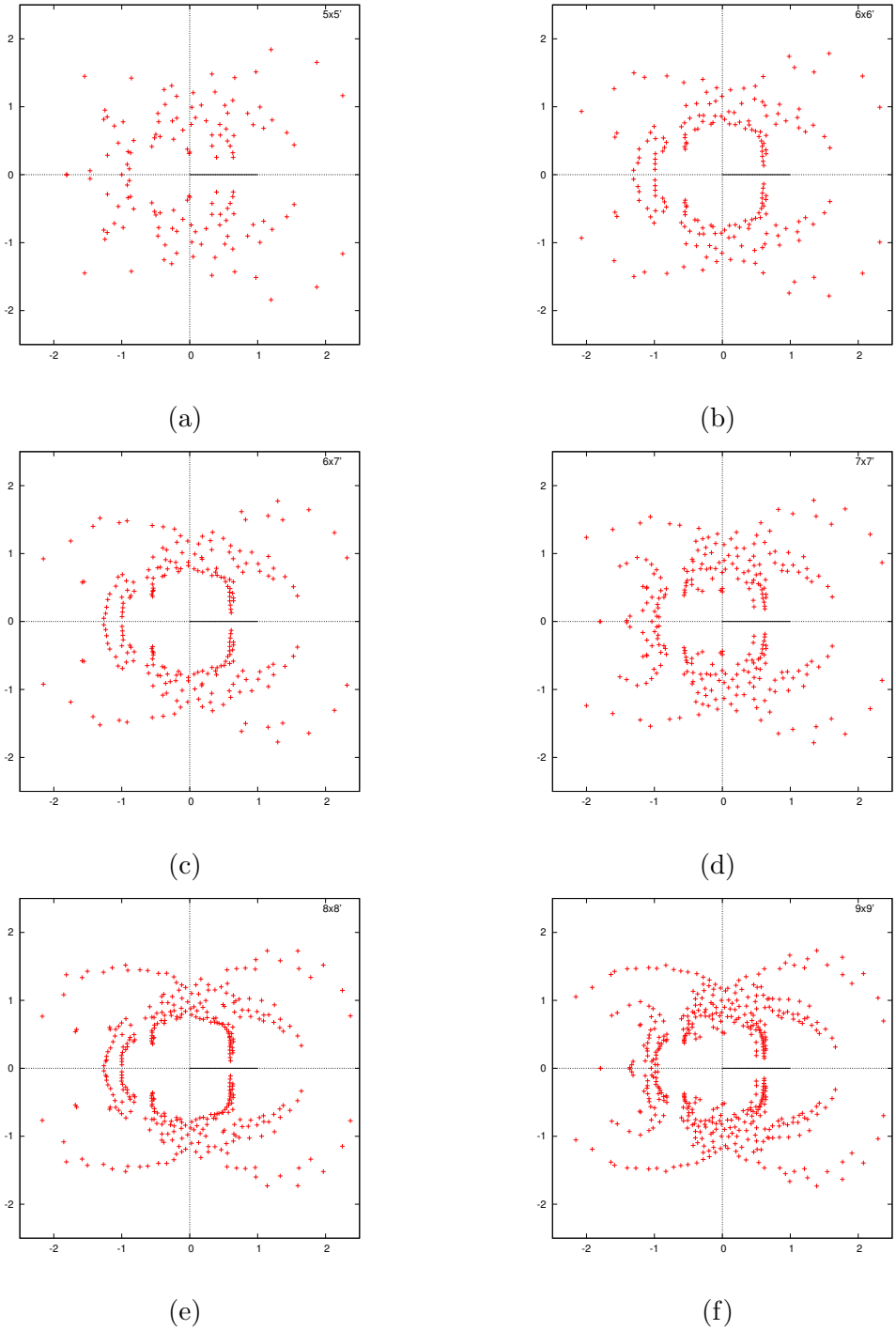

(a) (b) (c) (d) (e) (f)

Figure 6.6: Zeros distribution for $\chi = (3, 2, 0)$ 5-state model.

Next, we present the distribution of $\chi = (3, 1, 0)$ in Figure 6.5 and $\chi = (3, 2, 0)$ in Figure 6.6. Both figures are related to each other through their number of steps of the energy penalty. The $\chi = (3, 2, 0)$ has $(1, 2)$ energy step. This step is the inverse steps of $\chi = (3, 1, 0)$ which has $(2, 1)$ energy step.

For $\chi = (3, 1, 0)$ there exist single line of zeros in ferro region approaching the real axis. The antiferro region shows the emergence of two lines but it is not very clear either the lines will remain or merge at the thermodynamic limit.

For $\chi = (3, 2, 0)$ in Figure 6.6, there exist several distinct lines approaching the real axis. We claim that at the limit two circular arcs will approach the real axis in the ferro region. This observation is obvious based on the increasing number of zeros in this region. In the antiferro region, we can see that as the lattice size increases, a thick single band is approaching the real axis. The emergence of two lines in odd case is just due to the boundary effect. If the antiferromagnetic phase transition exists, this case has only a single transition given by the single line of dense zeros near the real axis.

A further comparison is made between Figures 6.7 and 6.8. Both cases are related to each other through their number of steps (energy penalty) that is $(3, 1)$-step for $\chi = (4, 1, 0)$ and $(1, 3)$-step for $\chi = (4, 3, 0)$. The ferro region in Figure 6.7 presents the existence of single limiting critical point. On the other hand, there exist two lines approaching the real axis in antiferro region. This behaviour suggests the antiferro region may have single or double transition point in the limit $N \to \infty$.

Conversely, the case shown in the Figure 6.8 is opposite to the one in Figure 6.7. The antiferro region is expected to give single transition whereas the ferro region shows a strong possibility of multiple transition points as $N \to \infty$.

Figure 6.9 shows the distribution of zeros for $\chi = (5, 3, 0)$ with energy penalty $(2, 3)$-step. Although the lattice size is considered to be small, we can already see the expected number of critical points for this system. At $N = 6$, the Figure 6.9b suggests the possibility of multiple transition at the ferro region and single transition at the antiferro region. The smooth line in Figure 6.9b gives a clue of boundary

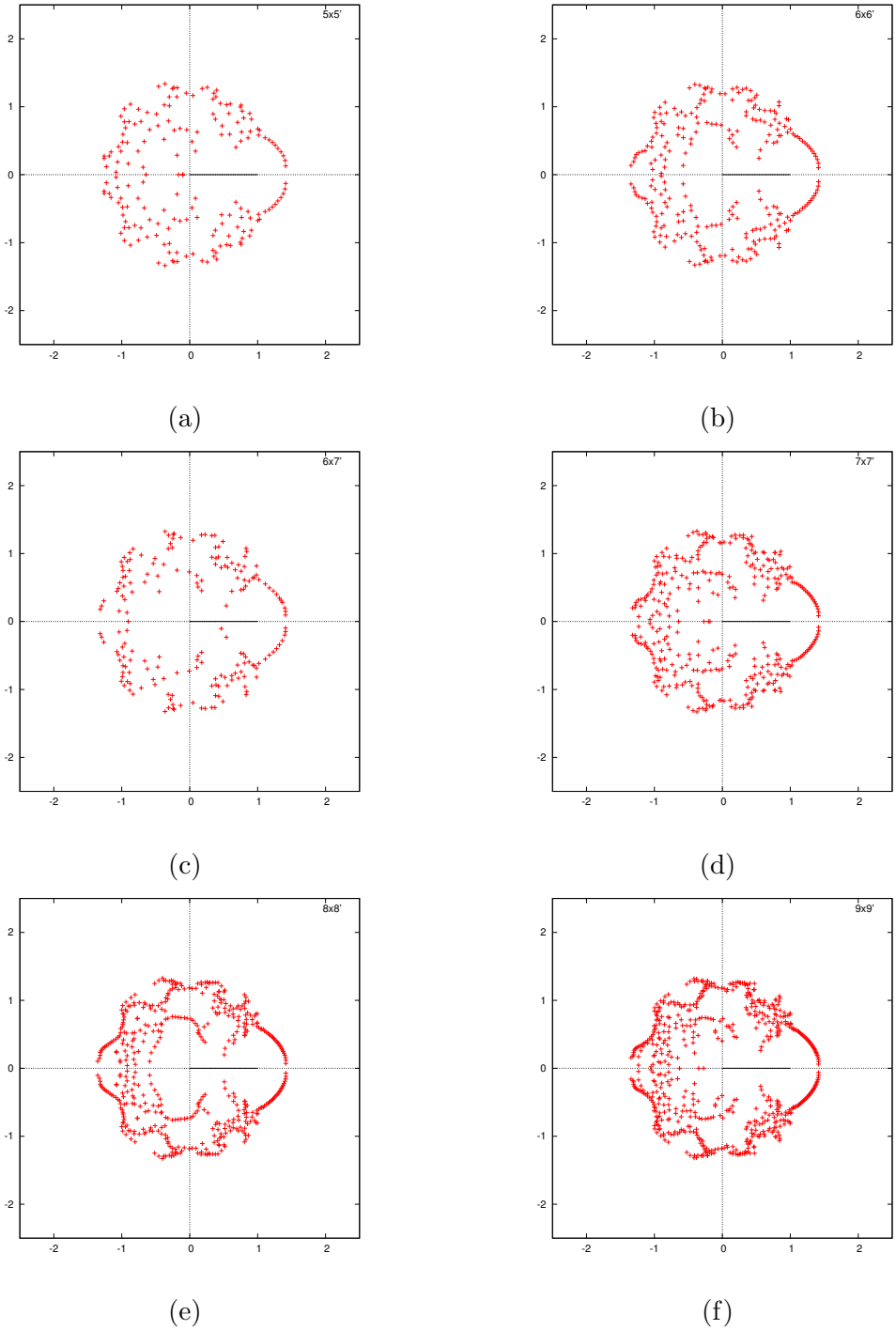

(a) (b) (c) (d) (e) (f)

Figure 6.7: Zeros distribution for $\chi = (4, 1, 0)$ 5-state model.

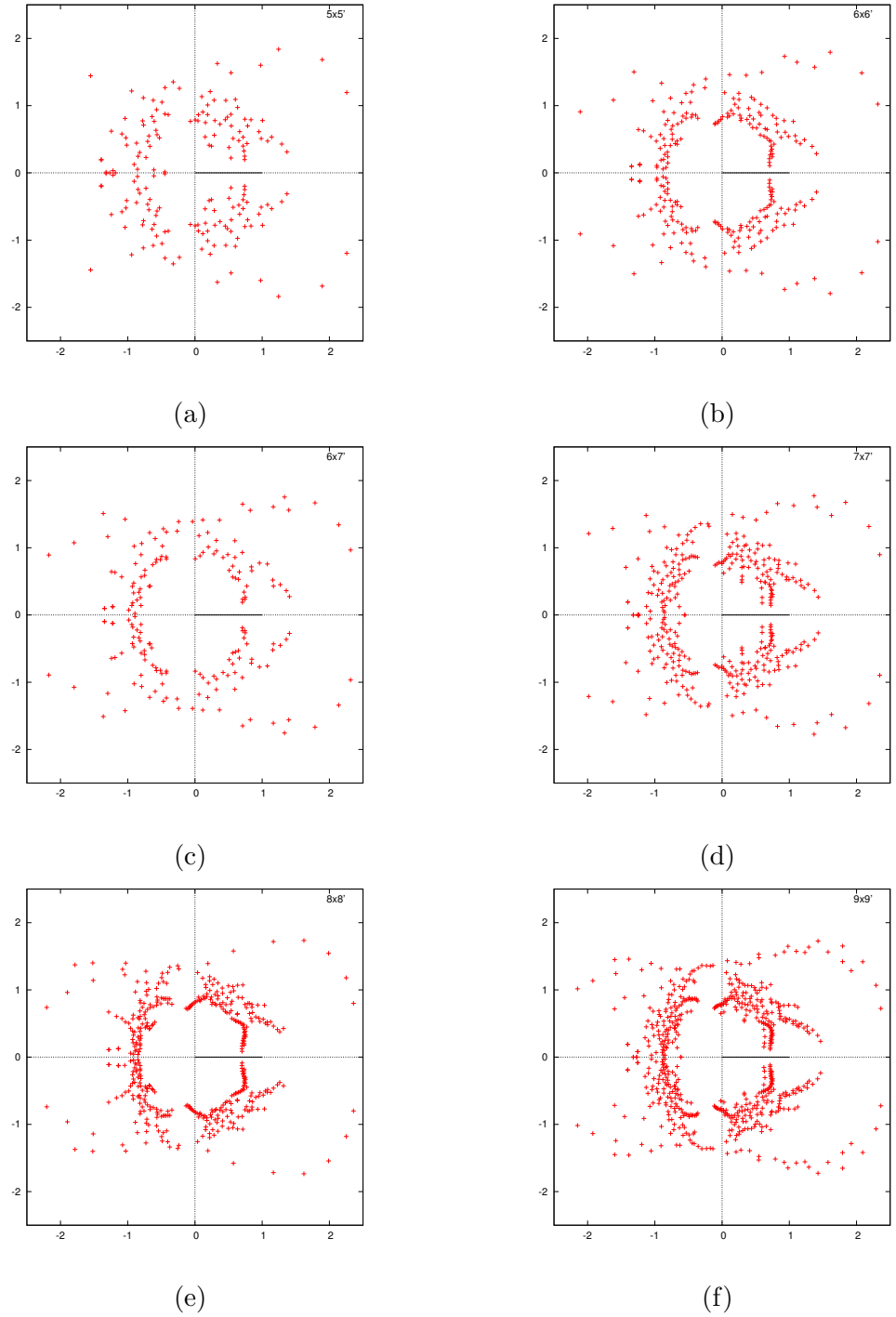

(a) (b) (c) (d) (e) (f)

Figure 6.8: Zeros distribution for $\chi = (4, 3, 0)$ 5-state model.

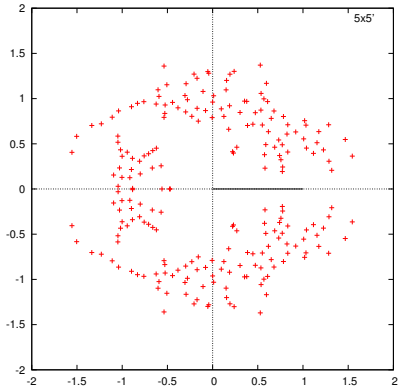

(a)

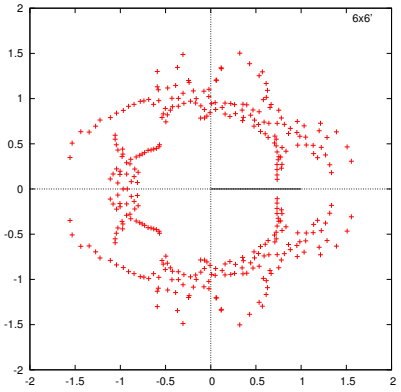

(b)

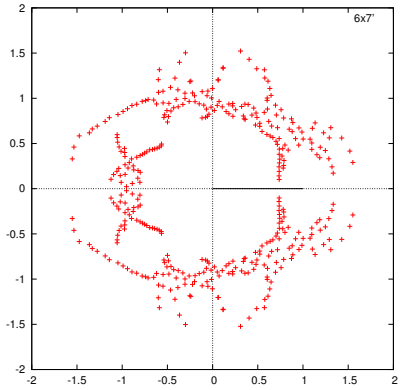

(c)

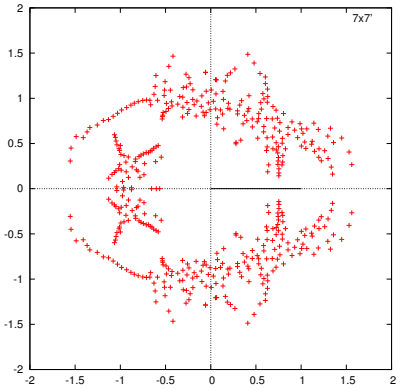

(d)

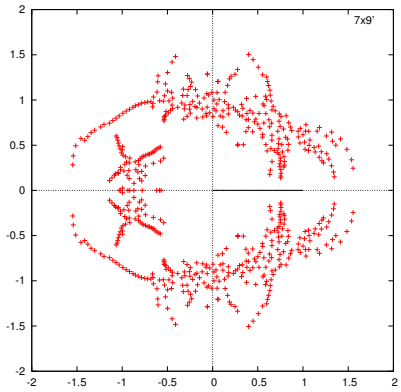

(e)

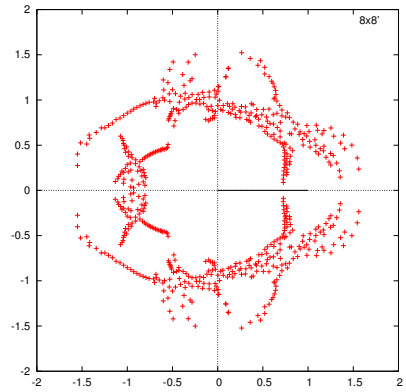

(f)

Figure 6.9: Zeros distribution for $\chi = (5, 3, 0)$ 5-state model.

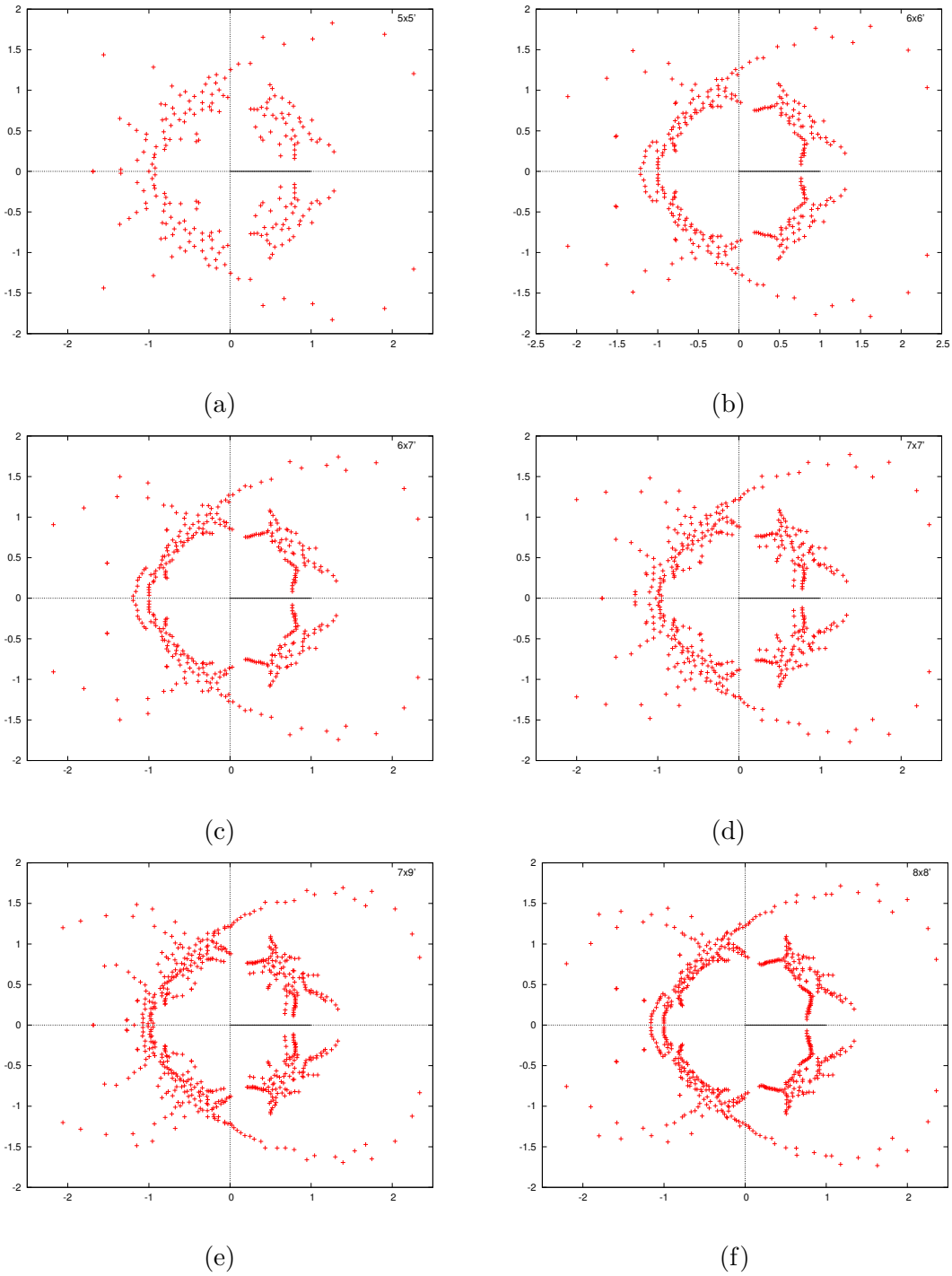

(a) (b) (c) (d) (e) (f)

Figure 6.10: Zeros distribution for $\chi = (5, 4, 0)$ 5-state model.

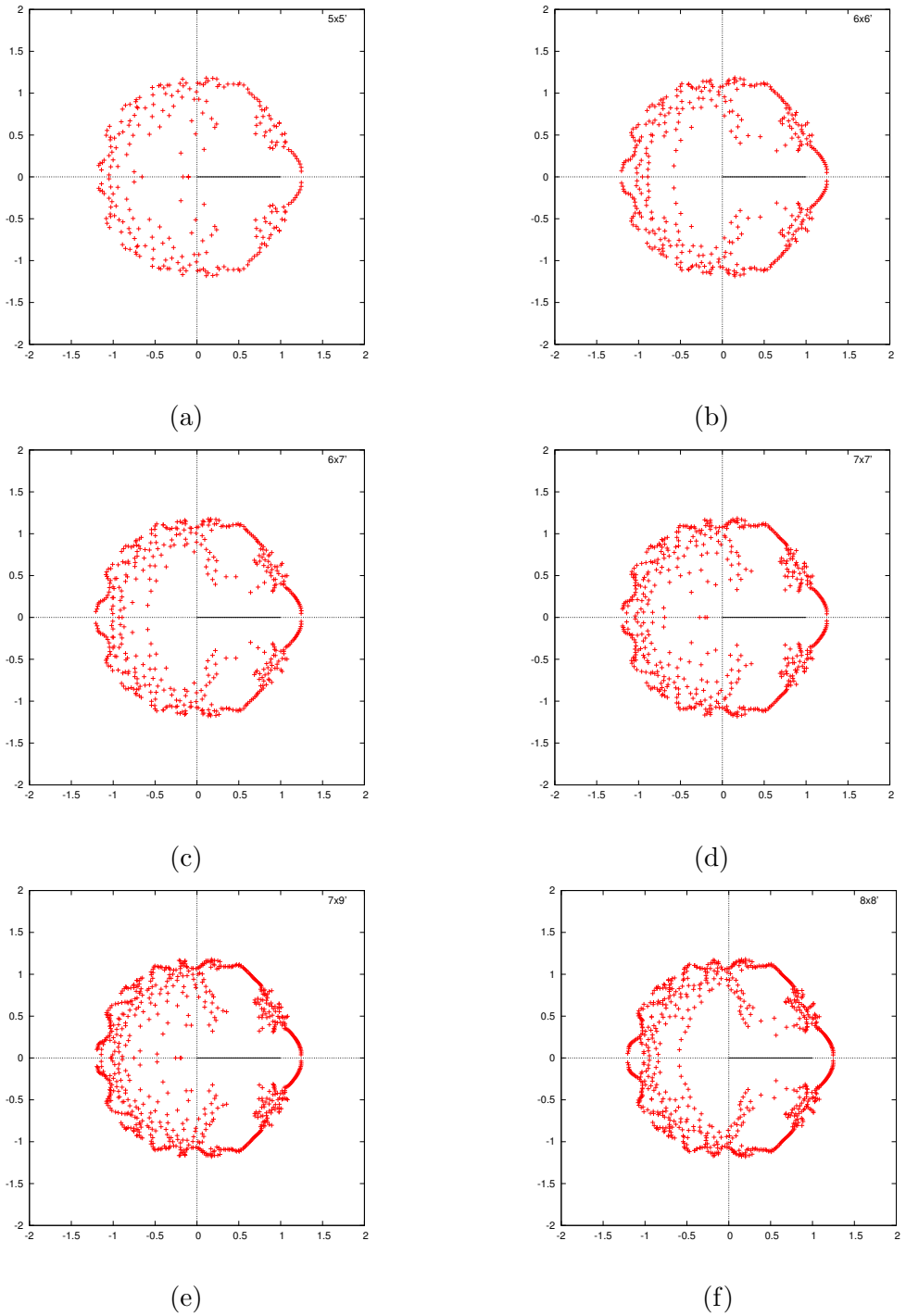

(a) (b) (c) (d) (e) (f)

Figure 6.11: Zeros distribution for $\chi = (6, 1, 0)$ 5-state model.

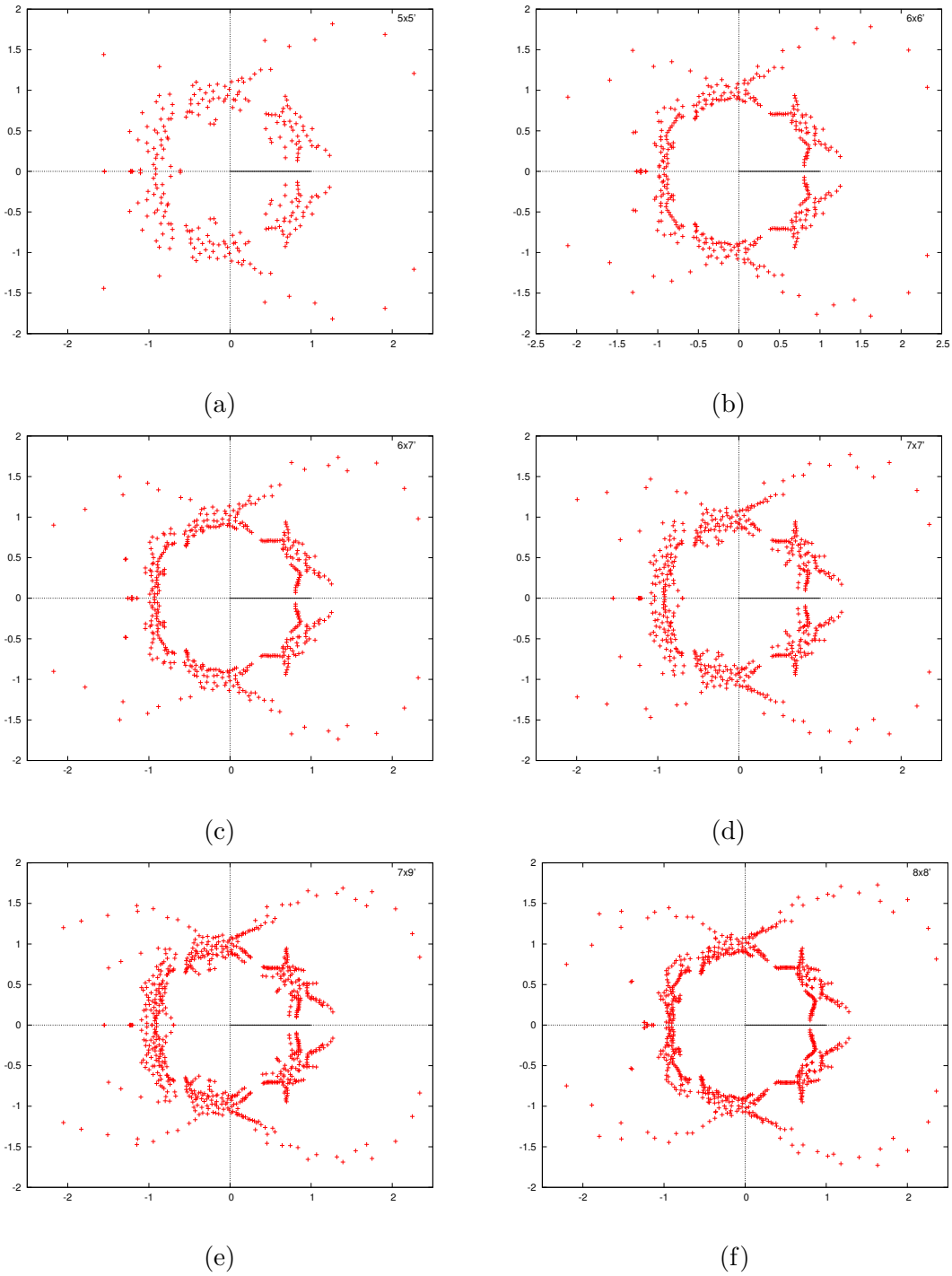

(a) (b) (c) (d) (e) (f)

Figure 6.12: Zeros distribution for $\chi = (6, 5, 0)$ 5-state model.

effect in the odd N case; for example at $N = 7$. It is evidenced from this structure that the number of transitions is two in ferro region and one in antiferro region.

Figures 6.11 and 6.12 are more examples with inverse relation through the number of penalty steps. The case $\chi = (6, 1, 0)$ in Figure 6.11 can only suggest the existence of single transition in the ferro region while it is not clear for the antiferro part. Interestingly for $\chi = (6, 5, 0)$ in Figure 6.12, the distribution in the ferro region shows multiple lines approaching the real axis. This ferro region corresponds to the antiferro part of $\chi = (6, 1, 0)$.

This result is interesting because at previous example between $\chi = (3, 1, 0)$ and $\chi = (3, 2, 0)$, the number of transitions is also opposite to each other. We can investigate two cases that is related by the energy penalty step by considering only one of the cases.

6.2.2 6-state: Z_6-symmetric

We continue with square lattice of the Z_6-symmetric model. Refer Table 6.3. Similar to the Z_5-symmetric case, the study on 6 by 7 square lattice was described by Martin [58].

For 6-state model, the degree of partition function polynomial increases rapidly due to the higher number of states ($Q = 6$) as the lattice size increases. Thus only small cases are available due to computing limitation. We consider the study of 6-state model on square lattice up to 8 by 8 lattice size, i.e. $|V| = 64$.

Figure 6.13 presents the zeros distribution for $\chi = (2, 1, 0, 0)$ with $(1, 1, 0)$-step. The zeros distribution in the ferro and antiferro regions indicates that there is only a single transition point in each region. For even N, the zeros distribution shows smoother and visible pattern than those for odd N.

Interestingly, for the case $\chi = (2, 1, 1, 0)$ with $(1, 0, 0)$-step, the zeros shown in Figure 6.14 have a stable pattern approaching the real axis as the size increases. Both physical regions have clear behaviour of a smooth line indicating the existence of single transition.

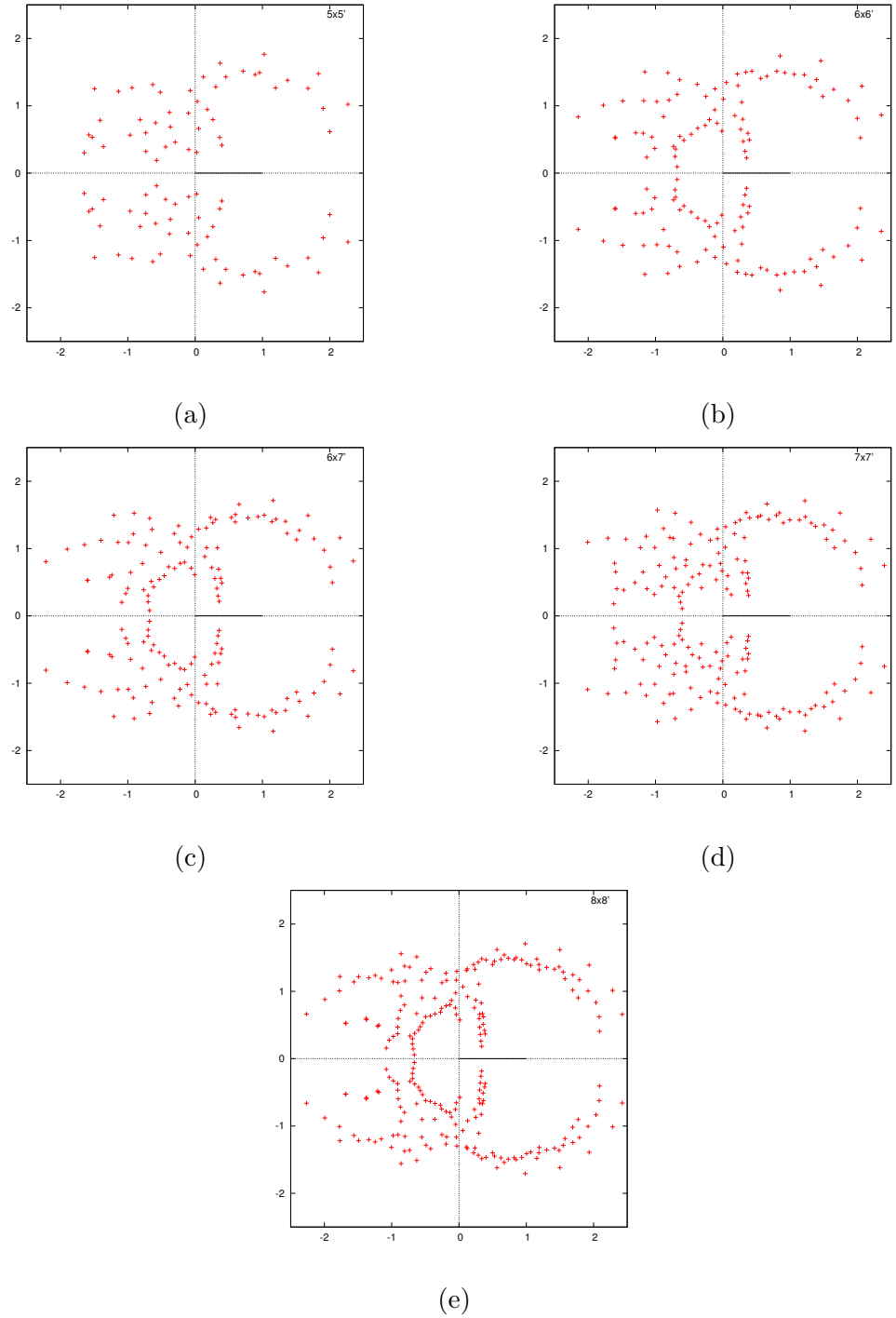

(a) (b) (c) (d) (e)

Figure 6.13: Zeros distribution for $\chi = (2, 1, 0, 0)$ 6-state model.

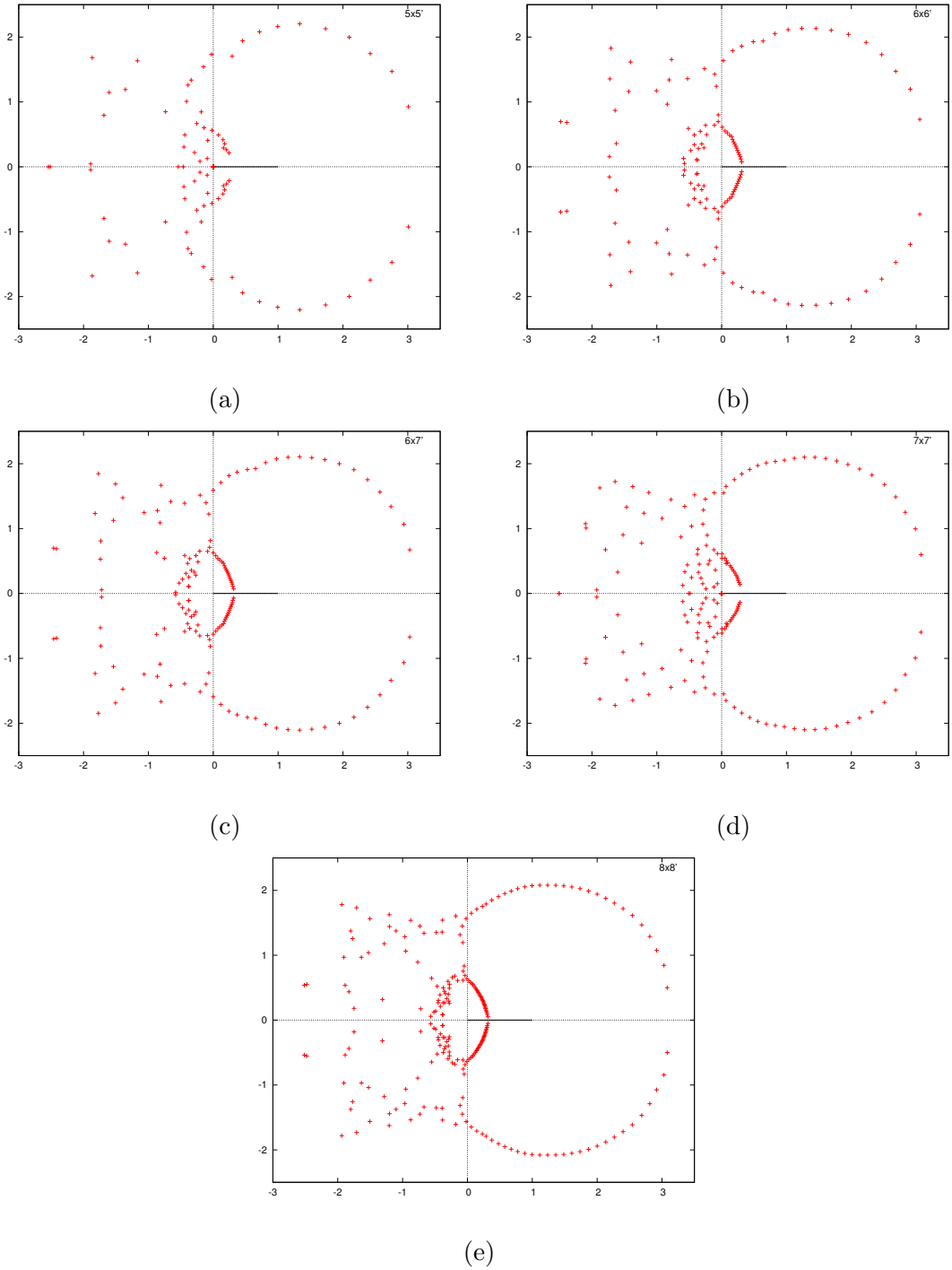

(a) (b) (c) (d) (e)

Figure 6.14: Zeros distribution for $\chi = (2, 1, 1, 0)$ 6-state model.

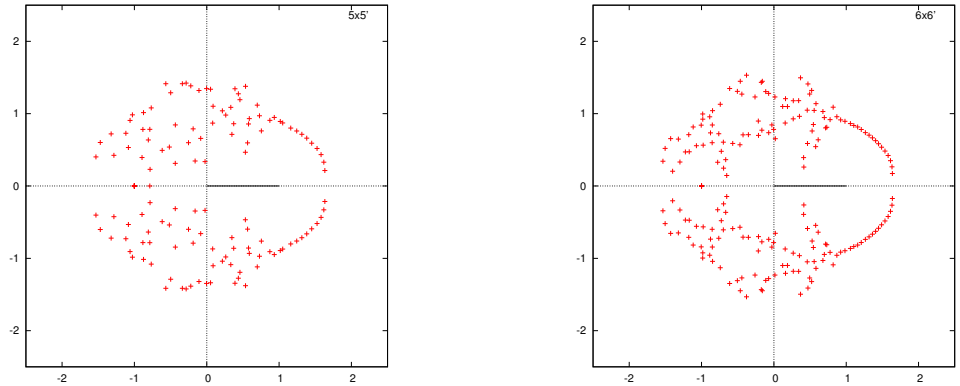

(a)

(b)

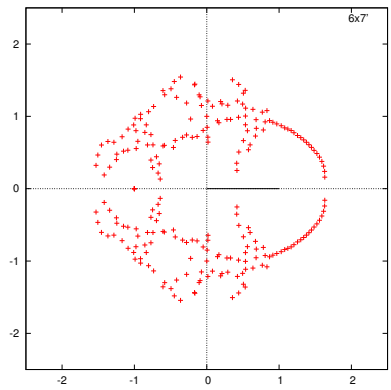

(c)

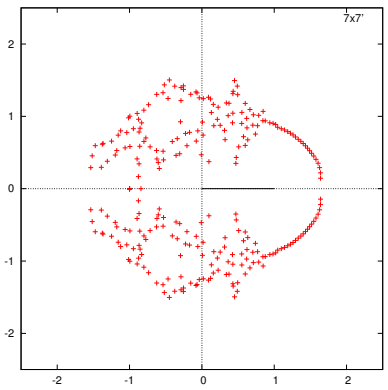

(d)

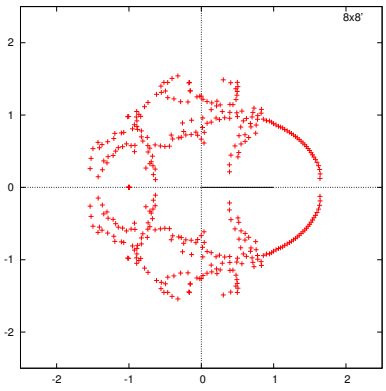

(e)

Figure 6.15: Zeros distribution for $\chi = (3, 1, 0, 0)$ 6-state model.

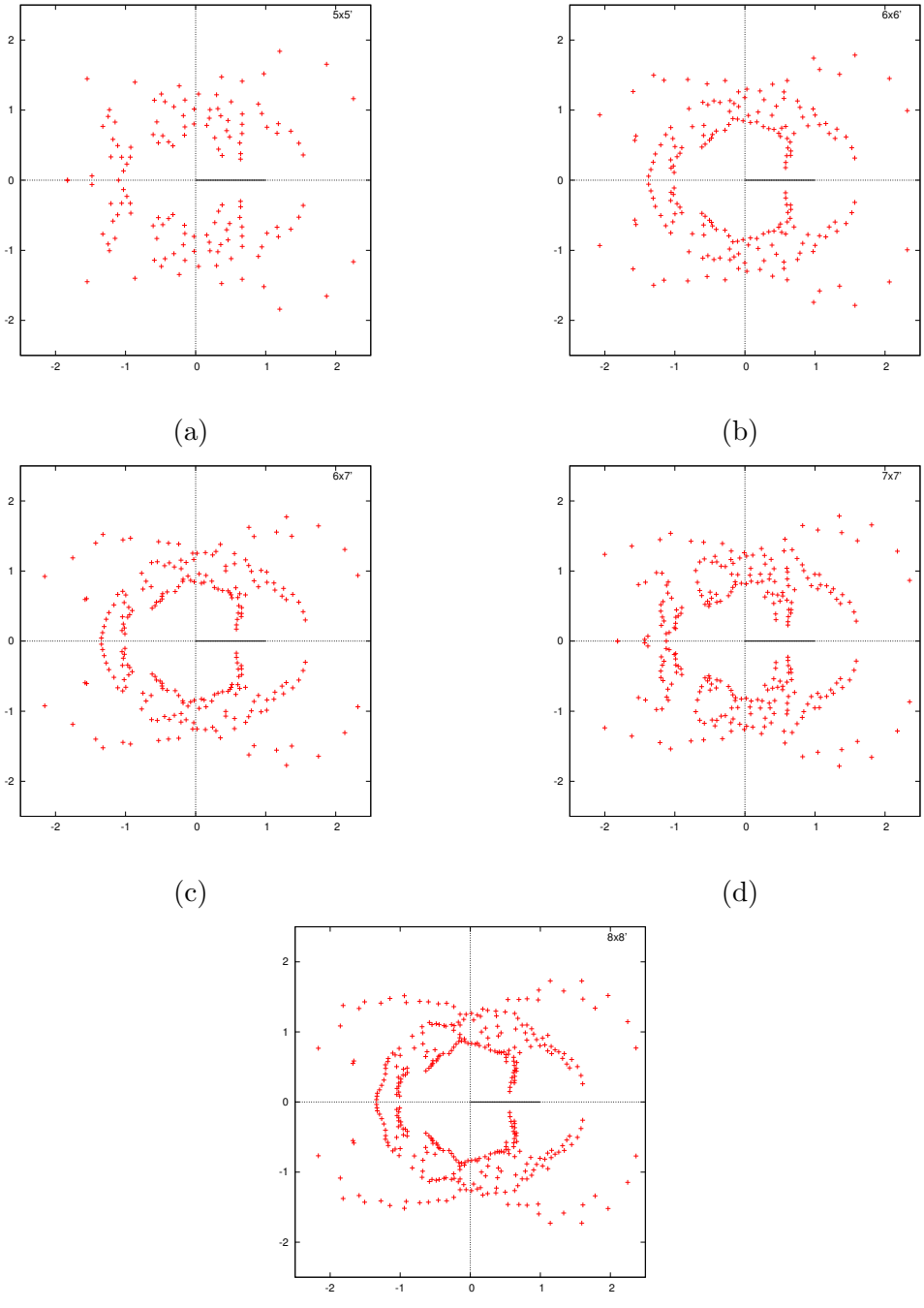

(a) (b) (c) (d) (e)

Figure 6.16: Zeros distribution for $\chi = (3, 2, 0, 0)$ 6-state model.

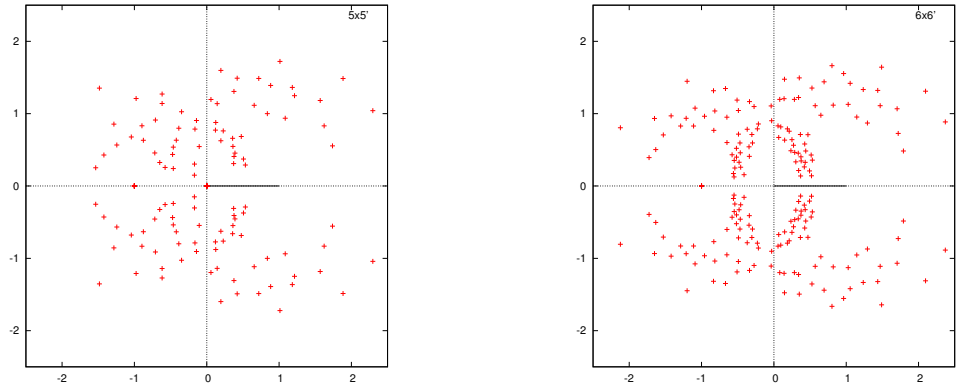

(a)

(b)

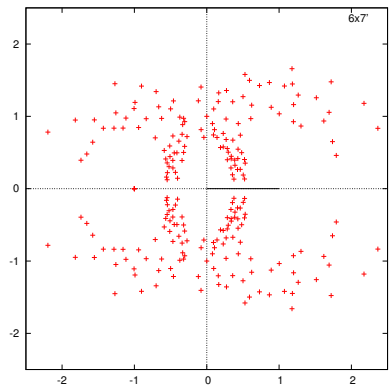

(c)

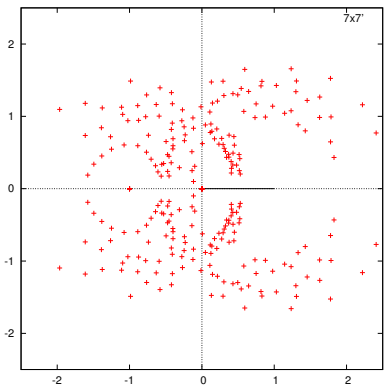

(d)

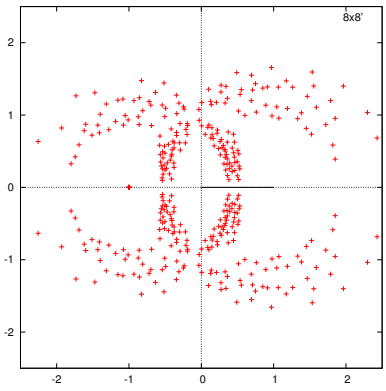

(e)

Figure 6.17: Zeros distribution for $\chi = (3, 2, 1, 0)$ 6-state model.

To proceed, the next case is shown in Figure 6.15 with $\chi = (3, 1, 0, 0)$ where the energy penalty is in the $(2, 1, 0)$-step. Here there is a branch of dense points in the antiferro region getting closer to real axis. It is expected that the ferro and antiferro regions have only a single transition point in the limit.

The distribution for $\chi = (3, 2, 0, 0)$ is illustrated in Figure 6.16. In this case there exist two possible transition points in the ferro region and only single point in the antiferro region.

The final case of 6-state for $\chi = (3, 2, 1, 0)$ is shown in Figure 6.17. The ferro region suggests the existence of two transition points at thermodynamic limit. However for the antiferro region, it is hard to infer the number of transitions. The big arm branch in this region has two brief lines emanating from the arm. Two possibilities can be predicted. First the two small lines will eventually merge at a point close to real axis. Second the small lines will go further to real axis separately. The first statement suggests the existence of single transition point. The latter means the existence of two transition points.

So far we only describe the figures based on our observation directly on the distribution structure in all the complex-e^{β} plane. In the next section, further discussion of the result and more comparison among these cases will continue.

6.3 Discussion

We highlight few more details for comparison among the zeros distributions of Z_5- and Z_6-symmetric models in this section.

In general, the distribution is affected by the boundary condition and the finite size effect especially in the odd N case. In this case, we can see for example in Figure 6.12d that some of the zeros in the antiferro region are not nicely distributed on a smooth line.

As the lattice size increases, we can distinguish the zeros movement towards the real axis for even and odd N. Interestingly, the zeros movement in the ferro region

looks more stable as compared to the antiferro region. The zeros in the antiferro region for even N shows a smoother line than the odd N near the real axis.

The results for the Z_5- and Z_6-symmetric models show the emergence of visible lines as the number of zeros increases. As the lattice size increases, more zeros in the distribution form some branches in physical and non-physical region. A visible pattern of distribution can be seen where the zeros get closer to the real axis. At thermodynamic limit $N \to \infty$, the zeros is expected to touch the real line at critical point of the phase transition.

Consider one layer of a square lattice with vertical spins $\sigma(j_s) = k \pmod{Q} \equiv s$ with $s = 0, 1, 2, \cdots, N-1$. This is one of the antiferromagnetic ground state where the vertices have spins with multiple of Q repeated in the vertical direction. The number of ways for a system to be in this ground states is high. However, the most probable kind of ground state is still an open question.

From all the figures in this chapter, we can see that the transition points are vary based on the energy list χ. The choice of χ value differs by their energy step relative to the first element of the energy list. We call this the first energy followed by second, third and so on. Denotes the energy step as α_i where index i determine the sequence of the energy difference.

Figures 6.18 to 6.19 show the zeros distributions of the Z_5-symmetric model on 6 by 6 square lattices with all their considered χ values. The χ with an energy step $\alpha_1 < \alpha_2$ gives two arcs of zeros distribution in ferro region. This difference shows the existence of more than one transition point in the limit. The case with $\alpha_1 > \alpha_2$ has only single arc in this region which implies single transition point. For the $\alpha_1 = \alpha_2$ like the case of $\chi = (2, 1, 0)$, this case has either one or two transition points. The exact number of transitions for this case is not clear. From this example, we may predict the number of transitions based on the energy penalty step. This problem is still open. We need bigger lattice to provide more evidence for this idea.

The Z_5- and Z_6-symmetric model zeros distributions show the existence of line of zeros in the antiferro region. This observation does not exist for the 5- and 6-state

Potts model on square lattice (as discussed in § 5.3).

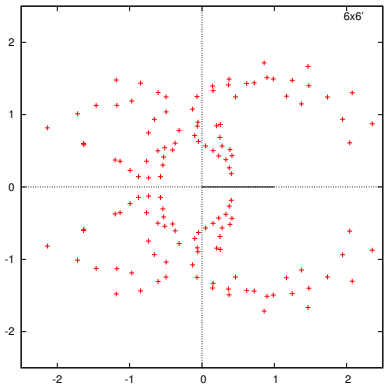

(a) $\chi = (2, 1, 0)$

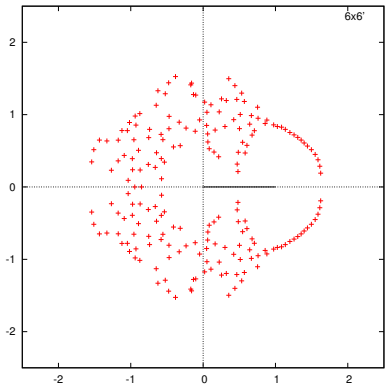

(b) $\chi = (3, 1, 0)$

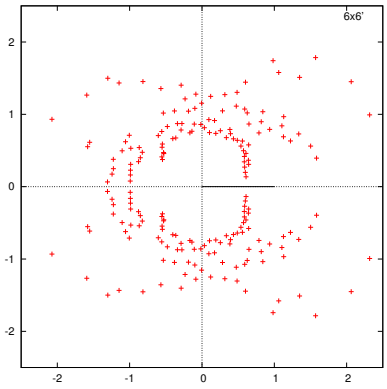

(c) $\chi = (3, 2, 0)$

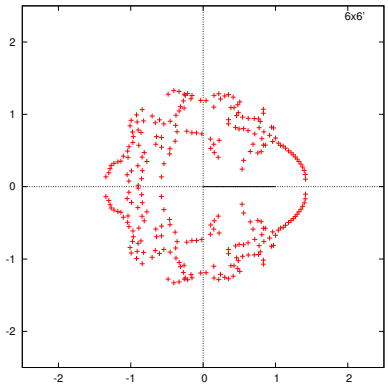

(d) $\chi = (4, 1, 0)$

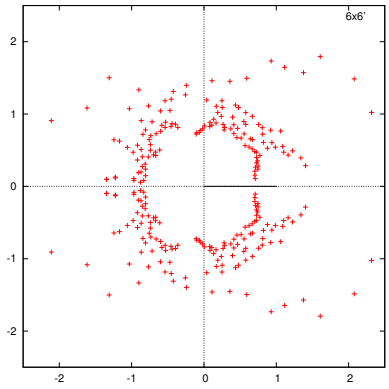

(e) $\chi = (4, 3, 0)$

Figure 6.18: Zeros distribution for several χ of 6 by 6 on square lattice.

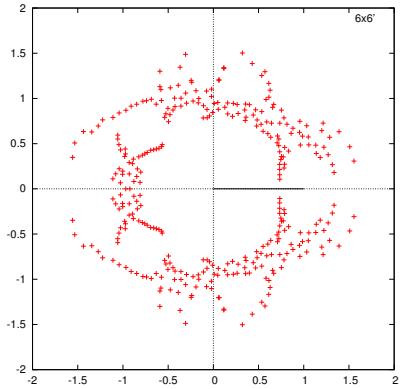

(a) $\chi = (5, 3, 0)$

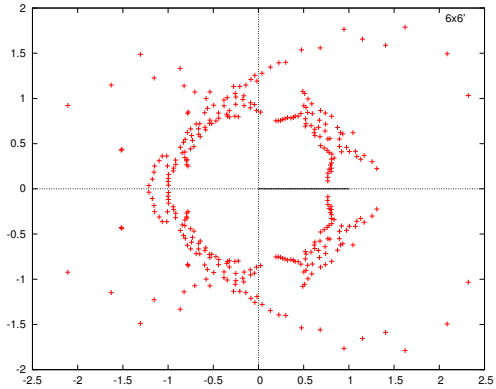

(b) $\chi = (5, 4, 0)$

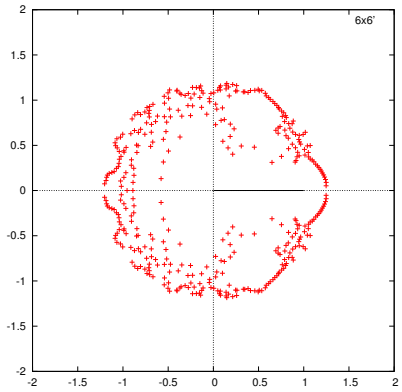

(c) $\chi = (6, 1, 0)$

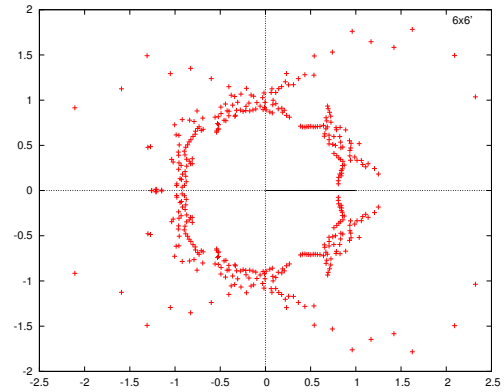

(d) $\chi = (6, 5, 0)$

Figure 6.19: Zeros distribution for several χ of 6 by 6 on square lattice (cont.).

6.3.1 Energy losses in configurations

Here we discuss the configurations of the Z_Q-symmetric model relative to choices of the energy penalty.

Given a lattice graph $\Gamma = (V, E, f)$. We can illustrate the spin configuration $\sigma \in \Omega$ by their value of spin orientation. The configuration can be pictured by their spin value at each site of the lattice. Consider Figure 6.20a for example.

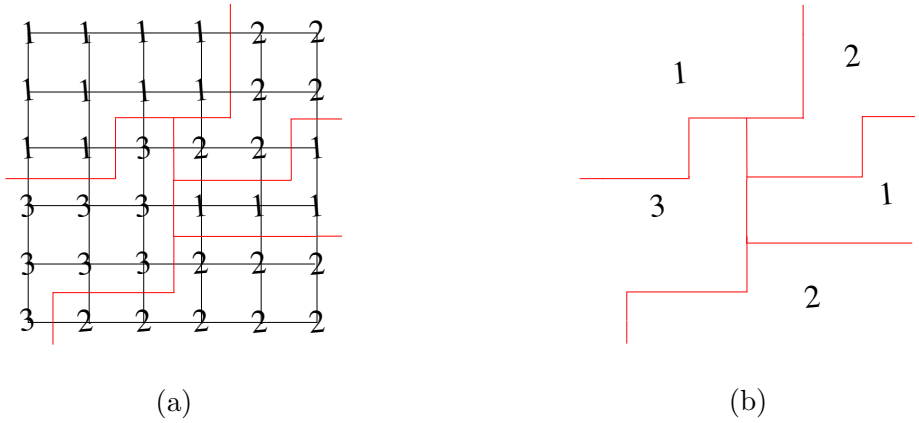

(a) (b)

Figure 6.20: a) Value of spin configurations associated to the lattice sites and b) regions of aligned spin configurations.

Let $V_i \subseteq V$ has the same associated spin configuration, that is the spin variable spin in the same direction. We can divide the configuration by regions of aligned spins by drawing a line on the dual lattice for any not align pair. The line is drawn in red in Figure 6.20a.

From here, a simplified version can be illustrated by only writing the spin orientation as representative in the region that has been separated. Configuration in Figure 6.20b for example represents the configuration in Figure 6.20a.

Suppose there is a configuration behaves as in Figure 6.20b. As the temperature decreases, the system changes towards the ferromagnetic ground state. Eventually the lines are forced to shrink as the temperature T is lowered down. This shrinking behaviour suggests the existence of tension along the line. We call this a *string tension*.

For the study on the Potts model, the line separating the spin region gives no significant difference for the study. It assigned a 0 value for any pair of spin variables with different spin. However this is different for the Z_Q-symmetric model. The line separation shows significant correspondence to the total energy of the system.

For neighbouring vertices with points to directions close to each other (small degree), the configuration state is almost stable at the ground state. The energy varies according to the choices of χ.

Refering to Figures 6.20 and 6.21, some configurations may also have a point of intersection between the line separations. This intersection is called *vortex*. The length of the line separation corresponds to the value of the total energy penalty.

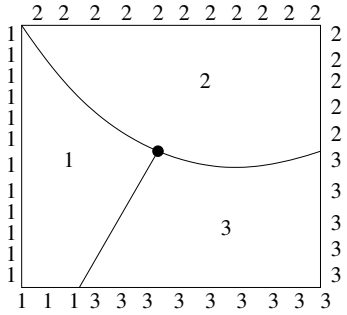

Figure 6.21: A configuration with fixed boundary condition.

Here we observe that the first kind of disordered states is the one with small variation. Many microstates have small energy penalty. As the temperature varies, the first phase corresponds to the kind of ordered state with slow varying angle. Then it is followed by a transition to another phase (small disorder) and then to a completely disordered state.

The largest magnitude of the Hamiltonian represents the ground state where the free energy is at minimum. For a configuration state represented by some line separation, one can determine the Hamiltonian energy of that particular state. Since the length of the line corresponds to the value of the energy penalty, therefore the ground state can be described by the shortest length of line separation. The shortest line means lowest energy penalty.

The Z_Q-symmetric model is the final model we have considered in this thesis. We give evidence that the distribution of this model for specific value of χ may exhibit multiple transitional phases. The analytic structure of the zeros distribution highlights the possibility of this occurrence.

Chapter 7 will continue with the analysis of the zeros distribution particularly related to the value of specific heat critical exponent. This is then followed by the analysis for multiple phases in Chapter 8.

Chapter 7

Analysis on zeros density of partition function

Here we study the relation between the specific heat critical exponent [58, 101] and the zero distribution of the partition function.

The hypothesis is that the exponent can be computed from (sufficiently large) finite lattice distributions. (The hypothesis was proposed in [55], but at that time the accessible lattices were too small for testing.)

We test this first using our methods on the Onsager/Kaufman Ising solution, where we both have access to all the finite partition functions Z, and also know the exact exponent. Then we apply our methods to the square lattice 3-state Potts model (which is not integrable, but for which the folklore is certain that $\alpha = 1/3$ [101]).

Suppose we heat ice. Assume that the heat is transferred at the same rate. It takes some time before the ice turns to water completely. The existence of two phases of solid ice and liquid water show the process of phase transition. This point is the melting point in Figure 7.1.

Continuously adding the heat will eventually increase the temperature and stop at the boiling point. This point is another phase transition point where water starts to change into steam.

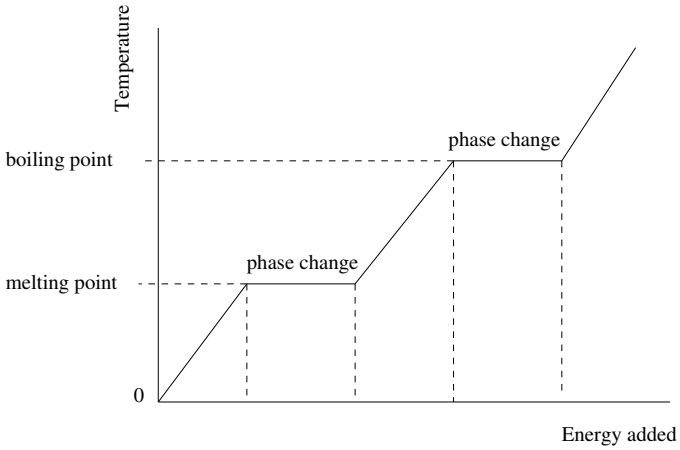

Figure 7.1: Phase change diagram.

Recall that the discontinuity in a first derivatives of logarithm of partition function is the evidence of the first order phase transition. This means a discontinuity in the internal energy. However if the first derivative of logarithm of partition function is continuous and its second derivative is discontinuous, this corresponds to the second order phase transition. This means a discontinuity in the specific heat.

7.1 The specific heat critical exponent

Recall from § 1.3 that the specific heat is defined by

$$\frac{C_V}{k_B} = -\beta^2 \frac{d^2 \ln Z}{d\beta^2} \tag{7.1}$$

Given a critical point at $\beta = \beta_c$, the specific heat may diverge at this point (see (7.3) for examples). The critical exponent α is defined by the specific heat relation

$$C_V \sim (\beta - \beta_c)^{-\alpha}. \tag{7.2}$$

The critical temperature T is a dependence of the detail of atomic interaction of the system. So any critical temperature we get from our models is not realistic in the laboratory. But the exponent α has universal property [7, 58] which depends only

on few fundamental parameters [101]. For our model with short-range interaction, the exponents depend on the dimensionality of the system and Q, but not on J or units of $\mathcal{H}$.

Consider the Ising model on a square lattice. As shown in the Onsager's zeros distribution in Chapter 4, at the thermodynamic limit the zeros give locus of points with two circles where one of them cut the positive real axis at $1 + \sqrt{2}$. This is a critical point. A sudden peak in the graph of specific heat over β (in Figure 7.2) indicates a change in the phases of the system. The peak in the graph shows the occurrence of a phase transition when the specific heat is at infinity. This is also an indication of a discontinuity in the second derivative of a free energy [27].

The Onsager's solution specific heat [75] near the critical point β_c is given by

$$\frac{1}{k_B} C_V \sim \frac{8\beta_c^2}{\pi} \left[-\log \left| 1 - \frac{\beta}{\beta_c} \right| + \log \left| \frac{1}{2\beta_c} \right| - 1 - \frac{\pi}{4} \right]. \tag{7.3}$$

Figure 7.2 shows the graph of specific heat with divergence at the critical point β_c.

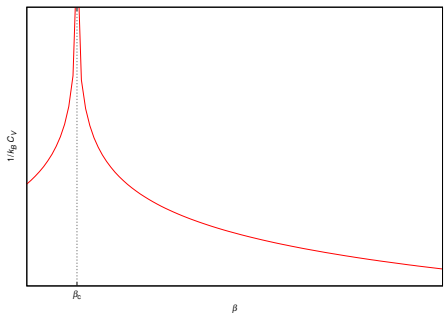

Figure 7.2: Specific heat of square lattice Ising model (Onsager's solution).

For a finite lattice, the specific heat graph for example for 3-state Potts model is shown in Figure 7.3. The graph has a peak which becomes larger as the lattice size increases.

We claim that there exist a power law relation through the line density distribution of zeros of the partition function near the phase transition point. This relation has been discussed by Martin [55, 56, 58] and also the earlier study by Fisher [26]. To support this claim, we show an approximation towards the experimental

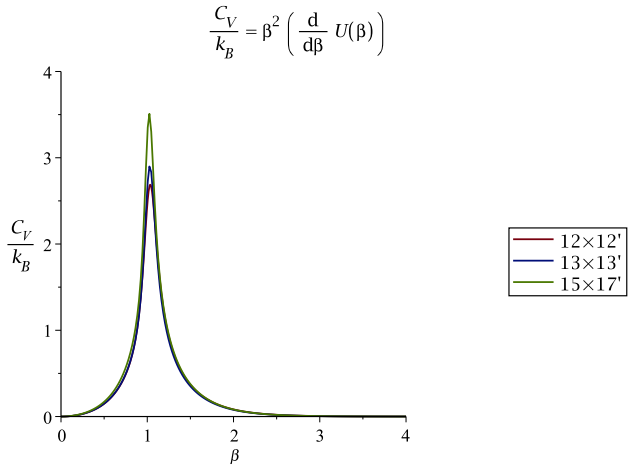

Figure 7.3: Specific heat in the 3-state Potts model on square lattice with lattice sizes, $N = 12, 13, 15$.

value [42, 101] extracted directly from the zeros distribution. We study this by computing the multiplicity of the zeros and plot them in log-log plots (in § 7.3).

7.2 Zeros and α-exponent

This section discusses the relation between the zeros distribution of Z on the complex plane and α-exponent of specific heat. We derive the α-exponent approximation from the partition function.

First consider a toy model partition function $Z = x^N + 1$ (we refer to § 4.3 for its zeros distribution). Here we can write

$$Z = \prod_{r=0}^{N-1} \left(x - e^{\frac{i\pi}{N}(2r+1)} \right).$$

At limit $N \to \infty$, we have the free energy given by

$$\begin{aligned}\lim_{N\to\infty} f &= \lim_{N\to\infty} \frac{1}{N} \ln Z \\ &= \lim_{N\to\infty} \frac{1}{N} \ln \prod_{r=0}^{N-1} \left(x - e^{\frac{i\pi}{N}(2r+1)} \right) \\ &= \lim_{N\to\infty} \frac{1}{N} \sum_{r=0}^{N-1} \ln \left(x - e^{\frac{i\pi}{N}(2r+1)} \right).\end{aligned}$$

By Taylor expansion for $x = e^{\beta}$ and small β, we have

$$\begin{aligned}\lim_{N\to\infty} f &\sim \lim_{N\to\infty} \frac{1}{N} \sum_{r=0}^{N-1} \ln \left(1 + \beta - \left(1 + \frac{i\pi}{N}(1+2r) \right) \right) \\ &= \lim_{N\to\infty} \frac{1}{N} \sum_{r=-\frac{N-1}{2}}^{\frac{N-1}{2}} \ln \left(\beta + \frac{\pi i}{N}(2r+N) \right).\end{aligned}$$

As $N \to \infty$ the zeros are distributed uniformly with a fixed density. We could write the free energy with the zeros distribution line density denoted $a(y)$ as

$$\lim_{N\to\infty} f \sim \frac{1}{2\pi} \int_{-\infty}^{\infty} a(y) \ln(\beta + iy)\, dy$$

where $a(y) = 1$.

Suppose we replace this constant density with other density which varying as we move in the complex plot. We have the internal energy

$$\begin{aligned}U = -\frac{df}{d\beta} &\sim -\frac{1}{2\pi} \int_{-\infty}^{\infty} \frac{a(y)}{\beta + iy}\, dy \\ &= \frac{i}{2\pi} \int_{-\infty}^{\infty} \frac{a(y)}{y - i\beta}\, dy \qquad (7.4)\end{aligned}$$

that has pole at $y = i\beta$ and $a(y) = a(-y)$. This distribution give a first order phase transition [58].

Alternatively, suppose the line density $a(y)$ has power law relation [58], for small y, that is

$$a(y) \sim |y|^{1-p} \ (0 \le p < 1). \qquad (7.5)$$

This gives a continuous internal energy function and a divergence in specific heat at $p = 0$. This corresponds to a second order phase transition.

By examining the asymptotic behaviour of $U(\beta)$ as $\beta \to 0$ [58], we may obtain specific heat critical exponent for $0 < p < 1$. The specific heat is given by

$$\frac{dU}{d\beta} \overset{\beta \to 0}{\sim} \beta^{-p}.$$

This relation gives the specific heat critical exponent $\alpha = p$.

Suppose we consider a model that, like the two-dimensional Ising model, has a line distribution of partition function zeros (for example as a function of e^{β}) in the complex neighbourhood of the critical point.

Our hypothesis is that for sufficiently large lattices the distribution of zeros of the partition function determines the α exponent. Specifically the hypothesis is that the exponent is determined by fitting the 'line density' to a power law dependence on distance from the critical point.

We can model this with a uniform positional distribution that has varying zeros multiplicity. We could also vary the line separation between zeros. But for a finite lattice approximation of continuum density, these two suggestion are similar [55].

Consider the zeros complex plane. We denote an equal range of imaginary part of the zeros as y. Let $a(y)$ be the multiplicity of zeros for each y. The partition function can now be written in this form; for a suitable $n \in \mathbb{N}$ (with respect to the zeros distribution),

$$Z = \prod_{y=1}^{n} \left(\beta + i\frac{y}{n}\right)^{a(y)} \tag{7.6}$$

where y is arranged in increasing distance from critical point. The partition function has zeros that are less dense near the critical point to more denser zeros as we move out in the complex plane. Let N be the size of the system. This gives the free

energy

$$f = \frac{1}{N} \ln Z = \frac{1}{N} \ln \prod_{y=1}^{n} \left(\beta + i\frac{y}{n}\right)^{a(y)} = \frac{1}{N} \sum_{y=1}^{n} a(y) \ln(\beta + iy). \quad (7.7)$$

Taking the logarithm on both sides of relation (7.5), we have

$$\log a(y) \sim (1-p) \log |y| \quad (7.8)$$

which gives a gradient $(1-p)$ in the log-log scale plane.

The idea of zeros multiplicity in function (7.6) will be used in analysing our zeros data near the real axis in complex plane zeros distribution. We use relation (7.8) to approximate the value of specific heat critical exponent α. We discuss this by notion of line density of zeros distribution in the next section.

7.3 Analysis on zeros density distribution

In this section, we analyse the line density of the zeros distribution. The line density is measured by the number of zeros in a subset of points in the complex zeros distribution plane. The α-exponent is determined by fitting a straight line into the log-log graph. This will gives the gradient $m = 1 - p$ and $\alpha = p$.

For the finite lattice, we know that the finite size effects (explained in Chapter 4) are present in the zeros distribution. This also affect the log-log analysis. For sufficiently large enough size, we expect the gradient of the log-log graph will become stable hence converge to the result in thermodynamic limit.

If this is true, then the problem of finding the critical exponent of a specific heat can be reduced to a problem of finding the log-log gradient. We may be able to determine the log-log gradient by increasing the lattice sizes. Hence we can determine the critical exponent. This simplification will assist the calculation of this α-exponent.

Three cases have been considered using this log-log analysis. They are briefly listed as follows:

1. The 2-state Potts model and Ising model on square lattice - finite cases from Onsager's solution.

2. The 3-state Potts model on square lattice.

3. The accumulated case of the 3-state Potts model on square lattice.

The accumulated case above will be explained further in § 7.3.3.

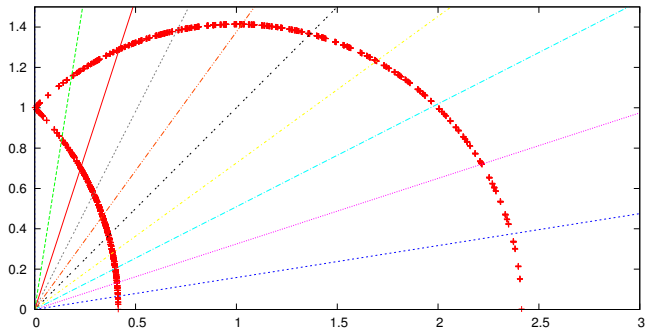

Figure 7.4: Example: first quadrant with bin of equal size for square lattice Ising model, $N = 50$.

Consider the complex plane for zeros distribution. We call each space with equal size a bin. See Figure 7.4. First, the first quadrant of complex plane is divided into several bins of equal angle. Then the total number of zeros in each bin over distance from the real axis is plotted in the log-log plot. The gradient of the logarithmic plot is determined to represent the power law relation for comparison with the known result.

Let $b \in \mathbb{N}$ be the number of total bins with equal angle from origin i.e. $\theta = \dfrac{\pi}{2b}$. And let a_i be the number of zeros in each bin where $i = 1, 2, \cdots, b$. The number of zeros is counted only for those in the ferromagnetic region.

The linear regression line fitting is used to fit the line of the zeros data. Due to the quantisation effect in the finite case, the linear fitting is done only on the angle near the transition point (first few bins). The y-axis is the logarithmic scale for the number of zeros a_i and the x-axis is the logarithmic scale for distance from real axis in the complex plane. The distance is represented by a simple numbering with $x = 1, 2, ..., b$.

Let m denotes the gradient of the linear fit. For comparison, we manually fit the line on the log-log graph.

7.3.1 The 2-state Potts model and Ising model – finite case from Onsager's solution

Here we describe the analysis on 2-state Potts model on square lattices of sizes 19 by 19 and 20 by 20. We also analyse the Onsager's Ising model zeros distribution with lattice sizes 49 by 49, 50 by 50, 99 by 99 and 100 by 100.

Table 7.1: Approximated slope m of log-log plane for $19 \times 19'$ and $20 \times 20'$ square lattices. The manual column is our own estimate directly on the log-log graph.

Lattice size	$19 \times 19'$			$20 \times 20'$		
Bin, b	Lin. reg.	Std. dev.	Manual	Lin. reg.	Std. dev.	Manual
6	0.93899	0.16400	1.00	0.91110	0.21020	0.90
7	0.72474	0.12319	0.80	0.97427	0.12869	1.00
8	1.09710	0.22530	1.00	1.13670	0.27250	0.90
9	0.87645	0.10518	0.95	1.02096	0.11154	1.00
10	0.95920	0.07519	1.00	1.07383	0.10632	0.90
11				1.000e+00	2.415e-16	1.00

See Table 7.1. This table describes the approximation for gradient m of the log-log plot for square lattice 19 by 19 and 20 by 20 of 2-state Potts model. The standard deviation of the linear regression analysis is also shown in this table. The column with total number of bins b is the variable for testing. As we vary the value of b, we check the gradient and its standard deviation.

For 19 by 19 lattice size, it can be seen in Table 7.1 that the approximation

reaches low standard deviation when we take the number of bins, $b = 10$. This approximation suggests that the approximated value of α-exponent is nearly zero i.e. $\alpha_{19} = 1 - 0.95920 = 0.0408$.

For comparison, we further test the zeros data for 20 by 20 lattice case. This size improvement shows that the lowest standard deviation started to emerge when number of bins is at $b = 11$. This approximation gives the approximated value of α-exponent to be zero (1-1=0). Figures 7.5 and 7.6 present the linear regression line fitting for the 19 by 19 and 20 by 20 case with increasing number of total bins.

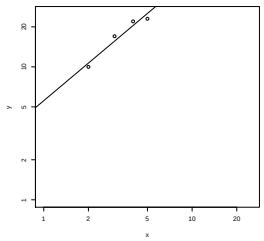

(a) Number of bins, $b = 6$.

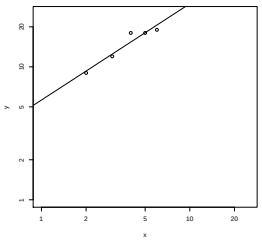

(b) Number of bins, $b = 7$.

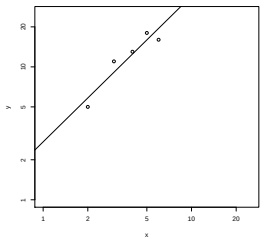

(c) Number of bins, $b = 8$.

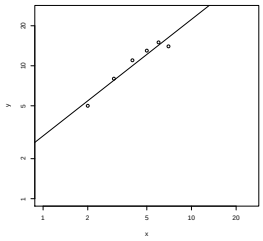

(d) Number of bins, $b = 9$.

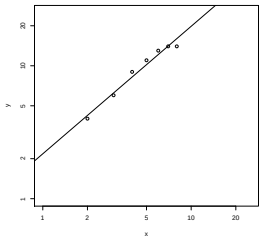

(e) Number of bins, $b = 10$.

Figure 7.5: Lattice 19×19 : Linear regression analysis on log-log graphs.

From the known result [101], this observation is very promising since we know that $\alpha = 0$ for the Ising model. For a large lattice size, the log-log gradient analysis is a very convincing approach in finding the critical exponent of specific heat.

We examine the zeros from Onsager's partition function on $49 \times 49, 50 \times 50, 99 \times 99$ and 100×100 square lattices. Tables 7.2 and 7.3 describe the approximation of log-log linear fitting gradient by linear regression analysis and also by our own estimation.

Table 7.2: Approximated slope m of log-log plane for $49 \times 49'$ and $50 \times 50'$ square lattices. The manual column is our own estimate directly on the log-log graph.

Lattice size	$49 \times 49'$			$50 \times 50'$		
Bin, b	Lin. reg.	Std. dev.	Manual	Lin. reg.	Std. dev.	Manual
6	0.70680	0.17581	0.80	0.68589	0.17008	0.85
7	0.96394	0.12327	0.95	0.74285	0.13096	0.90
8	0.88348	0.07914	0.90	0.89385	0.09973	1.00
9	0.94430	0.05673	1.05	0.85755	0.06194	0.90
10	1.02143	0.15312	1.00	1.05898	0.12823	1.15
11	0.90537	0.08267	1.25	0.97027	0.06215	1.00
12	0.96817	0.08687	1.10	0.89355	0.06381	1.00
13	0.88986	0.07570	1.10	0.97750	0.04518	1.10
14	0.96536	0.07308	1.00	1.05585	0.05983	1.00
15	0.99628	0.09292	1.00	0.98123	0.08653	1.00
16	0.97097	0.07456	0.95	1.04545	0.06624	1.05
17	1.04496	0.07042	0.95	0.96997	0.09009	1.10
18	1.01593	0.07278	1.10	0.95723	0.07614	0.95
19	1.03028	0.07994	1.00	0.97725	0.06966	1.00
20	0.95314	0.08499	0.90	0.94095	0.06692	1.00
21	1.01374	0.07093	1.00	0.98264	0.08228	1.00
22	0.97289	0.04845	0.95	0.93796	0.06808	1.00
23	1.00671	0.07221	0.95	1.05704	0.07892	1.20
24	1.02687	0.06218	1.05	1.13146	0.06805	1.00
25	0.96594	0.04661	1.00	1.01301	0.05130	1.00
26	0.95291	0.05226	1.00	1.01507	0.03550	0.95
27	0.97771	0.05102	0.95	0.93749	0.04586	1.10
28	0.97275	0.04557	1.00	1.00687	0.03802	1/00
29	0.97189	0.04521	1.00	0.95440	0.05054	1.05
30	1.00256	0.08744	1.05	0.95792	0.06627	1.05

Table 7.3: Approximated slope m of log-log plane for $99 \times 99'$ and $100 \times 100'$ square lattices. The manual column is our own estimate directly on the log-log graph.

Lattice size	$99 \times 99'$			$100 \times 100'$		
Bin, b	Lin. reg.	Std. dev.	Manual	Lin. reg.	Std. dev.	Manual
6	0.98823	0.09576	1.15	0.98618	0.10626	0.90
7	0.92509	0.07922	1.15	1.08718	0.06377	1.05
8	0.88728	0.08189	1.05	1.01864	0.05231	1.05
9	1.00604	0.07324	1.05	1.07185	0.06142	0.95
10	0.95626	0.07023	1.00	1.11431	0.05931	1.05
11	1.04726	0.06063	1.00	1.08076	0.04094	1.00
12	0.98669	0.04702	1.10	1.04617	0.03913	1.00
13	0.97308	0.05435	1.10	1.08313	0.05358	1.05
14	0.95910	0.04875	1.00	1.05595	0.02985	1.10
15	1.00735	0.05186	1.00	1.04609	0.05617	1.00
16	0.96391	0.04085	0.90	1.02435	0.04026	1.10
17	0.95895	0.04149	0.95	1.02347	0.03518	1.10
18	0.97073	0.03453	1.05	1.01396	0.02934	0.95
19	0.97381	0.03949	1.00	1.01797	0.03956	0.95
20	1.00459	0.06219	1.05	1.07274	0.03707	1.05
21	0.98633	0.04489	1.00	1.07150	0.04394	1.00
22	0.99341	0.03493	1.10	1.05187	0.02727	1.05
23	0.93009	0.03275	1.00	1.03297	0.01873	1.05
24	0.96870	0.02774	1.05	0.99994	0.02763	0.95
25	1.06193	0.03289	1.05	1.01458	0.03217	1.10
26	0.94521	0.03168	1.00	1.01586	0.02909	0.90
27	0.92396	0.03373	1.05	0.99821	0.02324	1.10
28	0.96805	0.03442	1.00	1.02952	0.02803	1.00
29	0.98326	0.03249	1.00	1.03293	0.03717	1.00
30	0.96172	0.04282	0.95	1.04274	0.03229	1.00

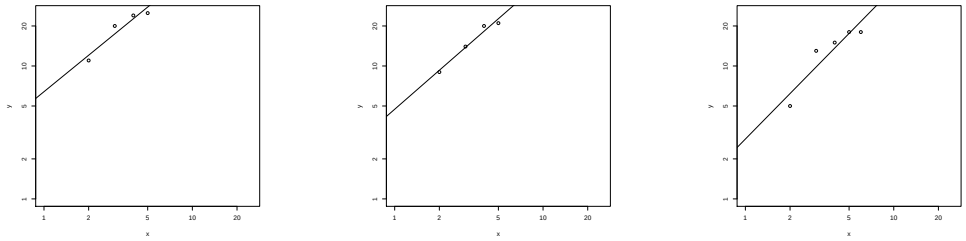

(a) Number of bins, $b = 6$. (b) Number of bins, $b = 7$. (c) Number of bins, $b = 8$.

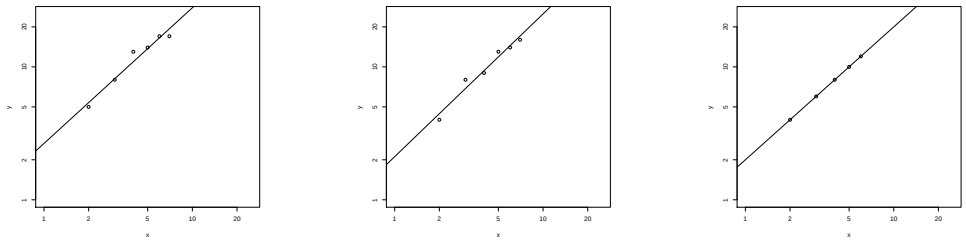

(d) Number of bins, $b = 9$. (e) Number of bins, $b = 10$. (f) Number of bins, $b = 11$.

Figure 7.6: Lattice 20×20 : Linear regression analysis on log-log graphs.

Figures 7.7, 7.8, 7.9 and 7.10 show the linear regression line fitting for $49 \times 49, 50 \times 50, 99 \times 99$ and 100×100 square lattices respectively. The approximation gives many results with small deviation when we change the value of b. The gradients are mostly very close to $m \sim 1$ i.e. $0.9 < m < 1.1$. For some bins, the quantisation effect may dominate which are evident by the large standard deviation. For $m \sim 1$, this approximately gives the value of specific heat exponent $\alpha \sim 1 - 1 = 0$. This analysis will converge to the known result − as shown in [101, p. 46].

For 100 by 100 square lattice, one can see that the log-log graph line fitting is very close to the points. The change in the number of bins does not give a huge effect on the distribution. The slope is approximately $m \sim 1$ which gives $\alpha = 0$.

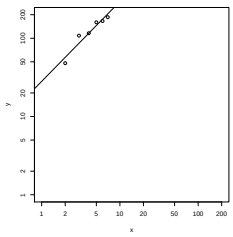

(a) Number of bins, $b = 10$.

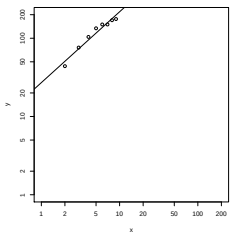

(b) Number of bins, $b = 11$.

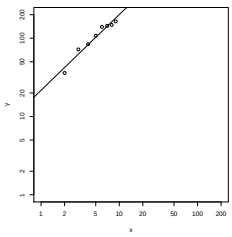

(c) Number of bins, $b = 12$.

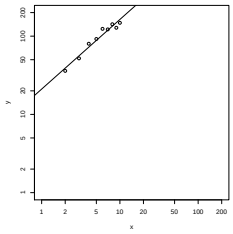

(d) Number of bins, $b = 13$.

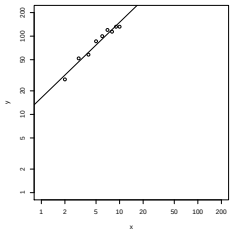

(e) Number of bins, $b = 14$.

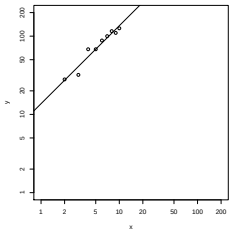

(f) Number of bins, $b = 15$.

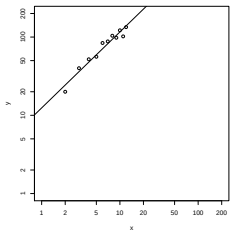

(g) Number of bins, $b = 16$.

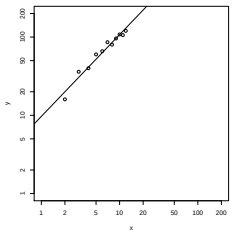

(h) Number of bins, $b = 17$.

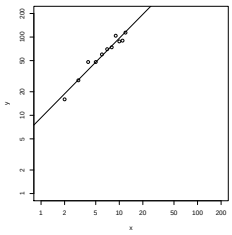

(i) Number of bins, $b = 18$.

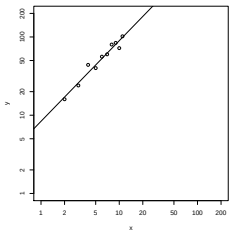

(j) Number of bins, $b = 19$.

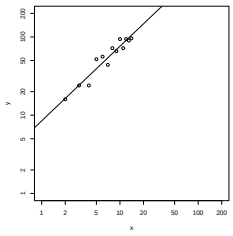

(k) Number of bins, $b = 20$.

Figure 7.7: Lattice 49×49 : Linear regression analysis on log-log graphs.

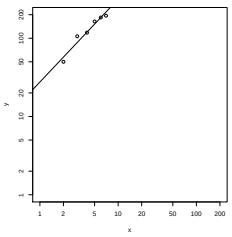

(a) Number of bins, $b = 10$.

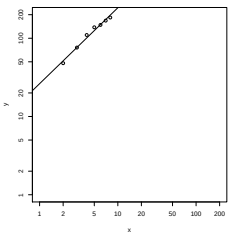

(b) Number of bins, $b = 11$.

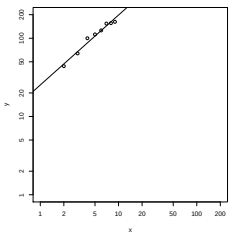

(c) Number of bins, $b = 12$.

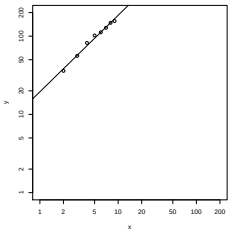

(d) Number of bins, $b = 13$.

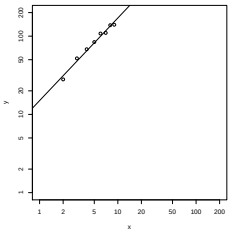

(e) Number of bins, $b = 14$.

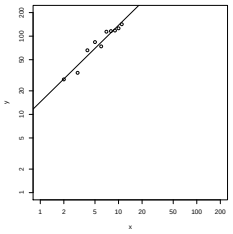

(f) Number of bins, $b = 15$.

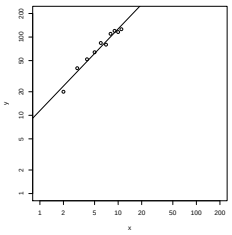

(g) Number of bins, $b = 16$.

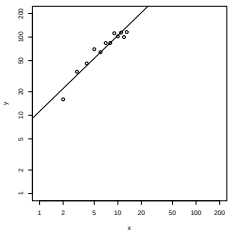

(h) Number of bins, $b = 17$.

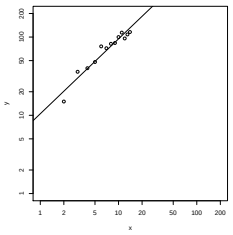

(i) Number of bins, $b = 18$.

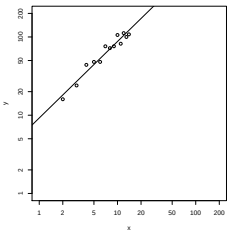

(j) Number of bins, $b = 19$.

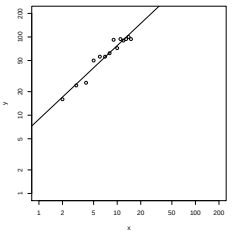

(k) Number of bins, $b = 20$.

Figure 7.8: Lattice 50×50 : Linear regression analysis on log-log graphs.

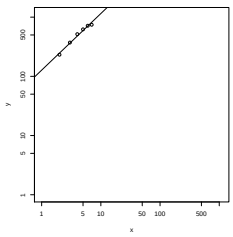

(a) Number of bins, $b = 10$.

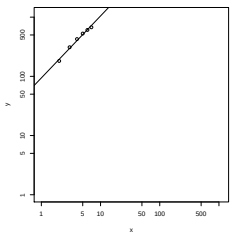

(b) Number of bins, $b = 11$.

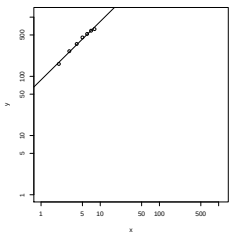

(c) Number of bins, $b = 12$.

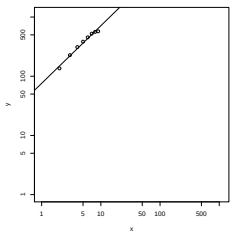

(d) Number of bins, $b = 13$.

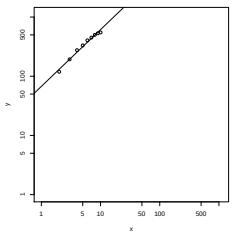

(e) Number of bins, $b = 14$.

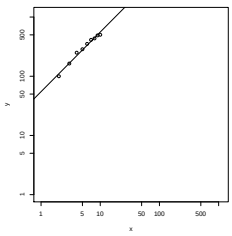

(f) Number of bins, $b = 15$.

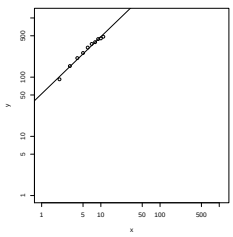

(g) Number of bins, $b = 16$.

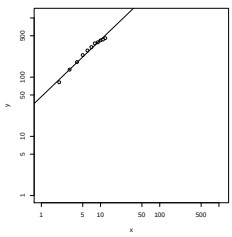

(h) Number of bins, $b = 17$.

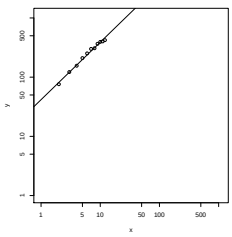

(i) Number of bins, $b = 18$.

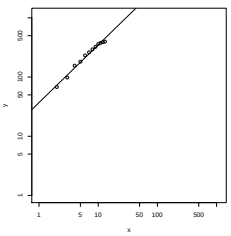

(j) Number of bins, $b = 19$.

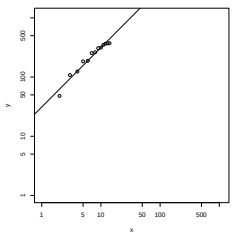

(k) Number of bins, $b = 20$.

Figure 7.9: Lattice 99×99 : Linear regression analysis on log-log graphs.

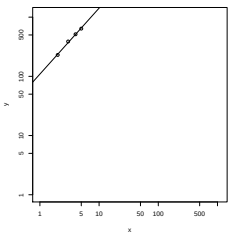

(a) Number of bins, $b = 10$.

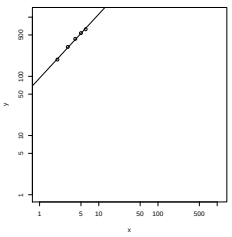

(b) Number of bins, $b = 11$.

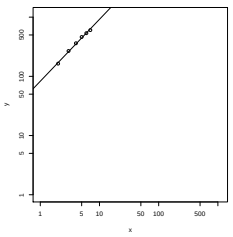

(c) Number of bins, $b = 12$.

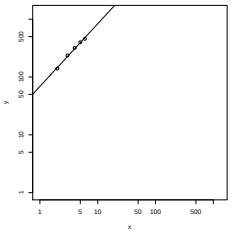

(d) Number of bins, $b = 13$.

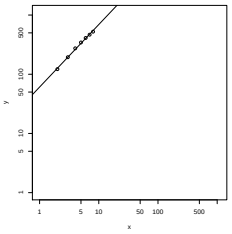

(e) Number of bins, $b = 14$.

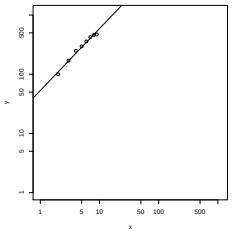

(f) Number of bins, $b = 15$.

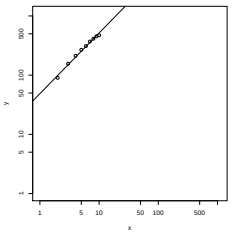

(g) Number of bins, $b = 16$.

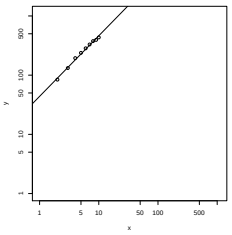

(h) Number of bins, $b = 17$.

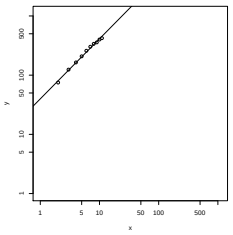

(i) Number of bins, $b = 18$.

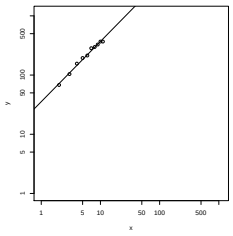

(j) Number of bins, $b = 19$.

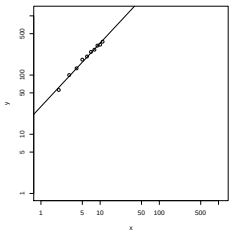

(k) Number of bins, $b = 20$.

Figure 7.10: Lattice 100×100 : Linear regression analysis on log-log graphs.

7.3.2 The 3-state Potts model

Here we present the analysis on several largest cases for the 3-state Potts model zeros distributions that we managed to produced in this thesis.

See Tables 7.4 and 7.5. The gradient m for individual case for 12 by 12, 13 by 13, 14 by 14 and 15 by 17 square lattices are presented in these tables with the comparison between linear regression analysis and our manual estimation. As before, the standard deviation of the linear regression analysis is also shown in these tables.

The linear regression line fitting for 12 by 12 square lattice is shown in Figure 7.12. Based on the result in Table 7.4, one can see that the standard deviations are mostly over 0.1. We suspect the number of zeros is not enough in the first quadrant (see Figure 7.11a) to approximate the limiting slope through the log-log analysis. The zeros are still too far from the real axis in the complex plane. The zeros in antiferromagnetic region is not counted for the log-log graph.

Table 7.4: Approximated slope m of log-log plane for $12 \times 12'$ and $13 \times 13'$ square lattices. The manual column is our own estimate directly on the log-log graph.

Lattice size	$12 \times 12'$			$13 \times 13'$		
Bin, b	Lin. reg.	Std. dev.	Manual	Lin. reg.	Std. dev.	Manual
6	0.59478	0.10304	0.70	0.54000	0.18192	0.80
7	0.90741	0.06768	0.90	0.74789	0.13769	0.55
8	0.59781	0.11707	0.60	0.76448	0.08011	0.60
9	0.69353	0.10397	0.75	0.77963	0.12546	0.60
10	0.76040	0.11860	1.00	0.65835	0.05620	0.75

Table 7.5: Approximated slope m of log-log plane for $14 \times 14'$ and $15 \times 17'$ square lattices. The manual column is our own estimate directly on the log-log graph.

Lattice size	$14 \times 14'$			$15 \times 17'$		
Bin, b	Lin. reg.	Std. dev.	Manual	Lin. reg.	Std. dev.	Manual
6	0.58580	0.16110	0.75	0.49330	0.11493	0.60
7	0.76880	0.09357	0.60	0.53440	0.13894	0.80
8	0.69276	0.11134	0.70	0.61090	0.08523	0.70
9	0.67331	0.08984	0.60	0.70270	0.08235	0.60
10	0.74003	0.09145	0.70	0.71160	0.10301	1.00
11				0.71280	0.04786	0.70
12				0.70470	0.06792	0.70

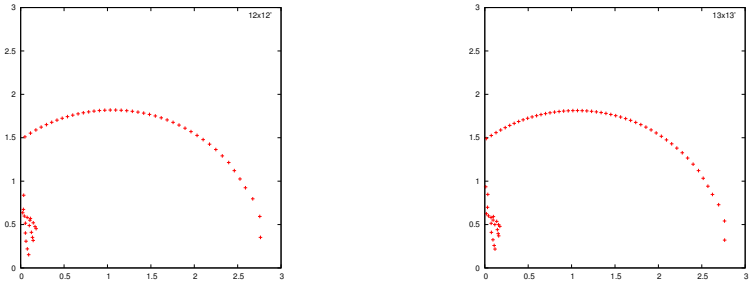

(a) (b)

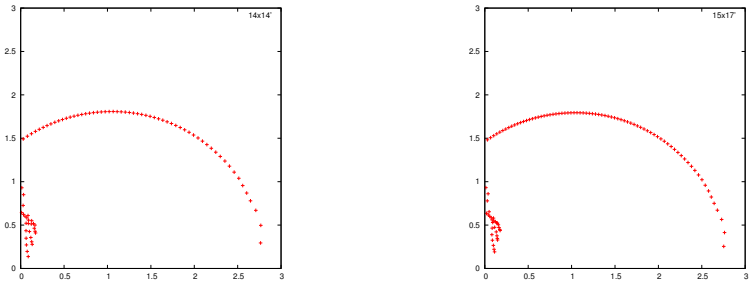

(c) (d)

Figure 7.11: Zeros distribution at quadrant 1 for 3-state Potts model on square lattice of a) 12 by 12, b) 13 by 13, c) 14 by 14 and d) 15 by 17.

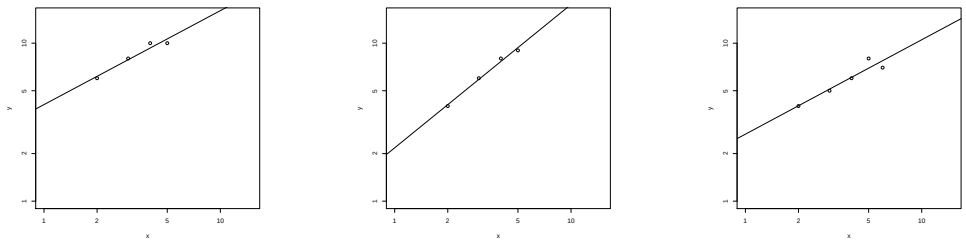

(a) Number of bins, $b = 6$. (b) Number of bins, $b = 7$. (c) Number of bins, $b = 8$.

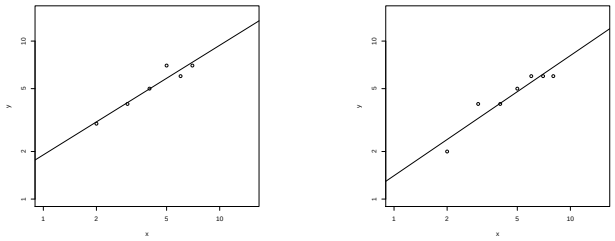

(d) Number of bins, $b = 9$. (e) Number of bins, $b = 10$.

Figure 7.12: Lattice 12x12 : Linear regression analysis on log-log graphs.

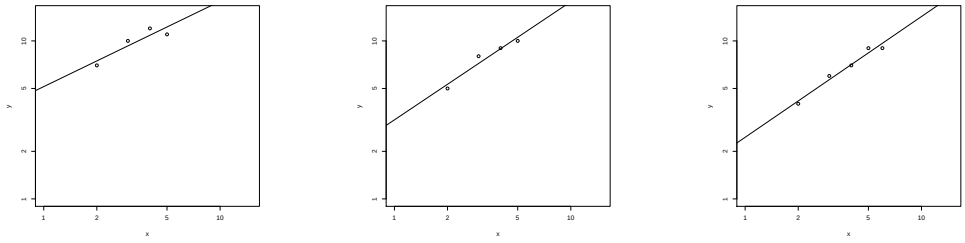

(a) Number of bins, $b = 6$. (b) Number of bins, $b = 7$. (c) Number of bins, $b = 8$.

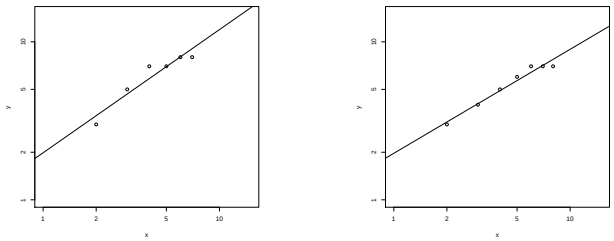

(d) Number of bins, $b = 9$. (e) Number of bins, $b = 10$.

Figure 7.13: Lattice 13x13 : Linear regression analysis on log-log graphs.

Consider the 13 by 13 square lattice. The linear regression line fitting is shown in Figure 7.13. Similar to 12 by 12 case, the standard deviation in Table 7.4 gives values mostly more than 0.1. The number of zeros in the first quadrant (see also Figure 7.11b for 13 by 13 case) are not enough to suggest a good gradient approximation.

Next, Figures 7.14 and 7.15 present the linear regression line fitting for larger cases with 14 by 14 and 15 by 17 lattice sizes respectively. More zeros are located in the first quadrant of the complex-e^{β} plane for larger cases (see Figure 7.11).

As the total number of bins b changes we observe the emergence of the gradient with small standard deviation, for example in the case with 15 by 17 lattice size. The approximation converge to the known value from experiment (also the folklore theory) for the α-exponent of 3-state Potts model i.e. $\alpha = 1/3$ [98, 101].

In Table 7.5, the estimation for the case with total number of bins equal to 11 and 12 has estimated gradient value of 0.7128 and 0.7047 respectively. This estimations is the closest approximation we have so far. This value gives α close to 1/3. The bigger the lattice size, a better convergent sequence can be made from this analysis.

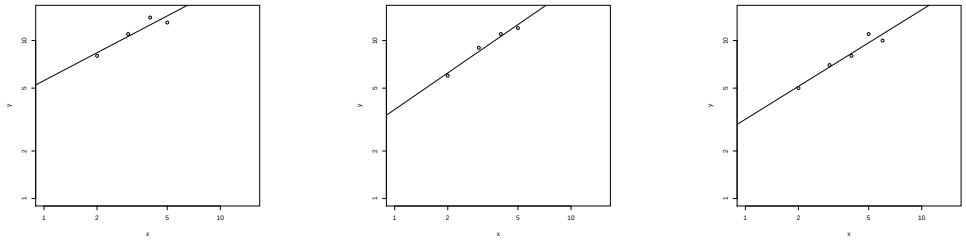

(a) Number of bins, $b = 6$. (b) Number of bins, $b = 7$. (c) Number of bins, $b = 8$.

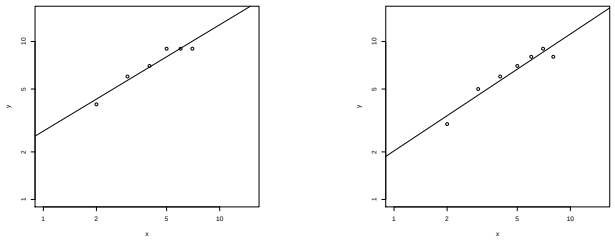

(d) Number of bins, $b = 9$. (e) Number of bins, $b = 10$.

Figure 7.14: Lattice 14x14 : Linear regression analysis on log-log graphs.

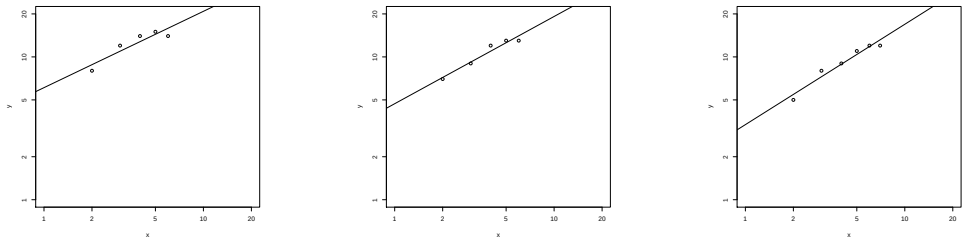

(a) Number of bins, $b = 7$. (b) Number of bins, $b = 8$. (c) Number of bins, $b = 9$.

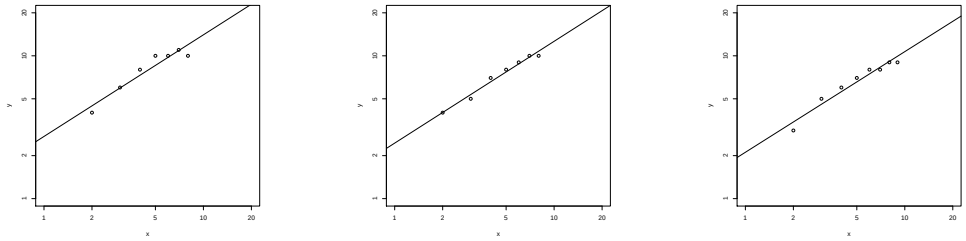

(d) Number of bins, $b = 10$. (e) Number of bins, $b = 11$. (f) Number of bins, $b = 12$.

Figure 7.15: Lattice 15x17 : Linear regression analysis on log-log graphs.

For some estimation however, the quantisation effect may dominate, for example as shown in 15 by 17 case when the total number of bins $b = 10$. Our manual estimation and the linear regression approximation do not coincide each other. The reason for this is due to the data chosen for the linear regression line fitting. The line is fitted on the data that may dominated by quantisation effect or finite size effect (that includes points that are far from the critical point). In contrast, our manual fitting give us more freedom in choosing the points from the bins that is near to the critical point. The linear graph shown in 7.15d convinced us that the estimation is affected by the finite size effect.

7.3.3 The accumulated case of 3-state Potts model

In this section we consider another type of zeros data collection for testing.

Table 7.6: Approximated slope m of log-log plane for accumulated zeros from $12 \times 12', 13 \times 13', 14 \times 14'$ and $15 \times 17'$ square lattices. The manual column is our own estimate directly on the log-log graph.

Lattice size	All zeros		
Bin, b	Lin. reg.	Std. dev.	Manual
6	0.54650	0.13678	0.75
7	0.76419	0.10170	0.65
8	0.66258	0.08293	0.80
9	0.70973	0.08226	0.80
10	0.71434	0.08326	0.75
11	0.72440	0.11357	0.70
12	0.83374	0.11708	0.65
13	0.79471	0.11728	1.20
14	0.72016	0.05601	0.80
15	0.67004	0.04927	0.75
16	0.70098	0.05753	0.80
17	0.73147	0.04802	0.80
18	0.74239	0.03766	0.70
19	0.66271	0.05214	0.70
20	0.69746	0.06845	0.75
21	0.65775	0.05629	0.80
22	0.62372	0.06816	0.70

To add more varieties to the study, we consider a case with zeros taken from several big lattice cases that we have investigated. The zeros are now taken from

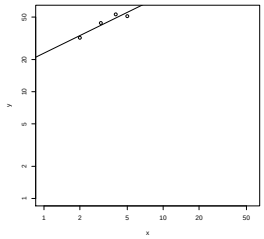

(a) Number of bins, $b = 6$.

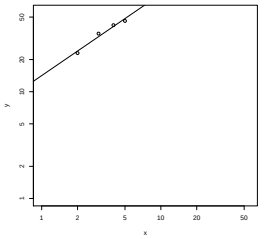

(b) Number of bins, $b = 7$.

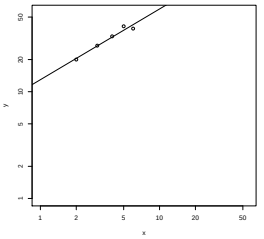

(c) Number of bins, $b = 8$.

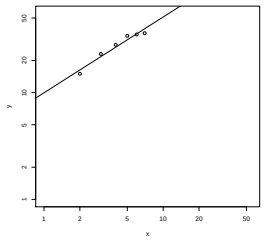

(d) Number of bins, $b = 9$.

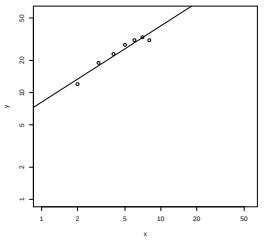

(e) Number of bins, $b = 10$.

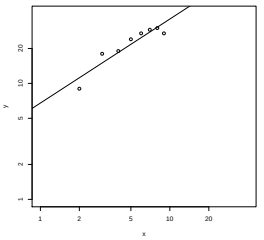

(f) Number of bins, $b = 11$.

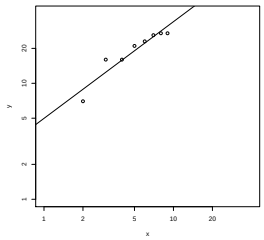

(g) Number of bins, $b = 12$.

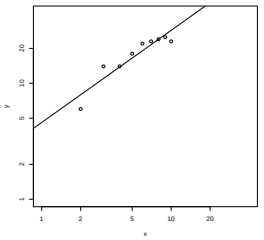

(h) Number of bins, $b = 13$.

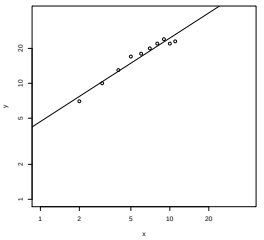

(i) Number of bins, $b = 14$.

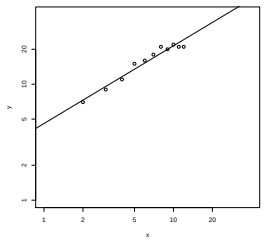

(j) Number of bins, $b = 15$.

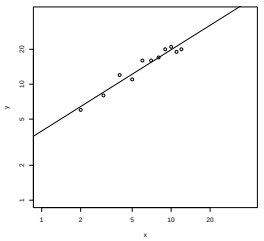

(k) Number of bins, $b = 16$.

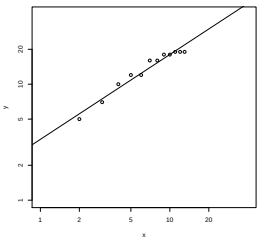

(l) Number of bins, $b = 17$.

Figure 7.16: Lattice $12 \times 12'$ to $15 \times 17'$: Linear regression analysis on log-log graphs.

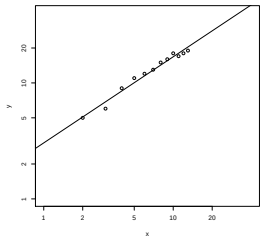
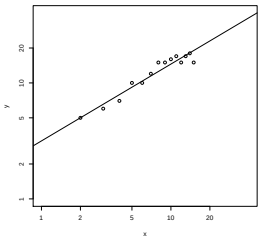
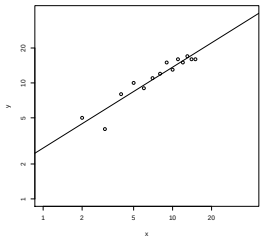

(a) Number of bins, $b = 18$. (b) Number of bins, $b = 19$. (c) Number of bins, $b = 20$.

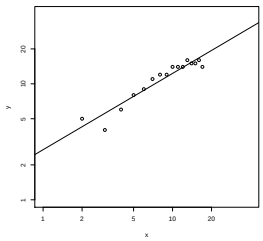
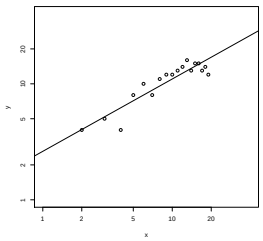

(d) Number of bins, $b = 21$. (e) Number of bins, $b = 22$.

Figure 7.17: Lattice $12 \times 12'$ to $15 \times 17'$: Linear regression analysis on log-log graphs (cont.).

all these lattices i.e. 12 by 12, 13 by 13, 14 by 14 and 15 by 17. We call them the accumulated zeros data.

As before, the number of zeros in each bin is computed and plotted in the log-log plot. Again, we vary the number of total bins b. For this case, we let $b = \{1, 2, \ldots, 22\}$.

See Table 7.6 for the approximated value of the linear regression and our manual estimation. Figures 7.16 and 7.17 show the log-log plot and their linear regression line fitting.

Since a lot of zeros are now involved, we can investigate and vary the total number of bins b into larger values as compared to the individual case in the previous section § 7.3.2. Table 7.6 shows several results of estimation from linear regression analysis with small standard deviation less than 0.1. In the last five estimation from $b = 19$ and above, we have several nice estimations with small deviation. These estimations are very close to the known α-exponent value of 1/3.

This result suggests that the analysis produces a good approximation if we have many zeros data. The higher number of bins means smaller range of distance (or small angle θ) in the imaginary axis of the complex plane zeros distribution. The estimation particularly involves the zeros that is very close to the critical point x_c.

The analysis is done on the 3-state Potts model case and the Ising model because we can directly compare our estimation with the result from [101]. The promising results from this analysis can be extended to zeros distributions for other models and lattices. This is an open problem since more experimental result and bigger lattice result are needed for checking and comparison. In the next chapter, we continue with an analysis for a model with multiple phases.

Chapter 8

Analytical machinery for multiple phases in Z_Q-symmetric model

In this chapter we investigate the energy and entropy relation [27] relative to phase transitions in terms of our exact solutions.

We discuss the possibility of multiple transitions between fully ordered and disordered states. Next we study the polynomial term of the partition function Z and plot the accumulated value of the terms towards $Z = 0$ at complex coupling values that are roots of Z close to the transition points. The final section contains graphs of the specific heat. This analysis is focused on the 2- and 3-state Potts models and the Z_5- and Z_6-symmetric models.

8.1 Candidates for 3 phase models

The solved case of Ising model [75, 92] for example showed the existence of single phase transition at $x = 1 + \sqrt{2}$ in the ferromagnetic (ferro) [44] region.

On the other hand, the study of Z_Q-symmetric model partition function showed the possibility of multiple phase transitions for some energy function χ [58]. Recall the result in Chapter 6. For specific χ, as defined in § 6.1, we can see in Figure 8.1, a pattern of zeros distribution with single arc for example when $\chi = (3, 1, 0)$ and

double arc for example when $\chi = (3, 2, 0)$ which move close to the positive real axis as the lattice size increases (see also § 6.2).

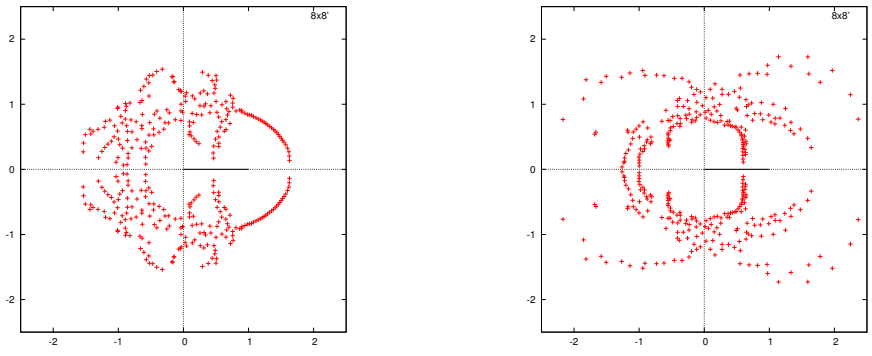

(a) (b)

Figure 8.1: The 8 by 8 zeros distribution for a) $\chi = (3, 1, 0)$ and b) $\chi = (3, 2, 0)$.

8.2 Energy vs entropy

We describe the idea of energy and entropy competition in a model partition function in this section. First we describe the idea of energy-entropy in a model of phase transition. Then we describe a modification aiming to explain two transitions.

To support the existence of two transitions, a new kind of transition mechanism as compared to order/disorder transition is needed for explanation. The claim is that there are two stages of disordered state in the system. From first stage to the second stage, this change corresponds to the second phase transition − for example from a fairly disordered to a completely random disordered state.

8.2.1 Single order/disorder phase transition

Recall the expectation value (1.4) of an observable quantity $\mathcal{O}$ of physical system given by

$$\langle \mathcal{O} \rangle = \sum_{\sigma \in \Omega} p(\sigma) \mathcal{O}(\sigma) \tag{8.1}$$

where $p(\sigma) = \dfrac{e^{-\beta\mathcal{H}}}{Z}$.

We shall observe the energy-entropy competition as we vary the temperature T [52, 58]. Recall that $\beta = 1/(k_B T)$.

At low T (high β), $e^{-\beta\mathcal{H}} \to 0$ as $\beta \to \infty$. The system preferred to be in the ordered state. The dominant contribution is coming from the high magnitude of $\mathcal{H}$ despite the low entropy. At low T the energy dominate the system.

In contrast, at high T (low β), $e^{-\beta\mathcal{H}} \to 1$ as $\beta \to 0$. The system is not dominated by $\mathcal{H}$ but by the number of configurations that give the entropy of the system. The configuration with relatively little order among the spins may be regarded as representative of the system. At high T the entropy dominate the system.

At low T where the system is in ordered state, there is a strong interaction between all the particles and its neighbours. At high T, the system is in disordered state where the spin variables prefer to point at different directions.

Peierls [78] shows a rigorous arguments to support the emergence of phase transition between order (low energy in the Potts model) and disorder (high entropy). Peierls in his paper describes the phase transition by the emergence of line separations in the dual picture of configurations as in § 6.3.1.

8.2.2 Two phase transitions

For the system with two phase transitions we can describe the transition mechanism by the idea of two different stages of entropy appearance. The idea of the second phase transition can also be described through the behaviour of the line separation (see § 6.3.1).

The increase in temperature will drive the line separations to become longer (see Figure 8.2) or change the distance among the vortices. This system will have extra entropy from this long string lines which then balance out the energy penalty due to the different spin orientation. This energy and entropy competition drives the second phase transition. At large enough temperature, the fairly disordered state

reach its criticality where the second transition can take place.

Our claim is that the second phase transition is not only driven by the long edges of line separation but also by the roughness of the long string. See Figure 8.2b for example. In the long range region, the long line separation between vortices has higher entropy than the shorter line.

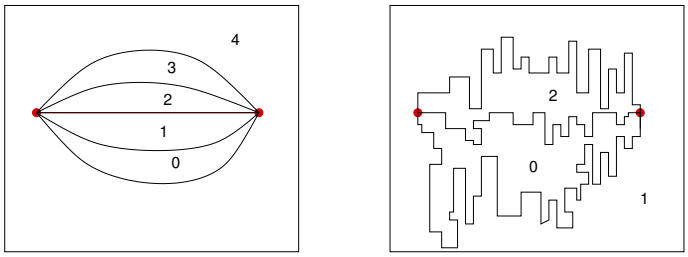

(a) (b)

Figure 8.2: Example of vortex-antivortex pair with a) smooth line separation and b) rough line separation.

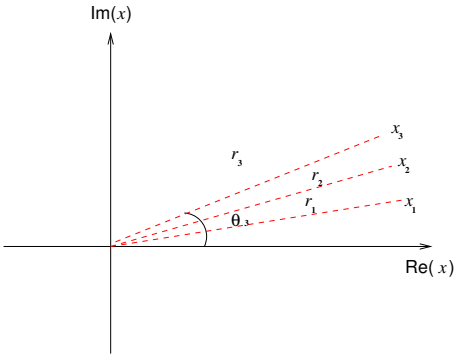

Figure 8.3: Illustration of some zeros of Z for the first, second and third closest to the positive real axis.

Recall the definition of partition function (1.1) and $x = e^{\beta J}$. The value of x in the partition function can be written in terms of angle below:

$$Z = \sum_j a_{|E|-j}\, x^{-j} = \sum_j a_{|E|-j}\, r^{-j}\, (e^{\sqrt{-1}\theta})^{-j} \tag{8.2}$$

where $x = re^{i\theta}$. The coefficient of the partition function corresponds to the entropy associated by Hamiltonian $\mathcal{H}$. The magnitude $r = \sqrt{Re(x)^2 + Im(x)^2}$ corresponds

to the magnitude of complex zeros of the partition function. The angle θ is measure from the real positive axis. These three components are the main factors contributing to the energy-entropy competition in this system.

The concept of two different stages in the disordered phase may be extended to more disordered stages as we increase the value of temperature. These different stages mean other energy-entropy battle in the microscopic detail of the configuration state. The configuration state is transformed to more random disordered state where the vortex-antivortex pair may become very close to each other and the configuration states are at random.

8.3 Z_Q-symmetric model partition function

We describe the line separation in a configuration state and further relate them to the energy-entropy competition in a partition function. Recall Ω as the set of all configuration states and $\sigma \in \Omega$. We consider the Z_5- and Z_6-symmetric models on square lattice in this section.

The configuration state σ can be illustrated by the local spin boundaries between two different spin configurations drawn on the dual lattice. For a state σ that has one variable in different orientation from the rest of the spin variables, the total energy is reduced by 4 corresponding to 4 dual edges (see Figure 8.4a).

Similarly, if there are two neighbouring spin variables with the same orientation but different from the orientation of the others, the total energy is reduced by 6 (see Figure 8.4b). The partition function can be written with exponent given by the value of energy penalty. The energy penalty is drawn as the edges of line separation in the dual lattice.

In this thesis, we are always interested to study the behaviour of configuration states near the phase transition. We analyse the partition function polynomial relative to its zero value. The accumulated summations of the polynomial terms are plotted for specific value of the root x.

(a) (b)

Figure 8.4: Example of configuration and line separation on dual lattice with a) 1 spin flip and b) 2 same spin flip.

8.3.1 Individual term of partition function polynomial

The order-disorder transition is driven by the domination of either the energy or the entropy at particular T. This domination is represented by a typical configuration which manifests the bulk behaviour of the system.

In principle the determination of the typical configuration is not a simple investigation. Instead of finding the typical configuration for a specific T, we investigate the typical energy value from the partition function Z. We study the accumulated summation of the term in the polynomial Z with respect to some values of x which gives $Z = 0$.

Here we calculate the magnitude of each term of the partition function and compute their accumulated summations. The extreme contribution is given by the longest line in the picture of the accumulated summations.

8.3.2 The picture of polynomial term contribution

In this section, we present the graphs of the accumulated terms contribution with respect to some roots x. The partition function (1.1) can be written in this form:

$$\begin{aligned} Z' &= \frac{1}{x^{|E|}} \sum_{\sigma \in \Omega} x^{\widetilde{\mathcal{H}}(\sigma)} \\ &= \sum_{j=0}^{|E|} a_{|E|-j}\, x^{-j} \\ &= \sum_{j=0}^{|E|} a_{|E|-j}\, \tilde{x}^{j} \end{aligned} \tag{8.3}$$

where a_j is the coefficient of the polynomial, $\tilde{x} = 1/x$ and $\widetilde{\mathcal{H}}$ is as in (1.2). The above partition function (8.3) is written based on the energy penalty given by the length of line separation in the dual lattice.

We compute the accumulated summations of the partition function as below. Let $Z_j = a_{|E|-j}\,\tilde{x}^j$ and $p_0 = Z_0$. We have

$$\begin{aligned} p_1 &= p_0 + Z_1 \\ p_2 &= p_1 + Z_2 \\ p_3 &= p_2 + Z_3 \\ &\vdots \\ p_{|E|} &= p_{|E|-1} + Z_{|E|}. \end{aligned}$$

The difference between two accumulated summations $|p_{j+1} - p_j|$ is the net contribution of each new term $j+1$. The length of the line from p_i to p_{i+1} is the total contribution given by the term Z_{i+1}. Here we study the step by step terms cancellation of the partition function by plotting each value of p_j. The root x of Z is chosen close to critical point in the positive real axis.

Recall that for $T \sim 0$, the Boltzmann weight $\tilde{x} = e^{-\beta J}$ is close to 0. This value shows the energy domination. The system is in an ordered state. In contrast, for $T \to \infty$, all the Boltzmann weight has weight equal to 1. The entropy represented by the coefficient of the partition function polynomial is dominating the system. The middle term of the polynomial with the highest entropy is the most probable state.

At low T when $\tilde{x} = 0$, only the constant term in the polynomial survives. This term represents the ordered state when all spin variables spin in the same direction.

We may explain the partition function by this condition. Let $n, m \in \mathbb{N}$. The first n terms of the polynomial are representing the ordered state i.e. ferromagnetic (ferro) state [41, 44, 45]. And the final m terms correspond to another kind of ordered state i.e. antiferromagnetic (antiferro) state. The middle part is the most

disordered part. We claim that the typical energy value is given by the largest energy contribution towards $Z = 0$.

We plot the value of accumulated contribution for each term in polynomial $Z = 0$. Each line segment in the plot is the magnitude of each of the polynomial term. The term with the longest line has the highest contribution to $Z = 0$.

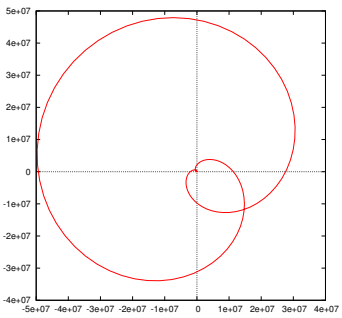

(a) x_1: longest length: 99

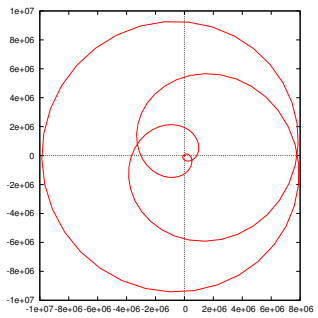

(b) x_2: longest length: 91

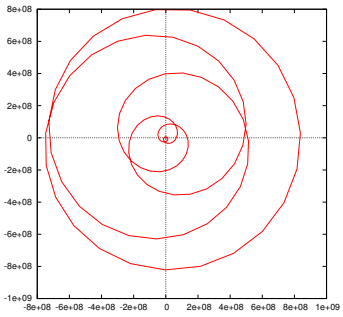

(c) x_3: longest length: 121

Figure 8.5: 2-state Potts model on 18 by 18 square lattice with a) $x_1 = 2.42196 + .0287144\,I$, b) $x_2 = 2.42216 + 0.462357\,I$, c) $x_3 = 2.26734 + 0.641372\,I$.

The pictures of the accumulated terms contribution for 2-state Potts model are presented in Figure 8.5 on the 18 by 18 square lattice with three values of x (denoted as x_1, x_2, x_3). For each x, the largest contribution is given by the terms at degree $j = 99, 91$ and 121 for the first, second and third closest zeros, respectively. One can see the summations form some loops before reaching the 0 value. To study for the model that exhibits two phase transitions, we compare the picture with respect to the zeros from different transition arc.

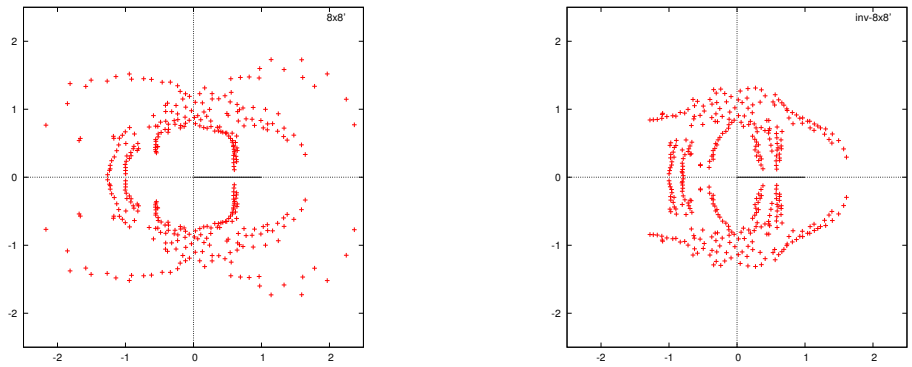

(a) (b)

Figure 8.6: Zeros distribution for a) $x = e^{\beta J}$ and b) $\tilde{x} = e^{-\beta J}$ with $\chi = (3, 2, 0)$.

Figure 8.6 presents the zeros distributions of x and $\tilde{x}$ for $\chi = (3, 2, 0)$. For the first quadrant in range $(1, \infty)$, we call from left, the curve approaching the positive real axis as the first curve and then followed by the second curve. The first curve in the Figure 8.6a corresponds to the second curve at range $(0, 1)$ in Figure 8.6b. Similarly, the second curve in Figure 8.6a corresponds to the first curve in Figure 8.6b.

Eventually, the two lines in the $(0, 1)$ region (in Figure 8.6b) will touch the real axis at the limit. The zeros for the first transition is taken from the second curve and the zeros for the second transition phase is taken from the first curve of the Figure 8.6a.

Figures 8.7 through 8.10 will present the winding diagrams of the accumulated summations of the partition function for the Z_5-symmetric model on 8 by 8 square lattice with three different values of χ and x.

Let $r = |x|$ be the magnitude of x. If we approximate the x value by this magnitude i.e. $x = r$, the polynomial term accumulated summations will always grow and positive. The largest length between two neighbouring terms is contributed by the same degree of Hamiltonian $\mathcal{H}$ when $x = a + b\,i$. All the contributions are affected by the energy and entropy of the system.

Let M be the degree of the polynomial Z. The degree of the polynomial

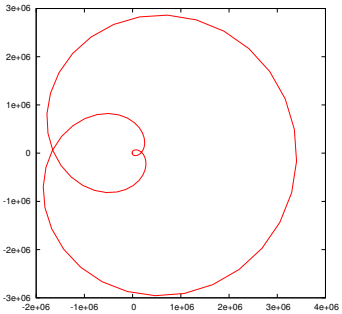

(a) x_1: longest length: 64

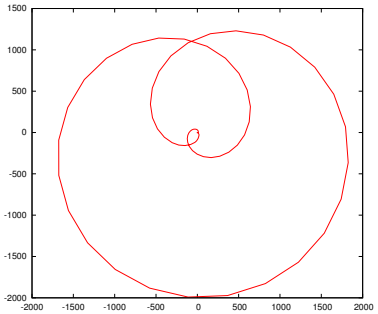

(b) x_2: longest length: 35

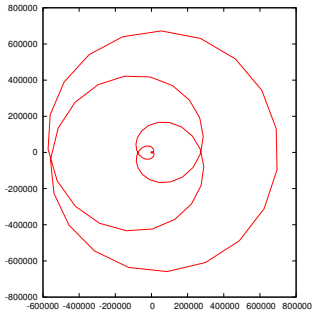

(c) x_3 : longest length: 60

Figure 8.7: Z_5-symmetric model on 8 by 8 square lattice with $\chi = (2, 1, 0)$: a) $x_1 = 2.10969 + 0.479109\, I$, b) $x_2 = 2.42248 + 0.665705\, I$ and c) $x_3 = 2.07525 + 0.734082\, I$.

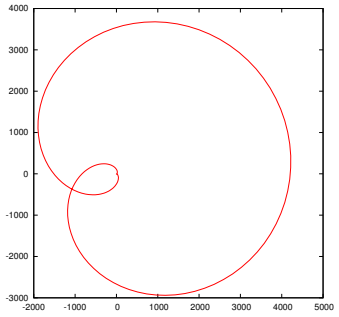

(a) x_1: longest length: 88

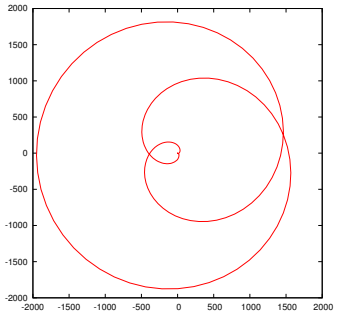

(b) x_2: longest length: 86

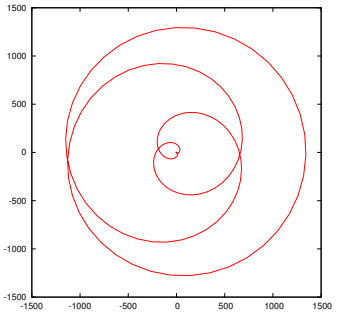

(c) x_3: longest length: 84

Figure 8.8: Z_5-symmetric model on 8 by 8 square lattice with $\chi = (3, 1, 0)$: a) $x_1 = 1.62980 + 0.137975\, I$, b) $x_2 = 1.62659 + 0.205334\, I$ and c) $x_3 = 1.61877 + 0.270632\, I$.

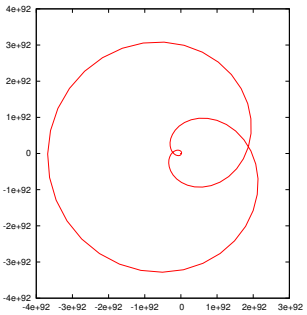

(a) x_1: longest length: 86

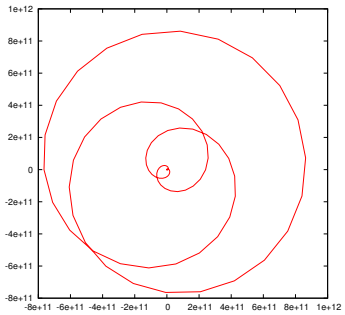

(b) x_2: longest length: 89

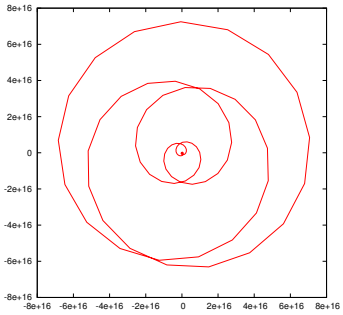

(c) x_3: longest length: 117

Figure 8.9: First curve: Z_5-symmetric model on 8 by 8 square lattice with $\chi = (3, 2, 0)$: a) $x_1 = 1.64360 + 0.334788\,I$, b) $x_2 = 1.58838 + 0.476209\,I$ and c) $x_3 = 1.37846 + 0.546351\,I$.

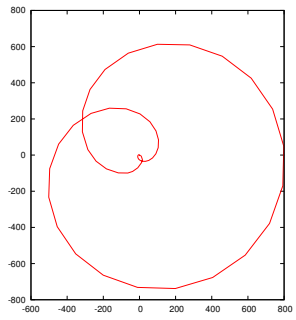

(a) x_1: longest length: 26

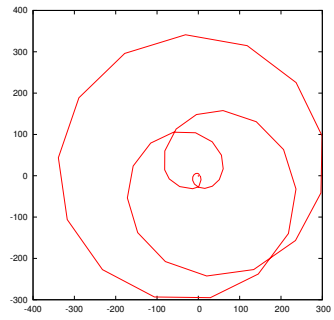

(b) x_2: longest length: 25

Figure 8.10: Second curve: Z_5-symmetric model on 8 by 8 square lattice with $\chi = (3, 2, 0)$: a) $x = 2.36582 + 0.771200\,I$ and b) $x = 2.24748 + 0.114699\,I$.

partition function for the 8 by 8 square lattice with $\chi = (3, 2, 0)$ is equal to 360. In general, let a square lattice have N_y row and N_x column vertices with open horizontal and periodic vertical boundary conditions. Take the energy list denoted as $\chi = (\chi_1, \chi_2, ..)$. Then the degree of the polynomial is given by

$$M = \chi_1(2N_xN_y - N_y).$$

For any $m_i < M \in \mathbb{N}$, let $(0, m_1)$ be the first range consists of m_1+1 terms. Next, the (m_1+1, m_2) be the second range consists of m_2-m_1 terms. Then $(m_2+1, M/2)$ be the third and so on. This categorisation can be illustrated as below:

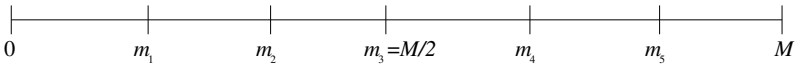

Figure 8.11: Polynomial range categorisation for $\tilde{x}$.

The first term with zero degree is in the ferromagnetic state where all spin variables point in the same direction. No energy penalty gives zero degree in the polynomial. The second part is where the energy penalty increases. The energy penalty is represented by the non-zero degree of the polynomial. The middle part of the polynomial is the range where the system is in a random and completely disordered state. This part has the highest number of entropy. The final part is again the ordered part of antiferromagnetic state. Each spin variable prefers to point in different direction from its neighbours.

For $\chi = (2, 1, 0)$ and $\chi = (3, 1, 0)$, their zeros distributions suggest the existence of a single phase transition. The largest contributions for the terms cancellation towards zero value are described in the Figures 8.7 and 8.8. The largest contribution for both cases have small degree exponent.

We claim that the term that gives the largest contribution marks the occurrence of a phase transition. With the high number of spin directions for $Q = 5$, the system can be in total disordered state even with small energy penalty. The observations for both cases of $\chi = (2, 1, 0)$ and $\chi = (3, 1, 0)$ are similar to the 2-state Potts model which also exhibit only one phase transition.

The $\chi = (3, 2, 0)$ in addition is another example for the Z_5-symmetric model. For this case, there exist a possible multiple phase transitions shown by the double curve in the ferro region of the zeros distribution. The largest contributions for 5 different zeros in this case fall into two different ranges of polynomial terms. Figures 8.9 and 8.10 show the diagrams for the zeros taken from the first and second curve of zeros distribution with $x = e^{\beta J}$, respectively.

The largest contribution for the zeros in second curve falls in the early part of the polynomial. The degree of the polynomial term is small suggesting a little disorder for the zeros in the second curve. In contrast, the largest contribution for the zeros in the first curve falls into the part that is closer to the middle part of the polynomial. This behaviour suggests a different kind of disordered phase will emerges.

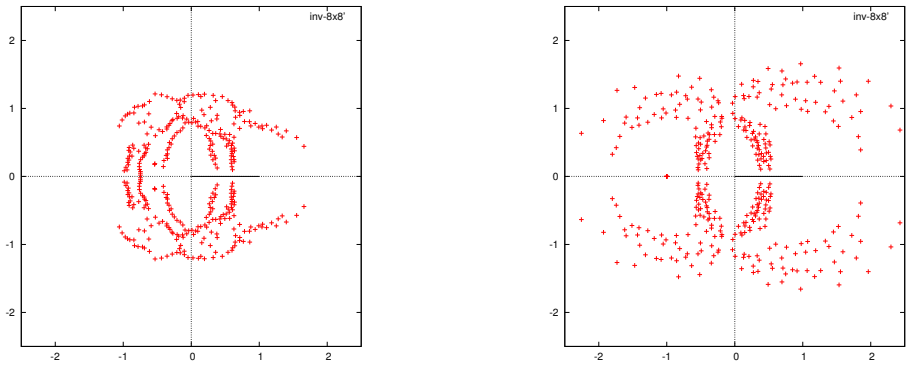

(a) (b)

Figure 8.12: Zeros distribution for $\tilde{x} = e^{-\beta J}$ with a) $\chi = (3, 2, 0, 0)$ and b) $\chi = (3, 2, 1, 0)$.

The Figures 8.14 through 8.19 present the accumulated summations graphs for the Z_6-symmetric model. The case with $\chi = (2, 1, 0, 0)$ in Figure 8.14 is believed to exhibit only one phase transition based on the comparison of its zeros distribution and the graph of specific heat (shown in § 8.4).

See Figures 8.14a and 8.14b. In both cases, their typical energy fall approximately in the same energy range. In contrast, Figure 8.14c shows different

value for its large term contribution. Since we know that this case only has one transition point, we know that this different is due to the finite effect on the zeros value. The third zeros lies off the curve in the zeros distribution as compared to the first and second zeros (see Figure 8.13).

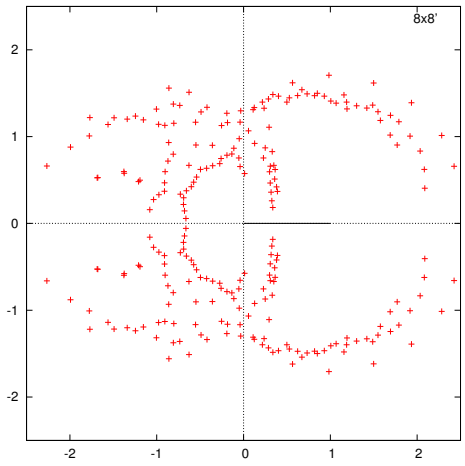

Figure 8.13: Zeros distribution for $x = e^{\beta J}$ with $\chi = (2, 1, 0, 0)$.

The case with $\chi = (3, 1, 0, 0)$ in Figure 8.16 also shows the existence of one phase transition based on its zeros distribution in complex plane. All the three largest term contributions are approximately in the same degree range.

For $\chi = (3, 2, 0, 0)$, this case is another example which exhibits two phase transitions. See Figure 8.15. The existence of two curves in the ferro region near the positive real axis gives evidence of this claim (see Figure 8.12). The graph of accumulated summations for the zeros in the first curve is shown in Figure 8.17 and the second curve is shown in Figure 8.18 .

For $\chi = (3, 2, 1, 0)$ the first and second zeros fall into approximately the same energy range. However for the third zeros the largest contribution is given by energy penalty at term $\tilde{x}^{32}$. This distribution may be either because of the finite size effect on its zeros distribution or due to the existence of multiple transitions. To exactly check this observation, a bigger lattice is needed for investigation, i.e. $N > 8$.

In the thermodynamic limit, we expect the largest terms contribution will be given by a significant value as compared to the contributions from other terms

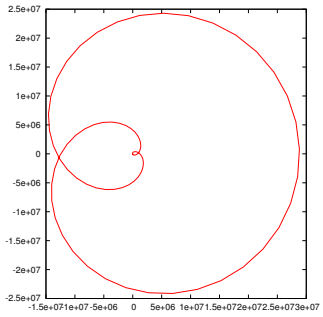

(a) x_1: longest length: 73

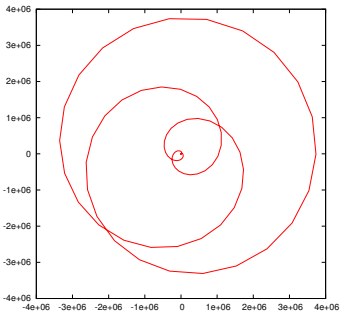

(b) x_2: longest length: 68

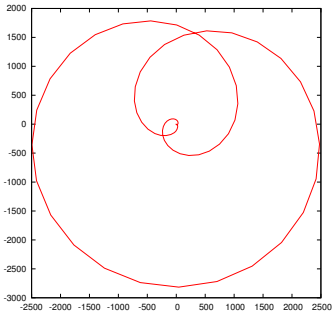

(c) x_2: longest length: 36

Figure 8.14: Z_6-symmetric model on 8 by 8 square lattice with $\chi = (2, 1, 0, 0)$: a) $x = 2.08847 + 0.405804\,I$, b) $x = 2.08267 + 0.622161\,I$ and c) $x = 2.42583 + 0.658524\,I$.

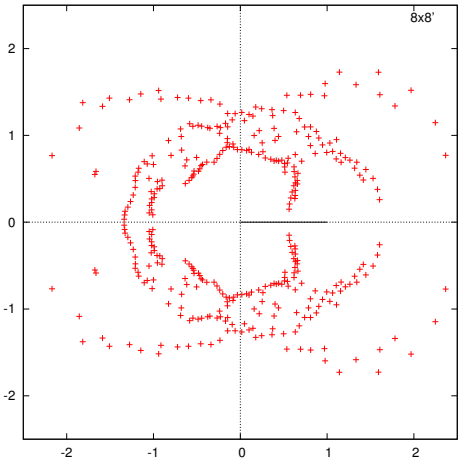

Figure 8.15: Zeros distribution for $x = e^{\beta J}$ with $\chi = (3, 2, 0, 0)$.

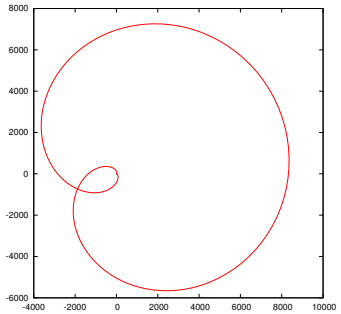

(a) x_1: longest length: 100

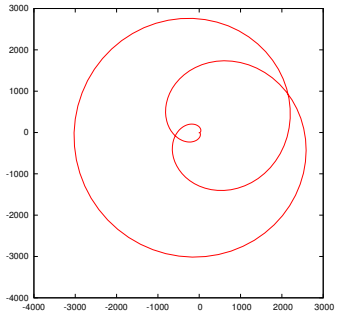

(b) x_2: longest length: 94

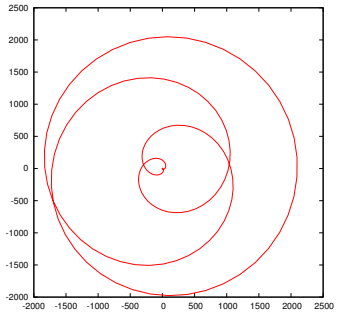

(c) x_2: longest length: 92

Figure 8.16: Z_6-symmetric model on 8 by 8 square lattice with $\chi = (3, 1, 0, 0)$: a) $x = 1.64122 + 0.123280\,I$, b) $x = 1.64234 + 0.186484\,I$ and c) $x = 1.63573 + 0.247940\,I$.

in the polynomial. This feature will differentiate the largest term contribution at thermodynamic limit as compared to the finite case.

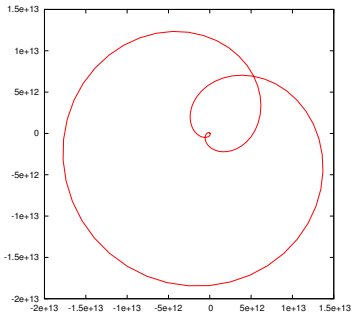

(a) x_1: longest length: 132

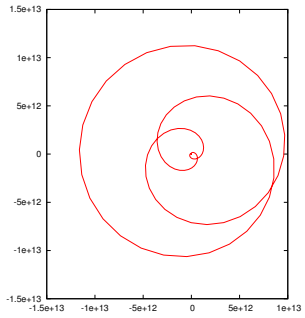

(b) x_2: longest length: 102

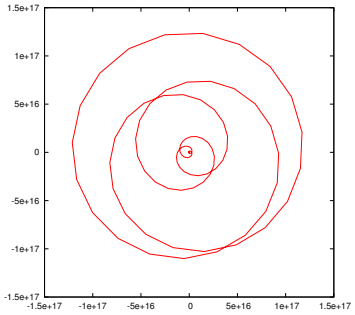

(c) x_2: longest length: 102

Figure 8.17: First curve: Z_6-symmetric model on 8 by 8 square lattice with $\chi = (3, 2, 0, 0)$: a) $x = 1.60486 + 0.259279\,I$, b) $x = 1.58125 + 0.37801\,I$ and c) $x = 1.41710 + 0.486042\,I$.

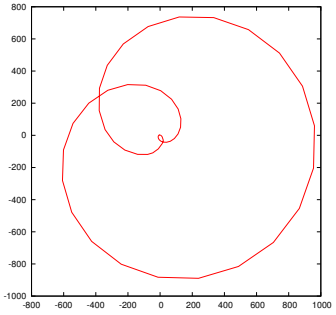

(a) x_1: longest length: 25

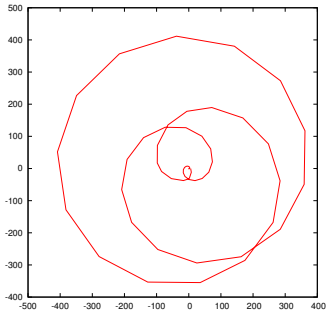

(b) x_2: longest length: 26

Figure 8.18: Second curve: Z_6-symmetric model on 8 by 8 square lattice with $\chi = (3, 2, 0, 0)$: a) $x = 2.36594 + 0.771063\,I$ and b) $x = 2.2475 + 1.14668\,I$.

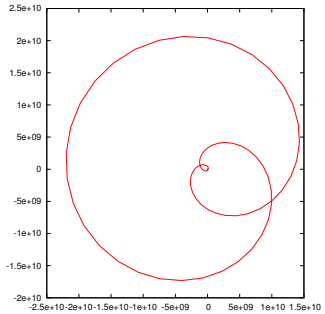

(a) x_1: longest length: 85

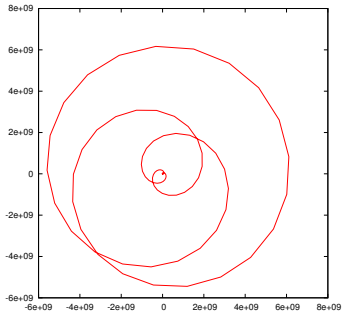

(b) x_2: longest length: 83

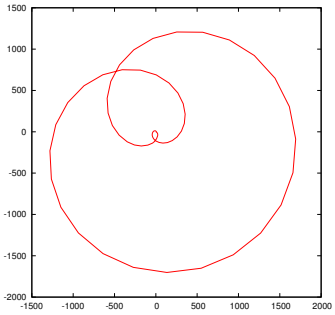

(c) x_2: longest length: 32

Figure 8.19: Z_6-symmetric model on 8 by 8 square lattice with $\chi = (3, 2, 1, 0)$: a) $x = 1.85197 + 0.390385\,I$, b) $x = 1.81864 + 0.584863\,I$ and c) $x = 2.43082 + 0.682177\,I$.

8.4 Graph comparison of specific heat

In this section we present a list of graphs for specific heat formula that are generated from the partition function.

At constant volume V, a specific heat is defined by the amount of heat $\tilde{Q}$ required to increase a temperature T, i.e. $C_V = \left(\frac{\partial \tilde{Q}}{\partial T}\right)_V$. In statistical mechanics, the specific heat equation can be generated from the partition function (see § 1.3). The specific heat is given by

$$\frac{C_V}{k_B} = -\beta^2 \frac{d^2 \ln Z}{d\beta^2}.$$

A sudden peak in the graph of specific heat over β is the signal of phase transition [7, 35]. A discontinuous peak at thermodynamic limit is due to the discontinuity of the second derivative of free energy.

We present the specific heat graphs for the 2- and 3-state Potts models and also the Z_5- and Z_6-symmetric models for some energy list χ.

8.4.1 2- and 3-state Potts models' specific heat

Figure 8.20 shows the graph of specific heat for the 2-state Potts model on the square lattice with size $N = 16, 18$ and 20. From this plot, as the size increases the peak of the graph also increases and the graph become steeper.

Similarly, Figure 8.21 shows the specific heat graph for the 3-state Potts model on the square lattice of size $N = 12, 13$ and 15. Here the sharp peak in the graph increases as the size increases. This behaviour in the middle of the graph is similar to the 2-state Potts model. However the peak shown here is given by a smaller lattice size as compared to the 2-state case. At infinite size, the peak is expected to be discontinuous at β_c that is at the critical temperature T_c of phase transition. The single peak is in accordance with the prediction of the single transition through the existence of a particular single curve in the graph of zeros distribution in the complex plane. The specific heat graph support this single transition claim.

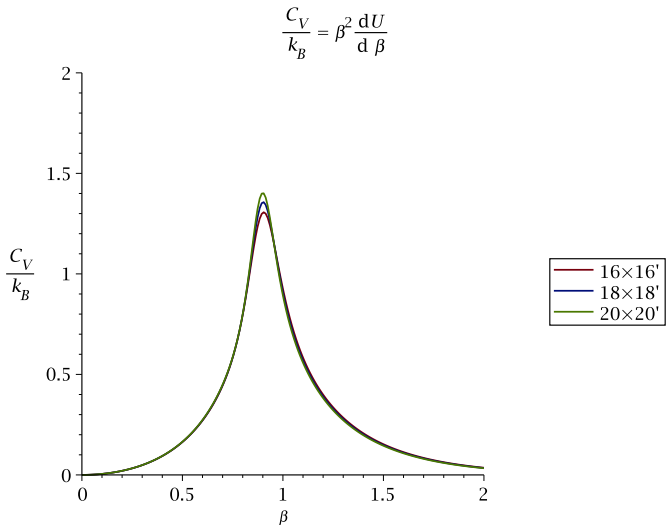

Figure 8.20: Specific heat plot for $\frac{C_V}{k_B}$ vs β with $N = 16, 18, 20$.

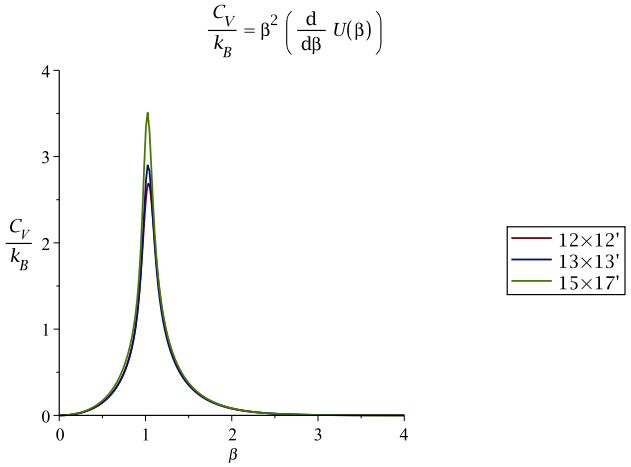

Figure 8.21: Specific heat plot for $\frac{C_V}{k_B}$ vs β with $N = 12, 13, 15$.

8.4.2 Z_5- and Z_6-symmetric models' specific heat

Here we continue with the specific heat graph for the Z_Q-symmetric model with $Q = 5$ and 6 for some value of χ.

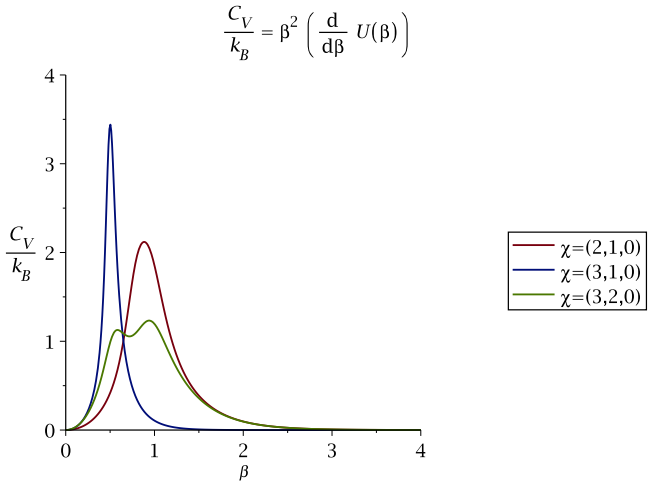

(a)

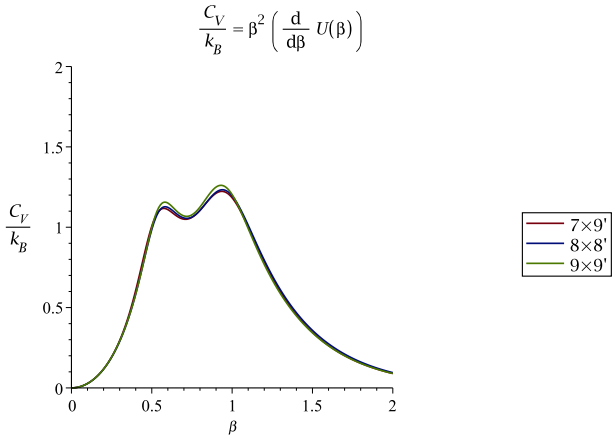

(b)

Figure 8.22: Z_5-symmetric model: Specific heat graph for a) 8×8 with different χ and b) $7 \times 9, 8 \times 8, 9 \times 9$ for $\chi = (3, 2, 0)$.

Figure 8.22 shows the specific heat graph for Z_5-symmetric model with three

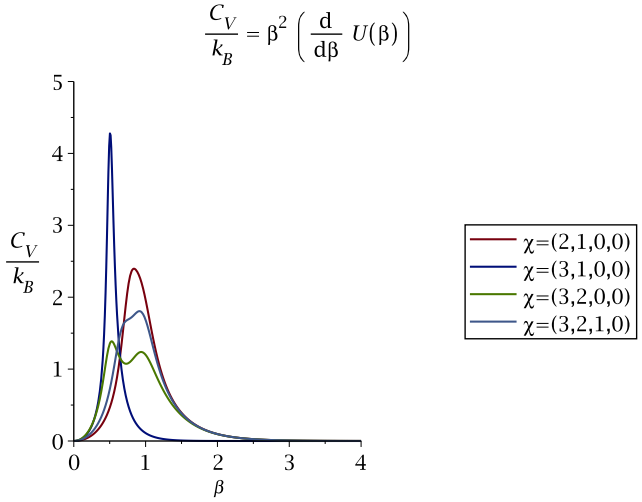

(a)

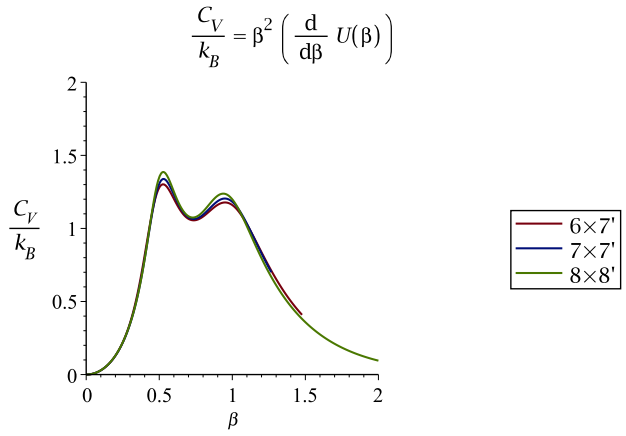

(b)

Figure 8.23: Z_6-symmetric model: Specific heat graph on square lattice a) 8×8 with different χ and b) $6 \times 7, 7 \times 7, 8 \times 8$ for $\chi = (3, 2, 0, 0)$.

energy list $\chi = (2, 1, 0), (3, 1, 0)$ and $(3, 2, 0)$. We can see the different peak behaviour among these three χ values. For the $\chi = (2, 1, 0)$ and $\chi = (3, 1, 0)$, the single peak suggests a single phase transition whereas for the $\chi = (3, 2, 0)$ the two peaks suggest two phase transitions. Figure 8.22b presents the graph for $\chi = (3, 2, 0)$ for three increasing lattice size $N = 7, 8, 9$.

We further consider the case of Z_6-symmetric model. Figure 8.23 presents the graph of specific heat with $\chi = (2, 1, 0, 0), (3, 1, 0, 0), (3, 2, 0, 0), (3, 2, 1, 0)$. The specific heat curves for $\chi = (2, 1, 0, 0)$ and $\chi = (3, 1, 0, 0)$ each has only single peak that corresponds to single transition.

The graph for $\chi = (3, 2, 1, 0)$ however has a peak which is not entirely sharp. As shown in the zeros distribution, it has a possibility of either single or double curve move closer to the positive real axis. A bigger lattice is needed to describe this case correctly.

The graph for $\chi = (3, 2, 0, 0)$ in contrary shows obvious multiple peaks. These two peaks are the evidence for two phase transitions. This observation is in accordance with the multiple curves in the positive real axis of its zeros distribution. We plot for this case with different lattice size as in Figure 8.23b. The bigger the size, the sharper the peak will be.

8.5 Discussion

The study of polynomial terms of partition function is aimed to find the largest term contribution of this function. This term is believed to have the most domination over the cancellation of magnitude in its partition function. The largest contribution will suggests a typical energy penalty that exists near the transition point.

As expected, the first kind of transition is just between the ordered and disordered phases. The largest contribution is represented in the region just after the fully ordered state represented by the constant term of the polynomial. Then we can see that the zeros in the second curve has the largest contribution somewhere

between the first disordered state and the middle part of the polynomial. Here the energy penalty is high given by many edges in the dual lattice. This observation suggests a different kind of disordered phase will starts to emerge soon afterwards. We illustrate these phases in Figure 8.24.

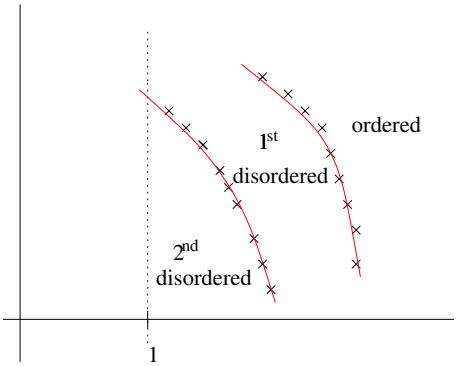

Figure 8.24: Ordered-disordered states illustration (not scaled).

The distinction between these two kind of disordered phases will be more obvious at large lattice and certainly at the thermodynamic limit. The graph of specific heat meanwhile shows the existence of phase transition through the peak in the graph.

The study of the polynomial term contribution support the determination of the multiple phase transitions. The study provides one more detail about the system i.e. the typical energy represented by the largest term contribution for $Z = 0$.

For the second phase transition however, it is not enough to determine the existence only based on the change in the details of configuration state. The Peierls' argument must be implemented again to support the existence of the second phase transition.

This problem is still open − no equivalent to Peierls' argument that prove the existence of two transitions. The possibility is evidence in the zeros distribution especially for Z_5- and Z_6-symmetric model. This observation is supported by the behaviour in the graph of specific heat.

Conclusion

We have studied the partition functions and their zeros for Ising, Q-state Potts and Z_Q-symmetric models on several crystal lattices. The zeros are plotted in complex Argand plane to study the analytic structure of the zeros distributions. Our research supports the claim that this structure suggests the behaviour of physical observables at thermodynamic limit related to phase transition.

The study of zeros distribution give the approximation of the physical critical exponent value. We can also simultaneously study the analytic structure at ferromagnetic and antiferromagnetic phases.

We may be able to exactly predict the locus of zeros if we can reach large enough lattice size. For the moment, although it is very interesting to further extend the zeros distribution to larger cases, the computing resources in hand is limiting our study. The implementation of parallel computing is one option for improvement.

Appendices

A Algorithm for zeros finding

The Newton-Raphson (NR) method is a numerical algorithms for finding roots of polynomial equation. The complex roots of partition function when $Z = 0$ are found using this method.

Let $n \geq 0$ and let the number of iterations x_n be the estimated zeros at iteration n and f be the polynomial function. Then the NR method is performed by the following iterative formula;

$$x_n = x_{n-1} - \frac{f(x_{n-1})}{f'(x_{n-1})}. \tag{A.1}$$

Theorem A.1. *Given a positive integer $n \geq 1$ and any choice of coefficients $a_0, a_1, ..., a_n \in \mathbb{C}$, such that $a_n \neq 0$, define the function $f : \mathbb{C} \to \mathbb{C}$ by setting*

$$f(z) = a_n z^n + ... + a_1 z + a_0, \forall z \in \mathbb{C}.$$

In other words, f is a polynomial function of degree n. Then

1. given any complex number $w \in \mathbb{C}$, we have that $f(w) = 0$ if and only if there exists a polynomial function $g : \mathbb{C} \to \mathbb{C}$ of degree $n - 1$ such that

$$f(z) = (z - w)g(z), \forall z \in \mathbb{C}.$$

2. there are at most n distinct complex numbers w for which $f(w) = 0$. In other words, f has at most n distinct roots.

3. (Fundamental Theorem of Algebra, restated) there exist exactly $n+1$ complex numbers $w_0, w_1, ..., w_n \in \mathbb{C}$ (not necessarily distinct) such that

$$f(z) = w_0(z - w_1)(z - w_2)...(z - w_n), \forall z \in \mathbb{C}.$$

In other words, every polynomial function with coefficients over $\mathbb{C}$ can be factored into linear factors over $\mathbb{C}$.

For numerical computation, let TOL be the predetermined tolerance (or estimated error) and x_0 be the initial value. The NR method calculate the

zeros of polynomial by iteration up to the predetermined stopping condition, i.e. $|x_n - x_{n-1}| < \text{TOL}$.

Let n be the degree of partition function $Z = \sum_{i=0}^{n} a_j x^j$ where a_j is the polynomial coefficient. Let f be a differentiable function $f : \mathbb{R} \to \mathbb{R}$ and f' is the derivative of f. Take function $f = Z$.

Let x_0 be the initial guess and x^* be the approximated solution to the equation $P_i(x) = 0$. The algorithms below summarise the steps taken for the computation of Newton-Raphson method. Let TOL$= 10^{-300}$.

Algorithm A.2. (Newton-Raphson method).
INPUT polynomial f, degree n, initial value x_0, tolerance TOL
OUTPUT zeros x^*
STEPS
1. For k from 0 to ... do Step 2 and 3.
2. Compute

$$x_{k+1} = x_k - \frac{f(x_k)}{f'(x_k)}.$$

3. If $|x_{k+1} - x_k| <$TOL, then set $x^* = x_{k+1}$. Exit k loop.

Algorithm A.3. (Zeros of Polynomial with refinement).
INPUT polynomial f, degree n, tolerance TOL
OUTPUT Zeros x^*
STEPS
1. Set initial value x_0 and $P_0(x) = f(x)$.
2. For i from 0 to $n - 1$ do Steps 3 through 9.
3. Do Newton-Raphson method (A.2).
4. Refinement. Set $x_0 = x^*$ and $f(x) = P_0(x)$.
5. Do Newton-Raphson method (A.2).
6. Set $\overline{x^*}$ be the complex conjugate of x^*.
7. Deflation. Compute for new P_{i+1}

$$P_{i+1} = \frac{P_i}{(x - x^*)(x - \overline{x^*})}.$$

8. Set $i = i + 1$.
9. Set new initial guess $x_0 = x^*$.
10. Stop

A.1 On error estimation

Here we state some challenges we have faced in computing the partition function and its zeros.

Let the initial value x_0 be a complex number $x_0 = a + bi$, $a, b \in \mathbb{R}$. It is known that as the number of iterations n increases, the rounding error is also expected to increase.

To reduce the error and at the same time increase the accuracy of the calculation, a computational library known as GNU multiple precision (GMP) [102] is used in all the programming code. The GMP is a library with unlimited precision arithmetic. It allows the computer to perform many computations with large values − exceed the standard integer range predetermined by ordinary computer. However, this library increases the usage of computer memory very rapidly. Thus, bigger memory is needed for large computation.

A.2 Refinement and convergence

To increase the accuracy of the roots finding, we add one more step to refine our approximation. Let Z_G be a partition function of graph G. Let P_i be a polynomial function where $i = 0, 1, 2, ...$ and set $P_0 = Z_G$. Denote x_i as the approximated zero for P_i. For every approximated zeros x_i, we take new deflated polynomial

$$P_{i+1} = \frac{P_i}{x - x_i}$$

for $i = 0, 1, ...n - 1$ and n is the degree of Z_G.

Theorem A.4 (The Complex Conjugate Root Theorem)**.** *Let $f(z)$ be a polynomial with real coefficients. Suppose $a + bi$ is a complex root of the equation $f(z) = 0$, where a and b are real and $b \neq 0$. Then $a - bi$ is also a root of the equation.*

Proof. Let the polynomial $f(z)$ as below

$$\begin{aligned} f(z) &= a_0 + a_1 z + a_2 z^2 + ... + a_n z^n \\ &= \sum_{r=0}^{n} a_r z^r = 0 \end{aligned}$$

where all a_r are real. Then

$$\begin{aligned}
\overline{f(z)} &= \overline{\sum_{r=0}^{n} a_r (z)^r} = \overline{0} \\
&\sum_{r=0}^{n} \overline{a_r (z)^r} = 0 \\
&\sum_{r=0}^{n} \overline{a_r} (\overline{z})^r = 0 \\
&\sum_{r=0}^{n} a_r (\overline{z})^r = 0 \\
&f(\overline{z}) = 0.
\end{aligned}$$

Therefore, the zeros appear to be in conjugate pair. □

By the complex conjugate root theorem A.4, for any polynomial with complex zero, its complex conjugate is also a zero of the polynomial. For each P_i, the NR method is implemented to find the remaining zeros.

For refinement, the NR method is implemented on the original Z_G. At each P_i when $i > 0$, we take the approximated zero x_i' as the initial value for NR method on Z_G. The new root from this step is accepted as the new approximated zero x_i of Z_G. This step is repeated each time we find the root for the polynomial P_i.

At some condition, we may have a convergence problem when there exist two or more zeros located very close together or when there exist zeros with multiplicity greater than 1. The existence of real zeros may also contribute to the problem. Thus it is worth to check the possible real zeros from the beginning of the computation.

For the case where two or more zeros are close together, we can choose different initial value after some number of iterations where it can redirect the program to compute the zeros finding. A lot of checking need to be done in order to detect this.

B Onsager's solution

We present the Onsager's solution using rotational matrix approach as discussed by Kaufman in [40].

Note that the horizontal and vertical nearest neighbour interaction for the square lattice can be represented by rotational matrix

$$M_R(\theta) = \begin{pmatrix} \cos(\theta) & \sin(\theta) \\ -\sin(\theta) & \cos(\theta) \end{pmatrix}$$

where the $\det(M_R(\theta)) = 1$, so the complex eigenvalues are $\exp(\pm i\theta)$.

Denote W as the rotational matrix and $W_{ab}(\theta)$ be the matrix rotation in ab-plane. For any i and $2N$ dimensions of rotational matrix, let

$$w_{ii+1}(\theta) = \mathbb{1}_{i-1} \oplus M_R(\theta) \oplus \mathbb{1}_{2N-i-1}.$$

The idea is to replace the product of $V_1 = \left(\prod_{i=1}^{N} t_i\right)$ and $V_2 = \left(\prod_{i=1}^{N} t_{i(i+1)}\right)$ (from (4.2)) by a matrix rotation $W = W_1 W_2$. The W_1 and W_2 are rotational matrices given by

$$W_1 = \prod_{i=1}^{N} w_{2i\,2i-1}(2i\theta)$$

and

$$W_2 = \prod_{i=1}^{N} w_{2i+1\,2i}(2i\theta').$$

Let $c = \cos(2i\theta), c' = \cos(2i\theta'), s = \sin(2i\theta)$ and $s' = \sin(2i\theta')$. For example, if $N = 4$,

$$W_1 \;=\; w_{12}w_{34}w_{56}w_{78} = \begin{pmatrix} c & s & & & & & & \\ -s & c & & & & & & \\ & & c & s & & & & \\ & & -s & c & & & & \\ & & & & c & s & & \\ & & & & -s & c & & \\ & & & & & & c & s \\ & & & & & & -s & c \end{pmatrix}$$

$$W_2 = \begin{pmatrix} c & & & & & & & -s \\ & c & s & & & & & \\ & -s & c & & & & & \\ & & & c & s & & & \\ & & & -s & c & & & \\ & & & & & c & s & \\ & & & & & -s & c & \\ s & & & & & & & c \end{pmatrix}.$$

Then

$$W = W_1 W_2 = \prod_i^{2N} w_{a_i b_i}(\theta_i) \tag{B.2}$$

where all $\{a_i, b_i\}$ are distinct. Let $z = e^{\frac{2\pi ik}{N}}$ so $z^N = 1$. Since the dimension of a rotational matrix is smaller than the dimension of transfer matrix $\mathcal{T}$, the problem of finding the eigenvalue for partition function is reduced to only for finding the eigenvalue of the corresponding rotational matrix.

Using Fourier transform, we define vector

$$f_z = \begin{pmatrix} 1 \\ z^2 \\ z^4 \\ z^6 \\ \vdots \\ z^{2N-2} \end{pmatrix}$$

where $v_z = f_z \otimes \begin{pmatrix} 1 \\ 0 \end{pmatrix}$ and $v'_z = f_z \otimes \begin{pmatrix} 0 \\ 1 \end{pmatrix}$.

Then

$$\begin{aligned} W_1 \begin{pmatrix} v_z \\ v'_z \end{pmatrix} &= \begin{pmatrix} c & -s \\ s & c \end{pmatrix} \begin{pmatrix} v_z \\ v'_z \end{pmatrix}, \\ W_2 \begin{pmatrix} v_z \\ v'_z \end{pmatrix} &= \begin{pmatrix} c' & -zs' \\ -z^{-1}s' & c' \end{pmatrix} \begin{pmatrix} v_z \\ v'_z \end{pmatrix} \end{aligned}$$

and

$$W \begin{pmatrix} v_z \\ v'_z \end{pmatrix} = \begin{pmatrix} cc' + ss'z^{-1} & cs'z - sc' \\ -cs'z^{-1} + sc' & ss'z + cc' \end{pmatrix} \begin{pmatrix} v_z \\ v'_z \end{pmatrix} \tag{B.3}$$

where we denote image of W as $W^{(z)} = \begin{pmatrix} cc' + ss'z^{-1} & cs'z - sc' \\ -cs'z^{-1} + sc' & ss'z + cc' \end{pmatrix}$. Since the $det(W^{(z)}) = 1$, we write the eigenvalues as $\lambda_\pm = e^{\pm l_z}$.

For example, suppose we have an Ising model on N by M square lattice. From Martin [58] and Valani [92], the transfer matrix have the largest magnitude of

eigenvalue given by λ_0

$$\lambda_0 = \exp\left(\frac{1}{2}\sum_{k=1}^{N} l_{e^{2i\pi k/N}}\right). \tag{B.4}$$

Denote $\lambda = \lambda_0$. The eigenvalues of rotational matrix are e^{l_z} and e^{-l_z}. Then by the relation between the transfer matrix and the rotational matrix, the sum of eigenvalues is equal to the trace of $W^{(z)}$ [84, p. 249]

$$e^{l_z} + e^{-l_z} = 2\left(\cos(2i\theta)\cos(2i\theta') + \frac{z+z^{-1}}{2}\sin(2i\theta)\sin(2i\theta')\right).$$

For large M, the partition function

$$Z_{NM} \sim \lambda^M. \tag{B.5}$$

Using identities $\cosh(x) \equiv \dfrac{e^x + e^{-x}}{2}, \cosh(x) \equiv \cos(ix)$ and $\sinh(x) \equiv i\sin(ix)$, we have

$$\cosh(l_z) = \cosh(2\theta)\cosh(2\theta') - \frac{z+z^{-1}}{2}\sinh(2\theta)\sinh(2\theta') \tag{B.6}$$

where l_z is the solution for the eigenvalue (B.4). Using identities $\sinh(2\theta') = \sinh(2\theta)^{-1}$ and $\coth(2\theta') = \cosh(2\theta)$ in isotropic case $\theta = \theta'$ gives

$$l_z = \cosh^{-1}\left(\coth(2\theta')\cosh(2\theta') - \frac{z+z^{-1}}{2}\right).$$

Again, using identity for simplification that is

$$\begin{aligned}\cosh^{-1} x &= \ln(x) + \frac{1}{\pi}\int_0^{\pi} \ln(1 + x\cos y)\, dy \\ &= \frac{1}{\pi}\int_0^{\pi} dy \ln(2x - 2\cos y),\end{aligned}$$

this gives

$$\begin{aligned}l_z &= \frac{1}{\pi}\int_0^{\pi} \ln\left(2\big(\coth(2\theta')\cosh(2\theta') - \frac{z+z^{-1}}{2}\big) - 2\cos y\right) dy \\ l_{e^{2i\pi k/N}} &= \frac{1}{\pi}\int_0^{\pi} \ln\left(2\coth(2\theta')\cosh(2\theta') - 2\cos(2\pi k/N) - 2\cos y\right) dy.\end{aligned}$$

Substitute this into Equation (B.4), we get

$$\ln\lambda = \frac{1}{2}\sum_{k=1}^{N}\frac{1}{\pi}\int_0^{\pi} dy \ln\big(2\coth(2\theta')\cosh(2\theta') - 2\cos(2\pi k/N) - 2\cos y\big). \tag{B.7}$$

The above integral can be discretise using the following sum;

$$\int_0^{\pi} f(y)\,dy \sim \frac{\pi}{M}\sum_{r=1}^{M} f(\pi r/M). \tag{B.8}$$

Therefore, we have

$$\begin{aligned}
\ln\lambda &\sim \frac{1}{2}\sum_{k=1}^{N}\frac{2}{M}\sum_{r=1}^{M}\ln\big(2\coth(2\beta)\cosh(2\beta)-2\cos(2\pi k/N)-2\cos(2\pi r/M)\big)\\
&= \sum_{k=1}^{N}\frac{1}{M}\ln\prod_{r=1}^{M}\big(2\coth(2\beta)\cosh(2\beta)-2\cos(2\pi k/N)-2\cos(2\pi r/M)\big)\\
&= \frac{1}{M}\ln\prod_{k=1}^{N}\prod_{r=1}^{M}\big(2\coth(2\beta)\cosh(2\beta)-2\cos(2\pi k/N)-2\cos(2\pi r/M)\big).
\end{aligned}$$

This gives

$$\lambda^M = \prod_{k=1}^{N}\prod_{r=1}^{M}\big(K-2(\cos(2\pi k/N)+\cos(2\pi r/M))\big) \tag{B.9}$$

where

$$K=\frac{(1+e^{-4\beta})^2}{e^{-2\beta}(1-e^{-4\beta})}. \tag{B.10}$$

Without loss of generality, we derive the partition function for the zeros distribution as

$$\begin{aligned}
Z_{NM} &\sim \lambda^M\\
&= \prod_{k=1}^{N}\prod_{r=1}^{M}\big(K-2(\cos(2\pi k/N)+\cos(2\pi r/M))\big).
\end{aligned} \tag{B.11}$$

For $y=e^{2\beta}$ and $C=\cos(2\pi k/N)+\cos(2\pi r/M)$, each factor in (B.11) can be written in a polynomial form when $Z=0$. We can find the zeros for each factor where

$$\begin{aligned}
K-2(\cos(2\pi k/N)+\cos(2\pi r/M) &= 0\\
e^{-8\beta}+2Ce^{-6\beta}+2e^{-4\beta}-2Ce^{-2\beta}+1 &= 0\\
y^{-4}+2Cy^{-3}+2y^{-2}-2Cy^{-1}+1 &= 0\\
y^4-2Cy^3+2y^2+2Cy+1 &= 0
\end{aligned} \tag{B.12}$$

for any N by M square lattice with $k=1,2,...,N$ and $r=1,2,...,M$.

C Coefficient of partition function

Here we present one example of partition function coefficient. The coefficient of 3-state Potts model on 15 by 17 square lattice is given below:

Degree	Coefficient
0	292747664813781057148613736814232155007103703449 6
1	250629094205791710036093951670291161267563721523200
2	112126344456763294560865233519942129088271652697478 40
3	348184989462262219267971485562991018963027441810479360
4	84154854497325899311301185214447906819142468711847483 20
5	16839477002061193779549454192299796048075725282728207 8560
6	2898888300548412776521260189674548404504296458442009489280
7	4406522817328446991610169744331184967687787434680932253 6880
8	6026378653307089929676700678107580681539281080409255073078 80
9	7520011885393468229004786042061947241324556272574374214729160
10	8655984585475022752081914396984065573314355125111351142778693 6
11	9270762139017311000464526049301951323589342760412449076033006 60
12	9304053571146475249632201637622822290138930599396359883251119080
13	8800572996820980642335157661331367959626984626455750550103397688 0
14	7883989939819970588432899353730783880590504003668256646701920048 00
15	6716923539551525044204187229564265113345069166504680890980577045340
16	5461606149431429110909392128051825681068190033835523452886258029621 0
17	4251330375101748474689840944548569178805817538678931917508234306855 50
18	3176454749506222370900295569501155646093838955639214738135013519909180
19	2283451637124050973619341588695467554033493388771521713222189963670665 0
20	1582604741182872570149537004857903127136182257556121704670740206985615 12
21	1059461968612007308753616751023841811139249768287439416508640747158192310
22	6861937772260283431932238556311772866637088053818399465509340549041877320
23	4306262569637582648472510238085891238280630685016050855987635389323782662 0
24	2621971668537258127837045860478221780470508958405116263410632666597411282 30
25	1550802727504766024575661523335210209991531405541991925065957411008282377742
26	8920030374995383068526620081731836581820868226772074028537823773008746926080
27	4994547288598574703421120748670484882962603139541722214255242314619181853615 0
28	2724886101309093558314844683883205650118486534848489579703322750059761613230 00
29	1449750383497213334245028046164511945019370685997826099605737517496433364857750
30	7527875258050685315104247944077419411841987985313952476143324535199998928786420
31	3817702414769916004313633874413946914333593784095523086268724514006088614662807 0
32	1892237257469276758455439651823983681713478958271928587580772150506957585100288 10
33	9172038714305950479878510491933651055939676568326262545066717772188996632451646 50
34	4350382268187902932099040874311827910877212701668962337103577621571908285736290430
35	2020217025907775115432580096938360329428793837418269737562777345617741640507359498
36	9189680423958532651794982978988135020150143559100644859029278711280500657162894591 0
37	4096788475591895717203871279125050503737226393491972501566156886933839955984827568 20
38	1790704303909575164172859002980213344947563327183834111052525241166541623971020729210
39	7677616653267073570778227224989480998166419981943087842970668382768273959248365198760
40	3230172340405590973986213340831390041116594272200752163863110427014925289130206070515 0
41	1334094398351487450222806381423852305771328495356694481363793526039178256447819452497 10
42	5410844041942696855410587785253357116977655674572011084616232588896735698281166377212 40
43	2155801926858579864066764969315862838542508828031213921589772034995881211817961440515500
44	8440307874294537521520790824136503745183084960624858839587966886237060677971248563885 20
45	3248227892643145347042773993803285193658988870522726105266451528769641232815219879605833 4
46	1229136474441677517266306124562662459249780292941515329777436159010945967973787660979591 20
47	4574458512569163802957163487499732464194450174685752470825308773686976809245406073536812 30
48	1674866271485273432805278809205619081827047817558166393275203231486791626494970582833371930
49	6034357296321008999534931967917909598290795096564203853869628192792527661154657090844953380

50 213991719372243667546504103738257371416758805983876235133365322850028710600301770174718504285
51 747098640902561591640606269561194404924249836391794326193246569724504429071623309183539210 10
52 256844077216258865312449757620081521505147050208653904012081071181001176747712746670611909140
53 869687615416246063680073912102885545489730244945974817753430057210634435279861312818842912670
54 290099350649970450748056950499275432299379803201129174608669056947644682803053046047924775 0750
55 953463203670742858471610914983263946894124033194934072622539184201102827309781457145887723654 0
56 308827060667107990357680968543001662205140993815613282201264130623786744916399729835340758957 20
57 985957620985981473105668790078830431656350936249135240141673453642623106876799528881292365635 40
58 3103178873909047792081383420972932244292126961681267125168665502815430843946268107155945495055 40
59 963013284127765163604367916475689470870303610194957136999619494580593246039146163419477396991790
60 294715596271936677527588746893651796440964755117575544907246372430549158076439842759063944634997 0
61 889580309963040702646850061196450847863984719309155068875133042876869919924862246378632655899491 0
62 264875459717005741499820175512937835702676196951280835681219410293974813162123233592537183345701 40
63 778096987484303441054970123811327517101488445352605370598815714245502542003375789845992795150742 90
64 225538062713975200655766905502351597142829877030933055069560607991176531065924723793940424719465 30
65 645143819305537832756243297592811647489366480074213941044171441382694276791946415088871772712341336
66 182137021311353106521966502496772677389267734355397420296914008708532596447499026427010937479295368 0
67 507571634097770936809605128154422361494863101087005264870786252102431487706337690005370408944991 4100
68 139638257496130625145568289584824939700875029425309494520536622583863599143004989131820169591615 39960
69 379287204251850444513547738762645035037667125210779842954403935967589094654449074660874186596886782 00
70 101726863059696719457755868893179928942764276482915961544791508702644766203599560750739408357357613746
71 269433840150602725377561198270872749270769360729751227502995577658380161886921461355295672627208545290
72 704792711107569185255828983281399009860304274752392828885648304813081410953762783711219499144553515130
73 182098204073988622572261066569567680192271377634772185066215640500675292968347744010243519164086328 6330
74 464756715990823745164801713880787429017678220450330420469492259859295884605210438271895228835814764 6050
75 117181968943050961639914411875165149423664429158561095305528952503793961514971073594107667586635136337 14
76 291910028010126635607767514927002246860681390088731352187409382409308945497490199973247655537422690940 60
77 718500459074021159034055323268029750584313220060550767459936952406270205363396417073681303930754289375 50
78 174755299398306723743312043649254599199196816501161206609612924912633771144241932322162348277685988320370
79 420042452928028410775302879941792514513072437334438778850726330848906273790940140281125089301018433174290
80 997811829018391595381380045856120712099869676601698624429555621283112973626615361657947228458560416247624
81 234276503598022860856165784071406374337229090217467641005859231443316644756405514601062176578879770430294 0
82 543706301381319514942785669970705862135220681696084778271811223590278842528780505818940573003468908541097 0
83 124734169237800017906780913461853917021527174993903905583125887425319030374082851228579107973726101341753 10
84 282892121396762753502751115441023588031895434535592634189799998496098040154738933914065021739375191034945 60
85 634305609399376396712395748541941599250173767101903748420475848193397557210271123874336027385275465112 3688
86 140619503868016947382004595088292019765763847386135731583049259038537501100772911844332474807170439366065430
87 308239304348617390841077467544927187977809619413188494616124853075691959323899212326455776157712999307716090
88 668114958146044942221313509013740763904480401037347088393857266092315323899947528725538091638372031723788220
89 143205452226689477025951947736033376894502151040014839964836630319784093431097875935197821478798941272197340
90 303554550742060446249181415510915913405856652604318352230149573445323321174594642325058527396570314323204106 4
91 636364099079556146258752984189436681720847352684063100247408089335369606896846621575922606593202592292303625 0
92 131943643296549763864554212515187872946966272593061072237834750851980692812623525834421344049757592549502289 0
93 270586789024134198651384233426639238070536786160473604661529280370799573867223596725727014443714142347948237820
94 548884253098134872854616983757497834850415507816229676480382057210731086928750468452418467235346691271779596 00
95 110136458021132849833875226246892130685652356365544309624731504279264440194591966120436536652212139925620699394
96 218613530431886539297046994044803721309096281029818957560902213208195060756179012619696848696896937630851127930
97 429276781362437651152228060282214313256023489249308143827391731548296149112024602588973398997453672439140517700
98 833931591195985304683701811486715370815971971752630434695304159144620595499691086262296029494817842212613595560
99 160277951835728151764437036999008590712157969456966944794586189294091197368942109444432245199963631501730741 0880
100 304778681940225738998365062235104023918021395452508677132506857115961888976722323125452704613602676953622429775 8
101 573428689342087295295473981224431001808301995340233070545945412176967203752180697456308642131104443177831967166 0
102 106751589424981893930864506755163767974860011567244749811623926766282172853079223964149026123680440764947814165 20
103 196645931921229625484467722239380280624391835120545437003752404897458149107890300808636856092289377247524957714 00
104 358448178045280216190520805256791065450018880032983634089833851791396797158399358535329591383693604035568031324 70
105 646566559665747234434836646442820078496208530863077664889410339115781626634618013416928506867032615964443771099 70
106 115414340328397574386338295916875100822432663276013229306056400549307567781057717295542550888015610958123810512 400
107 203882421926633523432737190270500856682614359493761590275116138493343617150332475107922409396234648750012144409040
108 356440195269863271632637843207580801485389849008189017792078315302327392952935082355134101720691668218406091836350
109 616727706328139223548455042842199764222435121105767016173492646358136760029061098527653331744467807507892971311 40

110 1056118852094698226680216855195661253533324717382595406241654230745879582793231075264981432065226550946311062227438
111 1790016276140849753296209510846435737754707186600624512123872891666409133988665132436808069604979900946648950584910
112 3002880011360252889405570024428136550500163409561869106538108140643350691053850328040941321082130959622543892685580
113 4986174087890595888703047977722043793805695412543360772326985122648297955796133936885544908593125505353122043196 30
114 8195146005170721743000351378750844763591907317946596741559388076380076439395878678616603448205981273694057542624240
115 1333265998150879067258514366058848424694264827136019497641657832528422606112553742802218310861353522535600887569 1758
116 2147130977496706751188061745492029353297199657633759947558374333898586842325859997631292383928544439581969354962816 0
117 3422885825654794593882416617750686270396538722608622540251364807968005078081358400814802756217278631362328064268052 0
118 5401678080083684333055820397166423892418981577326612892390629416666319362271567345064949125019634932283745325374087 0
119 8438736578435581250736349901399820105200209497862537122451500239494102639303949974272467170071898375550516733167 0700
120 1305113935901928883841938306184320902946274369256230986882177821204337669760729524751719412557307942283071285521684 44
121 1998256810896053325060175702049557396799637683810788541696708860503857907023890340793176731865874249376582388724556 20
122 3028973519155837271869505772802825449551289982316046394925321575873340921619116792584097733278713372543999136553058 80
123 4545589302525083504839561948882578340502650359502392978644708706968474457798095896763180640597022639433181023880661 0
124 6753743046188520074921993661579654151052303193634344252408368887505648138710729940730529287200771859899191509075852 30
125 9934989657351220050333665850415522929428807740306914493545031006520149659293561681283514946947008017227242737677381 26
126 1446997024088975895351351384234584583676568673884587019202139888107500170197675793305303404408472547827546282579473700
127 2086670362456572310930302512678901514790756473284117744989889850916448816905857864360261095733253913413230106761090770
128 2979439643212847546108273416519622149422962524036119543888953953143683268690346587504433504163011003565664019024618710
129 4212290470142958229151712777926927028446459308950907237228050323618808242725149403627355930906644989084412171485067320
130 5896758693140582121263517929206588196154727346021344439745924822932071576876949602066954887084553415443966241487697368
131 8173875078067151648615569567423430148955625726557065634310518070337736653173663884595823126824496010144162710128638597 10
132 1121942075081284032893278980136206688004975228691695593452141315416402075194892481767197796931286895789971606744951101 0
133 1524926182060304776811484168202313990579483997719641446834251288663743901639803921051832333657156131806789051593991 3990
134 2052443717512313230769791289997823158717481853171692882770223910532831312217506108287465837403672324932703387697898217 0
135 2735557273503358964777003803789999393941151177638502343401061967572950157907403147841084235899963463202096122811612185 0
136 3610609616013119351390245936439007030637615629677018836160341318228653385973683489841682977595724322507089625959190127 0
137 4719363840584126357870677648664807675838269452563298834849407094325591765999438077403567468519733377155327788225416688 0
138 6108894518350567262167652694156899100731739700058674654365770142084008121550107143200430610305681729677364822802501249 0
139 7831159633840809464653247500552396423703358357296584327921701496880495628963574542141553607006942217160674730792063107 0
140 9942185881039799230730031883886390299887230647816356202415457528865527816372991350542082460482945100261161521189644680 6
141 1250080922978114382213889113527207434387746728760478000075647950598950935165450348181144336594862998506599908383486425460
142 1556692959336353509953831121855307335599612152291054509537391336928590275081214154111226922413261069580311331056677082050
143 1919926338797004777981956225568577546155106208263912184761086941162953804799568256026955993231639405514856212340035495 10
144 2345261052054261530202977113265100607000808505844498720298710018708610696643350423318076282671707859052914938325058630
145 2837469173968246851644297727762205049103147831467689914899037630590899417452711850123123229259430868801292147733031141 64
146 3400265623175776775852708561681094698118654250745925576321969507327233379625398663804683104939566327629603628302841 4290
147 4035940478394512913803940776033509528039309528510759323593241342354277446564728542755716872336188854672591785539965465 10
148 4744991688714405305625606367988739258557074233780477769217368337789500466553889598166112118258492460155457912629445265 20
149 5525780637495065297991487943588525647016764611432224607927941426667047968238314078677456099573091860781200132055260723 90
150 6374235497661290074079688029135329895327616223013044956675689503182095081940290018551592449826185056275513147028970860198
151 7283628219565773867153153492645950477856241805509590040141682219686203491380889141721726549555667197668953833708353074 80
152 8244449974350196296550435000096464004958892052661274947351449340143249537230457685585856876837764534109824608412625085 80
153 9244406724972854431892401203985982246284728799017512029035096164501716801846488763969313568203353465734009167424109099320
154 1026855128289183058223809069345772659180166844829109090117117246517671318283603832030203587025521351600605143368601352260
155 1129956090916562902588335308610153215731958230278931477494529468092565803520737540357164599804131465434601357527060336622
156 1231816063060050658688367560353836269986993881589598177076889970177546394722874437144847727021229535428923818925897844820
157 1330368256245200802170469598180851402420278454100144120461185732154584855596210673473401051058359041189028524790610720 70
158 1423474141734920096466674808578990294825276258095835307299184706187637041151754521270805256902276670783787566554780961730
159 1508999688979036903947153546175146334091642661537910102516981242377157862932517817801856808846699906555289380880675720
160 1584896560540491280762978268759192413835549397498354280733893867353639334577704454031193916499541646363317388312768390136
161 1649283960717260272266337308051114914110170609395433436966624964477534770111776283011893020831396174289079559531486600800
162 1700526554616638073500041653082152855238837735020239680356794815395830033928180272700395014803671232653077498398308219190
163 1737303924247442991092570434037077881330572663550933757249920038353279972634721587452183112671373751213505699343791171980
164 1758667418197155843742212770167707399901393698016929675729799878319620718052926993356323161842014252516625564479241575970
165 1764080960275169852129690639151561431147628077926147158181288332272359419171455644712919212808493138264759463557088392584
166 1753443358676031278811825054568529508454589862388007427522936552677387242412730138578362579534413158446078706199908625300
167 1727090823808138685002437978908504332540162186577451500988889741291612236222505537704166262365851409088687870789868647070
168 1685779664983814063660514017302204255759630104159285399398359783374883262223065567816289105388250331326110127186654343510
169 1630650390174642322203909195452136834574651689069354676839973796832520761230973293561666851768888667538450146680009694 10

170	15631755773307595180717202493337810916320346133709373660312793610459733870420114581818697555484116093117969664161613101 32
171	14850948305413918134461330008327001309302225877288635135126308489924525201962354102979043596918783014808650246113892979 30
172	13983408101776123470965772489702906849928071549750295355029272777575613125165178563538494817968473713552007753955778995 0
173	13049606901987449091354433842357042765106126164140103467896844557701670547885643919317334380182264250486830168779375881760
174	12070374346278089786904247329881545494434089135289755221720516447150485570536999897507852064316599476980396172901302190 40
175	11066150146863697533317259663372252667902502228616624754859858794022853140860717623663777983466752632279305746155554924 36
176	10056311500671730631652770433205338685144975568059604614596368214107517143920555788205917909805143405311583671715500428 80
177	90586041432112630047180799674121993678760281262559884050206175043664576398431333540617143849534085346745539148127304992 0
178	80886967005612152184392311145332518322245072882154437236886254307214984828922822520951266670484908502344429872983980912 0
179	71598687385668740048861416271323356304572068669200764921609834748309937672316317283347959722349267607417641139418850821 0
180	62828338948699730279715365694828841564915286788887797985475576827956264491319488572126577981881937223404485860545140049 2
181	54656913692264065973044330495103582133898415825547754982924690030585934424780092867765410769805993524031779178326160881 0
182	47139923489253126426941169941169471907939166576845773475548022741802728554735779064327174099949316271008427934048038120
183	40309029876019143312359828587064848929341030152937525954684923931344236701821284327770706291225903913205506031676114936 0
184	34174424788547618906267803638578978925003321041729386409260638776639658138137440762009516106029527114841228923553271100 0
185	28727735374838619842006547094370237843793273869091517425923592872573971876418486989348189804727105534029232094307954342 8
186	23945230404500322597815627292775025379609456581495337502482122388855530746529744470503120235981680884312579504758401231 0
187	19791123975571333324365341271213242535540996809006723676719294554260997682418744479017442546225414153803371923706287220 0
188	16220800632256424777442249344611375925708470232391098007719053386552391439785686273073873737579981552603154856121147493300
189	13183820869321386686954913702135486751911923706904581317541541139051503649998432647454258164097798595585278724653938240 0
190	10626603663460661140530547489114247203164715785568858670627725896487164536562734110082163266454929210665824705909285246 6
191	8494719928971786626814327237473784088037711683176422703223192652075512309774096914297624361600059367100555933048150379 0
192	6734765069903900234268024559497695242195200684368411110607669748801280565123257128181006375899065806205544025386315264 0
193	5295808255461549618761888076080435312525671557502583544863788685365700537175980459853882708307567021984334733477117879 0
194	4130439590070704999780039928617005650403755930241330093569464328958527899007964419823710979650327857974098516817466802 0
195	3195453581693348742476316880862270786268855137612211669672455811871028874301273206166277849026279473187125622557636322 82
196	2452218404366976508173796642455680810043861553770601393477946705157298444281105438378658586013941285647801687129715604 0
197	1866786010236456700736422776122767126690732059254908809719687292709573167081282927934955642968557070030090241577545892 0
198	1409799063848107874226732780966201841890089881866377595253182140901425513167657088010343022164639643509038236128546350 0
199	1056247982145188869049736914721332890534282836311950238859548409769876613999137479621325143029847110907052890544222374 0
200	785126125460718192715827293771098592178484055692869872390060484611564257309891300756538794998633294386323038461922651 0
201	579024385663461960031142309075285199327921430320714005668034511983651520589915085534540429720663628294317793259361520
202	423698911460422952075918713150128578301513162226873618227235976734201995329807012425107192343465888677381508936450269 0
203	307638182497271589431264457074496708243927209955454500855065938307429562703570120300043799996759270646160205028911879 0
204	221648597916688242246500438900759010607572976117092912641418539344088131003688673906921044227942535250758704143716466 0
205	158471513667639724558035169962628467472436915994376986760352569931915113798267741939377415630823731722858438961358429 4
206	112439426829897511494861760736001678887012511246821514378217149671954792001091522366230735660758985955894997588678622 0
207	791748219782345662060799027827342804908166900071036747871006051501083494019907577565532508734754165201190371985350940
208	553320292020364456635882152753697742977341593302325326299408938375366000110740372259446263756259536554382713192729150
209	383801982903420944991258496550578186047887508765454529148366062064243833816680775594584244870254784089231386202015142 0
210	264240350264235065217973431837196135533380713113998395617469476582673182208976495655099193699522306235799877087055460
211	180581249625961023237988712580882027691691448826578447690681838420498644709373125833258005793171936060263898588314760
212	122503402249199084162050907149717474942071478573736678730667241392468806613653947835511635626168147340268922702500600
213	82498508300361741381002221611797512302056049753649691278758099539829429581951751574583259873277798623753756396079470
214	55155273463928545267432704168770663862521838496467165608479771778544106150424902774500669280177153797395604042756570
215	36609316116465229823788261880379867929180242272881180660753074852839075655064880923071048178980235851265535964051648 8
216	24125732806718697669133711932574940825214108037225916906036275700152808510963955404212936414733624484477044550464220
217	15786087093839687991252748732908086159320652754530680151894123946847703254004551212171736616117621402390814914543670
218	10256386437734085126822816707864959143875733895929129008177611068640719231525115277349728186786902847382995842805970
219	66169983481569339040707040096113755655801587223600170346607516991927858459265283086383062314610561315725152211158 40
220	42393118116854053114616987970026455436717399240541988350514100408624824585578585130430510372366717848336579036737 18
221	26972322032160305734106007844487003466737192064458000956134302658806800883490567536747507307323467889320762738957 80
222	17043192223164693572409680612451700181799181998181920861650441375165099068640599413570578211405909384947314097421 00
223	10695822810940309591111357482662763459694973410669595475431139045215328443097324631251915464985381532830409385508 30
224	66669800176816371688225966472694675935225564150248094372712949572350824698464073888691669845127108438985319736002 0
225	41277830897364235604403893029985391969041786998163339750274218623566159039510083350563352320936219539084269905171 6
226	25386242253841014808110134696275607484387273731659104036481889286578871457948137879320992828034753414857529767761 0
227	15509396478304090318576400099233957716824327419132909383031273856800628110426038918248298742315114895562011675355 0
228	94129855866244287662397481415417555019493151678599541762015244259668675072944412354274317291297927894465132989070
229	56756681806227973765900815059624343302643117170212864336387264931793568480320337417441897249345716248197455495000

230 340004601394786800968672934204064825743960173760894285044959870637012239670541480647633785039476121934853552453 96
231 202372670191324511278994487303034627951849428045854393138299252179605634852945020153237068573601955797699260435 20
232 119684872555293365804239463256235875773293208853889118379313281618749535445466961718158417076854696296341991442 00
233 703344405672636761437194541542846408412609565005712144616464362449463551502305069754104162522381262348657030785 0
234 410732634551464227411725545149069004557815926433918134950862668632703635303504624926438865165460308665176080511 0
235 238360219648586840632188564240566399876431163248724718973334058354545709272416461148143761274062224357630433744 4
236 137471509220321491840657632296607062991137512398694731407726613702265125727507293620804202618416753951980817226 0
237 787983116923680116689540748783992893453283097806566904094383548630430590641572314535299728808788348312290222290
238 448918296354673933425312881012425092568505304399422787171305383472780078415708680584785670582225724608124357910
239 254205377480825092051849008647108540464629845651970896475481627975773289544564561761375674649860267206290945800
240 143083647335835470776261439591286580122103214010143329543192518934409291320054550813572982175290468678797573488
241 800578407431917655580753361246905843046587888734519825059426406681379468477599966349833001150238168914099796 50
242 445294215523154245057101400939072919605239923798492173891410195435522079708410193136476398030287200836174909 30
243 246229566821696684918498063558069300491619420775629562777386319033378092351835170475539121241908673228358629 20
244 135364228977395767371996043447485483761553672797127666658660586936380296628650003603764905669427976892616995 0
245 739875645371612539371609716823050096857500650599133027151286040208650187357140758939881794180476752306958802 4
246 402091722279871294240256622649425699673691547892067824837386650432249951647065239618072094068568510617515246 70
247 217281889593836452877131969924301040854305432298922190266910201303828470530528695320413129930198636216407203 0
248 116754672299291694534783052439436008311653487909631585873940693833861187091747771969125504659664297982840497 0
249 623875066845607705032728796537652165110359821490039337481391141457187159875751653984110676141387368513150280
250 331523116575677524857400898780827320079174262519876934829377215155164332128111948975239159508909039918009764
251 175203574994768247807444841612279488455255431406800054193078545350966063590892132049942009446580696748045790
252 920884427673822110861445283101137272020032599851722882642550391833592828882217505118592600515033718398275260
253 481415749293370841865504291897182924291335117203355030201926774421957544391740340762092638336275317157661 20
254 250327383981939779405920089404753559824870058250213595320596456979064132183384267487511977664470975625401 90
255 129475963686661213903475898364827430161830310969917902582452442499160782798799141907020146296685054439310 86
256 666165915863375059703757567373364085036923640694743707649500995456811105007760064421420322764521315850972 0
257 340963418813144274507003304087171647039716198242317625057683494861113475672441331944600841453078248029587 0
258 173614047079152963358182804001609561523227967517564720725560155744563645880393688149823192373606568271953 0
259 879494478685090017412291057001119432443078359247684769002977802220091445312300694797216526924551611175682 0
260 443273691723182816360229179133643981414375923906817474436493016408067643244284705709173206064727887908892
261 222290391855953287369388451026186510920711575082588056173528581272476501856665849327728792364246989962420
262 110917109976051136644317339602609365211754007064378138181246828582042629967977723648867402810773278867850
263 550712142192789311765204698883661864280164697614206734917612300436281349464355438346879430655535197449 90
264 272093429899048356667148062740257208006214480429760165772106119519174540225333278656111006375632310947 90
265 133782007060900414305833866918706517630189096182517367329689803615452845517278134737141675744896937607 26
266 654609747963990844828449539569675389153386891712558181854759287704067817513707116459661882497960082811 0
267 318780029460183687067013995920822826748159979935906363652061214649267590373453848403482650145716243450
268 154504914132033670816307840968109166647091975574385679359155523619082875230467808318882395773515275644 0
269 745340331005696025675116213651002972306262486411905517616129562336842576576393983704146097376883459990
270 357887532631021303106959260175418408523619143019931071722773070892150288953429665126291974194527370072
271 171055299864644143827485735232378226561070775723280926679064596349695959228063702594077639596105509510
272 813847095269259109968094843780430651183726104408677725025510156862157862911561728391787844436675123 10
273 385463824139261559942487133194191076642828035953079018075461706352301902094987099226302787515510305 20
274 181751109620615896975069682940248411935241250080313597437478091987712105442592067792628677249947694 10
275 853180994191588493411215198342897938556915380228271967590501710541181327997045862088457035810558084 4
276 398743718597529510502994759771179175121767239896957081173355254115408874195740053146900392060211 310
277 185546578029839118208097863323690394249219232698959567565572076669738353575344010233109101327154286 0
278 859678754371322477065064900720084297508796557266457643324743957350290127884907148890943038964227760
279 396607784362000584362859469034910628374041383104776216314686646465982179770013148031679015476599040
280 182198846054036602353318598568535997174557170477176472310409290698364789035603556483258350507838552
281 833502331511495175192235595465879792201699756200238829836921646982775136533099533922248672982967 00
282 379718882820893011932159774105131600763480494970582224585747074371786561263147279780788981910976 60
283 172277685170406083647979942046120230916192099472859317975910425510390783132547579560603527773057 70
284 778438860606528783397734655543220356543359014060935055201679526150791262219337263573234782889746 0
285 350320649464726881393173542063942688779515534587906020725414019030683560698656066398534701079005 8
286 157025334840515651359970036930123614824599676259706899902912465356413168705922960632390781379921 0
287 701057125499872249136653630380320005914452040256095284226686171944636589889469341152465680806840
288 311769493999114226339991526168215033863385712592391453301192519613068750274396613400605271157850
289 138110633459670793489442235761092859294499343222152566506525797972658056009842489924126878373370

290 609467541129068135564914042822353835426430921962268036911865467897223711519528449249834661053 14
291 267929543995901889579454724049219046856103572432931501601874859836428571633913780920736885699 30
292 117342059296328875918994415138548312532606080256122034203730628690608297180234195519689355467 40
293 511995710994764841549992829286414375584459254373892227027885404100315534794187250745955221938 70
294 222574200466514570336878619759910384601922543707005168557059620993220621854311215829897944524 0
295 964040980150521303983037642503745441733780548661664546002986607573515237170665236111168084462
296 416049080486909726620687225945269612631058044532433423607639149599011070560695958243811752980
297 178911472469134668942802868777031032913499766815526406347371964488217086703409777490159383510
298 766641733018862985041049410152520276378272639115347826851061957311822606923712003329630540 30
299 327358329651070985238176410222286764727300844318171962443577910262455033040166305792614297 00
300 139298672614787255910425639597617231810121278583326080778351459776611746337367716058667671 12
301 590716522167887155402076611836355776441226834223862294422162250470288301580986872776621491 0
302 249652362366926762200818574362434130159312967618593788380526403692303754209779974714910113 0
303 105155617829983539139844074576422843129446334360538523472862527745074190945754134564342563 0
304 441453829080043004494493222001390307763820551693640657366637311431437663834134153838857750
305 184718264003952264969258328460100293520389464178505424609794557522155001450024738957318832
306 770409850070758347048169761203674083439128235562176451474308090535873861017196026149830 40
307 320285235754966526716344227526597148446290958276349014954832754581391473153352187319830 30
308 132730507839492581704069090833751377231890512992632488127710079206888747245786577704425 10
309 548326147165113715632924494623334528081383453503583994919273368042027703116809816468206 0
310 225817254154155625922356960919695694903936076634303901181333012956066848929726642603729 6
311 927130456884986513164493098197508655508108553533208835232624884015470354428910758473280
312 379494706230139545787785403983467253919309335783916074961547328665346122219100314936550
313 154870012496705575846917788052403770872673945867276438780441756047879471166192291860820
314 630146137663254321404650515283419604366378872223719344704578009823176623562788956749 90
315 255648452180829878896517663308068393932520847852909284293690994143929880551036319326 8
316 103416212753932112050104227589529469911933244704588049481306375754637059480668755233 80
317 417151028018775086711162672803837576932774868673335101453112105480442709494746758147 0
318 167792645374724854320878897094230319127268641902771085325705616706744542293852357388 0
319 673043544279484968205988814795843183448873474171800343681747620899180975325885732120
320 269227744910601721819045355291093942818649560621282345830601885192796907745303427556
321 107403564171123683567307643781195392676685038491441007283096011991258912170511929880
322 427322422018235066828365256309930140960386676493363387410233103898206611271052633 70
323 169569101053627876964170024867635122393860803416831173069085822770481050401547226 10
324 671131794381121481775201936495181162885311026523423053290397315095396344996871014 0
325 264944588742540796789782724863142230626949793522090922847517008687063163955422184 4
326 104328893919084195872992068471004716684505219679783443971142701298124083624866750 0
327 409800713745515870547320382671474281355187580098124647486132959607215622695909190
328 160574180323123790375916588622112269035063212558781442887041253672574966648040820
329 627668079340442327924224231790272473451109128240410974223461204183431927865808 60
330 244766637707844906837920743489729819493922741403545812713601746960032983650702 08
331 952267304472101944496140522120870645767579372720252120194236107269664547291803 0
332 369629577479100016594044961190185265098668463628691190571901418809307341000900 0
333 143150400320797242971023910361695114108917511187374799294226270296684730797171 0
334 553163276370226837212538901734476775621804950129624072175098908852726379601950
335 213287814504999244235189925639551974931955610661193352215145897284749360825478
336 820630732154797850708908171728687288666412760135659002675300748936885133948760
337 315076289407197727346344570925432715618597667119982478501792010908252432974 80
338 120722199989582027402680789000060867342771697611957506176645781665135501517 30
339 461614417717905435857988510790306691063909344930902289661228481706534732506 0
340 176161006257525607302773558908508769761524435839000499944826699242039892323 0
341 670958763856484613275861186079019225332377785266526216602584384794905075360
342 255067411614231641079368540137855376697888307616662387257768012975057350430
343 967842526848129099090605553438014379245765314045985114436559016081692210 20
344 366574700078040467391059079490299991144991244300333336244693662761515723 50
345 138594434881307531344058149544093870540557456873384210726283155966274126124
346 523084706718079470799934974892531779026485961985978331501951755123421700 0
347 197087245044673860664977930010717228460779798624884825902545973641402728 0
348 741348681884151968674785095037160777641184125713174363560385788534291020
349 278407633196373077252865671333761760592929737169152770859082529782333610

350	1043881808992259705982713856415218420479605947268156007246800014720328 08
351	3907957735585330844594592661003661106541005376298816125505981757168060 0
352	1460808426659255559459134580445193149496500134401651024113023770545449 0
353	5452527107883040419349750764202004610467022581206240394419001503778430
354	2032261311746467922648571963245397225813119610709015571261856459286560
355	7564044406450649832993062455417150834379582054156255238531356154009 0
356	2811490896036297356532262129492595067594493381004403673802230348575 00
357	1043619695219577821859643074904588133507921934374409949744695166155 30
358	3868880040230758560447233336722232454583923625076958306732223991763 0
359	1432450538248410314792237677262455323928462112232120766200876193755 0
360	5297107985885322084041906380200183336085628061132663881635194581022
361	1956481469265843264429639143086463970418747840635023407560104365620
362	7217764260930302985696659540584306816654294453325552783477091527 10
363	2659692345691399847032424054545646673228023217733979680576226780990
364	9789780320107831502073936143135029172521598262379451046952757505 0
365	3599463225178898128675140475528388047667298256560335908284545922 0
366	1322012386647189371100679798561356300027504475418969770730386716 0
367	4850375218770909740377543073927898637244714472074981165517119220
368	1777728782963339380508668125724423961304021504647911003136014350
369	6508990407729203022255385844242141042572212500662515125762500 90
370	2380820168703001950440196961319985938229515621902207709159916 30
371	8699825256582424131158065376959623439522134204839927069724837 0
372	3175929476497951008180693093719893214096184324668275811384334 0
373	1158276472801432621654094254297379645388251422329968624532411 0
374	4220254518203455701052244065042195128207960306065305457659710
375	1536219681608075766363847797348183927089558917348292018781996
376	5586744773226388146896754002145583375567701420918075670017 00
377	2029817697379145619790017315515616870114668078564448299090 10
378	7367991978359395297105982956555272193904047489580724600822 0
379	2671995536030749036965206791460032720671573882661844630800
380	9680922289760120585416667517395955654080988772101918562806
381	3504221201478452105078377134657078066874075193329107616110
382	1267239913295791686531046733356408154202526799438767664580
383	4578433960277182603558817824710622155385817877089930631 60
384	1652584030908422175272349000108302011154260579741497927 30
385	5959308123623130426186231391687808743239653764913181588 6
386	2146893744489679644697213845057923112191404805012731215 0
387	7726876217950066020507028827563816944982814693579290970
388	2778253668220970404766243335201560498590692075193643900
289	9979523477923951916061635932925625924695181553410897 30
390	3581069205201282344030291010588525472734208953639817 32
391	1283734710346703642226417046716267602458895088893359 20
392	4597183199999131277227800855999432536412170950697667 0
393	1644584687004798365352503302028751768628765612965489 0
394	5877087919596339162047374990048543496492347807885230
395	2097987659317841314370575539655929282801969752316306
396	7481202802385693265463802259146879824569987412429 20
397	2664773673571563509438730780819791640295782900346 20
398	9481170732094306477478590386892429533052966970508 0
399	3369522546456033103029191481728856112356100126875 0
400	1196110335565024282472556231466472217467760904643 4
401	4240938763541794461620260426100782104232130893020
402	1501867897209514546756012058307128937792218498970
403	5312160845767253370716962342480249385723765082 00
404	1876596498539385905321765872371613022376800193 30
405	6620959251941270710533933980546460891650449625 4
406	2332980166361902053840221902929003469914879669 0
407	8209765329630007661929846928051799320063962350
408	2885154665895064351375397817745283357389506120
409	1012546201826143529345989269517695485334973470

410	354859432004617995408116287222442620846642266
411	124188560316112193199493764454662781404431220
412	43398843209732911228258318884763721450637930
413	151437426449073862674425494968869992587776160
414	527634954596571933620235068941120717381902O
415	183554700298935630201070142844119268381471O
416	63755105583597856332458983253562276204759O
417	22108912843264584112540219104201706511340O
418	765433978565842420565744369009543768030 70
419	26455777454036744071170383699684960210910
420	91282968165225400852099148391209671153 44
421	31441186795099715962252274455914397166 10
422	10810132272592039130876880260615943165 90
423	37099534825848983999979796295132982O660
424	12708465807051116129642913786459882222O
425	43449659859330678750374930995710275238
426	14826165756474112306472381983708806180
427	50489468285334911905012077786722133 30
428	17158586283816374424703618619456261 40
429	58190231007518407097826608523277032O
430	19691751775883618754017480497169424 6
431	66490907878965090282613179379919820
432	22400612756699512891008681727445130
433	75292923311727288958504930382759 70
434	25247546621568104084193053069540 10
435	84456058191801432357832213578239 4
436	28181269707737038038330384718935O
437	937959220556829109685756162865 60
438	31136477853796788558374255563050
439	10308415816796044222065696541740
440	34034171210058712457447210589 66
441	11205124854411125643454046264 10
442	36783599119727393931359804190O
443	12039394526871663009298264524O
444	39284164234229947428482378550
445	12778584955973003784521168082
446	41431703552514002794520678 40
447	13389209317061646588105169 20
448	43119306761941125586018350O
449	13839331723992520021799676O
450	44253449299641932480688288
451	14099024296691022273180750
452	44742572879608373319734 40
453	14147730617149281150482 10
454	44538802964432061154479O
455	13964063783075537778968 4
456	43586485006827749778540
457	13556331531368316465390
458	41919107388901630840 80
459	12903926851109306788 80
460	395358469036192647396
461	120762928927652770980
462	36548417940201818550
463	11014181443509355620
464	3307225528666158120
465	990706243935624174
466	291477487001919120
467	85733015763564810
468	25246047782745090
469	7399696043175570

470	2086326646454628
471	599101822655130
472	174116764660860
473	49520192753070
474	12988896122430
475	3699657010116
476	1076263554150
477	288545344020
478	66595291470
479	20069636040
480	5894444562
481	1379596770
482	255032280
483	97330650
484	27450810
485	4768380
486	603600
487	428220
488	95850
489	8730
490	540
491	1530
492	180
493	0
494	0
495	3

Bibliography

[1] Abe, R. (1967). Logarithmic singularity of specific heat near the transition point in the Ising model. *Progress of Theoretical Physics*, 37(6):1070–1079.

[2] Andrews, G. E., Baxter, R. J., and Forrester, P. J. (1984). Eight-vertex SOS model and generalized Rogers-Ramanujan-type identities. *Journal of Statistical Physics*, 35(3):193–266.

[3] Ashkin, J. and Teller, E. (1943). Statistics of two-dimensional lattices with four components. *Phys. Rev.*, 64:178–184.

[4] Atkins, P. W. and de Paula, J. (2006). *Physical Chemistry*. W.H. Freeman & Co., New York, seventh edition.

[5] Baxter, R. J. (1973). Potts model at the critical temperature. *Journal of Physics C: Solid State Physics*, 6(23):L445.

[6] Baxter, R. J. (1995). Solvable model in Statistical Mechanics, from Onsager onward. *Journal of Statistical Physics*, 78(1-2):7–16.

[7] Baxter, R. J. (2007). *Exactly Solved Models in Statistical Mechanics*. Courier Dover Publications, third edition.

[8] Baxter, R. J. (2011). Onsager and Kaufmans calculation of the spontaneous magnetization of the Ising model. *Journal of Statistical Physics*, 145(3):518–548.

[9] Bhanot, G. and Sastry, S. (1990). Solving the Ising model exactly on a 5x5x4 lattice using the connection machine. *Journal of Statistical Physics*, 60:333–346.

[10] Bowley, R. and Sanchez, M. (1996). *Introductory Statistical Mechanics*. Oxford: Clarendon.

[11] Bragg, W. and Bragg, W. (1915). *X Rays and Crystal Structure*. Bell.

[12] Brush, S. G. (1967). History of the Lenz-Ising model. *Rev. Mod. Phys.*, 39:883–893.

[13] C, M. (2000). *Matrix analysis and applied linear algebra*. SIAM.

[14] Callen, H. (1985). *Thermodynamics and an Introduction to Thermostatistics*. Wiley.

[15] Chandler, D. (1987). *Introduction to Modern Statistical Mechanics*. Oxford University Press.

[16] Chen, C.-N., Hu, C.-K., and Wu, F. (1996). Partition function zeros of the square lattice Potts model. *Physical review letters*, 76(2):169.

[17] Cipra, B. A. (1987). An introduction to the ising model. *The American Mathematical Monthly*, 94(10):937–959.

[18] De Graef, M. and McHenry, M. E. (2007). *Structure of Materials: An Introduction to Crystallography, Diffraction and Symmetry*. Cambridge University Press, first edition.

[19] Diestel, R. (2006). *Graph Theory*. Electronic library of mathematics. Springer.

[20] Domb, C. (1949). Order-disorder statistics. I. *Proceedings of the Royal Society of London A: Mathematical, Physical and Engineering Sciences*, 196(1044):36–50.

[21] Einhorn, M. B., Savit, R., and Rabinovici, E. (1980). A physical picture for the phase transitions in Z_n symmetric models. *Nuclear Physics B*, 170(1):16 – 31.

[22] Elitzur, S., Pearson, R. B., and Shigemitsu, J. (1979). Phase structure of discrete abelian spin and gauge systems. *Phys. Rev. D*, 19:3698–3714.

[23] Enting, I. and Wu, F. (1982). Triangular lattice Potts models. *Journal of Statistical Physics*, 28(2):351–373.

[24] Feldmann, H., Guttmann, A. J., Jensen, I., Shrock, R., and Tsai, S.-H. (1998a). Study of the Potts model on the honeycomb and triangular lattices: Low-temperature series and partition function zeros. *Journal of Physics A: Mathematical and General*, 31(10):2287.

[25] Feldmann, H., Shrock, R., and Tsai, S.-H. (1998b). Complex-temperature partition function zeros of the Potts model on the honeycomb and kagomé lattices. *Phys. Rev. E*, 57:1335–1346.

[26] Fisher, M. E. (1965). The nature of critical points. In Britten, W. E., editor, *Lectures in Theoretical Physics*, volume 7c, pages 1–159. University of Colorado Press, Boulder.

[27] Ford, I. (2013). *Statistical Physics: An Entropic Approach*. John Wiley and Sons, Ltd.

[28] Geim, A. K. and Novoselov, K. S. (2007). The rise of graphene. *Nature Materials*, 6(3):183–191.

[29] Ghulghazaryan, R. G. and Ananikian, N. S. (2003). Partition function zeros of the one-dimensional Potts model: the recursive method. *Journal of Physics A: Mathematical and General*, 36(23):6297.

[30] Gibbs, J. W. (1902). *Elementary Principles in Statistical Mechanics*. Yale University Press. Reprinted by Dover, New York, 1960.

[31] Hales, T. (2012). *Dense Sphere Packing, A Blueprint for Formal Proof*. Cambridge University Press.

[32] Hamermesh, M. (1962). *Group theory and its applications to physical problems*. Addison-Wesley, Reading, Massachusetts. Reprinted by Dover, New York, 1989.

[33] Hill, T. (1960). *An Introduction to Statistical Thermodynamics*. Addison-Wesley series in chemistry. Dover Publications.

[34] Hintermann, A., Kunz, H., and Wu, F. Y. (1978). Exact results for the Potts model in two dimensions. *Journal of Statistical Physics*, 19(6):623–632.

[35] Huang, K. (1987). *Statistical Mechanics*. John Wiley & Sons Ltd., second edition.

[36] Huse, D. A. (1984). Exact exponents for infinitely many new multicritical points. *Phys. Rev. B*, 30:3908–3915.

[37] Ising, E. (1925). Beitrag zur Theorie des Ferromagnetismus. *Zeitschrift fur Physik*, 31:253–258.

[38] Katsura, S. (1967). Distribution of roots of the partition function in the complex temperature plane. *Progress of Theoretical Physics*, 38(6):1415–1417.

[39] Katsura, S. and Ohminami, M. (1972). Distribution of zeros of the partition function of the lattice gases of fisher and of temperley. *Physics Letters A*, 40(4):283 – 284.

[40] Kaufman, B. (1949). Crystal Statistics. II. Partition function evaluated by spinor analysis. *Phys. Rev.*, 76:1232–1243.

[41] Kittel, C. (2004). *Introduction to Solid State Physics*. Wiley, eighth edition.

[42] Kogut, J. B. (1979). An introduction to lattice gauge theory and spin systems. *Rev. Mod. Phys.*, 51:659–713.

[43] Kosterlitz, J. M. and Thouless, D. J. (1973). Ordering, metastability and phase transitions in two-dimensional systems. *Journal of Physics C: Solid State Physics*, 6(7):1181–1203.

[44] Kramers, H. A. and Wannier, G. H. (1941a). Statistics of the two-dimensional ferromagnet. Part I. *Phys. Rev.*, 60:252–262.

[45] Kramers, H. A. and Wannier, G. H. (1941b). Statistics of the two-dimensional ferromagnet. Part II. *Phys. Rev.*, 60:263–276.

[46] Krieger, M. H. (1996). *Constitutions of Matter: Mathematically Modeling the Most Everyday of Physical Phenomena*. Cinema and Modernity Series. University of Chicago Press.

[47] Kubo, R. (1943). An analytic method in Statistical Mechanics. *Busseiron-kenkyu*, 1:1–13.

[48] Landau, L. and Lifshitz, E. (1968). *Statistical Physics*, volume 5. Pergamon Press, second revised and enlarged edition.

[49] Lane, S. (1998). *Categories for the Working Mathematician*. Graduate Texts in Mathematics. Springer New York.

[50] Lee, T. D. and Yang, C. N. (1952). Statistical theory of equations of state and phase transitions II. Lattice gas and Ising model. *Phys. Rev.*, 87:410–419.

[51] Maillard, J. M. and Rammal, R. (1983). Some analytical consequences of the inverse relation for the Potts model. *Journal of Physics A: Mathematical and General*, 16(2):353.

[52] Mandl, F. (1988). *Statistical Physics*. John Wiley & Sons Ltd., second edition.

[53] Marsden, J. and Hoffman, M. (1999). *Basic Complex Analysis*. W. H. Freeman.

[54] Martin, P. (1982). Discrete abelian gauge models on small three-dimensional lattices. *Nuclear Physics B*, 205(2):301–312.

[55] Martin, P. P. (1983). Finite lattice Z(3) models in two and three dimensions. *Nuclear Physics B*, 225(4):497–504.

[56] Martin, P. P. (1985). Potts models and dichromatic polynomials. In Giacomo M. D′Ariano and Mario Rasetti, editors, *Integrable Systems in Statistical Mechanics*, pages 129–142. World Scientific.

[57] Martin, P. P. (1988). Exact finite lattice results for Z_n symmetric spin models. *J. Phys. A: Math. Gen*, 21:4415–4421.

[58] Martin, P. P. (1991). *Potts Models and Related Problems in Statistical Mechanics*, volume 5. World Scientific Pub Co Inc.

[59] Martin, P. P. (2000). Zeros of the partition function for the triangular lattice three-state Potts model II. `http://www1.maths.leeds.ac.uk/~ppmartin/ZEROS/pdf/q3tri2x.pdf`.

[60] Martin, P. P. and Maillard, J. M. (1986). Zeros of the partition function for the triangular lattice three-state Potts model. *Journal of Physics A: Mathematical and General*, 19(9):L547.

[61] Matveev, V. and Shrock, R. (1996). Complex-temperature properties of the two-dimensional Ising model for nonzero magnetic field. *Phys. Rev. E*, 53:254–267.

[62] McCoy, B. M. and Wu, T. T. (1973). *The Two-dimensional Ising Model*. Harvard University Press.

[63] McCoy, N. H. and Janusz, G. J. (2001). *Introduction to Abstract Algebra*. Harcout Academic Press, 6 edition.

[64] McKie, D. and McKie, C. (1974). *Crystalline Solids*. Thomas Nelson & Sons, Limited.

[65] McQuarrie, D. A. (2000). *Statistical Mechanics*. University Science Books.

[66] Montroll, E. W. (1941). Statistical Mechanics of nearest neighbor systems. *The Journal of Chemical Physics*, 9(9):706–721.

[67] Montroll, E. W. (1942). Statistical Mechanics of nearest neighbor systems II. General theory and application to twodimensional ferromagnets. *The Journal of Chemical Physics*, 10(1):61–77.

[68] Newell, G. F. and Montroll, E. W. (1953). On the theory of the Ising model of ferromagnetism. *Rev. Mod. Phys.*, 25:353–389.

[69] Ninio, F. (1976). A simple proof of the perron-frobenius theorem for positive symmetric matrices. *Journal of Physics A: Mathematical and General*, 9(8):1281.

[70] Niss, M. (2005). History of the Lenz-Ising model 1920-1950: From ferromagnetic to cooperative phenomena. *Archive for History of Exact Sciences*, 59(3):267–318.

[71] Novoselov, K. S., Jiang, D., Schedin, F., Booth, T. J., Khotkevich, V. V., Morozov, S. V., and Geim, A. K. (2005). Two-dimensional atomic crystals. *Proceedings of the National Academy of Sciences of the United States of America*, 102(30):10451–10453.

[72] Oguchi, T. (1949). Statistics of the three-dimensional ferromagnet. *Phys. Rev.*, 76:1001–1001.

[73] Oguchi, T. and Taguchi, Y. (1986). Transfer matrix and finite-size scaling for the Ising model on two- and three-dimensional lattices. *Progress of Theoretical Physics Supplement*, 87:23–32.

[74] Ono, S., Karaki, Y., Suzuki, M., and Kawabata, C. (1967). Statistical mechanics of three - dimensional finite Ising model. *Physics Letters A*, 24(12):703–704.

[75] Onsager, L. (1944). Crystal Statistics. I. A two-dimensional model with an order-disorder transition. *Phys. Rev.*, 65:117–149.

[76] Papoulis, A. and Pillai, S. (2001). *Probability, Random Variables and Stochastic Processes with Errata Sheet*. McGraw-Hill Series in Electrical and Computer Engineering. McGraw-Hill.

[77] Pearson, R. B. (1982). Partition function of the Ising model on the periodic 4x4x4 lattice. *Phys. Rev. B*, 26:6285–6290.

[78] Peierls, R. (1936). On Ising's model of ferromagnetism. *Mathematical Proceedings of the Cambridge Philosophical Society*, 32:477–481.

[79] Potts, R. B. (1952). Some generalized order-disorder transformations. *Mathematical Proceedings of the Cambridge Philosophical Society*, 48:106–109.

[80] Priestley, H. (2003). *Introduction to Complex Analysis*. OUP Oxford.

[81] Quarteroni, A., Sacco, R., and Saleri, F. (2007). *Numerical Mathematics*. Springer, Berlin.

[82] Sands, D. E. (1993). *Introduction to Crystallography*. Courier Dover Publications.

[83] Savit, R. (1980). Duality in field theory and statistical systems. *Rev. Mod. Phys.*, 52:453–487.

[84] Schneider, H. and Barker, G. (1968). *Matrices and linear algebra*. Holt, Rinehart and Winston.

[85] Shackelford, J. F. (2000). *Introduction to Materials Science for Engineers*. Prentice-Hall, Inc, fifth edition.

[86] Stephenson, J. (1987). On the density of partition function temperature zeros. *Journal of Physics A: Mathematical and General*, 20(13):4513.

[87] Swendsen, R. (2012). *An Introduction to Statistical Mechanics and Thermodynamics*. Oxford Graduate Texts. OUP Oxford.

[88] Syozi, I. (1972). Transformation of Ising models. In Domb, C. and Green, M. S., editors, *Phase Transitions and Critical Phenomena*, volume 1, pages 269–329. Academic Press, London.

[89] Ter Haar, D. (1952). Statistics of the three-dimensional ferromagnet: II. Comparison of various approximation methods. *Physica*, 18(11):836–840.

[90] Ter Haar, D. (1953). Statistics of the three-dimensional ferromagnet III. Some numerical results. *Physica*, 19(112):611–614.

[91] Thomas, G. and Goringe, M. (1981). *Transmission Electron Microscopy of Materials*. TechBooks, Fairfax.

[92] Valani, Y. P. (2011). *On the Partition Function for the Three-dimensional Ising model*. PhD thesis, Engineering and Mathematical Sciences, City University, London.

[93] Villain, J. (1975). Theory of one- and two-dimensional magnets with an easy magnetization plane. II. the planar, classical, two-dimensional magnet. *J. Phys. France*, 36(6):581–590.

[94] Wannier, G. (1966). *Statistical Physics*. Dover Books on Physics. Dover Publications.

[95] West, D. (2001). *Introduction to Graph Theory*. Featured Titles for Graph Theory Series. Prentice Hall.

[96] Wilde, R. E. and Singh, S. (1998). *Statistical Mechanics: Fundamentals and modern applications*. John Wiley & Sons Ltd.

[97] Woolfson, M. M. (1997). *An Introduction to X-ray Crystallography, Second Edition*. Cambrigde University Press, second edition.

[98] Wu, F. Y. (1982). The Potts model. *Rev. Mod. Phys.*, 54:235–268.

[99] Yang, C. N. and Lee, T. D. (1952). Statistical theory of equations of state and phase transitions I. Theory of condensation. *Phys. Rev.*, 87:404–409.

[100] Yang, H., Hernandez, Y., Schlierf, A., Felten, A., Eckmann, A., Johal, S., Louette, P., Pireaux, J.-J., Feng, X., Mullen, K., Palermo, V., and Casiraghi, C. (2013). A simple method for graphene production based on exfoliation of graphite in water using 1-pyrenesulfonic acid sodium salt. *Carbon*, 53:357–365.

[101] Yeomans, J. M. (1992). *Statistical Mechanics of Phase Transitions*. Oxford University Press.

[102] The GNU Multiple Arithmetic Library. (2016). Retrieved from *https* : *//gmplib.org*.